Magnetic Properties of Transition Metal Oxides from First-principles

A DISSERTATION
SUBMITTED TO THE FACULTY OF THE GRADUATE SCHOOL
OF THE UNIVERSITY OF MINNESOTA
BY

Dominique Marie-Louise Gautreau

IN PARTIAL FULFILLMENT OF THE REQUIREMENTS
FOR THE DEGREE OF
DOCTOR OF PHILOSOPHY

Advisor: Turan Birol

August 2022

Acknowledgements

First, I would like to thank my advisor, Turan Birol, who has helped me immeasurably throughout my years in graduate school. He always allowed time for me to explore new ways to delve into the details of my projects, and he was accommodating whenever I experienced hardships in graduate school or in life. I am truly grateful to Turan for being sympathetic, supportive, and generous with the time he dedicated to helping me become a better researcher.

I am also grateful to the exceptional students and researchers that Turan brought together into his group. To Arpita Paul, for enduring all my questions about group theory and magnetism. To Amartya Saha and Fan Yang, for sharing many great conversations with me in the office, and Hwanhui Yun, who I always looked forward to chatting with about life and research. And to Shutong Li, for not only teaching me a great deal during our machine learning group sessions, but for becoming a good friend.

To all the students, post-docs, and professors I had the pleasure of collaborating with over the years, especially Sajna Hameed, Zhentao Wang, Damjan Pelc, Ana Najev, Vipul Chaturvedi, Rafael Fernandes, Martin Greven, and Chris Leighton. I learned a lot from our conversations and all of our work together.

I am grateful, too, for the funding that has enabled my work. The research in this thesis was mostly funded by the U.S. Department of Energy through the University of Minnesota Center for Quantum Materials, under Grant No. DE-SC-0016371, but was also partially supported by the National Science Foundation through the University of Minnesota MRSEC under Award Number DMR-2011401. Additionally, many parts of the numerical calculations were perfomed through the Minnesota Supercomputing Institute (MSI) at the University of Minnesota.

I would also like to thank the professors who generously dedicated their time to be

on my oral and thesis committees.

I am especially thankful for the friends I made throughout my time here. To Saumitran Kasturirangan, Jackson Olsen, and Derek Sincavage, for dragging me on walks around our neighborhood during the pandemic, and for the movie nights, the evening rounds of basketball, and the many, many coffee break chats. To Dmitry Chichinadze, for all the car rides, especially that one last-minute ride to the airport. And a special thanks goes to Zac Cohen, who always checked that I made it home safely from my light-rail journeys after our nighttime labs and discussions. I'm sure this "thank you" is also, in part, from my mom.

To my old and lifelong friends, now scattered across the country: Seraph Luby, Jessica Dias de Oliveira, Ashwin Srikrishna, Havalend Steinmuller, Leslie Ynalvez, and many others who I have been fortunate enough to have kept in touch with over the years. They frequently remind me of easier times from my past, and of better times to come.

I am endlessly thankful to my family. To my brother, Jean-Claude, for sparking my interest in materials science. To my kind and loving dad, Gill Gautreau, who lives every day with enthusiastic curiosity. He taught me that the joy of learning can last a lifetime. To my mom, Michele Deshotels, whose love and phone calls are both never-ending. I grew up watching the effort she put into work every day, and because of that, never doubting that a woman could be successful in whatever field she chose.

And finally, to Dan Phan, who I consider my best friend – for believing in me and encouraging me to continue even when I felt like giving up. I'm grateful for all the help he gave in coaching me while I practiced for my written exams, for the time he spent listening to my many practice talks, and for the effort he put into answering my constant stream of questions throughout our courses together. He always supported me when times were hard, and most importantly, he managed to make me laugh every day for the past six years.

Dedication

To my parents, Gill Gautreau and Michele Deshotels,
and to my best friend, Dan Phan.

Abstract

Due to the strong coupling between the spin, lattice, and orbital degrees of freedom, transition metal oxides exhibit a wealth of exotic phases, such as ferroelectricity, superconductivity, and magnetic ordering. In this thesis, I focus on the magnetic properties of three transition metal oxides. The first study I discuss in this thesis is on the botallackite cuprate $Cu_2(OH)_3Br$ [1]. I present the results for the excitation spectrum of the material, obtained through a combination of first-principles methods, linear spin wave theory and exact diagonalization. Our calculations of the dynamical structure factor highlight the coexistence of magnon and spinon excitations in the system, and our results qualitatively agree with experimental results obtained through inelastic neutron scattering.

I then turn to the rare-earth titanates ($RTiO_3$) compounds, which are well-known to transition from a predominantly ferromagnetic state to a predominantly G-type antiferromagnetic state with increasing rare earth radius. This extraordinary behavior arises from the high sensitivity of the exchange interactions to the crystal structure of $RTiO_3$. As such, the rare-earth titanates are natural candidates for exploring the possibility of controlling a system's magnetic behavior through the application of uniaxial or biaxial strain. I discuss the results of our comprehensive study of the rare-earth titanates, in which we used a combination of first-principles and analytical methods to show that the application of uniaxial or epitaxial strain in $RTiO_3$ should lead to a host of magnetic and structural phase transitions. This study is then followed by a description of the collaborative works I have participated in [2, 3], in which I provided first-principles and analytical calculations to complement experimental and theoretical analyses of $RTiO_3$.

I then discuss my contribution to the joint experimental and theoretical investigation of $(Pr_{1-y}Y_y)_{1-x}Ca_xCoO_{3-\delta}$ (PYCCO) [4]. In this work, my coauthors demonstrate that simultaneous first-order spin-state/valence-state/metal-insulator transitions can be experimentally induced in PYCCO with applied epitaxial strain. Studying this system from first-principles, I provide evidence that the strain-tunable phase transitions in PYCCO are directly analogous to the first-order thermal phase transitions observed in $Pr_{0.5}Ca_{0.5}CoO_3$.

Contents

List of Tables

List of Figures

Chapter 1

Introduction

1.1 Density Functional Theory

All of the varied properties of a material– its color, structure, conductivity, magnetic behavior, etc.– fundamentally derive from quantum mechanics. In theory, one should be able to derive the behavior of any desired property of a compound through an application of the Schrödinger equation to the $\sim 10^{23}$ particles in the compound [7]. This point was understood as early as 1929, when Dirac noted that "the underlying physical laws necessary for the ... whole of chemistry are thus completely known" [8]. Unfortunately, a theoretical investigation of the Schrödinger equation, as applied to a large number of interacting particles, is a highly nontrivial problem, which has been intensely studied since the advent of the Schrödinger equation itself [9, 10, 11, 12, 13, 14, 15]. Indeed, Dirac in the same sentence as above, concludes that the many-electron Schrödinger equation is "much too complicated to be soluble," and argues that "approximate practical methods of applying quantum mechanics should be developed."

The difficulty of the so-called many-body problem may not be surprising in retrospect, given the hindsight provided by the many decades of experimental and theoretical developments since the birth of quantum mechanics. Some materials are metallic, while others are insulating. Some are spin ices [16], while others are superconductors [17]. A whole host of exotic phenomena appear in materials, including ferroelectricity [18], superfluidity [19], magnetism [20], and the quantum Hall effect [21]. Yet all materials are simply a collection of atoms. In short, the whole is more than the sum of its

parts. Simply understanding the underlying fundamental laws governing the individual particles in a material does not in any way imply that one understands the emergent, collective behavior of the entire system. This adage was emphasized by Anderson, who eschewed the reductionist philosophy of Dirac, and emphasized the emergent behavior that can arise in the many-body systems, proclaiming that "More is different" [22].

This is not to say that an ab-initio analysis of the many-body problem is hopeless. In particular, in the following section I provide an overview of density functional theory (DFT), which in theory allows one to obtain the ground state of a many-body system by mapping it to a one-electron problem [23, 24, 25]. While various approximations employed in practice imply that the results obtained from DFT are not exact, DFT has become an invaluable tool to study the chemistry and physics in many materials from first-principles. Indeed, even when DFT cannot capture the subtle correlations which give rise to various emergent phenomena, it can often provide useful first steps for different analytical or computational approaches.

1.1.1 The Many-body Schrödinger equation

We begin with a review of the many-body problem. The energy of a system of interacting electrons and nuclei is given by [7]

$$E_{\text{tot}} = \langle \Psi | H | \Psi \rangle \,, \tag{1.1}$$

in which Ψ is the many-body wavefunction, and H is the many-body Hamiltonian

$$H = \underbrace{-\sum_i \frac{\hbar^2}{2m_e}\nabla_i^2 - \sum_I \frac{\hbar^2}{2M_I}\nabla_I^2}_{\substack{\text{kinetic energy operators} \\ \text{for the nuclei and electrons}}} + \underbrace{\frac{1}{2}\sum_{i\neq j}\frac{e^2}{|\mathbf{r}_i - \mathbf{r}_j|}}_{\substack{\text{Coulomb repulsion} \\ \text{between electrons}}} + \underbrace{\frac{1}{2}\sum_{I\neq J}\frac{e^2 Z_I Z_J}{|\mathbf{r}_i - \mathbf{R}_J|}}_{\substack{\text{Coloumb repulsion} \\ \text{between nuclei}}} - \underbrace{\sum_{i,I}\frac{e^2 Z_I}{|\mathbf{r}_i - \mathbf{R}_i|}}_{\substack{\text{Coulomb attraction} \\ \text{between the} \\ \text{electrons} \\ \text{and nuclei}}} . \tag{1.2}$$

Here, we use lowercase indices to denote the electrons and uppercase indices to denote the nuclei. Therefore, $\mathbf{r}_i$ is the position operator acting on the ith electron and $\mathbf{r}_i$ is the position operator acting on the Ith nucleus. Similarly, Z_I and M_I denote the charge and mass of the Ith nucleus, while e and m_e denote the charge and mass of an electron.

$\hbar$ is the reduced Planck constant.

In general, solutions to the Schrodinger equation, $H\Psi = E\Psi$, may contain cross terms between the electrons and nuclei. However, the nuclei are much more massive than the electrons, and therefore timescales describing the motion of nuclei are much longer than those of electrons. Because of this, one can think of the nuclei as fixed. In this case, the operator $-\sum_I \frac{\hbar^2}{2M_I}\nabla_I^2$, describing the kinetic energy of the nuclei, gives zero. Meanwhile, the operator $\frac{1}{2}\sum_{I\neq J}\frac{e^2 Z_I Z_J}{|\mathbf{R}_i - \mathbf{R}_J|}$, describing the repulsion between nuclei, yields a constant term, which can be subtracted from the energy without affecting the wavefunction solutions. This approximation is called the clamped-ion approximation, and can be summarized by the following Hamiltonian:

$$H = -\sum_i \frac{\hbar^2}{2m_e}\nabla_i^2 + \frac{1}{2}\sum_{i\neq j}\frac{e^2}{|\mathbf{r}_i - \mathbf{r}_j|} - \sum_{i,I}\frac{e^2 Z_I}{|\mathbf{r}_i - \mathbf{R}_i|} \tag{1.3}$$

in which Ψ now denotes only the electronic part of the many-body wavefunction, that is, $\Psi = \Psi(\mathbf{r}_1, \mathbf{r}_2, ...\mathbf{r}_N)$. To make this more clear, we can rewrite the operator describing the interaction between the electrons and ions as:

$$V_n(r) = -\sum_I \frac{Z_I}{|\mathbf{r} - \mathbf{R}_I|} \tag{1.4}$$

so that the Hamiltonian can be written as a function of only the electronic operators:

$$H(\mathbf{r}_1, \mathbf{r}_2, ..., \mathbf{r}_N) = -\sum_i \frac{\hbar^2}{2m_e}\nabla_i^2 + \sum_i V_n(\mathbf{r}_i) + \frac{1}{2}\sum_{i\neq j}\frac{e^2}{|\mathbf{r}_i - \mathbf{r}_j|} \tag{1.5}$$

Even with the clamped-ion approximation, the Schrödinger equation resulting from this Hamiltonian is difficult to solve. Analytically, it has only been solved exactly for a system with one electron. To solve it numerically for anything but the simplest of systems would require a great deal of computational resources [26, 25]. This is because, for a system of N electrons, this is a function of $3N$ variables, as it is a function of the position of each electron in the system. For a real-space sampling of g points along one direction (that is, a grid of size g^3), we would need to store g^{3N} numbers. The storage required, then, scales exponentially with the number of electrons in the system, and this makes working with this Hamiltonian (Eq. 1.5) infeasible.

1.1.2 Kohn-Sham equations

Because it is not viable to solve the Schrodinger equation resulting from the above Hamiltonian (Eq. 1.5), we must reformulate the problem of finding physical observables in a way that circumvents solving the many-body Schrodinger equation. It is to this end that we turn to the Hohenberg-Kohn theorems [23], which provide the central ideas behind density functional theory. The first Hohenberg-Kohn theorem states that given the ground state electron density $n_{\text{gs}}(\mathbf{r})$, one can in principle reconstruct the ground state wavefunction Ψ, and therefore obtain any ground-state observable of interest. Focusing on the ground-state energy, this theorem states that there exists a functional $F[n]$, such that $F[n_{\text{gs}}] = E_{\text{gs}}$. This is by itself quite profound, implying that rather than requiring the entire many-body wavefunction $\Psi(\mathbf{r}_1, \mathbf{r}_2, ...\mathbf{r}_N)$, which is a function of $3N$ coordinates, to obtain the ground-state energy, one only requires the ground-state density $n_{\text{gs}}(\mathbf{r})$, a function of only 3 variables. The second Hohenberg-Kohn theorem states that this functional $F[n]$ is minimized when $n(\mathbf{r})$ equals the ground state density $n_{\text{gs}}(\mathbf{r})$.

These two theorems lead to a drastic reformulation of the many-body problem. Rather than solving the N-electron Schrodinger equation, the Hohenberg-Kohn theorems imply that it is sufficient to minimize the energy functional $F[n]$ and obtain the ground-state electron density $n_{\text{gs}}(\mathbf{r})$. From $n_{\text{gs}}(\mathbf{r})$, we can then obtain any observable of interest. Unfortunately, the Hohenberg-Kohn theorems do not explicitly construct the functional $F[n]$, but only prove that such a functional exists. In order to find the appropriate functional, we can try to evaluate the expectation value of Eq. 1.5,

$$E = F[n] = \langle \Psi[n] | - \sum_i \frac{\hbar^2}{2m_e} \nabla_i^2 + \sum_i V_n(\mathbf{r}_i) + \frac{1}{2} \sum_{i \neq j} \frac{e^2}{|\mathbf{r}_i - \mathbf{r}_j|} | \Psi[n] \rangle \tag{1.6}$$

where $|\Psi[n]\rangle$ is the many-body wavefunction. Of the three terms in the expectation value, the second term, which describes the interaction between the electrons and the nuclei, can be written in terms of the density $n(\mathbf{r})$ as follows:

$$\sum_i \langle \Psi[n]| V_n(\mathbf{r}_i) |\Psi[n]\rangle = \sum_i \int d\mathbf{r} \langle \Psi[n]| \delta(\mathbf{r}-\mathbf{r}_i) V_n(\mathbf{r}) |\Psi[n]\rangle \tag{1.7}$$

$$= \int d\mathbf{r} V_n(\mathbf{r}) \sum_i \langle \Psi[n]| \delta(\mathbf{r}-\mathbf{r}_i) |\Psi[n]\rangle \tag{1.8}$$

$$= \int d\mathbf{r} V_n(\mathbf{r}) n(\mathbf{r}). \tag{1.9}$$

Using this, the energy then becomes

$$E[n] = \int d\mathbf{r} V_n(\mathbf{r}) n(\mathbf{r}) \underbrace{- \langle \Psi[n]| \sum_i \frac{\hbar^2}{2m_e} \nabla_i^2 |\Psi[n]\rangle}_{T} + \underbrace{\langle \Psi[n]| \frac{1}{2} \sum_{i \neq j} \frac{e^2}{|\mathbf{r}_i - \mathbf{r}_j|} |\Psi[n]\rangle}_{H_{ee}} \tag{1.10}$$

Unfortunately, there is no simple method to rewrite the latter two contributions in terms of the electron density $n(\mathbf{r})$. As such, we make an approximation in order to find the electron-electron and the kinetic energy terms. Assume that we begin with a wavefunction that is a product state:

$$\Psi(\mathbf{r}_1, \mathbf{r}_2, ..., \mathbf{r}_N) = \psi_1(\mathbf{r}_1)\psi_2(\mathbf{r}_2)...\psi_N(\mathbf{r}_N). \tag{1.11}$$

Using this, we find

$$T = -\sum_i \int d\mathbf{r} \psi_i^*(\mathbf{r}) \frac{\nabla^2}{2m_e} \psi_i(\mathbf{r}). \tag{1.12}$$

Additionally, using our product state wavefunction, we can write

$$H_{ee} \approx H_{\text{Hartree}} = \frac{1}{2} \int \int d\mathbf{r} d\mathbf{r}' \frac{n(\mathbf{r}) n(\mathbf{r}')}{|\mathbf{r} - \mathbf{r}'|}, \tag{1.13}$$

in which $n(\mathbf{r}) = \sum_i |\psi_i(\mathbf{r})|^2$ is the electron density for our product state wavefunction. To obtain the above expression, traditionally referred to as the Hartree energy, we had to include extra terms in the sum where $i = j$ – in other words, the above expression includes artificial self-interaction energies. This is not the only issue with the Hartree energy. In particular, since we obtained this expression by using a wavefunction that

doesn't satisfy the Pauli exclusion principle, the Hartree energy neglects all the effects of exchange. Moreover, using a product state as our wavefunction means we are also ignoring the effects of correlations. Similar qualms hold for the kinetic energy, which we also obtained using our product state ansatz.

To correct for these effects, we must include a correction term in our functional, $E_{\rm xc}[n]$ – this is referred to as the exchange-correlation functional. Using this, we finally have

$$E[n] = \int d\mathbf{r} V_n(\mathbf{r}) n(\mathbf{r}) - \sum_i \int d\mathbf{r} \psi_i^*(\mathbf{r}) \frac{\nabla^2}{2m_e} \psi_i(\mathbf{r}) + \frac{1}{2} \int \int d\mathbf{r} d\mathbf{r}' \frac{n(\mathbf{r}) n(\mathbf{r}')}{|\mathbf{r} - \mathbf{r}'|} + E_{\rm xc}[n] \tag{1.14}$$

With this, we now have a density functional which is in principle exact! Although we obtained the kinetic and Hartree energies using a product state wavefunction, all exchange and correlation effects neglected by this ansatz are in principle accounted for by the correction term $E_{\rm xc}[n]$. At this point, one only needs to derive a suitable expression for $E_{\rm xc}[n]$. This has been the subject of intense study over the years, and there are many different exchange-correlation functionals which have been proposed [27, 28, 29, 30, 31, 32].

With this, we can obtain the ground state energy by minimizing this functional with respect to the density. Since $n(\mathbf{r})$ is given in terms of the Kohn-Sham orbitals $\psi_i(\mathbf{r})$, we can minimize $E[n]$ by setting the functional derivative $\delta E / \delta \psi_i(\mathbf{r}) = 0$, subject to the constraint that the Kohn-Sham orbitals are orthonormal, $\int d\mathbf{r} \psi_i^*(\mathbf{r}) \psi_j(\mathbf{r}) = \delta_{ij}$. We then obtain the Kohn-Sham equations:

$$\big[-\frac{1}{2m_e} \nabla^2 + V_n(\mathbf{r}) + V_H(\mathbf{r}) + V_{xc}(\mathbf{r}) \big] \psi_i(\mathbf{r}) = \varepsilon_i \psi_i(\mathbf{r}), \tag{1.15}$$

where

$$V_H(\mathbf{r}) = e^2 \int d\mathbf{r}' \frac{n(\mathbf{r}')}{|\mathbf{r} - \mathbf{r}'|} \tag{1.16}$$

and $V_{\rm xc}[n] = \delta E_{\rm xc} / \delta n$. Solving these Kohn-Sham equations self-consistently gives the Kohn-Sham orbitals which satisfy the minimum energy condition, and thus gives the

ground state density. Schematically, the method one uses to solve the Kohn–Sham equations self-consistently is shown in the following diagram:

$$n(\mathbf{r}) \longrightarrow \underbrace{V_H(\mathbf{r}), V_{\mathrm{xc}}(\mathbf{r}) \longrightarrow \psi_i(\mathbf{r})} \tag{1.17}$$

In words, we begin with some initial guess for the electron density $n(\mathbf{r})$. Using this guess, we obtain the Hartree potential $V_H(\mathbf{r})$ and the exchange-correlation potential $V_{\mathrm{xc}}(\mathbf{r})$. The nuclear potential $V_n(\mathbf{r})$ is independent of the electron density, and is solely determined through the atomic positions. We can then use these potentials in the Kohn-Sham equations, solving for the Kohn-Sham orbitals $\psi_i(\mathbf{r})$ and eigenvalues ε_i. With these orbitals, we can again obtain the electron density using $n(\mathbf{r}) = \sum_i |\psi_i(\mathbf{r})|^2$. This iterative process until the output density agrees with the input density within some desired tolerance. In fact, it is more efficient in practice to instead check for the convergence of the energies rather than the densities.

1.1.3 DFT+U and spin-polarized calculations

Although DFT includes the effects of electron-electron repulsion through the exchange correlation functional and Hartree terms, these terms are sometimes not sufficient to account for the strength of correlations in the system. For example, for some systems such as NiO and MnO, DFT will predict a metal when the system is in fact a Mott insulator [33, 34, 35, 36]. This is due to the fact that the exchange correlation functionals used in DFT calculations are determined assuming that the electronic densities vary slowly as a function of position. As such, they work best in this limit, rather than in systems that have more localized orbitals. To account for this, DFT can be extended to explicitly include a Hubbard U [37, 38] on different orbitals, for example on highly localized orbitals such as d- or f-orbitals [39, 40, 36]. By construction, then, DFT+U includes the effects of correlations better than DFT alone. To be more concrete, consider the following Hubbard Hamiltonian given by

$$H_{\mathrm{int}} = \frac{U}{2} \sum_{mm'\sigma} n_{m,\sigma} n_{m',-\sigma} + \frac{U-J}{2} \sum_{m \neq m',\sigma} n_{m,\sigma} n_{m',\sigma}. \tag{1.18}$$

This Hamiltonian gives the Coulomb repulsion on a single atom. Here, m and m'

label the orbital degrees of freedom on the atom (i.e. the d or f levels), σ labels the spin degree of freedom, and $n_{m\sigma}$ is the occupation of the orbital m and spin σ. In essence, Eq. 1.18 says that electrons on an atom repel each other with energy U. However, if two electrons have the same spin, they interact with energy $U - J$, i.e. the Hubbard repulsion is reduced by the Hund interaction J.

With this, one can add H_{int} to the DFT energy functional and better model the correlations on the correlated d and f levels. However, when adding H_{int} to the energy functional, one should also in principle subtract out the repulsion and correlations already included at the LDA or GGA level, as to avoid double counting. This is a highly nontrivial issue, and there are multiple methods which have been proposed in the literature [41, 40, 39, 42]. In any case, once one has decided on a double-counting correction E_{dc}, one can add $H_{\text{int}} - E_{dc}$ to the DFT energy functional. This is essentially what was done by Dudarev et al [36], starting from the above expression for H_{int}. We note that in the above expression for H_{int}, the Coulomb repulsion between two electrons is always U, regardless of which orbitals the two electrons occupy. This only holds if one assumes that the overlap integrals are approximately independent of the two orbitals being occupied. A similar statement holds for the Hund interaction J. In principle, one should instead take the orbital structure into account when writing H_{int}. Doing so leads to a more refined interaction [40].

Lastly, we note that so far, we have not discussed what values of U and J are appropriate to use. In practice, it is common to consider U and J as free parameters, which should be determined by fitting the resulting structure, band gap, or other empirical quantities to experiment. Alternatively, Cococcioni and de Gironcoli have proposed a method to calculate the correct U values from first-principles [43].

This introduction of spin implies a generalization of the DFT formalism to include spin density as well as electron density in the energy functional. In the early 1970s, Barth and Hedin [44] and Rajagopal and Callaway [45] extended the formalism of DFT to include relativistic effects, making it possible to use DFT to study magnetic materials. While Kohn and Sham had previously shown that only the electron density is needed to find the ground state energy of a system (that is, the ground state energy is a functional of the electron density, $E = F[n(\mathbf{r})]$), Rajagopal and Callaway, starting from the Dirac equation, showed that the energy of a magnetic system is a functional of

the relativistic 4-current. This 4-current is actually composed of three quantites, which are the electron density, the spin density, and the electron current density. In typical spin-DFT implementations, however, only the electron and spin densities are needed, while the electron current density can be neglected. That is, the energy is a functional of only $n(\mathbf{r})$ and $s(\mathbf{r})$. Both the spin and electron densities can be written in terms of the density matrix as follows:

$$n(\mathbf{r}) = \sum_{\alpha} n_{\alpha\alpha}(\mathbf{r}) \tag{1.19}$$

$$s(\mathbf{r}) = \frac{\hbar}{2} \sum_{\alpha\beta} n_{\alpha\beta}(\mathbf{r}) \sigma_{\alpha\beta} \tag{1.20}$$

where the density matrix, $n_{\alpha\beta}(\mathbf{r})$ is given by

$$n_{\alpha\beta}(\mathbf{r}) = \sum_{i} \phi_i^*(\mathbf{r};\alpha)\phi_i(\mathbf{r};\beta) \tag{1.21}$$

Defining both $n(\mathbf{r})$ and $s(\mathbf{r})$ in this way shows that the ground state energy is a functional of the density matrix ($E = F[n_{\alpha\beta}(\mathbf{r})]$). From here, everything follows in analogy to the nonmagnetic DFT formalism.

1.2 Group Theory

In materials science, group theory is both a convenient and powerful tool for studying scenarios in which the states of a system can be classified by their symmetries [46, 47, 48, 49]. This is because group theory is, essentially, the study of symmetries.[1] To illustrate this idea, we can use the perovskite crystal structure in its cubic and distorted forms. Fig. 1.1 shows a perovskite crystal belonging to the cubic $Pm\bar{3}m$ space group (Fig. 1.1(a)), and the orthorhombic $Pnma$ space group (Fig. 1.1(b)). To study the $Pnma$ crystal structure, we might try evaluating the total displacement of each atom away from its non-displaced counterpart in the cubic structure. We could then try to understand the effect of each atomic displacement on quantities of interest

[1] More rigorously, group theory is the study of groups, but every group is the symmetry group of some graph (from Frucht's theorem [50]).

(such as magnetic exchange constants, microscopic electric dipole moments, free energies, etc.). Because distortions can become quite complicated, this would not in general be an easy task. Additionally, all physical quantities of interest, such as free energies, magnetizations, or electric polarizations, can be classified by their symmetry properties. As such, it is more natural and useful to consider how these properties couple to distortion modes (i.e. phonons) rather than individual atomic displacements, since these modes have well-defined symmetry properties (i.e. they belong to some irreducible representation) and are therefore more interpretable. Even disregarding this point of interpretability, it would be infeasible to study how each atomic displacement affects a quantity of interest, since a crystal is composed of $\sim 10^{23}$ atoms. If we instead use the tools that group theory provides, we can decompose the total distortion into different displacement modes, which differ by their symmetries. This provides a way to systematically evaluate how each distortion mode affects quantities we care about and how each mode might be influenced by external, tunable means.

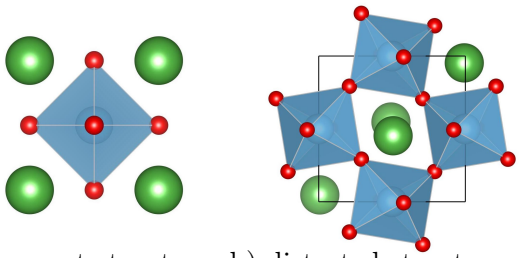

a) parent structure b) distorted structure

Figure 1.1: Cubic $Pm\bar{3}m$ parent $LaTiO_3$ structure and the distorted structure

To reiterate, we want to understand the total distortion (and its effect on various quantities) by decomposing it into simpler, linearly independent distortions. These basis distortions are called normal modes or distortion modes, and are determined from group theoretical considerations. Because distortion modes are reasonable to individually visualize, they may provide more intuition for an overall distortion than an exhaustive list of displacement coordinates for each atom in a distorted supercell. Moreover, different distortion modes may be caused by separate energy lowering mechanisms (for example, by being unstable on its own, or by being brought in through coupling to an unstable mode) and so separating a distortion into its contributions from each distortion mode

may also help with understanding the mechanisms of a phase transition.

In this chapter, I will introduce some essential concepts in group theory. These include representations, irreducible representations (irreps), and order parameter directions (OPD's).

1.2.1 Representations

A **representation** of a group G is defined as a homomorphism $\rho : G \to \mathrm{GL}(V)$ [46, 47, 49]. Here, $\mathrm{GL}(V)$ is the general linear group on a vector space V, which for our purposes will always be $\mathbb{C}^n$, the vector space consisting of all n-tuples of complex numbers. The general linear group $\mathrm{GL}(\mathbb{C}^n)$ is composed of the set of $n \times n$ invertable matrices with complex coefficients, and we can think of a representation ρ as a function mapping group elements to matrices with complex coefficients. For ρ to be a homomorphism, the set of matrices must obey the group's multiplication rules, i.e. if a group element a is represented by matrix $\rho(a)$ and a group element b is represented by $\rho(b)$, then $\rho(a)\rho(b) = \rho(ab)$. In the following, I will further explain representations and motivate their use through examples. Representations are not unique, which I will illustrate by constructing four different representations of the same group.

Consider a square with identical atoms attached to each of its corners. We take this square molecule to sit in two-dimensional space. The point group to which this molecule belongs is D_4, which consists of four-fold rotations about the center of the square, as well as reflections about the square's diagonals and the x and y axes, i.e. $D_4 = \{E, C_4, (C_4)^2, C_4^3, \sigma_{v1}, \sigma_{v2}, \sigma_{d1}, \sigma_{d2}\}$. Here, E is the identity operation, C_n corresponds to n-fold rotations, $\{\sigma_{v1}, \sigma_{v2}\}$ correspond to reflections through the x and y axes, and $\{\sigma_{d1}, \sigma_{d2}\}$ correspond to reflections through the square's diagonals. Recall that linear operators are determined by how they transform basis vectors. Therefore, to obtain a representation, we must first choose a basis.

To obtain our first representation, we choose the basis shown in Figure 1.2, where we have attached two basis vectors to each of our atoms.

We see that under a C_4 operation, basis vector $\boldsymbol{u_{1x}}$ is taken into $\boldsymbol{u_{2y}}$, basis vector $\boldsymbol{u_{1y}}$ is taken into $\boldsymbol{u_{2x}}$, and so on. Since we know how C_4 acts on each basis vector, we can construct the matrix representation C_4 in our basis $(\boldsymbol{u_{1x}}, \boldsymbol{u_{1y}}, \boldsymbol{u_{2x}}, \boldsymbol{u_{2y}}, \boldsymbol{u_{3x}}, \boldsymbol{u_{3y}}, \boldsymbol{u_{4x}}, \boldsymbol{u_{4y}})$.

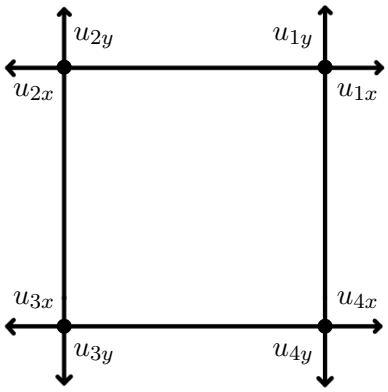

Figure 1.2: a square molecule (atoms at corners) with two basis vectors attached to each atom

This matrix $\rho(C_4)$ is 8×8, and reads

$$\rho(C_4) = \begin{pmatrix} 0 & 0 & 0 & 0 & 0 & 0 & 0 & 1 \\ 0 & 0 & 0 & 0 & 0 & 0 & 1 & 0 \\ 0 & 1 & 0 & 0 & 0 & 0 & 0 & 0 \\ 1 & 0 & 0 & 0 & 0 & 0 & 0 & 0 \\ 0 & 0 & 0 & 1 & 0 & 0 & 0 & 0 \\ 0 & 0 & 1 & 0 & 0 & 0 & 0 & 0 \\ 0 & 0 & 0 & 0 & 0 & 1 & 0 & 0 \\ 0 & 0 & 0 & 0 & 1 & 0 & 0 & 0 \end{pmatrix}. \tag{1.22}$$

The above construction can be done for any symmetry operation of the point group. The set of 8×8 matrices obtained this way is a representation of the point group D_4, which we shall denote ρ_8. Since the matrices of our representation are 8×8, we call the representation 8-dimensional. In general, a representation composed of $n \times n$ matrices is referred to as n-dimensional.

Although the above set of matrices was constructed using the 8-dimensional basis shown in Figure 1.2, we could have instead used the basis shown in Figure 1.3. In this case, each atom has one basis vector associated with it. Since there are four basis

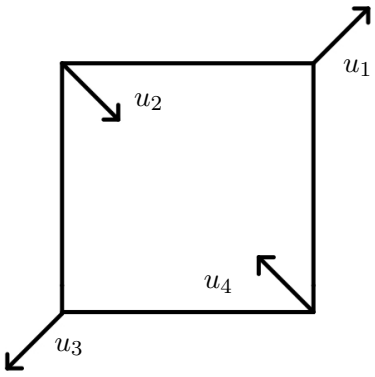

Figure 1.3: Square molecule with a single basis vector attached to each atom

vectors in total, the matrices describing our point group would now be 4×4, leading to a 4-dimensional representation ρ_4.

As another a representation of our point group, consider the two distortions shown in Figure 1.4, which we denote ϕ_1 and ϕ_2. Note that ϕ_1 and ϕ_2 only transform between themselves under all operations of the D_4 point group. For example, $\rho(C_4)\phi_1 = \phi_1$, $\rho(\sigma)\phi_1 = \phi_2$, $\rho(\sigma)\phi_2 = \phi_1$, etc. Thus, we can use ϕ_1 and ϕ_2 as basis vectors to construct a 2-dimensional representation ρ_2.

As a last example of a representation, consider the map ρ_1 which takes every group element to the number 1. This map is a valid representation, since it satisfies $\rho_1(a)\rho_1(b) = \rho_1(ab)$ for any group elements a and b. This representation is referred to as the trivial representation, and exists for any group G. A basis vector which transforms under the trivial representation is discussed in the following section.

With the above four examples, we have demonstrated that there can be many different representations of any given group. In passing, we note that a representation also does not need to be **faithful**. A representation ρ is faithful if it is injective [49]. That is, the matrices corresponding to two different group elements a and b, $\rho(a)$ and $\rho(b)$, must be distinct. The trivial representation ρ_1 is an exemplary example of an unfaithful representation, since ρ_1 maps all group elements to 1 by definition.

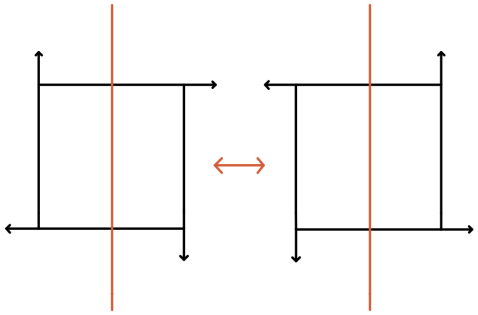

a) ϕ_1 basis vector b) ϕ_2 basis vector

Figure 1.4: The basis vectors ϕ_1 and ϕ_2, related by reflections through the σ mirror plane

1.2.2 Irreducible representations

At this point, we have constructed four different representations ρ_1, ρ_2, ρ_4, and ρ_8 of the point group D_4. However, we have not discussed why representations are useful, nor why one would prefer any given representation over any other. Indeed, to the latter point, in the above examples, only the 8-dimensional basis may seem natural, since the basis vectors naturally describe atomic displacements of this square molecule. To address these questions, we first define reducible and irreducible representations. Assume we are given a representation $\rho : G \to \mathrm{GL}(V)$. If there exists a nontrivial proper subspace $W \subset V$ such that $\rho(g)w \in W$ for all $g \in G$ and $w \in W$, then the representation ρ is **reducible**. If a representation is not reducible, it is **irreducible**. To make these definitions more concrete, we will refer to the previous example of the square molecule and its D_4 point group.

Examples of reducible and irreducible representations

One example of a reducible representation is the 8-dimensional representation ρ_8 that we introduced above. This can be seen by noticing that the four basis vectors $\{u_1, u_2, u_3, u_4\}$ of ρ_4 span a 4-dimensional subspace of the 8-dimensional space spanned by the basis vectors $\{u_{1x}, u_{1y}, ...\}$. Since all group elements take this 4-dimensional space into itself, our original criterion for reducibility is established, i.e. our 8-dimensional representation ρ_8 is reducible.

As a second example, consider the 2-dimensional representation ρ_2 constructed above in Fig. 1.4, furnished by the basis vectors ϕ_1 and ϕ_2. Now, instead of using ϕ_1 and ϕ_2 as our basis vectors, we could have chosen $\phi_+ = \phi_1 + \phi_2$ and $\phi_- = \phi_2 - \phi_1$ as the basis to describe our representation. As one can visually verify from Figure 1.5, under every point group operation, ϕ_+ is mapped onto itself. Mathematically, ϕ_+ can be used as a basis vector for a one-dimensional subspace W_+ of our original vector space (spanned by linear combinations of ϕ_1 and ϕ_2.) Since ϕ_+ is mapped into itself under every symmetry operation g of our group D_4, by definition, our original representation ρ_2 is reducible. One could have also proven the reducibility of ρ_2 using ϕ_-. Like ϕ_+, ϕ_- only transforms into ϕ_- or $-\phi_-$ under operations of the symmetry group D_4.

The important point is that ϕ_+ and ϕ_- do not transform into each other under any group operation. Thus, if we choose ϕ_+ and ϕ_- as a basis, our new 2-dimensional representation becomes diagonal, i.e. each matrix of our representation $\rho(C_4)$, $\rho(\sigma)$, etc. is diagonal. In fact, an equivalent definition of reducibility is that there exists a basis in which all representation matrices are block-diagonal. Representations which can be obtained via a unitary change of basis are said to be **equivalent**. In this language, a representation is said to be reducible if it is equivalent to a block-diagonal representation.

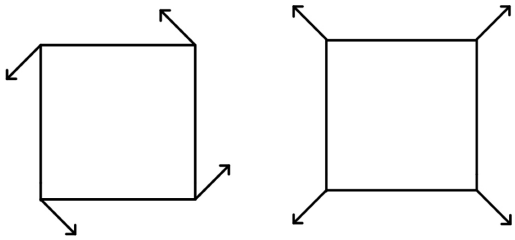

a) $\phi_- = \phi_2 - \phi_1$ b) $\phi_+ = \phi_1 + \phi_2$

Figure 1.5: The basis vectors ϕ_+ and ϕ_-

If we change basis from $\{\phi_1, \phi_2\}$ to $\{\phi_+, \phi_-\}$, as discussed above, we obtain a new, block-diagonal representation. From this representation, we may define a new 1-dimensional representation, furnished by the one basis vector ϕ_+.[2] We can do the same with ϕ_-, obtaining a different 1-dimensional representation. We note that the

[2]Note that ϕ_+ is unchanged by any of the symmetry operations of the group. As such, the 1×1 representation matrices are all given by 1. Therefore, the irreducible representation furnished by the basis vector ϕ_+ is also the trivial representation introduced in the previous section.

1-dimensional representations furnished by ϕ_+ and ϕ_- are irreducible, since there is no way to further diagonalize a 1×1 matrix. As a notational aside, the names of these irreducible representations (irreps) are A_1 and A_2, respectively.

With this, we now provide some intuition for irreducible representations and how they give us information about symmetry. Since the states ϕ_+ and ϕ_- are never mapped into each other under point group operations, one can loosely say that they have different symmetry properties. When we diagonalize our representation, what we are doing then is breaking up our vector space spanned by ϕ_1 and ϕ_2 into different subspaces, each of which have their own symmetry. The two different irreducible representations then describe the different symmetries of their respective basis vectors. To see this, note that if we take ϕ_+ and ϕ_- to correspond to distortions of this square molecule, ϕ_+ leads to a molecule which is still a square. The distortion ϕ_- however, leads to a rotated square, which no longer aligns with the diagonal mirror planes.

Although the above example involves 1-dimensional irreducible representations, in general, one can imagine a distortion that has components of a higher dimensional irrep. For this, we first describe a 2-dimensional irrep of our point group D_4. Consider the following vectors ϕ_3 and ϕ_4, as shown in Fig. 1.6. Under all point group operations, they transform into each other. Using these vectors as a basis, we can create a new 2-dimensional representation of D_4. Actually, the resulting representation is irreducible, though we do not prove this here; it is denoted E.

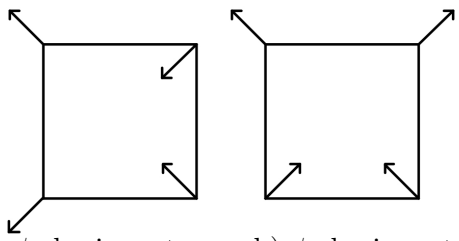

a) ϕ_3 basis vector b) ϕ_4 basis vector

Figure 1.6: The basis vectors ϕ_3 and ϕ_4

In fact, it is possible to find all the irreducible representations for any finite group, without ever referencing a specific basis. This is due to the Great Orthogonality Theorem, which is beyond the scope of this paper [47, 49]. Using the Great Orthogonality

Theorem and its corollaries, any representation (which is not already irreducible) can be reduced into different irreducible representations.

With the formalism of reducible and irreducible representations in hand, we now return to the questions posed at the beginning of this section, regarding the utility of representations. We begin by discussing the question of why any given representation would be preferred over any other. Typically, a representation is chosen depending on the physical context. For example, if one wishes to classify the normal modes of the square molecule discussed above, the 8-dimensional representation ρ_8 is most natural, since the basis vectors describe all of the possible displacive degrees of freedom of the system. If instead, one wished to obtain the energy eigenstates of a given compound, one could instead use atomic orbitals as basis states to furnish a representation of the symmetry group of the compound. Once one has a representation ρ, one can reduce ρ into a sum of irreducible representations ρ_i. The basis vectors of each irreducible representation then "have the same symmetry", while basis vectors corresponding to different irreducible representations "have different symmetries". This symmetry information is quite useful, in that we expect states corresponding to the same irrep to have the same energy, and we expect states corresponding to different irreps to have different symmetries. As such, by only using symmetry considerations, one can predict the degeneracies of different normal modes (in the case of atomic displacements) or energy eigenstates (in the case of quantum mechanics.)

Moreover, given a set of irreps of interest (perhaps obtained through the above procedure), one can expand any quantity of interest in powers of the amplitudes of the given irreps. This allows one to analyze how a given irrep affects the quantity of interest, even in cases where a microscopic model may be difficult to understand. We shall discuss this further below, when we discuss the coupling between distortion modes and magnetic couplings in the free energy.

1.2.3 Order parameter directions (OPD)

Before we define an order parameter, we must discuss how one breaks up a given distortion into irreducible representations. As a trivial example, consider the distortion generated from ϕ_+. As previously discussed, ϕ_+ transforms under the 1-dimensional

irreducible representation A_1. When describing this distortion, we then say it is composed solely of A_1, rather than describing the distortion with a vector of 8 elements and denoting the displacements of each atom. This way, it is easier to see the symmetry of the distortion: it is the vector that does not change under any symmetry operation of the point group.

As another example, consider the distortion ϕ_1, which can be seen in figure 1.4. Since $\phi_1 = \phi_+ + \phi_-$, we would describe the distortion as having equal parts A_1 and A_2, ϕ_+ transforming under A_1 and ϕ_- transforming under A_2.

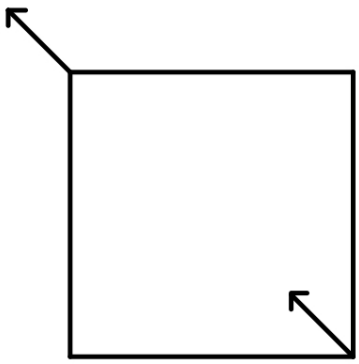

Figure 1.7: The $\phi = \phi_3 + \phi_4$ distortion

Although the above examples involve 1-dimensional irreducible representations, in general, one can imagine a distortion that has components of a higher dimensional irrep. Consider the distortion ϕ in figure 1.7. As one can see, $\phi = a(\phi_3 + \phi_4)$, where a is the amplitude of the distortion. As noted above, ϕ_3 and ϕ_4 transform under the E irrep. Thus, we would describe the distortion as being composed of the E irrep. However, since the E irrep is 2-dimensional, we must be more specific when describing our distortion. In our case, ϕ is equally composed of ϕ_3 and ϕ_4, which we denote (a, a), where a again denotes the amplitude of the distortion. This 2-component vector tells us how much of each basis vector we have. We call this vector the order parameter direction. In summary, given a distortion of our molecule, we can break it up into linear combinations of different distortions, which are basis vectors of irreducible representations. In an

abuse of language, we instead say that we break up our original distortion into different irreps (rather than basis vectors of different irreps). For example, if an irrep is 5-dimensional, we must also specify an order parameter direction, a 5-component vector, to tell us how much of the five basis vectors we have in our specific distortion.

1.2.4 Space groups and their representations

I originally introduced the utility of group theory using the example of distortions of a crystal. However, in the case of a crystal, we are not concerned with a point group but instead the symmetry group of a crystal. If we consider an infinite crystal, the symmetry group is called the space group. I now briefly review space groups, and provide the formalism to describe their representations.

Any crystal lattice has translational symmetry. In particular, for any crystal, there are basis vectors $\mathbf{a}$, $\mathbf{b}$, and $\mathbf{c}$ such that the crystal is symmetric under translations by any $\mathbf{t} = n_1\mathbf{a} + n_2\mathbf{b} + n_3\mathbf{c}$ for any integers n_1, n_2, and n_3. The set of translations T constitutes a subgroup of the space group and is known as the translation subgroup T of the space group G. In addition to this translational symmetry, a crystal may also contain point group symmetry elements, such as mirror planes or inversion centers. Moreover, a crystal may contain symmetry elements such as glide planes or screw axes, which do not exist in any point group. In this case, the space group is referred to as **nonsymmorphic**. In general, all symmetry operations of a space group G can be written as $\{R|\mathbf{t}\}$, where R is a point-group operation, and $\mathbf{t}$ is a translation. In particular, $\{R|\mathbf{t}\}$ takes a point $\mathbf{r}$ to $\{R|\mathbf{t}\}\mathbf{r} = R\mathbf{r} + \mathbf{t}$. For an extensive discussion of space groups and their symmetry elements, I refer the reader to [49, 51].

First, we restrict ourselves to the translation subgroup and its representations. Since all translations $\{1|\mathbf{t}\}$ commute with one another, the group T is abelian.[3] As such, all irreducible representations of T are one-dimensional [49]. Moreover, each irreducible representation $\rho_{\mathbf{k}}$ can be labeled by some crystal momentum $\mathbf{k}$ residing in the Brillouin zone of the crystal.

Under some translation $\{1|\mathbf{t}\}$, a basis vector $v_{\mathbf{k}}$ of the irreducible representation $\rho_{\mathbf{k}}$ transforms as

$$\rho(\{1|\mathbf{t}\})v_{\mathbf{k}} = e^{i\mathbf{k}\cdot\mathbf{t}}v_{\mathbf{k}}. \tag{1.23}$$

[3] A group is abelian if all of its elements commute [49].

Any state $v_{\mathbf{k}}$ satisfying the above (and therefore transforming under some irreducible representation $\rho_{\mathbf{k}}$) is referred to as a Bloch state. In words, Bloch states are mapped into themselves under translations, up to some phase factor $e^{i\mathbf{k}\cdot\mathbf{t}}$. Note that for this to be true, any Bloch state $v_{\mathbf{k}}$ must be delocalized over the entire crystal structure.

This can also be seen from the following: Consider a vector v, which is localized in some unit cell of the crystal. Depending on the physical context, v could correspond to an atomic displacement, an atomic orbital, or a spin flip of some magnetic moment, to list a few examples. With this v, we define $v_{\mathbf{k}}$ as follows:

$$v_{\mathbf{k}} = \sum_i \rho(\{1|\mathbf{t}_i\})e^{-i\mathbf{k}\cdot\mathbf{t}_i}v, \tag{1.24}$$

where the sum runs over all the translations of the crystal. This definition of $v_{\mathbf{k}}$ satisfies $\rho(\{1|\mathbf{t}\})v_{\mathbf{k}} = e^{i\mathbf{k}\cdot\mathbf{t}}v_{\mathbf{k}}$. From this equation for $v_{\mathbf{k}}$, it is easy to see that $v_{\mathbf{k}}$ has nonzero weight in all unit cells of the crystal and is therefore delocalized.

From this discussion, it is straightforward to construct states which transform under irreducible representations of the translation subgroup T. Given some set of localized states v_α, applying the above formula immediately yields a set of Bloch states $v_{\mathbf{k}\alpha}$.

So far, we have only discussed irreducible representations of the translation subgroup T of some space group G. However, as previously discussed, in general a space group may also contain other symmetry operations, corresponding to either point group or nonsymmorphic symmetry operations. These operations $\{R|\tau\}$ (where τ is a fractional translation if $\{R|\tau\}$ is nonsymmorphic) map a Bloch state with momentum $\mathbf{k}$ into another Bloch state with momentum $R\mathbf{k}$. Intuitively then, if we want to understand the symmetry properties of a Bloch state with momentum $R\mathbf{k}$, it is sufficient to understand the symmetry properties of the Bloch states with momentum $\mathbf{k}$. This intuition will be made precise in the below discussion.

With this, it is useful to define the star of $\mathbf{k}$ as the set of inequivalent momenta $\mathbf{k}_i$ which can be obtained by acting the symmetry operations $\{R|\mathbf{t}\}$ of space group G on $\mathbf{k}$. Two momenta $\mathbf{k}_1$ and $\mathbf{k}_2$ are considered equivalent, $\mathbf{k}_1 \equiv \mathbf{k}_2$, if they are equal up to some reciprocal lattice vector, i.e. $\mathbf{k}_1 = \mathbf{k}_2 + \mathbf{K}$. Rewording our intuition of the previous paragraph, if we understand the symmetry properties of our Bloch states at $\mathbf{k}$, we automatically know the symmetry properties of the Bloch states for all other

momenta in the star of $\mathbf{k}$.

From the above, it is sufficient to restrict ourselves to a specific momentum $\mathbf{k}$ in the star of $\mathbf{k}$ when trying to construct irreducible representations of a space group G. In particular, given some momentum $\mathbf{k}$, we define the little group $G_{\mathbf{k}}$, also known as the group of $\mathbf{k}$, as the set of symmetry operations $\{R|\mathbf{t}\}$ of G such that $R\mathbf{k} \equiv \mathbf{k}$. One can show that any representation of the little group $G_{\mathbf{k}}$ uniquely determines a representation of the entire space group G. Indeed, if we have a set of vectors $v_{\mathbf{k}\alpha}$ which furnish a basis of a representation $\rho_{\mathbf{k}}$ of the little group $G_{\mathbf{k}}$, we can construct a basis of a representation $\rho_{\mathbf{k}} \uparrow G$ of the entire space group G simply by acting the space group operations $\{R|\mathbf{t}\}$ on the basis vectors $v_{\mathbf{k}\alpha}$. This naturally leads to basis vectors for **all** momenta in the star of $\mathbf{k}$. This representation of G, $\rho_{\mathbf{k}} \uparrow G$, is referred to as the induced representation. This formalizes our above intuition that the symmetry properties of our Bloch basis can be understood by focusing on a single $\mathbf{k}$ in the star. The task of constructing representations of the whole space group G is therefore equivalent to constructing representations of the little group $G_{\mathbf{k}}$.

First, note that for all $\mathbf{k}$, $G_{\mathbf{k}}$ contains the translation group T as a subgroup. This is because translations do not affect the momentum $\mathbf{k}$ of a Bloch state, instead only modifying the phase of a Bloch state $v_{\mathbf{k}}$ by $e^{i\mathbf{k}\cdot\mathbb{t}}$. It is therefore convenient to work instead with the quotient group $\bar{G}_{\mathbf{k}} = G_{\mathbf{k}}/T$, known as the little cogroup of $\mathbf{k}$ [52]. One can think of $\bar{G}_{\mathbf{k}}$ as the set of symmetry operations $\{R|\mathbf{t}\}$ of $G_{\mathbf{k}}$, ignoring the translations by primitive lattice vectors $\mathbf{t}$. If G is symmorphic, $\bar{G}_{\mathbf{k}}$ contains only point group operations, and its irreducible representations can be easily found (and are indeed tabulated for all 32 crystallographic point groups.) If however G is nonsymmorphic, then $\bar{G}_{\mathbf{k}}$ may contain screw or glide operations, which contain fractional translations τ. This implies that $\bar{G}_{\mathbf{k}}$ is not a point group, and complicates the task of constructing irreducible representations of $\bar{G}_{\mathbf{k}}$. In this case, one must turn to projective representations, which is beyond the scope of this discussion. I refer the interested reader to Refs. [53, 49].

After obtaining a representation ρ of $\bar{G}_{\mathbf{k}}$, one can find a representation of G, $\rho \uparrow G$ through the induction procedure described above. So far, the process of obtaining irreducible representations for space groups has been quite general and abstract. To make this discussion more concrete, I determine the irreducible representations that the A-, G-, C-, and F-type magnetic orders correspond to in the cubic space group $Pm\bar{3}m$.

1.2.5 Determining Irreducible Representations of Magnetic Orders in the $Pm\bar{3}m$ space group

We first briefly review the method discussed above for determining the irreducible representation that a set of basis vectors transforms as, applied to the magnetic order parameters discussed here. Given a set of basis vectors describing a given magnetic order, we first determine their wavevectors $\mathbf{k}$ in the Brillouin zone of the crystal. More precisely, the wavevectors of these basis vectors correspond to the star of some wavevector $\mathbf{k}$. We then specialize to one wavevector in the star of $\mathbf{k}$, using the point group of the crystal to determine the little cogroup of $\mathbf{k}$, $\bar{G}_{\mathbf{k}}$. For convenience, we will also refer to $\bar{G}_{\mathbf{k}}$ as the group of $\mathbf{k}$. We then find how our basis transforms under operations of $\bar{G}_{\mathbf{k}}$, and obtain the irrep that this basis corresponds to. This last step is done by calculating the characters of our representation [49], and comparing the characters of our representation to online character tables on the Bilbao crystallographic server [54, 55, 56]. We work in the undistorted cubic structure of an ABO_3 perovskite, which has space group $Pm\bar{3}m$ (221).

A-type AFM

We first consider the A-type AFM mode shown in Fig. 1.8, where the moments are aligned with the wavevector. Here, the spins are located at the 1b Wyckoff positions (the corners of the cube drawn in Fig. 1.8), and the inversion center is on the A-site (the center of the cube drawn in Fig. 1.8.) There are three inequivalent X-points, that is, X-points that are not related by reciprocal lattice vectors, and hence, three vectors in the star of X: $\{(\pi,0,0),(0,\pi,0),(0,0,\pi)\}$.[4] After applying the point group operations of $Pm\bar{3}m$ to a given X point, we find that the group of X is D_{4h}. This is illustrated in Fig. 1.8, where we have drawn the four-fold axis in pink. In addition to the four-fold axis, there are also two-fold axes about the cubic x and y axes, the diagonal $x+y$ and $x-y$ axes, an inversion center at the center of the cube, as well as several mirror planes.

With this, we can apply the symmetry operations of D_{4h} to find how our A-type AFM mode transforms. We find that this mode only transforms into itself (or minus itself) under operations of the group of X, implying that the representation described by

[4] We work in units where the cubic lattice parameter a is 1.

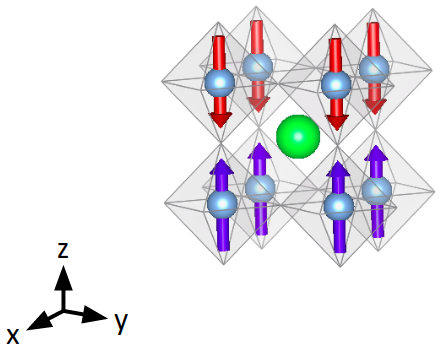

Figure 1.8: A basis vector for A-type AFM magnetic order. This vector transforms under the mX_1^- irrep.

D_{4h}	E	C_2^z	C_4^z	C'_{2z}	I	$C_2^z I$	$C_4^z I$	$C'_{2z} I$
χ	1	1	1	1	-1	-1	-1	-1

Table 1.1: The characters for the A-type AFM magnetic order, which corresponds to the mX_1^- irrep. We do not show the characters for all of the point group operations here, finding that the characters presented here are sufficient to determine the irrep label.

this A-type AFM order is one-dimensional. The characters we obtain from applying the operations of the D_{4h} point group are shown in Tab. 1.1.[5] Comparing these characters to online tables from the Bilbao crystallographic server, we find that this mode corresponds to the mX_1^- irrep. The m in front of the irrep name is to emphasize that this is a magnetic irrep. In particular, under inversion, the magnetic moments are unchanged. This is in contrast to atomic displacements, which obtain a minus sign under inversion.

Using this one-dimensional irrep, we can induce a representation of the full $Pm\bar{3}m$ space group.[6] Since there are three points in the star of X, the full order parameter corresponding to this induced representation is $3 \times 1 = 3$ dimensional.

If we instead consider the AFM-A mode where the moments are normal to the wavevector, the corresponding representation of the group of X is two-dimensional.

[5]Characters are defined as the traces of the various representation matrices. Since this magnetic order corresponds to a one-dimensional basis, the representation matrices are equal to their characters.

[6]We use the same name (here mX_1^-) to label both the representation of the group of $\mathbf{k}$ and its induced representation, describing the entire space group. However, it should be understood that these representations are in general not identical. We emphasize this in Sec. 4.2.2 by prepending a star to the labels of the induced representations.

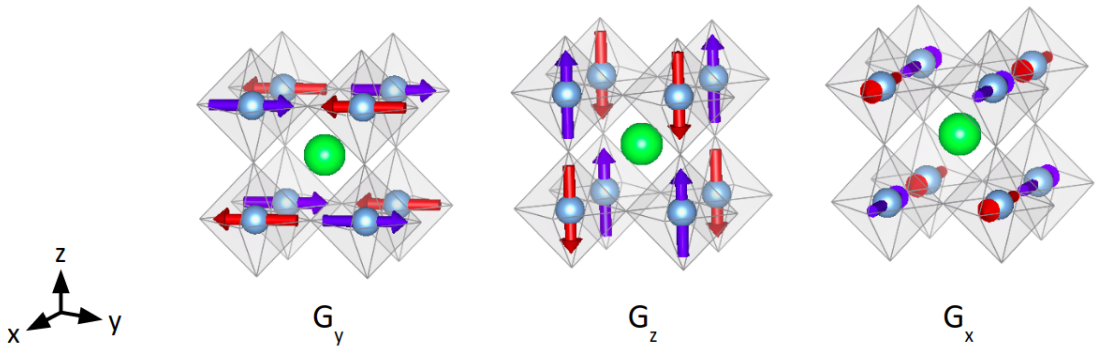

Figure 1.9: The basis vectors of the G-type type AFM order, which we find transform as under the mR_5^- irrep.

This is because if the wavevector is, say, $(0, 0, \pi)$, the moments can point along the pseudocubic x or y axes). Therefore, the dimension of the induced representation is $3 \times 2 = 6$-dimensional. Working analogously to the above example, we find that this AFM-A mode corresponds to the mX_5^- irrep.

G-type AFM

The G-type AFM magnetic order alternates in sign along all three cubic axes, and therefore corresponds to an R-point mode (π, π, π). Since the magnetic moment of the G-type AFM order can point in the x, y, or z direction, this representation is three-dimensional. These basis vectors are sketched in Fig. 1.9. Note that there is only one R-point in the star of R, since all corners of the cubic Brillouin zone are related by reciprocal lattice vectors. As such, all symmetry operations of our point group map the R point to itself, and the group of R is simply the entire point group of $Pm\bar{3}m$, O_h. In Tab. 1.2, we detail how these basis vectors transform into each other under different symmetry operations of group of R.

Comparing this to online tables, we find that this G-type AFM mode corresponds to the mR_5^- irrep. Note that unlike the X modes discussed above, the induced representation of the G-type AFM mode has the same dimension as the representation of the group of R. This is due the star of R only consisting of one wavevector. We have also repeated this analysis for the FM mode and the C-type AFM modes, listing the results in Tab. 1.3. Also listed in the Tab. 1.3 are the dimensions of the irreps. These

O_h	E	C_3	C_2	C_4	C_2'	I	C_3I	C_2I	C_4I	$C_2'I$
G_x	G_x	$-G_z$	$-G_x$	G_y	$-G_y$	$-G_z$	G_z	G_x	$-G_y$	G_y
G_y	G_y	G_x	$-G_y$	$-G_x$	$-G_x$	$-G_x$	$-G_x$	G_y	G_x	G_x
G_z	G_z	$-G_y$	G_z	$-G_z$	G_z	$-G_y$	G_y	$-G_z$	G_z	$-G_z$
χ	3	0	-1	-1	1	-3	0	1	1	1

Table 1.2: The characters for the AFM-G magnetic order, which corresponds to the mR_5^- irrep. As in Tab. 1.1, we do not show the characters for all point-group operations.

order parameters	FM	AFM-G	AFM-A $\parallel$	AFM-A $\perp$	AFM-C $\parallel$	AFM-C $\perp$
irreps	$m\Gamma_4^+$	mR_5^-	mX_1^-	mX_5^-	mM_2^+	mM_5^+
dimension	3	3	3	6	3	6

Table 1.3: The magnetic irreps obtained from our analysis. Here, the notation AFM-A $\parallel$ and AFM-A $\perp$ indicates a magnetic order which is parallel to the wavevector, respectively. Regarding the C-type AFM modes, recall that the spins in the C-type mode alternate in a checkerboard pattern within a plane, but is unchanged along an axis normal to this plane. Given this, AFM-C $\parallel$ (AFM-C $\perp$) describes the C-type AFM mode where the moment is parallel (perpendicular) to this special axis. We have also listed the dimension of each representation, which is the product of the size of the star of $\mathbf{k}$ and the size of the representation of the group of $\mathbf{k}$, for a given wavevector $\mathbf{k}$.

dimensions correspond not to the little cogroups, but to the induced representations describing the full space group.

1.2.6 Ginzburg-Landau Free Energy Expansion

One particularly fruitful application of the above machinery of representation theory is in the study of phase transitions. It is often quite difficult to obtain insights into a phase transition by looking at the microscopic details of a system. As such, to study the physics near a phase transition, it is common to employ a phenomenological Ginzburg-Landau approach, in which the free energy is expanded in terms of the relevant order parameters of the transition. Examples of possible order parameters include the magnetization in the case of a phase transition into a magnetically ordered phase (e.g. see Sec. 4.2), the electric polarization in the case of a transition into the ferroelectric phase, the superconducting gap for a phase transition into a superconducting phase, and structural mode amplitudes when dealing with structural phase transitions.

In the Ginzburg-Landau approach, one expands the free energy F in powers of

the relevant order parameters, with the constraint that F must be invariant under all operations of the symmetry group of the system. For example, consider the case of a isotropic ferromagnet, which we shall assume has time-reversal symmetry and spin-rotational symmetry. The order parameter of this system is the magnetization $\mathbf{m}$, which is a three-dimensional vector. Time reversal maps $\mathbf{m}$ to $-\mathbf{m}$, while a spin rotation maps $\mathbf{m}$ to $R\mathbf{m}$. Here, R is a 3×3 matrix in SO(3).

In this case, the free energy reads

$$F = a\mathbf{m} \cdot \mathbf{m} + b(\mathbf{m} \cdot \mathbf{m})^2, \tag{1.25}$$

where $\mathbf{m}$ is the vector-valued magnetization, and the coefficients a and b are determined by the microscopic details of the system. Here, we have kept terms only to quartic order, though one may include higher order terms if desired. Note that F by construction has both time-reversal and spin-rotational symmetry. Although this example is relatively simple, one would like to have a general formalism to obtain terms in the free energy for any symmetry group and any set of order parameters. To this end, we note that since F is invariant under all operations of the symmetry group, F transforms as the one-dimensional trivial irrep.[7] Therefore, we may construct terms in F for a given power n by taking a generic polynomial of order n composed of products of the order parameter components and applying the projection operator corresponding to the trivial irrep [47, 49].[8] From this, a simple algorithm to generate all terms in the free energy of order n is to apply the aforementioned projection operator to all possible monomials, stopping when one has obtained all invariant polynomials of order n [58]. In practice, we use the INVARIANTS software [59] to obtain the invariant polynomials. A concrete application of this formalism is given in Sec. 4.2, in which I obtain the invariant polynomials in the Ginzburg-Landau free energy expansion coupling the structural and magnetic degrees of freedom in the rare-earth titanates. Throughout the course of my research, I make extensive use of the Isotropy Software Suite [60, 61, 62] as well as the Bilbao Crystallographic Server [54, 55, 56].

[7] In the case of point groups, this irrep is denoted A_{1g}.

[8] In the case of a continuous group such as SO(3), there may be complications in defining the projection operator. We refer the interested reader to Ref. [57] for more details.

1.3 Theoretical Methods for Studying Magnetism

There are many theoretical methods for examining the magnetic properties of materials. In this chapter, I provide an overview of the methods which have been useful in my research.

1.3.1 Calculating Exchanges from Linear Regression and DFT

Using spin-polarized DFT calculations, we extract magnetic exchange constants as follows: after calculating the energy of different spin configurations using spin-DFT, we use linear regression to fit the energies to a classical Heisenberg Hamiltonian, $H = E_0 + \frac{1}{2}\sum_{ij} J_{ij}\mathbf{S}_i \cdot \mathbf{S}_j$.[9] Each spin configuration will have an associated equation, determined by the particular $\mathbf{S}_i \cdot \mathbf{S}_j$ terms. If we have N spin configurations, then we have N corresponding equations, which can be condensed into matrix form as follows:

$$\begin{pmatrix} E_1 \\ E_2 \\ \vdots \\ E_N \end{pmatrix} = \begin{pmatrix} 1 & \beta_{11} & \beta_{12} & \dots & \beta_{1m} \\ 1 & \beta_{21} & \beta_{22} & \dots & \beta_{2m} \\ \vdots & \vdots & \vdots & \ddots & \vdots \\ 1 & \beta_{N1} & \beta_{N2} & \dots & \beta_{Nm} \end{pmatrix} \begin{pmatrix} E_0 \\ J_1 \\ J_2 \\ \vdots \\ J_m \end{pmatrix} \tag{1.26}$$

where β_{ij} is the coefficient of J_j for spin configuration i. In practice the right and left-hand sides are not equal. We do not know the values for the set of exchanges J and the paramagnetic energy E_0. We can only try to find the set of values which minimizes a

[9] Although density functional theory in principle only allows us access to the ground state, we can in practice obtain the energy of many different spin configurations. In particular, the energy barrier between different spin configurations is often large, and a system will often stay in the spin configuration in which it was initialized. As such, we can initialize the system in different spin configurations and calculate their energies, even if these spin configurations do not correspond to the ground state.

measure of the difference in the RHS and LHS. As such, we define a cost function Θ

$$\Theta = \left\| \begin{pmatrix} E_1 \\ E_2 \\ \vdots \\ E_N \end{pmatrix} - \begin{pmatrix} 1 & \beta_{11} & \beta_{12} & \dots & \beta_{1m} \\ 1 & \beta_{21} & \beta_{22} & \dots & \beta_{2m} \\ \vdots & \vdots & \vdots & \ddots & \vdots \\ 1 & \beta_{N1} & \beta_{N2} & \dots & \beta_{Nm} \end{pmatrix} \begin{pmatrix} E_0 \\ J_1 \\ J_2 \\ \vdots \\ J_m \end{pmatrix} \right\|^2 \tag{1.27}$$

for which the optimal parameters of our model, E_0, J_1, ..., are obtained when Θ is minimized.

1.3.2 The Generalized Luttinger-Tisza Method

We begin with a brief overview of the Luttinger-Tisza method [63] and its generalization [64, 65]. Assume that the spin Hamiltonian of our system is given by a classical Heisenberg model:

$$H = \frac{1}{2} \sum_{ijab} J_{ij}^{ab} \mathbf{S}_{ia} \cdot \mathbf{S}_{jb} \tag{1.28}$$

In the above, $\mathbf{S}_{ia}$ corresponds to the spin in unit cell i, on atom a. In the classical version of this model, the Hamiltonian is a function of Np spins $\mathbf{S}_{ia}$, where $\mathbf{S}_{ia}$ is a three-dimensional vector, N is the number of unit cells, and p is the number of spins per unit cell. To obtain the classical ground state, we must minimize this $3Np$-dimensional function subject to the constraint that all spins are normalized to unity ($\mathbf{S}_{ia}^2 = 1.$) This has been termed the "strong" constraint. We recall that the spins are normalized to unity, because all factors of S have been absorbed into the definition of J_{ij}^{ab}. This minimization problem can be phrased as a Lagrange multiplier problem by introducing a different Lagrange multiplier for each spin. That is, we can minimize the Lagrangian

$$L = \frac{1}{2} \sum_{ijab} J_{ij}^{ab} \mathbf{S}_{ia} \cdot \mathbf{S}_{jb} - \sum_{ia} \frac{\lambda_{ia}}{2} (\mathbf{S}_{ia}^2 - 1), \tag{1.29}$$

where λ_{ia} are the Np introduced Lagrange multipliers and we have introduced a factor of $1/2$ for convenience. Though conceptually straightforward, minimization of this Lagrangian is in general intractable. To get around this, Luttinger and Tisza considered the following Lagrangian instead:

$$L = \frac{1}{2}\sum_{ijab} J_{ij}^{ab}\mathbf{S}_{ia}\cdot\mathbf{S}_{jb} - \frac{\lambda}{2}\left(\left(\sum_{ia}\mathbf{S}_{ia}^2\right) - Np\right), \tag{1.30}$$

Minimizing this Lagrangian is equivalent to replacing the Np "strong" constraints with one "weak" constraint $Np = \sum_{ia}\mathbf{S}_{ia}^2$. Setting the gradient of this Luttinger-Tisza Lagrangian with respect to spin $\mathbf{S}_{ia}$ equal to zero, we obtain

$$\sum_{jb} J_{ij}^{ab}\mathbf{S}_{jb} = \lambda\mathbf{S}_{ia} \tag{1.31}$$

Moving to momentum space, this equation becomes

$$\sum_{b} J^{ab}(\mathbf{k})\mathbf{S}_b(\mathbf{k}) = \lambda\mathbf{S}_a(\mathbf{k}), \tag{1.32}$$

where $J^{ab}(\mathbf{k}) = \sum_j J_{ij}^{ab}e^{i\mathbf{k}\cdot(\mathbf{R}_j-\mathbf{R}_i)}$ and $\mathbf{S}_a(\mathbf{k}) = 1/\sqrt{N}\sum_i e^{-i\mathbf{k}\cdot\mathbf{R}_i}\mathbf{S}_{ia}$. This can be viewed as an eigenvalue problem, where $J^{ab}(\mathbf{k})$ is a $p\times p$ - dimensional matrix.

We can diagonalize this matrix at each $\mathbf{k}$ to find p eigenvalues, which are guaranteed to be real from the hermiticity of $J^{ab}(\mathbf{k})$. Repeating this at each momentum, one obtains p eigenvalue bands which extend throughout the Brillouin zone. The momentum $\mathbf{q}$ of the optimal spin configuration is obtained by searching for the minimum eigenvalue $\lambda_{\min}(\mathbf{q})$ of this band structure. The eigenvector $\mathbf{S}_a(\mathbf{q})$ corresponding to this eigenvalue minimizes the original Hamiltonian subject to the weak constraint. At this point, one checks if the resulting spin configuration satisfies the strong constraint, as required.

One can show that the eigenvector corresponding to spin configuration $\mathbf{S}_a(\mathbf{k})$ satisfies the strong constraint if all of its components are equal in magnitude. If so, the spin configuration is physically allowed, and the energy of the spin configuration is $E = N\lambda_{\min}(\mathbf{q})/2$.

However, there is no guarantee that the resulting spin configuration satisfies the strong constraint. In fact, though this method works for Bravais lattices ($p = 1$), it

often fails in the case when there is more than one spin per primitive unit cell ($p > 1$). Indeed, when applied to our system, the original Luttinger-Tisza method fails to produce a spin configuration which satisfies the strong constraint.

We therefore employ the generalized Luttinger-Tisza method [64] of Lyons and Kaplan, and minimize the following Lagrangian:

$$L = \frac{1}{2}\sum_{ijab} J_{ij}^{ab}\mathbf{S}_{ia}\cdot\mathbf{S}_{jb} - \frac{\lambda}{2}\sum_{ia}(\alpha_a^2\mathbf{S}_{ia}^2 - \alpha_a^2). \tag{1.33}$$

Minimizing this Lagrangian is equivalent to replacing the previous weak constraint with a generalized weak constraint $N\sum_a \alpha_a^2 = \sum_{ia}\alpha_a^2\mathbf{S}_{ia}^2$, where we have introduced p parameters α_a. In doing so, we expand the constraint space, since there are more spin configurations which satisfy this generalized weak constraint than the original weak constraint. Therefore, we can possibly obtain a solution to this generalized minimization problem which also satisfies the strong constraint. Minimizing this new Lagrangian with respect to $\mathbf{S}_{i\alpha}$ and moving to momentum space, we obtain

$$\sum_b J^{ab}(\mathbf{k})\mathbf{S}_b(\mathbf{k}) = \lambda\alpha_a^2\mathbf{S}_a(\mathbf{k}). \tag{1.34}$$

We now define $\mathbf{P}_a(\mathbf{k}) = \alpha_a\mathbf{S}_a(\mathbf{k})$ and $\mathcal{J}^{ab}(\mathbf{k}) = J^{ab}(\mathbf{k})/(\alpha_a\alpha_b)$, where no sum is implied over a or b. With these definitions, Eq. 1.34 becomes

$$\sum_b \mathcal{J}^{ab}(\mathbf{k})\mathbf{P}_b(\mathbf{k}) = \lambda\mathbf{P}_a(\mathbf{k}). \tag{1.35}$$

This is an eigenvalue problem for the matrix $\mathcal{J}^{ab}(\mathbf{k})$. We can now work as in the original Luttinger-Tisza method to obtain the optimal eigenvalue and eigenvector $\mathbf{P}_a(\mathbf{k})$. The parameters α_a are determined by requiring the resulting spin configuration to satisfy the strong constraint. One can show that the eigenvector corresponding to spin configuration $\mathbf{S}_a(\mathbf{k})$ satisfies the strong constraint if all of its components are equal in magnitude. In this case, the resulting spin configuration can be written as

$$\mathbf{S}_{i\alpha} = \cos(\mathbf{k}_0\cdot\mathbf{R}_i + \phi_\alpha)\hat{\mathbf{u}} + \sin(\mathbf{k}_0\cdot\mathbf{R}_i + \phi_\alpha)\hat{\mathbf{v}}, \tag{1.36}$$

for some wavevector $\mathbf{k}_0$ and phases ϕ_α. Here, $\hat{\mathbf{u}}$ and $\hat{\mathbf{v}}$ are arbitrary orthonormal

vectors, reflecting the spin-rotational SU(2) symmetry of the Heisenberg Hamiltonian.

1.3.3 Calculation of Mean-field Transition Temperatures

With the exchange parameters obtained from the first principle calculations, we can estimate the magnetic transition temperature T_c based on a mean-field treatment of the classical Heisenberg model [66]:

$$H = \frac{1}{2}\sum_{ij} J_{ij}\boldsymbol{S}_i \cdot \boldsymbol{S}_j, \tag{1.37}$$

where J_{ij} is the Heisenberg interaction coupling spins i and j, and the spins are normalized by $|\boldsymbol{S}_i| = 1$. Unlike in the previous section, the indices i and j do not label a unit cell, but specific spins in the system. The sums are then over all of the spins of the system. With this, the above Hamiltonian is general enough to describe systems with any number of spins per unit cell. Taking $\mathbf{S}_i = \langle \mathbf{S}_i \rangle + \delta\mathbf{S}_i$ and expanding the Heisenberg Hamiltonian to $O(\delta S^2)$, we have

$$H = \frac{1}{2}\sum_{ij} J_{ij}\mathbf{S}_i \cdot \mathbf{S}_j \tag{1.38}$$

$$= \sum_{ij} J_{ij} \langle \mathbf{S}_j \rangle \cdot \mathbf{S}_i - \frac{1}{2}\sum_{ij} J_{ij} \langle \mathbf{S}_i \rangle \cdot \langle \mathbf{S}_j \rangle + O(\delta S^2). \tag{1.39}$$

We now ignore spatial fluctuations and take $\langle \mathbf{S}_i \rangle = m\mathbf{S}_i^{\mathrm{GS}}$, where $0 \leq m \leq 1$ is the order parameter and $\mathbf{S}_i^{\mathrm{GS}}$ is the ground-state configuration. The mean-field Hamiltonian becomes

$$H_{\mathrm{MF}} = m\sum_{ij} J_{ij}\mathbf{S}_j^{\mathrm{GS}} \cdot \mathbf{S}_i - \frac{m^2}{2}\sum_{ij} J_{ij}\mathbf{S}_i^{\mathrm{GS}} \cdot \mathbf{S}_j^{\mathrm{GS}} \tag{1.40}$$

$$= m\sum_{i} \mathbf{M}_i \cdot \mathbf{S}_i - \frac{m^2}{2}\sum_{i} \mathbf{S}_i^{\mathrm{GS}} \cdot \mathbf{M}_i, \tag{1.41}$$

where the mean-field $\mathbf{M}_i$ felt by spin $\mathbf{S}_i$ is defined as

$$\mathbf{M}_i = \sum_j J_{ij} \mathbf{S}_j^{\mathrm{GS}}. \tag{1.42}$$

With this, the partition function Z is

$$Z = \int \prod_i \frac{d\phi_i d\theta_i \sin\theta_i}{4\pi} e^{-\beta H_{\mathrm{MF}}} \tag{1.43}$$

$$= e^{\frac{m^2}{2}\sum_i \mathbf{S}_i^{\mathrm{GS}}\cdot\mathbf{M}_i} \int \prod_i \frac{d\phi_i d\theta_i \sin\theta_i}{4\pi} e^{-\beta m \mathbf{M}_i\cdot\mathbf{S}_i}. \tag{1.44}$$

Expanding the dot product $\mathbf{M}_i \cdot \mathbf{S}_i$ and evaluating the ϕ_i integrals, we obtain

$$Z = e^{\frac{m^2}{2}\sum_i \mathbf{S}_i^{\mathrm{GS}}\cdot\mathbf{M}_i} \int \prod_i \frac{d\theta_i \sin\theta_i}{2} e^{-\beta m M_i^z \cos\theta_i} \times I_0\left(\beta m \sin\theta_i \sqrt{(M_i^x)^2 + (M_i^y)^2}\right), \tag{1.45}$$

where $I_0(z)$ is a modified Bessel function of the first kind. Since we are only interested in the transition temperature T_{MF}, we expand the integrand taking $m \ll 1$. Completing the θ_i integrals, we obtain

$$Z \approx e^{\frac{m^2}{2}\sum_i \mathbf{S}_i^{\mathrm{GS}}\cdot\mathbf{M}_i} \prod_i \left(1 + \frac{\beta^2 m^2}{6}\mathbf{M}_i^2\right), \tag{1.46}$$

and

$$F = -T \ln Z \tag{1.47}$$

$$= -\frac{m^2}{2}\sum_i \mathbf{S}_i^{\mathrm{GS}}\cdot\mathbf{M}_i - \frac{1}{\beta}\sum_i \ln\left(1 + \frac{\beta^2 m^2}{6}\mathbf{M}_i^2\right). \tag{1.48}$$

The order parameter m is found by enforcing $\partial F/\partial m = 0$, which gives

$$\sum_i \mathbf{S}_i^{\mathrm{GS}}\cdot\mathbf{M}_i + \frac{\beta}{3}\sum_i \frac{\mathbf{M}_i^2}{1 + \frac{\beta^2 m^2}{6}\mathbf{M}_i^2} = 0. \tag{1.49}$$

To find the transition temperature, we take $m = 0$, finding

$$T_{\mathrm{MF}} = -\frac{\sum_i \mathbf{M}_i^2}{3\sum_i \mathbf{S}_i^{\mathrm{GS}} \cdot \mathbf{M}_i}. \tag{1.50}$$

So far, we have not assumed anything about the periodicity of our system. We will now assume that we have a periodic system with p spins per unit cell. With this, the Heisenberg Hamiltonian can be rewritten as

$$H = \frac{1}{2}\sum_{ij\alpha\beta} J_{ij}^{\alpha\beta} \mathbf{S}_{i\alpha} \cdot \mathbf{S}_{j\beta}, \tag{1.51}$$

and the formula for the transition temperature can be rewritten as

$$T_{\mathrm{MF}} = -\frac{\sum_{i\alpha} \mathbf{M}_{i\alpha} \cdot \mathbf{M}_{i\alpha}}{3\sum_{i\alpha} \mathbf{S}_{i\alpha}^{\mathrm{GS}} \cdot \mathbf{M}_{i\alpha}}. \tag{1.52}$$

Here the labels i and α index the unit cell and spin sublattice, respectively. We rewrite the above formula in momentum space, obtaining

$$T_{\mathrm{MF}} = -\frac{\sum_{k\alpha} \mathbf{M}_{k\alpha} \cdot \mathbf{M}_{-k\alpha}}{3\sum_{k\alpha} \mathbf{S}_{k\alpha}^{\mathrm{GS}} \cdot \mathbf{M}_{-k\alpha}}. \tag{1.53}$$

To simplify this, we first present a few useful relations. First, due to the translational symmetry of our system, we have $J_{ij}^{\alpha\beta} = J^{\alpha\beta}(\mathbf{d})$, where $\mathbf{d} = \mathbf{R}_i - \mathbf{R}_j$. Moreover, the spin-exchange symmetry implies $J_{ij}^{\alpha\beta} = J_{ji}^{\beta\alpha}$, or equivalently $J^{\alpha\beta}(\mathbf{d}) = J^{\beta\alpha}(-\mathbf{d})$. Recalling that $J^{\alpha\beta}(\mathbf{k}) = \sum_{\mathbf{d}} J^{\alpha\beta}(\mathbf{d}) e^{-i\mathbf{k}\cdot\mathbf{d}}$, the reality of the exchange constants implies that $J^{\alpha\beta}(-\mathbf{k}) = J^{\alpha\beta}(\mathbf{k})^*$. Combining these two properties, we also have that the $J^{\beta\alpha}(\mathbf{k})^* = J^{\alpha\beta}(\mathbf{k})$, i.e. the matrix given by $J^{\alpha\beta}(\mathbf{k})$ is Hermitian. Rewriting $\mathbf{M}_{k\alpha}$ in momentum-space and using the Hermiticity of $J^{\alpha\beta}(\mathbf{k})$, one finds $\mathbf{M}_{k\alpha} = \sum_\beta J^{\alpha\beta}(\mathbf{k}) \mathbf{S}_{k\beta}$. Inserting this into the formula for the transition temperature, the numerator becomes

$$\sum_{k\alpha} \mathbf{M}_{k\alpha}\mathbf{M}_{-k\alpha} = \sum_{k\alpha\beta\gamma} J^{\alpha\beta}(\mathbf{k}) J^{\alpha\gamma}(-\mathbf{k}) \mathbf{S}_{k\beta} \cdot \mathbf{S}_{-k\gamma} \tag{1.54}$$

$$= \sum_{k\alpha\beta\gamma} J^{\alpha\beta}(\mathbf{k}) J^{\gamma\alpha}(\mathbf{k}) \mathbf{S}_{k\beta} \cdot \mathbf{S}_{-k\gamma}. \tag{1.55}$$

To continue, we must have an expression for the ground-state spin configuration. We will assume that the ground-state spin configuration is of the form one would find from Luttinger-Tisza, i.e.

$$\mathbf{S}_{i\alpha} = \cos(\mathbf{k}_0 \cdot \mathbf{R}_i + \phi_\alpha)\hat{\mathbf{u}} + \sin(\mathbf{k}_0 \cdot \mathbf{R}_i + \phi_\alpha)\hat{\mathbf{v}}. \tag{1.56}$$

Here, $\hat{\mathbf{u}}$ and $\hat{\mathbf{v}}$ are arbitrary orthonormal vectors, the phases ϕ_α reflect the relative angles between the spins in a unit cell, and $\mathbf{k}_0$ is the wavevector reflecting the periodicity of the spin configuration. Using this, we can obtain $\mathbf{S}_{\mathbf{k}\alpha}$ calculate the dot product and sum over $\mathbf{k}$, after which the above becomes

$$\sum_{k\alpha} \mathbf{M}_{k\alpha}\mathbf{M}_{-k\alpha} = N \sum_{\alpha\beta\gamma} e^{-i\phi_\gamma} J^{\gamma\alpha}(\mathbf{k}_0) J^{\alpha\beta}(\mathbf{k}_0) e^{i\phi_\beta}, \tag{1.57}$$

where N is the number of unit cells in the system. Defining the p-component vector $\Psi = (e^{i\phi_1}, e^{i\phi_2}, ..., e^{i\phi_p})^T$ and the $p \times p$ matrix $J(\mathbf{k})$, whose matrix elements are $J^{\alpha\beta}(\mathbf{k})$, we can condense the above formula to

$$\sum_{k\alpha} \mathbf{M}_{k\alpha}\mathbf{M}_{-k\alpha} = N\Psi^\dagger J(\mathbf{k}_0)^2 \Psi. \tag{1.58}$$

With similar algebra, we find that $\sum_{k\alpha} \mathbf{S}^{\mathrm{GS}}_{k\alpha} \cdot \mathbf{M}_{-k\alpha} = N\Psi^\dagger J(\mathbf{k}_0)\Psi$, so that T_{MF} is given by

$$T_{\mathrm{MF}} = -\frac{\Psi^\dagger J(\mathbf{k}_0)^2 \Psi}{3\Psi^\dagger J(\mathbf{k}_0)\Psi}. \tag{1.59}$$

In the case of a single spin per unit cell, the above reduces to $T_{\mathrm{MF}} = -J(\mathbf{k}_0)/3$.

1.3.4 Linear Spin Wave Theory

In this section, I review how we obtain the magnon spectrum from the Heisenberg Hamiltonian:

$$H = \frac{1}{2} \sum_{ij} \mathbf{S}_i \cdot \mathbf{S}_j. \tag{1.60}$$

Unlike the previous sections, we will not work with the classical Heisenberg Hamiltonian, i.e. $\mathbf{S}_i$ and $\mathbf{S}_j$ should be understood as operators. To find the magnon spectrum however, we assume that we are given some classical ground state, which for example might be obtained via the Luttinger-Tisza method described above. With this Hamiltonian, we transform from spin operators $\mathbf{S}_i$ to bosons, using the Holstein-Primakoff transformation [67, 68]. In this method, rather than working in the structural unit cell, we work with a magnetic unit cell, which can in general be larger than the structural unit cell. To be specific, assume that we have m spins in a magnetic unit cell. We will also assume that the magnetic ground state is collinear, i.e. all spins are aligned or anti-aligned along a specific direction. For magnetic ground states which are non-collinear or incommensurate with the ground state, a more general analysis should be performed [69, 70].

For collinear systems, in which each spin can be considered to point either up or down, we introduce m types of bosons, each corresponding to a different spin (pointing either up or down) in the magnetic unit cell. For those spins which point up in the classical ground state, we introduce the Holstein-Primakoff bosons $a_{i,n}$ as follows:

$$S^z_{i,n} = S - a^\dagger_{i,n} a_{i,n} \tag{1.61}$$

$$S^-_{i,n} = a^\dagger_{i,n} \sqrt{2S - a^\dagger_{i,n} a_{i,n}} \tag{1.62}$$

The index i runs over the N spins which point up in the magnetic unit cell, while the index n runs over the different magnetic unit cells. Similarly, we introduce the following bosons for the spins which point down in the magnetic unit cell:

$$S^z_{i,n} = -S + a^\dagger_{i,n} a_{i,n} \tag{1.63}$$

$$S^-_{i,n} = \sqrt{2S - a^\dagger_{i,n} a_{i,n}}\, a_{i,n}. \tag{1.64}$$

After rewriting the Hamiltonian using the above transformation, we then expand the Hamiltonian in powers of $1/S$. The lowest order term is a constant which gives us the energy of the classical ground state. The next term is quadratic in the Holstein-Primakoff

bosons $a_{i,n}$, and diagonalizing this gives the spin wave spectrum to lowest order in $1/S$. **Linear spin wave theory (LSWT)**, which we consider here, corresponds to ignoring higher order terms that lead to a renormalization of the spin wave spectrum as well as magnon decay terms.

With this transformed Hamiltonian, we then move to momentum-space. The Hamiltonian can be written as

$$H = \sum_k \begin{pmatrix} \mathbf{a}_k^\dagger & \mathbf{a}_{-k} \end{pmatrix} H_0(k) \begin{pmatrix} \mathbf{a}_k \\ \mathbf{a}_{-k}^\dagger, \end{pmatrix} \tag{1.65}$$

where $H_0(k)$ is a $2N \times 2N$ matrix. The goal of LSWT is to transform this Hamiltonian into a form

$$H = E_0 + \sum_{k,n} \varepsilon_n(k) \alpha_{n,k}^\dagger \alpha_{n,k}, \tag{1.66}$$

which counts the magnons and correspondingly ascribes an energy ε_k to them. Here, $\alpha_{n,k}^\dagger$ and $\alpha_{n,k}$ are creation and annihilation operators for magnons in band n with momentum k, respectively.[10]

To do so, note that if H is diagonalized, then $[\alpha_{m,q}, H] = [\alpha_{m,q}, \sum_k (\varepsilon_{n,k} \alpha_{n,k}^\dagger \alpha_{n,k} + \frac{1}{2})] = \varepsilon_{m,q} \alpha_{m,q}$. With this, we can define a $2N \times 2N$ matrix M, such that $[\mathbf{v}, H] = M\mathbf{v}$, where $\mathbf{v}$ is the column vector $(\mathbf{a}_k, \mathbf{a}_{-k}^\dagger)^T$. One can show that M is block diagonal and composed of two $N \times N$ matrices. Moreover, it is only necessary to diagonalize one of these blocks, which we denote $\mathcal{M}(\mathbf{k})$. By diagonalizing $\mathcal{M}(\mathbf{k})$, we can find the Bogoliubov operators $\alpha_{n,k}$ and their associated energy eigenvalues $\varepsilon_{n,k}$. For each $\mathbf{k}$, there will be N positive bands and N symmetric negative bands. This symmetric spectrum is a consequence of the redundancy of our description. In particular, $\mathbf{a}_k$ and $\mathbf{a}_{-k}^\dagger$ are not independent degrees of freedom. Accordingly, these negative eigenvalues do not imply negative magnon energies, but rather that our Bogoliubov operator is instead a creation operator $\alpha_{n,k}^\dagger$ (and not an annihilation operator $\alpha_{n,k}$ as originally assumed). Additionally, it turns out that each of the magnon bands are two-fold degenerate. This can be understood from the fact that in an antiferromagnetic ground state (which we consider here), there are two symmetry-equivalent excitations: magnons which have

[10] We note that E_0 here includes not only the classical ground state energy, but also the zero-point energy of the new Holstein-Primakoff ground state.

$\Delta S_z = -1$ (which lower S_z on the spin-up sublattice), and magnons which have $\Delta S_z = 1$ (which raise S_z on the spin-down sublattice). As such, although there are N magnon bands, there are in reality only $N/2$ distinct magnon energies per momentum $\mathbf{k}$.

1.3.5 Exact Diagonalization

Although LSWT allows one to calculate the magnon spectrum of a spin system, it is significantly more difficult to access multi-magnon states, since one must take into account higher-order corrections to the Hamiltonian which allow for magnon-magnon interactions. Additionally, since LSWT calculations are built on magnon excitations, one cannot access spinon states, which are fractionalized magnon excitations. Exact diagonalization presents a solution to both difficulties. A thorough review of how to computationally implement exact diagonalization can be found in Ref. [71]. Here, I simply provide a brief overview of the underlying theory.

The idea behind exact diagonalization is straightforward. Given a system which we would like to investigate, we consider a finite-size cluster of N lattice sites. For this cluster, we then explicitly construct the exact Hamiltonian matrix, which can be diagonalized numerically. With the resulting energies and eigenstates, one can calculate any desired observable. Unlike with LSWT, there is no obstruction to finding multi-magnon (or multi-spinon) states.

However, since one is typically concerned with the thermodynamic limit, exact diagonalization is useful only if we can work with large system sizes so as to mitigate finite-size effects. This is a significant drawback, since the basis grows exponentially with system size (the size of the basis for N spin-1/2 particles is 2^N.) This makes implementing exact diagonalization computationally intensive.[11] However, exact diagonalization results on small system sizes may still yield important physical insights, as we discuss below.

Since we are concerned in this Thesis with magnetic properties of materials, we restrict ourselves to spin Hamiltonians. Assume we have a cluster of N spin-1/2 particles,

[11] Luckily, in practice we are only interested in the lowest-energy states. This allows us to use specialized, more computationally efficient diagonalization routines, such as the Lanczos algorithm. We discuss this further at the end of this section.

which occupy the sites of some lattice. To construct the matrix describing our Hamiltonian, we must first construct a basis on which our Hamiltonian acts. One natural basis is the set of product states, in which a single spin in a given product state is either $|\uparrow\rangle$ or $|\downarrow\rangle$. It is convenient to refer to $|\uparrow\rangle$ as $|1\rangle$, and $|\downarrow\rangle$ as $|0\rangle$. This allows us to assign a number to each product state through its binary representation. For example, the state $|\uparrow\downarrow\uparrow\downarrow\rangle \rightarrow |1010\rangle$. Since 1010 is $2^3 + 2^1 = 10$, $|\uparrow\downarrow\uparrow\downarrow\rangle$ is the tenth state in this basis of product states (the zeroth state is $|\downarrow\downarrow\downarrow\downarrow\rangle$). More generally, given an N-spin system, we can map each state to an N-digit binary number.

With this basis, we can in principle loop through each basis state and calculate how the Hamiltonian acts on each of the 2^N basis states. Using this information to construct a $2^N \times 2^N$ matrix, the spectrum can then be found by computationally diagonalizing this matrix. However, even for moderately sized values of N, this method becomes computationally intractable. For example, for a cluster with $N = 20$ spins, the memory needed to simply store the $2^{20} \times 2^{20}$ Hamiltonian matrix is 137 gigabytes!

Therefore, in order to implement exact diagonalization, we must find a way to reduce the size of the basis. This may be done by exploiting the symmetries of the system to block diagonalize the Hamiltonian. An added benefit of block diagonalizing the Hamiltonian is that we also obtain more information about the symmetries of different states of the system.

I now discuss how one would block diagonalize the Hamiltonian. Assume we have an operator A which commutes with the Hamiltonian H, i.e. $[A, H] = 0$. One can show that the Hamiltonian is block-diagonal in the basis of eigenstates of A. That is, if $A|a\rangle = a|a\rangle$ and $A|b\rangle = b|b\rangle$ for $a \neq b$, then $\langle a|H|b\rangle = 0$. In other words, H only mixes states with the same quantum numbers. Therefore, instead of diagonalizing the original $2^N \times 2^N$ matrix, it is sufficient to diagonalize the smaller blocks (labeled by different quantum numbers) separately. Each block describes how the eigenstates of A of a given quantum number are transformed under action of the Hamiltonian H. To implement this computationally, we must be able to construct a basis which spans the eigenstates of A with eigenvalue a. We can then see how the Hamiltonian acts on our basis and construct the block Hamiltonian in this subspace.

The above method of block diagonalization can easily be extended given more operators that commute with H. For example, assume we have three operators, A, B, and

C which commute with each other and H. one may block diagonalize H by working in the basis of simultaneous eigenstates of A, B, and C, labeled by $|a, b, c\rangle$. Each block is then labeled by the quantum numbers a, b, and c.

In practice, operators which commute with H are found by examining the symmetries of our system. In this Thesis, we are concerned with studying the Heisenberg model as applied to lattice systems. As a concrete example, let us work in two dimensions and label the lattice vectors of the crystal $\mathbf{a}$ and $\mathbf{b}$. To model the lattice structure, we impose periodic boundary conditions on our finite-size cluster. With these boundary conditions, translations by multiples of $\mathbf{a}$ or $\mathbf{b}$ leave the system invariant. The system therefore has translational symmetry, implying that translations corresponding to any integer multiple of $\mathbf{a}$ or $\mathbf{b}$ commute with H. Recall from our earlier discussion of group theory that translations by some lattice vector $\mathbf{R}$ leave Bloch states invariant up to a phase factor $e^{i\mathbf{k}\cdot\mathbf{R}}$. As such, the eigenstates of translation are simply the Bloch states, and the quantum number labeling each state is the crystal momentum $\mathbf{k}$. From this, if we work in a basis composed of momentum eigenstates, the Hamiltonian then is block diagonal in $\mathbf{k}$.

Other than translational symmetry, our Heisenberg Hamiltonian is symmetric under rotation of all the spins in our system. That is, the Hamiltonian has SU(2) symmetry. Therefore, we may block diagonalize by S^z_{tot} and S^2_{tot}. In practice, one does not typically block diagonalize by S^2_{tot} for computational convenience.[12] A system may also by symmetric under spatial-inversion and spin-inversion, for example, which could be useful for further block diagonalization.

I now discuss how to construct a basis of eigenstates for S^z_{tot}, given an eigenvalue s^z_{tot}. For convenience, we will instead label our states by the equivalent quantum number `num_up`, which is the number of $\uparrow$-spins in a given product state. A natural method to construct a basis corresponding to a given `num_up` is to loop through all 2^N product states and check if each state has the desired `num_up` spins. However, this is computationally inconvenient for large system sizes, since one has to loop through all 2^N product states, when there are only $\binom{N}{\texttt{num\_up}}$ states which we would like to obtain.

We therefore use a different method which generates all the states with a given

[12] According to [71], block diagonalizing by S^2_{tot} makes the Hamiltonian dense rather than sparse, which is undesirable because this requires more memory to store.

num_up. Consider the spin configuration corresponding to $2^{\texttt{num\_up}} - 1$. When converted to binary, one sees that this is the spin configuration with $\uparrow$ in the first num_up positions, and 0 otherwise. We then generate all other states with this by shifting the positions where the $\uparrow$ spins are located. By construction, each state generated by shifting these positions still has the same amount of num_up spins. By continually shifting the positions of the $\uparrow$ spins, we can obtain all states with a given num_up efficiently.

Having discussed how we generate the basis of S^z_{tot} states, we now turn to the issue of generating eigenstates of translation. Since the eigenstates of translation are Bloch states, generating eigenstates of translation is equivalent to generating Bloch states from our original spin configurations. This can be done by applying Eq. 1.24 from our discussion of group theory. In particular, given a spin configuration $|\text{config}\rangle$, a Bloch state with momentum $\mathbf{k}$ can be constructed using the definition below:

$$|\mathbf{k}(\text{config})\rangle = A \sum_j e^{-i\mathbf{k}\cdot\mathbf{R}_j} T(\mathbf{R}_j) \, |\text{config}\rangle \, . \tag{1.67}$$

In the above, A is a normalization factor to be determined and $T(\mathbf{R}_j)$ is the translation operator corresponding to the lattice vector $\mathbf{R}_j$. To use this basis to construct the block Hamiltonian, we must calculate the normalization factor A. To this end, we first note that the above definition of $|\mathbf{k}(\text{config})\rangle$ is sometimes redundant. For example, consider a chain of six spins arranged on a ring. If we apply the above definition for $|\mathbf{k}(\text{config})\rangle$ to the configuration corresponding to the classical Neel state $|N\rangle = |\uparrow\downarrow\uparrow\downarrow\uparrow\downarrow\rangle$, we find

$$|k(N)\rangle = A\big(|N\rangle + e^{-ika} \left|\tilde{N}\right\rangle + e^{-2ika} |N\rangle + e^{-3ika} \left|\tilde{N}\right\rangle + e^{-4ika} |N\rangle + e^{-5ika} \left|\tilde{N}\right\rangle \big) \tag{1.68}$$

$$= A(1 + e^{-2ika} + e^{-4ika})\big(|N\rangle + e^{-ika} \left|\tilde{N}\right\rangle \big) \tag{1.69}$$

where we have defined $\left|\tilde{N}\right\rangle = T(a) \, |N\rangle = |\downarrow\uparrow\downarrow\uparrow\downarrow\uparrow\rangle$ for notational convenience. In the above, the states $|N\rangle$ and $\left|\tilde{N}\right\rangle$ both appeared three times. This is because $|N\rangle$ is periodic under translations of length $2a$. Furthermore this redundancy led, upon simplification, to the sum of phase factors in the second line above. The normalization

factor A in the above example can now be seen to be $A = (\sqrt{2}\big|(1 + e^{-2ika} + e^{-4ika})\big|)^{-1}$.

For some values of k, the above sum of phase factors may be zero. This is equivalent to the statement that a given spin configuration is incompatible with certain values of k. For example, it is not possible to create a state with a nonzero k from the ferromagnetic spin configuration. To see if a given spin configuration is compatible with momentum k, we calculate the sum of phase factors above and see if it is nonzero. If so, we add the momentum state generated from the spin configuration to our basis. To be more specific, given a spin configuration, we loop through all translations $\mathbf{R}_j$ of our lattice. If some translation $T(\mathbf{R}_i)$ leaves the spin configuration invariant, we store the corresponding phase factor $e^{-i\mathbf{k}\cdot\mathbf{R}_i}$. If the sum of these phase factors is nonzero, the momentum state $|\mathbf{k}(\text{config})\rangle$ is allowed. We then calculate and store the corresponding normalization factor A corresponding to this state.

With this, we can now construct the basis given quantum numbers `num_up` and $\mathbf{k}$. The block Hamiltonian is then obtained by acting H on each of the eigenstates in our basis, and storing the corresponding matrix elements.[13] With this Hamiltonian matrix, we can numerically diagonalize the block Hamiltonians for different quantum numbers to obtain the spectrum of our finite-size cluster. In practice, we are not interested in the entire spectrum, but only the lowest-energy states. As such, we employ the Lanczos algorithm, which given some Hermitian matrix M and number n, obtains the n lowest eigenvalues as well as their corresponding eigenstates [72, 73, 71]. Since n is typically much smaller than the size of our basis, using the Lanczos algorithm yields the desired eigenstates and eigenvalues much more efficiently than brute-force matrix diagonalization.

After obtaining the eigenstates and eigenvalues, one can in principle calculate any desired observable. In particular, given some operator O, we can act O on our basis states to see how they transform. This then allows us to obtain the matrix elements of O in our basis. With these matrix representation of O, we can then calculate any desired expectation value. We note that this construction of O is essentially identical to the construction of the Hamiltonian matrix H.

[13] Even after implementing these symmetries, the block sizes can be relatively large. As such, it is more efficient to only store the nonzero matrix elements rather than the entire matrix. Since the Hamiltonian matrix turns out to be sparse, this leads to a significant reduction in the memory required to store the block.

Additionally, by looking at the symmetry of the states appearing in the ground-state manifold (also referred to as the tower of states [74]), group theory can be used to determine the possible symmetry-breaking long-range ordered states which occur in the thermodynamic limit [75, 76, 77].

Chapter 2

The magnetic excitation spectrum of the botallackite cuprate $Cu_2Br(OH)_3$

This chapter is adapted from my work *First-principles characterization of the magnetic properties of $Cu_2(OH)_3Br$* [1].

2.1 Introduction

Low dimensional spin-1/2 transition metal oxides and oxyhalides continue to be at the forefront of research investigating nonclassical phases such as quantum spin liquids. In this study, we examine the magnetic properties of the oxyhalide $Cu_2(OH)_3Br$ in the botallackite structure using first-principles density functional theory, linear spin-wave theory, and exact diagonalization calculations. This quasi-2D system consists of Cu^{2+} $S = 1/2$ moments arranged on a distorted triangular lattice. Our exact diagonalization calculations, which rely on a first-principles-based magnetic model, generate spectral functions consistent with inelastic neutron scattering (INS) data. By performing computational experiments to disentangle the chemical and steric effects of the halide ions, we find that the dominant effect of the halogen ions is steric in the $Cu_2(OH)_3X$ series of compounds.

Low-dimensional magnetism can give rise to a host of exotic phenomena. For example, in quasi-1D systems, the fractionalization of magnons into spinons has been both theoretically predicted and experimentally observed [78, 79, 80]. In addition to low-dimensionality, frustration also plays a key role in the magnetic behavior of a system, as in the Majumdar-Ghosh model, which predicts a valence-bond solid [81, 82] or in the Kitaev honeycomb model, which predicts a spin liquid [83]. In recent years, Kagome antiferromagnets have garnered extensive interest, especially the Herbertsmithite compound, which contains local spin-1/2 magnetic moments [84]. Despite large antiferromagnetic interactions ($J \sim 17$ meV) which couple nearest-neighbor spins, no signature of magnetic ordering is measured down to ~ 50 mK [85]. This makes Herbertsmithite a prime candidate for hosting a quantum spin liquid ground state. Herbertsmithite can be formed from paratacamite $Cu_2(OH)_3Cl$ by replacing one quarter of the Cu atoms with Zn atoms [86]. In this study, we shed light on the magnetic properties of a related series of compounds, the botallackite $Cu_2(OH)_3X$ series, where X = Cl, Br, or I, with a particular emphasis on $Cu_2(OH)_3Br$.

Previous experimental studies [87, 88, 89] show that the spin-1/2 copper moments of $Cu_2(OH)_3Br$ order antiferromagnetically on a distorted triangular lattice. More recent experiments [90] have used inelastic neutron scattering (INS) to probe the excitation spectrum, and revealed a diffuse continuum above the magnon bands, which may indicate a multi-spinon or multi-magnon continuum. While the distorted crystal structure hosts parallel chains with ferromagnetic and antiferromagnetic spin ordering, a complete picture of the magnetic ground state and excited states of this compound remains unknown. A detailed first-principles theoretical study on the magnetic properties of $Cu_2(OH)_3Br$, and the origin of the observed magnetic excitation spectrum is to this day missing, with the exception of [90] where we used the first-principles-determined parameters to obtain a spin wave spectrum which agrees with the experimentally observed magnon bands.

While all oxyhalide botallackite $Cu_2(OH)_3X$ compounds are antiferromagnets [89], the Néel temperature changes dramatically from 7.2 K to 10 K to 14 K upon changing X from Cl to Br to I. This seemingly suggests that the dominant superexchange pathways involve the halogen ions [89]. However, this is at the same time counter-intuitive, as the Cu – O distance is significantly smaller than the Cu–halogen distance [88]. This point

has not been clarified by using first-principles methods yet.

In this study, we elucidate the magnetic interactions as well as the resulting ground state and excitations in $Cu_2(OH)_3Br$ and related compounds. For this, we use density functional theory (DFT) to extract parameters of a minimal magnetic Heisenberg model, and we determine the excitation spectrum using linear spin wave theory and exact diagonalization. We repeat the first-principles calculations for different halide ions and different crystal structures to determine the effects of the crystal structure and the chemical differences between the halide ions on the magnetic interactions. Our results show that 1) even though the excitation spectrum is seemingly 1-dimensional, the magnetic Hamiltonian of $Cu_2(OH)_3Br$ is 2-dimensional, 2) the frustration between Cu ions on different 1-dimensional spin chains gives rise to the 1-dimensional-like behavior of the excitation spectrum, and 3) the predominant effect of the halide ion on magnetism is steric, i.e. different sizes of the halide ions change the crystal's structural parameters (such as Cu-O distances and bond angles), leading to an indirect effect on the magnetic exchange interactions, and hence the Néel temperature.

This chapter is organized as follows: In the following section, we discuss the methods used for our calculations. In Sect. 2.3, we introduce the botallackite structure, the magnetic energy expression, and the exchange constants of our model. In the first subsection of Sect. 2.4, we extract exchange coupling constants for the two-dimensional Heisenberg Hamiltonian and examine the classical magnetic ground state. In Subsect. 2.4.2, we discuss whether magnetic interactions are predominantly mediated through superexchange via the halogens by performing calculations with different structures and ions. In Subsect. 2.4.3, we use the DFT-obtained exchange constants to calculate the magnon dispersion relation within linear spin wave theory (LSWT). In Sect. 2.4.4, we perform exact diagonalization calculations to probe the nature of the quantum excitations. We conclude with a summary.

2.2 Methods

DFT calculations were performed using the Projector Augmented Wave approach as implemented in the Vienna Ab Initio Simulation Package (VASP)[91, 92, 93]. Results were obtained on a $2 \times 1 \times 1$ supercell using a $4 \times 8 \times 8$ k-point grid, along with the

PBEsol approximation to the exchange correlation functional [32]. To properly reproduce the local magnetic moments on the Cu ions, the rotationally invariant LSDA+U scheme introduced by Liechtenstein et al. with U = 4 eV and J = 0 eV was used [40]. The trends we report are qualitatively stable against variations of the U and J values within reasonable ranges. The reported results are obtained from collinear magnetic calculations. We also performed noncollinear calculations with spin-orbit coupling and obtained qualitatively very similar results, in line with the quenched orbital magnetic moments of the Cu ion.

In Sect. 2.4.2, for all comparisons between the different botallackite materials, we used the experimental structures with hydrogen atoms selectively relaxed, as the positions of the hydrogen atoms were not determined experimentally. This is in contrast to the results in Tab. 2.2 for $Cu_2(OH)_3Br$, in which the experimental H positions are reported in the literature, and hence no atoms were relaxed.

We performed exact diagonalization calculations using our in-house python code, following the standard formalism of [71]. To obtain eigenvalues and eigenvectors of our Hamiltonian matrices, we used the Lanczos algorithm as implemented in SciPy [72, 94, 95].

2.3 Crystal Structure and Magnetic Model

The botallackite structure consists of weakly bound layers as shown in Fig. 2.1. It is monoclinic with the space group $P2_1/m$. Each Cu ion is octahedrally coordinated with anions and has electronic configuration $3d^9$, and therefore a net spin-1/2 moment. The two different types of Cu ions (with either one or two halide ions in their coordination octahedra) form a distorted triangular lattice. Each anion octahedron shares six of its edges with co-planar neighboring octahedra (Fig. 2.1b). The planes are weakly bound to each other by hydrogen bonds (Fig. 2.1c). As a result, the electronic structure is very 2-dimensional, and we ignore all magnetic interactions between neighboring layers.

The Wyckoff positions for the atoms in space group $P2_1/m$ are presented in Table 2.1. There are two symmetry-inequivalent Cu atoms at Wyckoff positions 2a and 2e, which we denote as Cu_1 and Cu_2 respectively. The coordination octahedra surrounding the Cu_1 atoms are composed of four oxygen ions and two bromine ions. In contrast, the

Atom	Wyck. Pos.	Site Sym.
Cu_1	2a	$\bar{1}$
Cu_2	2e	m
H	2e	m
H	4f	1
O	2e	m
O	4f	1
X(Br, Cl, I)	2e	m

Table 2.1: Wyckoff positions and site symmetries of the atoms in the $Cu_2(OH)_3X$ botallackite with space group $P2_1/m$.

octahedra surrounding the Cu_2 atoms are composed of five oxygen ions and one bromine ion. The Cu_1 – Cu_1 nearest neighbor superexchange pathways are formed from shared O – Br edges, while the Cu_2 – Cu_2 nearest neighbor superexchange pathways are formed by shared O – O edges (Fig 2.2a). (Note that direct cation–cation interactions are often considerable in edge-sharing geometries as well [96].) We denote the exchange constants arising from the above pathways J_1 and J_2, respectively. Both Cu_1 – Cu_1 and Cu_2 – Cu_2 neighbors align along the b crystallographic direction. The only nearest-neighbor exchange interactions along the a direction are between Cu_1 – Cu_2 pairs. There are two symmetry-inequivalent Cu_1 – Cu_2 pairs, where the two octahedra share an edge containing either two oxygens, or an oxygen and a halogen ion. This leads to a significant difference between the exchange pathways and constants. We denote the exchange constants specifying these two inequivalent pathways J_3 and J_4 respectively. Thus, there are four nonequivalent nearest-neighbor Heisenberg couplings, as shown in Fig. 2.2a. We also consider exchanges J_5 and J_6, describing in-plane next-nearest neighbor Cu_2 – Cu_2 and Cu_1 – Cu_1 interactions, but find them to be negligible as discussed below. We do not consider any higher order exchange interactions, such as biquadratic or ring-like terms, since they are not expected to be strong in spin-1/2 systems [68, 97]. In other words, the magnetic model we consider is a Heisenberg model on a distorted triangular lattice:

$$\mathcal{H} = E_0 + \sum_{<ij>} J_{ij} \mathbf{S}_i \cdot \mathbf{S}_j. \tag{2.1}$$

	Exchange constant (meV)	Shared anions	Cu–Cu distance (Å)
$J1$	-1.4 ± 0.1	1 Br, 1 O	3.074
$J2$	4.8 ± 0.1	2 O	3.075
$J3$	0.8 ± 0.1	2 O	3.174
$J4$	0.4 ± 0.1	1 Br, 1 O	3.237
$J5$	0.1 ± 0.1	–	5.624
$J6$	0.0 ± 0.1	–	5.624

Table 2.2: Exchange constants for $Cu_2(OH)_3Br$ in the experimentally determined structure

We determine the paramagnetic energy E_0 and the exchange constants J_{ij} by linear regression from DFT energies. We consider a larger number (19) of magnetic configurations compared to the number of independent parameters in Eq. 2.1 to ensure that there is no over-fitting despite the number of free parameters in the model. The final sets of parameters reproduce the DFT energies with small errors and so no other terms are needed in the magnetic model. Additional information regarding the calculation of the spin exchanges, as well as the relative importance of the next-nearest-neighbor exchanges can be found in the Supplementary material [1].

2.4 Results

2.4.1 Classical magnetic ground state

The exchange values obtained from the DFT+U calculations for the model, including exchanges with nearest and next-nearest neighbors, are listed in Table 2.2. The next-nearest neighbor exchange constants J_5 and J_6 are both as small as 0.1 meV, which is comparable to the statistical error of the fit. (The systematic error of the DFT calculations is likely larger.) Furthermore, the values of J_1 through J_4 are not affected within the statistical error bars when we exclude J_5 and J_6 from our model. As a result, we henceforth consider only the nearest-neighbor exchanges J_1 through J_4.

Regarding the nearest-neighbor couplings, we see that J_1 and J_2 are the largest magnitude exchange constants and are negative and positive, respectively. This gives

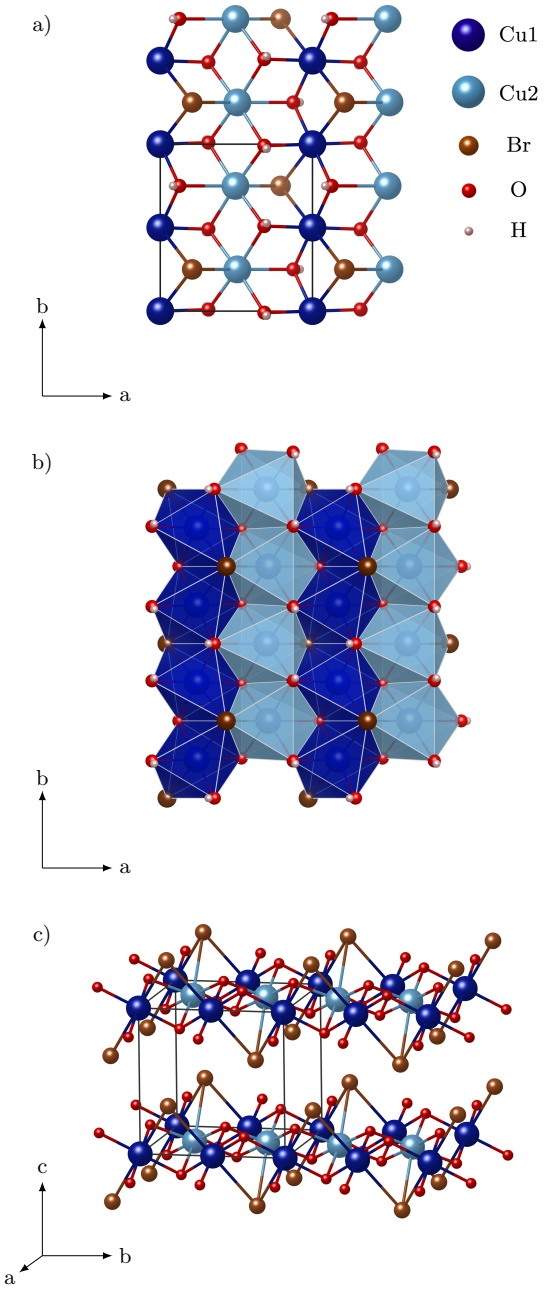

Figure 2.1: a) A unit cell of the botallackite structure and (b) the same diagram but showing octahedra. c) The botallackite structure forms ab-planes.

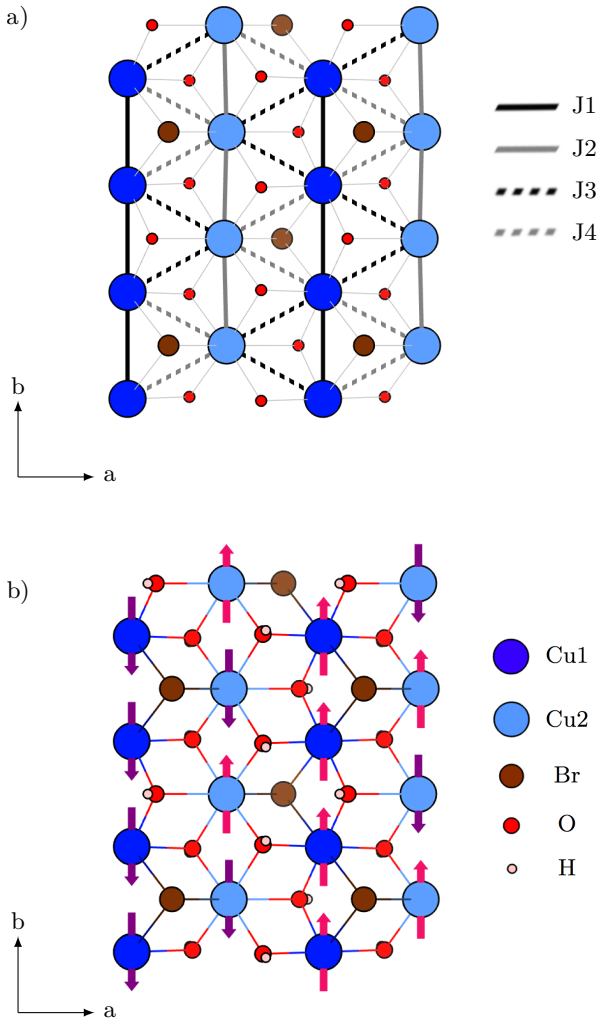

Figure 2.2: a) Definitions of the magnetic exchange constants and b) the proposed classical magnetic ground state.

rise to alternating ferromagnetic and antiferromagnetic chains which extend along the b-direction, in line with the experimental observations. Although the interchain couplings J_3 and J_4 are small, they are still relevant, in contrast to the negligible J_5 and J_6 couplings. This seems to contradict the results of inelastic neutron scattering results [90] which at first glance suggest that J_3 and J_4 are zero, since the spin-wave dispersion is flat in the interchain direction. However, as we discuss below, the inclusion of J_3 and J_4 preserves the relatively flat bands in the interchain direction.

The classical magnetic ground state can be determined by allowing the exchange constants to be satisfied in order of descending magnitude. Neutron measurements show collinearity within chains and canting between spins on different chains [90]. To include the effect of this noncollinearity, we would have to include anisotropic spin exchange and single ion anisotropy terms in the Hamiltonian which arise due to spin-orbit coupling. These terms are difficult to extract from DFT, due to the low symmetry of the botallackite compounds and the weakness of SOC therein. Our noncollinear DFT calculations that include spin-orbit coupling show that the effect of magnetocrystalline anisotropy is negligible compared to the symmetric nearest-neighbor exchanges. We ignore the effect of spin-orbit coupling in the rest of this study, and assume a collinear magnetic order.

We begin with satisfying J_1 and J_2, which results in ferromagnetic and antiferromagnetic chains extending along the b-direction, as discussed above. Next, the interchain coupling J_3 constrains the relative orientation of spins on neighboring chains, leading to the classical magnetic ground state shown in Fig. 2.2b. In this configuration, the spins on every other chain alternate in direction. This magnetic configuration agrees qualitatively with neutron scattering experiments [90]. We emphasize that the nonzero interchain coupling J_3 is necessary to reproduce the experimentally observed long-range magnetic order. We separately determine via the Luttinger-Tisza method [63, 98] that this result is the exact classical magnetic ground state of our model ((see the Supplementary Material of Ref. [1])).

2.4.2 Superexchange interactions

The Néel temperatures of the botallackite cuprates change substantially (from 7.2 K to 10 K to 14 K) when substituting different halogen atoms X into $Cu_2(OH)_3X$ (from X =

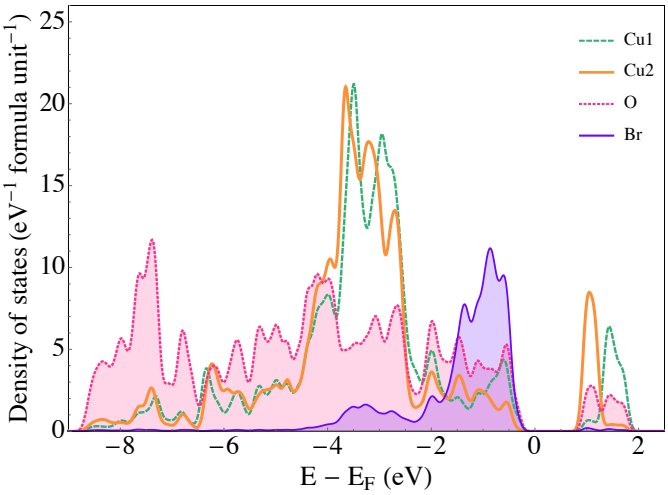

Figure 2.3: The projected density of states for the system in the antiferromagnetic ground state. The low energy DOS above the Fermi level has only a small contribution from the halogen states.

Cl to Br to I) [89]. This observation was interpreted as evidence of the halogen ions providing the dominant exchange pathways between the copper magnetic moments. However, the crystal structure itself suggests otherwise, since the copper–oxygen distances are much smaller than the copper-halogen distances. For example, in $Cu_2(OH)_3X$, while the copper–oxygen distances vary from around 1.9 to 2.3 Å, the copper–halogen distances are much larger at 2.88 Å. In this section, we present the first-principles projected density of states and the spin density in real space in order to examine the influence of the crystal structure and halogen ion type on the magnetic exchange parameters. Our results suggest that the dominant contribution to exchange is from direct hopping between the Cu ions and superexchange through the oxygen ions. Furthermore, we find that the largest effect of the different halogen ions is steric. That is, the halogen ions modify the magnetic interactions through changes in the crystal's structural parameters.

Fig. 2.3 shows the projected density of states (DOS), obtained from DFT calculations, for the bromide system in the proposed classical magnetic ground state. The Cu^{2+} ions each have a single hole in the d-shell, which corresponds to peaks in the DOS between 1-2 eV above the Fermi level. For the halogen-mediated superexchange to be significant, the Cu – Br hoppings would need to be large, which would lead to hybridization (mixing) of the spin-polarized Cu orbitals with Br–p orbitals. This Cu –

Br hybridization would appear in the DOS as Br weight in the same energy range as the low-lying, unoccupied Cu DOS. However, there is seemingly no Br weight in the DOS in this energy range, despite the high DOS of Br ions at the top of the valence band. This implies that superexchange is predominantly oxygen-mediated, as expected from the geometrical and crystal field considerations explained below.

In order to clarify the nature of hybridization between the Cu and O states, we explore the system's 'orbital ordering'. While the Cu ions are octahedrally coordinated, the site-symmetries are low enough to split the e_g orbitals. The different charges of the ligands enhance the effects of these low-symmetry crystal fields. As a result, while it is not possible to talk of a proper orbital ordering or a transition between orbitally ordered and disordered states, the alignment of the partially occupied d-orbital on each Cu atom can shed light on the source of the magnetic interactions. Fig. 2.4 shows the isosurface of spin density obtained from a DFT calculation in the antiferromagnetic state. When using local coordinate axes on each Cu ion, with the z-axis pointing towards the Br ions, the spin-polarized, half-filled orbitals have $d_{x^2-y^2}$ character and lobes pointing towards the oxygen atoms. This orbital occupation preference can be understood simply by electrostatic contributions to the crystal field: Br has -1 charge, as opposed to -2 of O, and the Cu-Br bond lengths (≈ 3Å) are significantly larger than the the Cu-O bond lengths (≈ 2Å). As a result, the electrons in the $d_{2z^2-x^2-y^2}$ orbital experience a lower electrostatic repulsion from the Br anions, and thus have lower energy.[1]

The improper orbital ordering[2] imposed by the strongly asymmetric crystal field leads to superexchange interactions dominated by Cu–O–Cu pathways: the oxygen p-orbitals sigma bond with the half-filled Cu $d_{x^2-y^2}$ orbitals, which leads to a large hopping element $t_{\mathrm{O-Cu}}$. In contrast, the bromine p-orbitals, which point to the center of the Cu

[1] In passing, we note that the double occupation of the $d_{2z^2-x^2-y^2}$ orbital would result in a greater electrostatic repulsion on the Br ions, which would in part be the cause of the longer Cu–Br distances as well. This can be considered in a similar vein as the Jahn–Teller effect, though in the botallackites the symmetry is already broken by the inequivalent anions.

[2] To clarify the distinction between proper and improper orbital order, consider the case where the crystal field is sufficiently symmetric so that there are at least two degenerate orbitals per Cu site. In this case, there are multiple orbital configurations which are energetically-equivalent. Any orbital order which arises in this case spontaneously breaks the symmetry of this system, and is referred to as proper orbital ordering. Improper orbital ordering in contrast occurs when the symmetry of the crystal field is sufficiently low such that the ground state orbital per Cu site is nondegenerate.

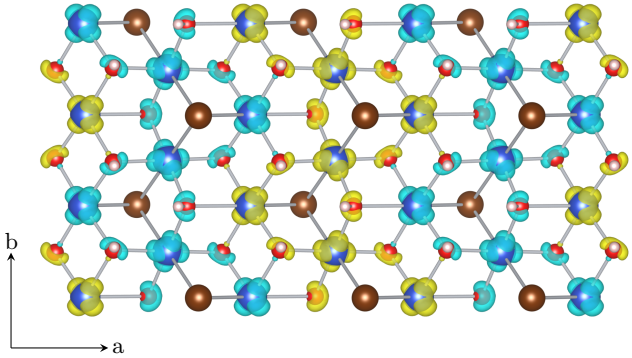

Figure 2.4: Isosurface of spin density, which shows orbital ordering, in the antiferromagnetic ground state. Positive and negative spin density are denoted by blue and yellow, respectively.

$d_{x^2-y^2}$ orbitals, have very small hopping $t_{\mathrm{Br-Cu}}$ due to the equal but opposite contributions to the hopping integral from different lobes of the $d_{x^2-y^2}$ orbital. (Note that we are only considering the hopping elements $t = \langle\psi_{Cu}|\mathcal{H}|\psi_O\rangle$ of the $d_{x^2-y^2}$ orbital, since the virtual excitations from the other, fully occupied orbitals to oxygen are forbidden by the Pauli principle.) Therefore, the Br ions likely have little role in mediating the magnetic exchange. This is substantiated by the lack of any visible spin-density on the Br ions, unlike the O ions, in Fig. 2.4.

Our findings and arguments so far suggest that the halogen cations do not directly mediate magnetic superexchange, which appears to contradict the large differences between the different botallackites' Néel temperatures observed experimentally [89]. However, an attribute of the different halogens that we have not yet considered is their different ionic sizes, which lead to changes in the lattice parameters as well as Cu–O–Cu angles. To disentangle the direct and indirect (crystal structure related) effect of the halogen ions on magnetism, we perform the following first-principles 'computational experiments': 1) Using the experimentally obtained $Cu_2(OH)_3Br$ structure, which we have thus far used to obtain the exchange constants J_1 through J_4, we repeat the DFT calculations to obtain the exchange constants, but with chlorine or iodine ions replacing the bromine ions. These calculations display the direct effect of the halogens without taking into account the indirect, steric effects of different ionic sizes. 2) We then use the experimentally measured $Cu_2(OH)_3Cl$ and $Cu_2(OH)_3I$ crystal structure parameters,

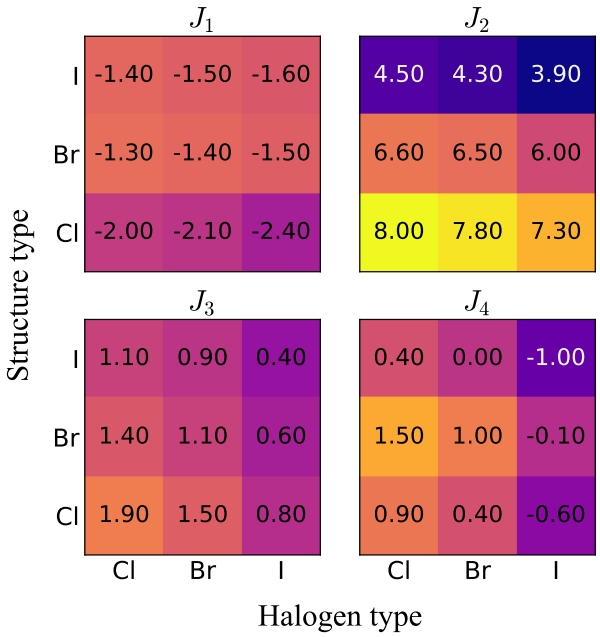

Figure 2.5: Color maps which show how the exchange constants vary with insertion of different halogen types into a given structure. Within a row of a given color map, the structure type is fixed. Moving from column to column corresponds to substituting different halogen atoms into this fixed structure. In the Cl and I compounds, the experimental uncertainty did not allow for the determination of the positions of the hydrogen atoms. Therefore, we have selectively relaxed the hydrogen atoms to obtain the lowest-energy structures. For consistency, we then also relaxed the hydrogen atoms in the Br compound. We point out that this relaxed-hydrogen structure is slightly different from the experimental Br structure obtained experimentally, leading to different exchange couplings, as calculated by DFT.

and calculate J_1 through J_4 for each ionic compound again. Comparing the J values of a particular compound in different crystal structures shows the strength of the indirect effect, i.e. the effect of the crystal structural changes on magnetism. The results of these calculations are shown in Fig. 2.5. Note that the $Cu_2(OH)_3Br$ structure used in these comparison calculations is not identical to the experimental structure used previously (see Fig. 2.5).

The results in Fig. 2.5 indicate that the intrachain couplings J_1 and J_2 are relatively unaffected upon substituting different halogen ions while keeping the crystal structure fixed. The largest difference in J_1 and J_2 for a fixed structure is no more than 20%. On the other hand, changing the crystal structure while keeping the stoichiometry fixed has a much stronger effect on these intrachain exchanges, which can be seen as a steeper color gradient in the vertical direction. In light of the arguments we introduce above, this result is not surprising. Since the predominant effect of the halogen ion is steric, we expect halogen-mediated exchange to be insignificant. The effect of halogen type is especially weak for J_2, which is the interaction between two Cu ions that share only O ligands. As a result, we conclude that the intrachain couplings overall are not halogen mediated, but rather depend on a combination of direct exchange and superexchange through the oxygen sites[3]

The trends are less clear and opposite for the interchain exchanges J_3 and J_4. For both J_3 and J_4, the changes are smaller in absolute terms compared to the intrachain exchanges, but larger in relative terms. Also, changing the halogens leads to a stronger difference than changing the crystal structure. J_3 decreases by more than a factor of two upon substitution of Cl with I. This is especially surprising, because the J_3 interaction couples two Cu ions that do not share a halogen ligand. The only sign change is observed in J_4, and only for compounds containing I. The different sign of J_4 in the iodide compound does not lead to a different classical magnetic groundstate, but relieves the frustration between the interchain exchanges. This stronger dependence of the interchain exchanges on the halogen ions can be explained by the fact that the

[3]We can gain insight into the nature of the intrachain interactions by further examining this improper orbital order. From Fig. 2.4, we see that the Cu_1 chains have antiferro-orbital order while the Cu_2 chains are ferro-orbitally ordered. From the Goodenough-Kanamori-Anderson rules, we then expect ferromagnetic coupling between Cu_1 spins within a chain and antiferromagnetic coupling between Cu_2 spins within a chain. This indeed agrees with the exchange couplings we extract from DFT, in which we find $J_1 < 0$ and $J_2 > 0$.

direct exchange, which exponentially depends on the Cu-Cu distance, contributes less to J_3 and J_4. The interchain nearest-neighbor Cu ions are farther from each other (by around 0.1 to 0.2 Å), and thus any change in the anion-mediated superexchange is more important.

Although we have shown that the largest exchanges in the system, J_1 and J_2, are not halogen-mediated, we note that the exact way in which the Néel temperature depends on the exchange constants is unclear. In the extreme limit of 1D compounds that host chains with no shared ligands, such as the $A_3BB'O_6$ family [99, 100, 101], two separate transitions with temperatures T_1 and T_2 may be observed, which are determined by intrachain and interchain interactions respectively. However, there is only a single transition observed in the botallackites. It is likely that the dominant exchange couplings J_1 and J_2 are not the main energy scales which determine the Néel temperature for this transition. Instead, T_N is likely determined by the much weaker interchain couplings J_3 and J_4, along with the interplanar coupling(s). This would explain the two-fold difference between T_N of the different oxyhalide botallackites.

2.4.3 Linear spin wave theory

We now apply the Holstein-Primakoff transformation [68] to our nearest-neighbor Heisenberg Hamiltonian to determine the spin wave spectrum of $Cu_2(OH)_3X$, for X=Cl, Br, and I. In this calculation, we take the classical magnetic ground state to be that which we determined from DFT calculations in Sect 2.4.1 (Fig. 2.2b), and the exchange parameters determined using the hydrogen-relaxed structures.

The results for our calculations are shown in Fig. 2.6 (dotted lines). We find that the bands along the intra-chain (k_y) direction are dispersive, while the bands along the inter-chain (k_x) direction are relatively flat, despite the nonzero values of J_3 and J_4. The relatively flat dispersion in the a-direction can be partially explained as due to the smaller values of the interchain couplings J_3 and J_4 compared to the intrachain couplings J_1 and J_2. However, another contributing factor is the competition between J_3 and J_4 in the chloride and bromide compounds. Indeed, despite having a smaller average of $|J_3|$ and $|J_4|$, the iodide compound has the largest bandwidth in the interchain direction (a,0). This is due to the fact that J_4 is ferromagnetic in the iodide compound, in contrast to the chloride and bromide compound. There is therefore no competition

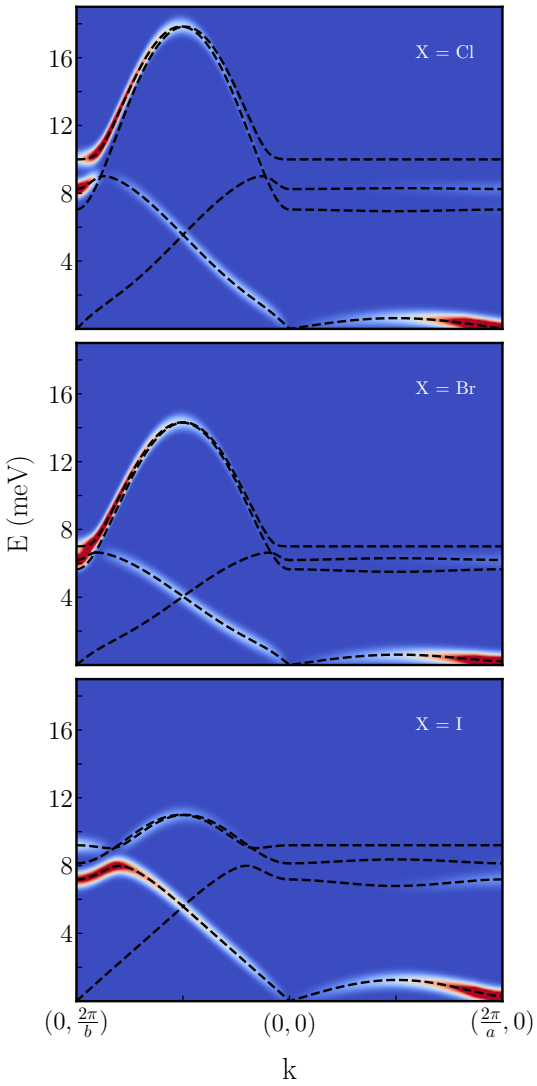

Figure 2.6: Results of the linear spin wave calculations. In addition to the dynamical structure factor $S(\mathbf{k}, \omega)$, the dashed lines show the dispersions of the 4 magnon modes. At each k-point, only 2 of the 4 modes have non-negligible spectral weight. The structure factors are broadened by a Gaussian of width 0.3 meV. The exchange constants used are obtained for the structures with relaxed hydrogen atoms (see discussion at the end of Sect. 2.4.2).

between J_3 and J_4, and as a result no frustration in the iodide compounds. To further test this idea, we set $J_4 = 0$ in the chloride and bromide compounds, relieving the frustration in the system, and recalculate the magnon bandstructure. This leads to an increase in the bandwidths along a axis as expected (see the Supplementary Material of Ref. [1]).

The dynamical structure factor $S(\mathbf{k}, \omega)$ is given by

$$S(\mathbf{k}, \omega) = \sum_{\alpha} \int \frac{dt}{2\pi} e^{i\omega t} \langle \psi_0 | S^{\alpha}_{-\mathbf{k}}(t) S^{\alpha}_{\mathbf{k}}(0) | \psi_0 \rangle \tag{2.2}$$

$$= \sum_{n,\alpha} |\langle \psi_{n,\mathbf{k}} | S^{\alpha}_{\mathbf{k}} | \psi_0 \rangle|^2 \delta(\omega - E_n(\mathbf{k}) + E_0) \tag{2.3}$$

We calculate $S(\mathbf{k}, \omega)$ within linear spin wave theory following Ref. [70] and show the result in Fig. 2.6 for the three different $Cu_2(OH)_3X$ structures. The magnetic unit cell has 8 atoms, and as a result, there are four doubly-degenerate magnon modes. However, at each wavevector, two of the four bands have negligible weight. This agrees with the neutron scattering data, which observes only two groups of excitations which are ferromagnetic and antiferromagnetic in character [90].

2.4.4 Exact diagonalization

Although linear spin wave theory is a useful tool to gain insight into the magnon excitations of spin systems, there are other excitations which cannot be probed using this method. Multi-magnon states require higher-order corrections to take into account the magnon-magnon interactions. Additionally, there are other, lower spin excitations such as spinons, which become important in low-spin systems. For example, the 1D antiferromagnetic Heisenberg chain shows no magnons in its excitation spectrum, and hosts only spinon excitations, which are fractionalized spin-1/2 objects.

Previous inelastic neutron scattering work claims to observe the coexistence of spinons and magnons, localized on the antiferromagnetic and ferromagnetic chains respectively in $Cu_2(OH)_3Br$ [90]. In order to understand the INS results better, it is necessary to perform calculations that can capture excitations beyond the scope of linear spin wave theory.

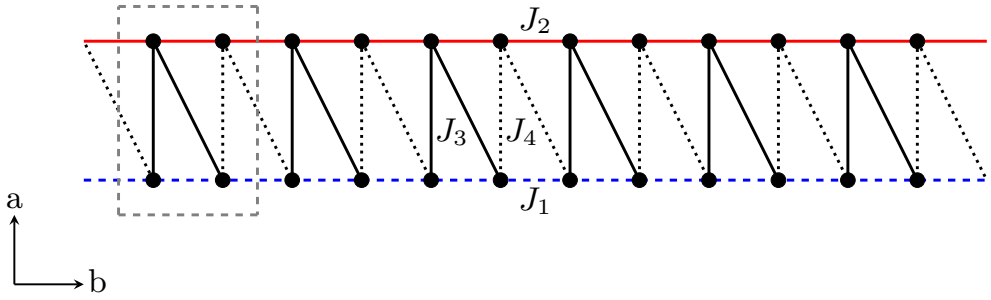

Figure 2.7: The 24-site cluster used in our exact diagonalization calculations, extending six unit cells in the b-direction and one unit cell in the a-direction.

For this reason, we performed exact diagonalization calculations. Exact diagonalization involves constructing the exact Hamiltonian matrix for a finite size cluster with periodic boundary conditions and Heisenberg interactions, which we then diagonalize numerically [71]. This, in principle, gives the exact spectrum of a material. In particular, multi-magnon and spinon states can be captured via exact diagonalization.

For our exact diagonalization calculation, we use a 24-site cluster that extends six unit cells in the b-direction, and one unit cell in the a-direction, shown in Fig. 2.7. The cluster is comprised of one ferromagnetic chain and one antiferromagnetic chain, each aligned along the b-direction. We impose periodic boundary conditions in the b-direction, and open boundary conditions in the a-direction. When obtaining the spectrum of our Hamiltonian, we exploit the SU(2) symmetry of our Heisenberg Hamiltonian and block diagonalize by S_z^{tot}. Additionally, we use the translation symmetry in the b-direction to block diagonalize by crystal momentum k. After implementing these symmetries, the resulting Hamiltonian block containing the ground state is $\sim 23,000 \times 23,000$. The Lanczos algorithm was used to find both the energies $E_n(\mathbf{k})$ and the corresponding weights $|\langle\psi_{n,\mathbf{k}}|S^{\alpha}_{\mathbf{k}}|\psi_0\rangle|^2$.

To investigate the effect of the interchain coupling, we calculate $S(\mathbf{k},\omega)$ for both decoupled chains ($J_3 = J_4 = 0$) and coupled chains, where J_3 and J_4 are the values extracted from DFT. The results are shown in Fig. 2.8, where we have used the exchange parameters obtained from the experimentally-determined Br compound (Tab. 2.2.)

Here, in addition to plotting $S(\mathbf{k},\omega)$, we also plot the upper and lower bounds of the 2-spinon continuum as determined from the Bethe ansatz with $J_{AFM} = J_2$ (orange lines) and the magnon band for a 1D ferromagnetic Heisenberg chain with $J_{FM} = J_1$ (green line).

As expected, in the case of zero interchain coupling, we simply have the superposition of a magnon band from the ferromagnetic chain, and the two-spinon continuum from the antiferromagnetic chain (Fig. 2.8a). That is, spinons and magnons coexist in isolated chains of the material. Once the interchain couplings are introduced, the material no longer hosts isolated one-dimensional AFM chains, and thus should not have a pure 2-spinon continuum. Instead, we expect the magnon and spinon excitations to mix with each other. Indeed, as we increase interchain coupling, the spectral weight inside the 2-spinon continuum smears out significantly (Fig. 2.8b).

To highlight the effect of introducing interchain coupling, we plot $S(\mathbf{k},\omega)$ as a function of ω for both the coupled and decoupled chains (Fig. 2.9) at several momenta ($k = \frac{2\pi}{b}$, $k = \frac{7}{6}\frac{2\pi}{b}$, and $k = \frac{4}{3}\frac{2\pi}{b}$), which are shown in the inset. In each panel, the position of the ferromagnetic band is shown as a dashed green line, and the bounds of the 2-spinon continuum are shaded in orange. The results for $S(\mathbf{k},\omega)$ for zero interchain coupling are shaded in pink, while $S(\mathbf{k},\omega)$ for nonzero interchain coupling is shown in purple.

For $k = \frac{4}{3}\frac{2\pi}{b}$ (bottom panel), we find that the introduction of nonzero interchain coupling leads to a smearing of the spectral weight inside the 2-spinon continuum and a transfer of some weight outside of the bounds predicted by the Bethe ansatz [102, 103]. However, because the ferromagnetic band and the continuum are well-separated in energy, the ferromagnetic band is only weakly perturbed by the presence of nonzero interchain coupling. In the middle panel ($k = \frac{7}{6}\frac{2\pi}{b}$), the energy of the ferromagnetic band is closer to the 2-spinon continuum, and the effect of nonzero interchain coupling is more pronounced. Here, as with $k = \frac{4}{3}\frac{2\pi}{b}$, there is transfer of weight outside the bounds predicted by the Bethe ansatz. However, there is also appreciable mixing between the magnon and spinon excitations. In this energy range where mixing occurs, between 2 meV and 4 meV, we expect magnon-spinon interactions to become significant. Finally, for $k = \frac{2\pi}{b}$, we see that the ferromagnetic band overlaps with the spinon continuum.

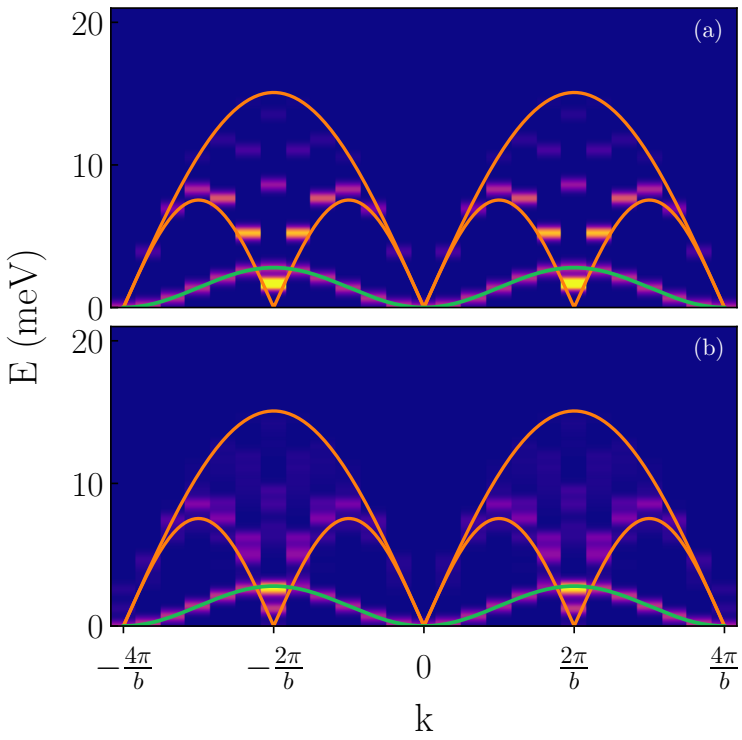

Figure 2.8: The dynamical structure factor $S(\mathbf{k}, \omega)$ calculated using exact diagonalization for $Cu_2(OH)_3Br$ in the case where (a) there is zero interchain coupling and (b) the interchain couplings J_3 and J_4 are set to their values obtained from DFT. Also plotted are the bounds of the 2-spinon continuum (orange) obtained from the Bethe ansatz where $J_{AFM} = J_2$ and the magnon band (green) for a 1D ferromagnetic Heisenberg chain where $J_{FM} = J_1$. The exchanges were found for the $Cu_2(OH)_3Br$ structure obtained from experiment, without any relaxation of atoms.

From the above arguments, we expect magnon-spinon interactions to become appreciable at this momentum. Indeed, we observe a substantial modification of the spectral weight at this intersection due to the presence of nonzero interchain coupling. However, what this implies for the character of the magnon and spinon excitations has yet to be determined.

Despite the presence of magnon-spinon interactions, the ferromagnetic magnon band is distinct from the spinon continuum for most wavevectors, which is consistent with the INS results [90], because of the difference of the magnitudes of J_1 and J_2. As a result, although there is mixing between magnon and spinon excitations, qualitatively distinct magnon-like and spinon-like excitations coexist for most wavevectors in $Cu_2(OH)_3Br$. In other words, although the magnetic model for this material is two-dimensional, the system's magnetic excitations retain a one-dimensional character, because of a combination of the relative strengths of intrachain interaction, the competition between the interchain couplings J_3 and J_4, as well as the weakness of these couplings compared with J_1 and J_2.

In addition to the above results, we repeat our calculations of $S(\mathbf{k}, \omega)$ in the $Cu_2(OH)_3X$ compounds, where X = Cl, Br, and I. In each compound, we have selectively relaxed the hydrogen atoms before obtaining the exchange constants in DFT (see App. 2.5 for details.) The results for the dynamical structure factor in each compound are shown in Fig. 2.10, and are qualitatively similar to the plots discussed above. As before, we observe a sharp ferromagnetic band and a spinon continuum in each compound. This is especially striking in the case of the Cl compound (where J_3 is on the order of J_1), and the Br compound (where both J_3 and J_4 are on the order of J_1.) This continued existence of the spinon continuum in these compounds suggest that magnons and spinons may coexist for relatively large values of the interchain couplings J_3 and J_4.

In the case of X = I, J_1 and J_2 are closer in magnitude than for the other oxyhalides, resulting in a larger range of momenta for which the ferromagnetic band intersects the spinon continuum. This suggests that magnon-spinon interactions may play a larger role in this compound, perhaps leading to the increase in spectral weight near the ferromagnetic band where it crosses the continuum.

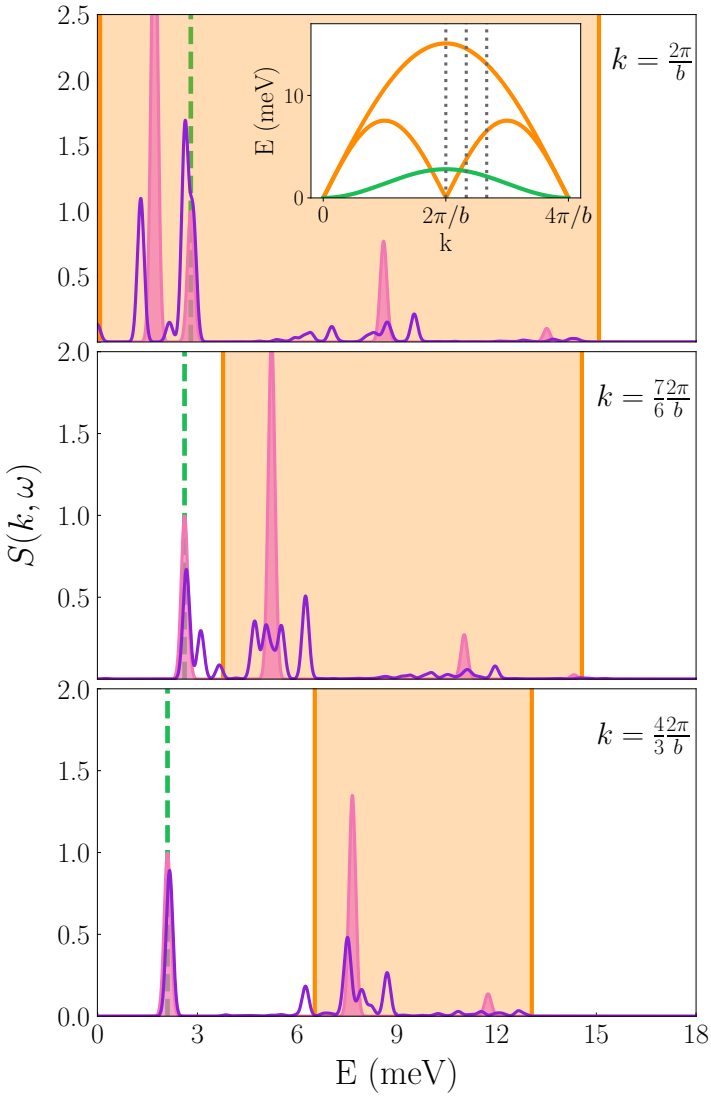

Figure 2.9: The dynamical structure factor $S(\mathbf{k}, \omega)$ at three momenta: $k = \frac{2\pi}{b}$, $k = \frac{7}{6}\frac{2\pi}{b}$, and $k = \frac{4}{3}\frac{2\pi}{b}$, as shown in the inset of the top panel. In each panel, the dashed green line shows the position of the magnon band for a 1D ferromagnetic Heisenberg chain with $J_{FM} = J_1$, while the shaded orange region delineates the bounds of the spinon continuum, as obtained from the Bethe ansatz, with $J_{AFM} = J_2$. The results for the case of zero interchain coupling are shaded pink, while the results for the case of nonzero interchain coupling are shown in purple.

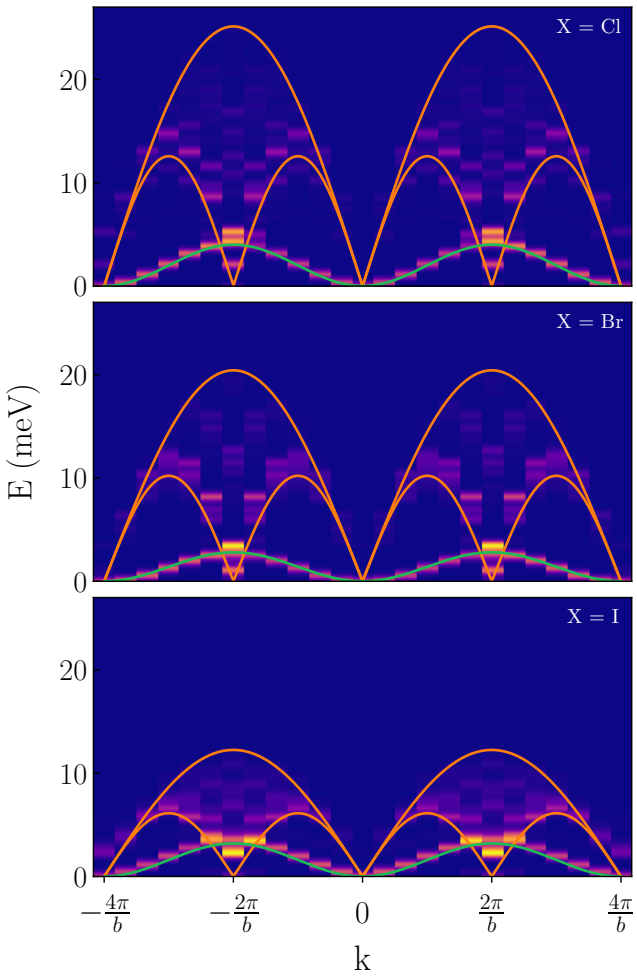

Figure 2.10: The dynamical structure factor $S(\mathbf{k}, \omega)$ calculated using exact diagonalization for the $Cu_2(OH)_3X$ compounds, where X = Cl, Br, and I. The exchanges are obtained from the experimental structures with the hydrogen atoms selectively relaxed. Also plotted are the bounds of the 2-spinon continuum (orange) obtained from the Bethe ansatz, with $J_{AFM} = J_2$, as well as the magnon band (green) for a 1D ferromagnetic Heisenberg chain, with $J_{FM} = J_1$.

2.5 Summary and Conclusions

In summary, to investigate the magnetic interactions in $Cu_2(OH)_3Br$, we performed first-principles DFT calculations and found the exchange constants. Using these first-principles values, we determined the classical magnetic ground state. We then obtained the magnon dispersion and dynamical structure factor using linear spin-wave theory, which are in good agreement with experiment. We find that the existence of interchain coupling is necessary to understand the magnetic order in the system. Furthermore, we find that the interchain coupling strength can be significant while continuing to preserve flat magnon bands in the interchain direction.

Additionally, we investigated the hypothesis that the magnetic exchange is halogen-mediated, as proposed by previous experimental studies. Through analysis of the projected density of states, spin-density plots, and calculations of various exchange constants in halogen-substituted structures, we find that the exchange is instead predominantly direct or oxygen-mediated.

We also calculated the dynamical spin structure factor using exact diagonalization to examine the effect of interchain coupling on the spinon continuum. We found that the spinon continuum continues to exist, even in the presence of nonzero interchain couplings. This coexistence of a magnon band and a spinon continuum, in addition to the general shape of the dynamical structure factor, is consistent with the experimental results. We posit that this is due to the different energy scales of spinons and ferromagnetic magnons, as well as the relative signs of interchain couplings J_3 and J_4. This is substantiated by linear spin wave theory results, which show that the interchain bandwidths in the a-direction scale with $J_3 - J_4$ (see the Supplementary Material of Ref. [1]) as long as J_3 and J_4 are not large enough to modify the classical ground state.

To the best of our knowledge, the cuprate oxyhalide botallackites are the first materials in which sharp ferromagnetic magnons coexist with deconfined spinons [90]. This botallackite structure could therefore be used as a model system to study magnon-spinon interactions. For example, it would be interesting to investigate how the spinon continuum and ferromagnetic band evolve with increasing interchain coupling, which can be experimentally induced with uniaxial pressure. Our above exact diagonalization and linear spin wave theory results suggest that the spinon continuum would continue

to survive with increasing uniaxial pressure along the a axis. However, as the interchain couplings become on the order of J_1 and J_2, competition between the intrachain and interchain couplings will begin to play an important role. In this regime, both strong spinon-magnon interactions and significant frustration will modify the spectrum, the lifetime of both quasiparticles, and the dynamical structure factor. While these questions are outside the scope of this study, we hope our results provide insight for future investigations.

Appendix

2.5.1 Crystal structure

We present a table of Wyckoff positions for the $P2_1/m$ space group in Tab. 2.3, extended to include the atomic coordinates.

Table 2.3: Wyckoff positions for space group $P2_1/m$. Positions for the atoms of the cuprate are identified.

Atom	No. of positions	Wyckoff notation	Site symmetry	Coordinates
H2, O2	4	f	1	(x,y,z) (-x,y+1/2,-z) (-x,-y,-z) (x,-y+1/2,z)
Cu2, H1, O1, Br	2	e	m	(x,1/4,z) (-x,3/4,-z)
–	2	d	-1	(1/2,0,1/2) (1/2,1/2,1/2)
–	2	c	-1	(0,0,1/2) (0,1/2,1/2)
–	2	b	-1	(1/2,0,0) (1/2,1/2,0)
Cu1	2	a	-1	(0,0,0) (0,1/2,0)

2.5.2 Calculating exchange constants from DFT

As discussed in the Chapter 2, we obtain the exchange constants by using linear regression (also see Sec. 1.3.1) to fit the DFT-obtained energies of different collinear spin configurations to a Heisenberg Hamiltonian

$$\mathcal{H} = E_0 + \sum_{ij} J_{ij} \mathbf{S}_i \cdot \mathbf{S}_j. \tag{2.4}$$

First, we include both nearest-neighbor couplings (J_1 through J_4) and next-nearest neighbor couplings (J_5 and J_6), leading to a 7-parameter model. Due to the large number of parameters in this model, we use a large number of spin configurations (19) to ensure that the resulting exchange constants are accurate, and not the result of overfitting. To obtain the set of spin configurations used in linear regression, we used a unit cell spanning 2 lattice constants in the a-direction and 1 lattice constant in the b-direction, thus containing 8 spins in total. We then chose a varied set of spin configurations, spanning the range of total magnetizations available for this choice supercell, i.e. from 8 μ_B (the ferromagnetic configuration) to 0 μ_B (complete antiferromagnetic configurations).

The results are shown in Fig. 2.11 where we have plotted the energies of the various spin configurations predicted from our model against their energies calculated from DFT. We see that the energies predicted by our model agree well with the energies calculated from DFT. Moreover, the numerical values for J_1 through J_6, presented in Tab. 2.4, are physically reasonable. In particular, we find that the next-nearest-neighbor exchanges J_5 and J_6 are insignificant compared to the values of the nearest-neighbor exchanges, suggesting that our model parameters (J_1 – J_4) are not the result of an overfit model.

We can further test this by removing the next-nearest-neighbor exchanges from our model, and fitting the resulting five-parameter model. The results are shown in Fig. 2.12, and in Tab 2.4. We see that the values of the nearest-neighbor exchanges remain relatively unchanged, suggesting that we are not overfitting. Moreover, the quality of fit remains good, implying that we have not underfit by excluding the next-nearest-neighbor exchanges.

We note that in both cases, the intrachain couplings J_1 and J_2 are larger in magnitude than the interchain couplings J_3 and J_4. As noted in the main text, a nonzero interchain coupling is crucial to stabilizing the magnetic order observed in experiment. Here, we show that the exclusion of J_3 and J_4 from our model also leads to an appreciably worse quality of fit. The results are shown in Fig. 2.13, where there is a significantly larger difference between the DFT-calculated energies and the energies predicted from this model, suggesting that we are underfitting by excluding J_3 and J_4 from our model.

Therefore, in the main text, we have included all nearest-neighbor exchanges J_1

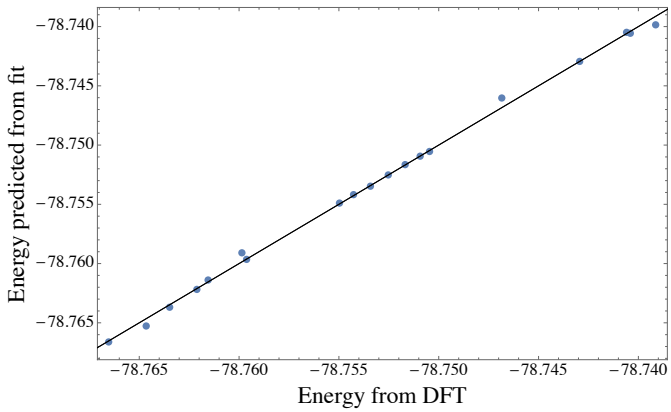

Figure 2.11: Linear regression fit for the model including J_1-J_6.

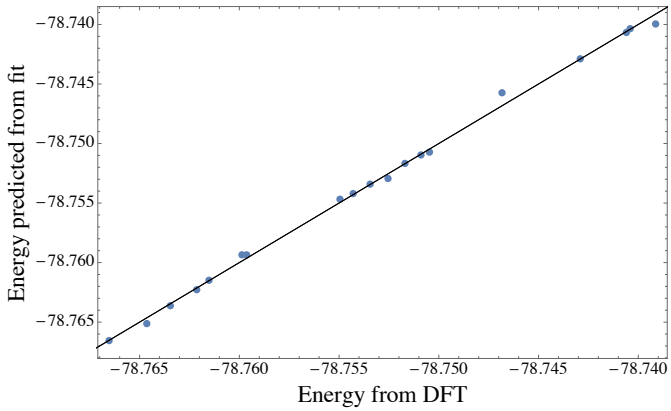

Figure 2.12: Linear regression fit for the model including J_1-J_4 only.

through J_4 in our model.

Table 2.4: Exchanges (in meV) found from fitting to the 3, 5, and 7-parameter models. Uncertainties are ± 0.1 meV.

Model	J_1	J_2	J_3	J_4	J_5	J_6
J_1 and J_2	-1.4	4.9	–	–	–	–
J_1 – J_4	-1.4	4.8	0.8	0.4	–	–
J_1 – J_6	-1.4	4.8	0.8	0.4	0.1	0.0

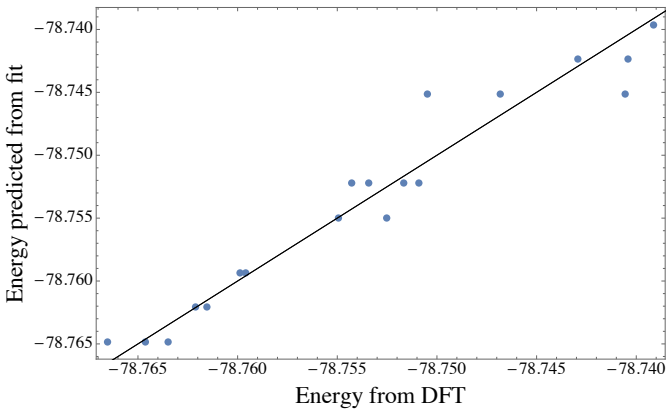

Figure 2.13: Linear regression fit for the model including only intrachain exchange couplings J_1 and J_2.

We also include a table of exchanges found with different values of U in Tab. 2.5. Though we use U = 4 eV in the calculations we present, our conclusions hold for a large range of U. In particular, we see that for all values of U, we have $|J_2| > |J_1| > |J_3| > |J_4|$. Additionally, we can use the Luttinger-Tisza method(described below) to find the classical magnetic ground state of our Heisenberg model for our different sets of exchange parameters. In doing so, we find that the magnetic ground state is independent of the U values used, for $U > 2$ eV. For the case of $U = 2$ eV, our Luttinger-Tisza calculations still give ferromagnetic and antiferromagnetic chains, albeit with canting between chains. These classical magnetic ground states are shown in Fig. 2.14.

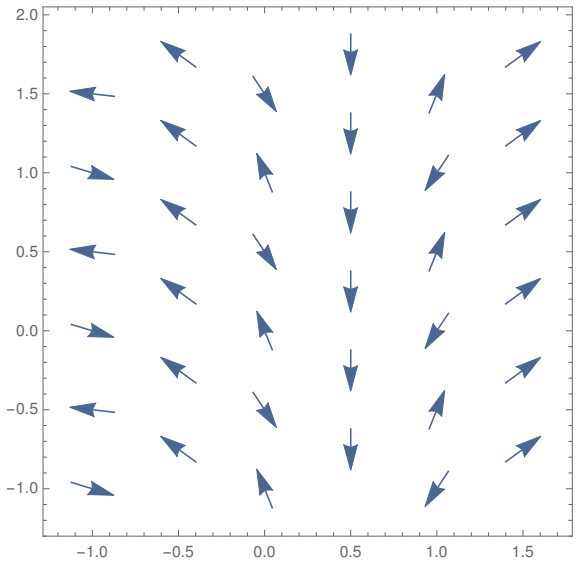

(a) $U = 2\text{eV}$

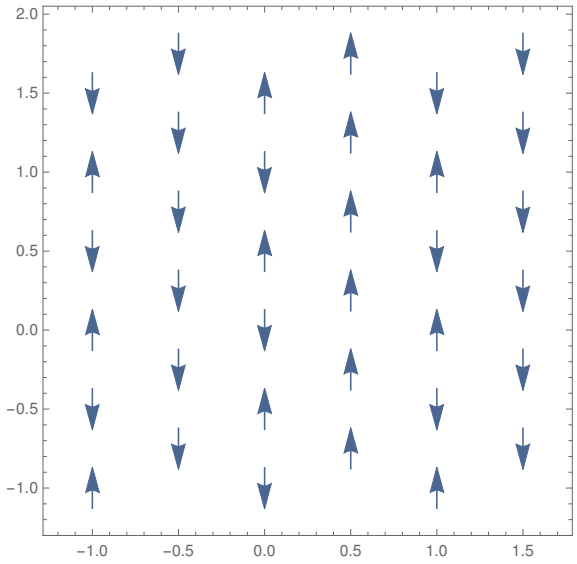

(b) $U > 2\text{eV}$

Figure 2.14: The classical magnetic ground state, as calculated from the Luttinger-Tisza method.

Table 2.5: Exchanges (in meV) found from fitting to the 5-parameter model with U = 2 eV through U = 6 eV. Uncertainties are ± 0.1 meV.

	J_1	J_2	J_3	J_4
U = 2 eV	-2.5	7.6	2.1	1.4
U = 3 eV	-1.9	6.1	1.3	0.8
U = 4 eV	-1.4	4.8	0.8	0.4
U = 5 eV	-1.1	3.8	0.5	0.3
U = 6 eV	-0.9	2.9	0.3	0.2

2.5.3 Luttinger-Tizsa

In this appendix, we apply the generalized Luttinger-Tisza method to the botallackite structure (see Sec. 1.3.2 for an overview), ignoring all but the nearest-neighbor exchanges J_1 through J_4. In the botallackite structure, there are four spins per structural unit cell. As an ansatz, we set $\alpha_1 = \alpha_3 = 1$ and $\alpha_2 = \alpha_4 = \alpha$. Defining $\beta = 1/\alpha$ for convenience, we obtain the following matrix for $\mathcal{J}^{ab}(\mathbf{k})$:

$$\mathcal{J}(\mathbf{k}) = \begin{pmatrix} 0 & \beta(J_3 + J_4 e^{i\mathbf{k}\cdot\mathbf{a}}) & J_2(1+e^{-i\mathbf{k}\cdot\mathbf{b}}) & \beta(J_3 e^{-i\mathbf{k}\cdot\mathbf{b}} + J_4 e^{-i\mathbf{k}\cdot(\mathbf{a}+\mathbf{b})}) \\ \beta(J_3 + J_4 e^{i\mathbf{k}\cdot\mathbf{a}}) & 0 & \beta(J_3 e^{i\mathbf{k}\cdot\mathbf{a}} + J_4) & \beta^2 J_1(1+e^{-i\mathbf{k}\cdot\mathbf{b}}) \\ J_2(1+e^{i\mathbf{k}\cdot\mathbf{b}}) & \beta(J_3 e^{-i\mathbf{k}\cdot\mathbf{a}} + J_4) & 0 & \beta(J_3 e^{-i\mathbf{k}\cdot\mathbf{a}} + J_4) \\ \beta(J_3 e^{i\mathbf{k}\cdot\mathbf{b}} + J_4 e^{i\mathbf{k}\cdot(\mathbf{a}+\mathbf{b})}) & \beta^2 J_1(1+e^{i\mathbf{k}\cdot\mathbf{b}}) & \beta(J_3 e^{i\mathbf{k}\cdot\mathbf{a}} + J_4) & 0 \end{pmatrix} \tag{2.5}$$

Using our DFT-obtained values for J_1 through J_4, we numerically find that the momentum $\mathbf{q}$ at which the minimum eigenvalue $\lambda_{\min}(\mathbf{q})$ occurs is $\mathbf{q} = (\pi, 0)$ for a large range of β, in agreement with the periodicity of the spin configuration discussed in the text. From the eigenvector $\mathbf{P}_\alpha(\mathbf{q})$, we can obtain the spin configuration from $\mathbf{S}_a(\mathbf{k}) = \mathbf{P}_a(\mathbf{k})/\alpha_a$. As desired, the resulting spin configuration satisfies the strong constraint, provided we take $\beta \approx 1.7$. Additionally, the resulting spin configuration is precisely the collinear magnetic order obtained in the text. We have thus shown that the collinear magnetic order discussed in the main text (obtained by satisfying the nearest-neighbor exchange constants one-by-one) is the exact classical ground state of our model.

A corollary of this discussion is that the noncollinear magnetic state observed in the experiments cannot be explained by the nearest neighbor Heisenberg model, even though the predominant features of it can be. Since our DFT results show that the next-nearest neighbor exchange couplings are negligible, and higher order spin terms

are not likely to arise in spin-1/2 systems, exchange anisotropy is most likely behind the experimental ground state magnetic structure.

2.5.4 Linear spin wave theory

In this section, we obtain the magnon spectrum of the botallackite structure from the Heisenberg Hamiltonian using linear spin wave theory (see Sec. 1.3.4 for an overview of this method.) As derived in the previous section, the classical magnetic ground state has momentum $(\pi, 0)$. Since the structural unit cell has 4 spins, we find that the magnetic unit cell has 8 spins in total. As described in Sec. 1.3.4, we can obtain the magnon spectrum through the following steps: (i) rewriting the Hamiltonian H in terms of the Holstein-Primakoff bosons a_{in} and expanding to quadratic order in the bosons, (ii) rewriting the transformed Hamiltonian in momentum space, so that H is written in terms of the Fourier operators a_{nk} and $a^\dagger_{nk}$, and (iii) calculating the matrix $M(\mathbf{k})$, obtained by calculating the commutator $[\mathbf{v}, H] = M\mathbf{v}$. Here, $\mathbf{v}$ is the column vector given by $(\mathbf{a}_k, \mathbf{a}^\dagger_{-k})^T$.

Note that $M(\mathbf{k})$ is 16×16, since $\mathbf{a}_k$ is an 8 component vector. However, $M(\mathbf{k})$ block-diagonalizes into two 8x8 matrices. The 8×8 block of M,denoted $\mathcal{M}(k)$, which we numerically diagonalize at each $\mathbf{k}$ to obtain the spin-wave spectrum is as follows:

$$\mathcal{M}(\mathbf{k}) = \begin{pmatrix} 2(J_2+J_3-J_4) & 0 & J_3 & J_4 e_a & 0 & J_2(e_a+e_b) & J_4 e_b & J_3 e_b \\ 0 & 2(J_4-J_2-J_3) & -J_4 & -J_3 & -J_2(1+e_{b-a}) & 0 & -J_3 e_{b-a} & -J_4 e_b \\ -J_3 & -J_4 & 2(J_1+J_4-J_3) & 0 & -J_3 & -J_4 e_a & 0 & -J_1(e_a+e_b) \\ J_4 e_{-a} & J_3 & 0 & 2(J_3-J_1-J_4) & J_4 & J_3 & J_1(1+e_{b-a}) & 0 \\ 0 & J_2(1+e_{a-b}) & J_3 & J_4 & 2(J_2+J_3-J_4) & 0 & J_4 & J_3 e_a \\ -J_2(e_{-a}+e_{-b}) & 0 & -J_4 e_{-a} & -J_3 & 0 & 2(J_4-J_3-J_2) & -J_3 & -J_4 \\ J_4 e_{-b} & J_3 e_{a-b} & 0 & J_1(1+e_{a-b}) & J_4 & J_3 & 2(J3-J_1-J4) & 0 \\ -J_3 e_{-b} & -J_4 e_{-b} & -J_1(e_{-a}+e_{-b}) & 0 & -J_3 e_{-a} & -J_4 & 0 & 2(J_1+J_4-J_3) \end{pmatrix} \tag{2.6}$$

where we have used the shorthand $e_a \equiv e^{i\mathbf{k}\cdot\mathbf{a}}$. For each $\mathbf{k}$, we have four positive bands and four symmetric negative bands. As explained in Sec. 1.3.4, these negative eigenvalues do not imply negative magnon energies, but rather that our Bogoliubov operator is instead a creation operator $\alpha^\dagger_{n,k}$ (and not an annihilation operator $\alpha_{n,k}$ as originally assumed).

2.5.5 Competition between J_3 and J_4: Interchain dispersion

From our linear spin wave theory calculations, we can investigate how the interchain dispersion depends on J_3 and J_4. In the main text, we argued that J_3 and J_4 should compete, leading to an interchain dispersion that goes as $J_3 - J_4$. Here, we present results which substantiate this claim. In Fig. 2.15, we obtain the magnon spectrum using the values of J_1, J_2, and J_3 obtained in the bromide compound, where the hydrogen atoms have not been relaxed. J_4 is varied between $J_4 = 0.0$ meV and $J_4 = 0.5$ meV. We see that the interchain bandwidths are largest for $J_4 = 0$ meV, i.e. when $J_3 - J_4$ is largest. Additionally, we see that as J_4 is increased (or equivalently, $J_3 - J_4$ is decreased), the interchain dispersion becomes flatter.

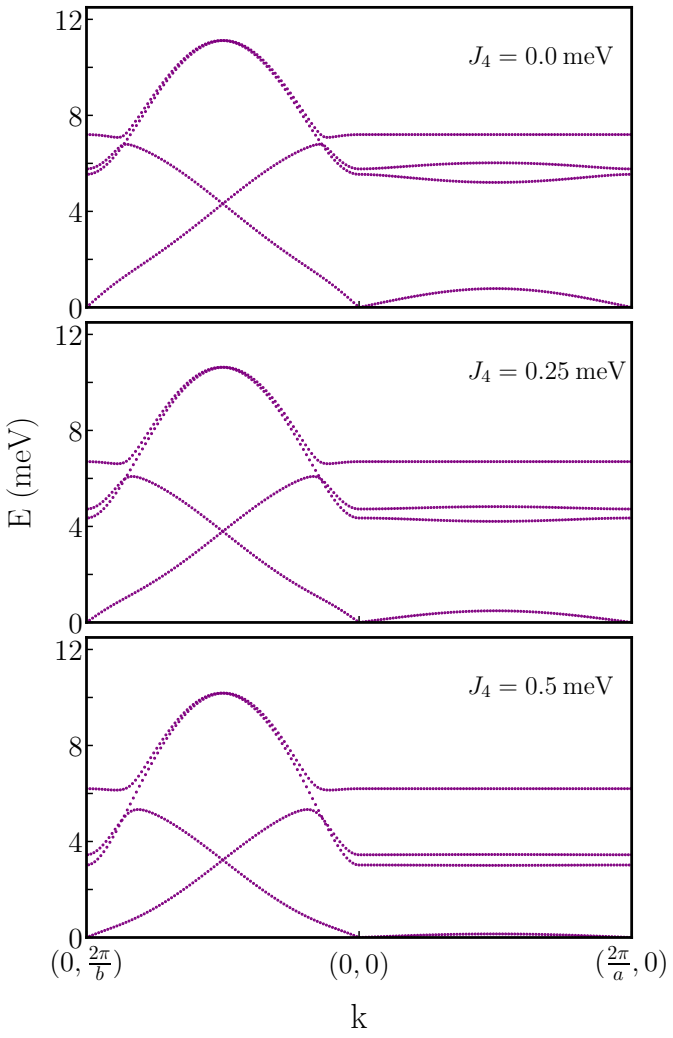

Figure 2.15: The magnon spectrum obtained using the values of J_1, J_2, and J_3 in the Br compound. We have varied the value of J_4 from 0 to 0.5 meV to observe its effect on the magnon spectrum.

Chapter 3

Magnetic and structural states of the perovskite rare-earth titanates as a function of strain

This chapter is adapted from my work *Strain-induced Magnetic and Structural Phase Transitions in the $RTiO_3$ Perovskites from First-principles* [in preparation].

3.1 Introduction

The perovskite rare-earth titanates $RTiO_3$ are Mott-insulating and exhibit strong couplings between lattice, spin, and orbital degrees of freedom [104]. Coupling between structural and electronic degrees of freedom is common among the transition metal oxides, accounting for their different exotic phases. In the case of $RTiO_3$, this strong spin-lattice coupling results in a ferromagnetic (FM) ground state for smaller rare-earth ions and a G-type antiferromagnetic (AFM) ground state for larger rare-earth ions [104]. This high sensitivity of the magnetic behavior of $RTiO_3$ to its structure suggests that it may be possible to experimentally tune, and ultimately control, the magnetic ground state of the rare-earth titanates through strain-engineering.

In recent years, the application of uniaxial and biaxial strain has shown promising results for tuning electronic properties in different systems. Epitaxial strain has

been applied to $SrTiO_3$ to induce room-temperature ferroelectricity [105], while uniaxial strain has been used to enhance the superconducting transistion temperature in Sr_2RuO_4 [106, 107]. Uniaxial strain has also been used to tune the metal-insulator transition in vanadium oxides [108, 109], modify the coupling between superconductivity and charge density wave order in the cuprates [110, 111], and to tune the coupling between the structural and magnetic transitions in the pnictides [112, 113].

With regard to the rare-earth titanates, all previous first-principles studies of the effect of biaxial strain on $RTiO_3$ [114, 115, 116, 117, 118, 119] have been restricted to a small selection of compounds and substrates. Moreover, these density functional theory (DFT) studies obtained the magnetic ground state by finding which of the A-type AFM, C-type AFM, G-type AFM, and FM states has the lowest energy. While such an analysis may be sufficient to obtain the magnetic ground state in some cases, this method is blind to the possibility of more exotic magnetic ground states. Indeed, given the rare-earth titanates' remarkable sensitivity to structural changes, it is feasible that interesting magnetic behavior could arise in $RTiO_3$ through the application of strain. In fact, we showed in Ref. [3] that a first-order transition could occur in $RTiO_3$ between two isosymmetric magnetic states. In this study, we also demonstrated that the position of the critical endpoint of the first-order phase boundary can be experimentally controlled via the application of uniaxial strain.

On the experimental side, recently, uniaxial strain has been used to tune ferromagnetism in bulk $Y_xLa_{1-x}TiO_3$ [2] resulting in a reduction or enhancement in T_c by up to a factor of $\sim$2, depending on the axis along which compression is applied. With respect to biaxial strain, although thin films of various $RTiO_3$ compounds have been grown [120, 121, 122, 123, 124, 125], to the best of our knowledge, there has been no experimental analysis of how the magnetic behavior of $RTiO_3$ varies with tensile or compressive biaxial strain.

The rare-earth titanates $RTiO_3$ crystallize in the orthorhombic *Pbnm* space group [126]. This orthorhombic structure is characterized by out-of-phase octahedral rotations about two of the pseudo-cubic axes and in-phase rotations about the third. In Glazer notation, this corresponds to the $a^-a^-c^+$ tilting pattern [127]. The *Pbnm* unit cell is shown in Fig. 3.1. Each Ti^{3+} ion has one electron in the $3d$ manifold and is octahedrally

coordinated by O^{2-} anions, resulting in a $t_{2g} - e_g$ crystal field splitting.[1] Due to the symmetry of the Ti crystal field, which is lower than O_h (due to both the tilting of the oxygen octahedra relative to the rare earths and the antipolar distortions of the rare earths), the energies of the t_{2g} orbitals are split, leading to orbital ordering at the DFT+U level. By varying the R ion in the perovskite structure, the structural distortions, and accordingly, the orbital order, are modified. The high sensitivity of the magnetic behavior in $RTiO_3$ to structural distortions follows from the dependence of the magnetic exchange interactions on the orbital ordering in the crystal.

In this chapter, we provide a comprehensive first-principles study of the effect of uniaxial strain, biaxial strain, and rare-earth ion substitution on the structural and magnetic ground states of the rare-earth titanates. For each relaxed structure, we perform additional first-principles calculations to extract the magnetic exchange parameters, which we then use to calculate how the structural and magnetic ground states of $RTiO_3$ evolve as a function of applied uniaxial and biaxial strain and rare-earth ion substitution. Moreover, we use the DFT-obtained exchange parameters to calculate the magnetic ground state and the mean-field transition temperature. Our DFT study of the magnetic behavior of the rare-earth titanates is comprehensive, with uniaxial and biaxial strain calculations totaling $\sim 1,500$ structures and ∼30,000 first-principles calculations.

To model the magnetic behavior of our system, we employ a Heisenberg Hamiltonian[2]. Our study reveals, in addition to the FM and G-type AFM (G) phases observed in the unstrained, bulk compounds, many additional magnetic phases which are stabilized under both uniaxial and biaxial strain. We also find several first-order structural

[1] In this work, we exclude $EuTiO_3$, which hosts Ti^{4+} cations [128], as well as $ScTiO_3$, which crystallizes in the cubic $Ia\bar{3}$ bixbyite structure [129].

[2] Although the Heisenberg model can in principle be used when there is no orbital order (in which case the orbital degrees of freedom are integrated out), the model we consider describes the magnetic interactions of Ti spins which exist on top of a frozen orbital order. This is due to the fact the exchange parameters are obtained from DFT, which, as a static mean-field theory, necessarily leads to frozen orbital configurations (which may differ depending on the spin configuration). In fact, the orbital order in the rare-earth titanates has been predicted theoretically in $LaTiO_3$ [130, 104] and $YTiO_3$ [131, 132, 133, 134], and has been experimentally indicated in $YTiO_3$[135, 136, 137, 138, 139, 140, 141, 142] and $LaTiO_3$[143, 144, 145]. From these studies, we do not expect orbital fluctuations to play a significant role in the magnetic properties of these compounds, and the absence of orbital fluctuations in our calculations should not affect our results significantly. For a different perspective, see the orbital liquid model, which assumes that the t_{2g} orbitals are degenerate and thus explicitly includes the orbital angular momentum degrees of freedom [146, 147, 148, 149, 150, 151, 152].

transitions. Epitaxial strain induces a first-order transition between isosymmetric orthorhombic $Pbnm$ structures ($Pbnm \rightarrow Pbnm$), similar to that theoretically predicted in $LaGaO_3$ in Ref. [153]. It also induces a transition between the orthorhombic $Pbnm$ structures (in which the c-axis is normal to the plane of the substrate), and monoclinic $P2_1/m$ structures (in which the c-axis lies in the plane of the substrate). This result mirrors that of previous studies [154, 155], which observe that epitaxial strain can induce changes in the octahedral tilting as well as the space group symmetry of a perovskite system.

This chapter is organized as follows: In Sec. 3.2, I review the computational details of our first-principles calculations. In Sec. 3.3, I classify the different Heisenberg exchange parameters for each symmetry-inequivalent structure, and provide an overview of the analytical methods we employ to obtain the magnetic ground state and mean-field transition temperature for a given crystal structure. I then discuss the results of our calculated the Heisenberg exchanges, magnetic ground states, and mean-field transition temperatures as a function of applied uniaxial and biaxial strain in Secs. 3.4 and 3.5 respectively. In Sec. 3.5, I also discuss the different structural phases which appear as a function of applied biaxial strain, as well as their associated magnetic behaviors. In Sec. 3.6, I summarize our results and suggest possible extensions of our work.

3.2 Computational Methods

DFT+U calculations were performed using the Projector Augmented Wave approach as implemented in the Vienna Ab Initio Simulation Package (VASP) [91, 92, 93]. To study the effect of uniaxial strain applied along a given orthorhombic axis, we fix the axis's associated lattice constant and relax the other two lattice constants, in addition to the fractional coordinates. Uniaxially strained structural relaxations are done in the primitive 4-Ti unit cell for strain values ranging from -3% to 3%. Here, 0% strain corresponds to the fully-relaxed bulk structure for each $RTiO_3$ compound. To model the effect of epitaxial strain on a square lattice substrate, we distinguish between the case in which the c-axis is normal to the plane of the substrate and the case in which the c-axis lies in the plane of the substrate. When the c-axis is normal to the plane, we take the primitive $Pbnm$ unit cell and fix $a = b = \sqrt{2}a_c$, where a_c is the lattice

constant of the cubic substrate. The lattice constant normal to the substrate and the fractional coordinates are then relaxed. In the case for which **c** is in the plane of the substrate, we use a $2 \times 2 \times 2$ pseudocubic supercell, containing 8 formula units. The in-plane pseudocubic lattice constants are then fixed to $2a_c$ and the remaining lattice constant and the fractional coordinates are allowed to relax.

In all relaxations, we use a $4 \times 4 \times 4$ k-point grid to sample the Brillouin zone. To extract the Heisenberg exchange interactions for a given structure, we calculate the energy of 20 different collinear spin configurations using DFT, which we then fit to a classical Heisenberg model using linear regression. In these calculations, a $2\sqrt{2} \times 2\sqrt{2} \times 2$ pseudocubic supercell containing 16 Ti atoms (a $2 \times 2 \times 1$ supercell in terms of the 4-Ti primitive unit cell) was used in order to distinguish between the different next-nearest-neighbor exchange interactions. Due to the size of the supercell in these exchange calculations, we use a $2 \times 2 \times 2$ k-point grid. In all calculations, we employ the PBEsol approximation to the exchange correlation functional [32]. We use the rotationally invariant LSDA+U scheme introduced by Dudarev et al. with U = 4 eV on the Ti $3d$ orbitals [36].

Due to the strong localization of the rare-earth f electrons, we expect the R-R and R-Ti exchange interactions to be significantly weaker than the exchange interactions arising from Ti-O-Ti superexchange. As such, the magnetic behavior in the $RTiO_3$ compounds is predominantly driven by the behavior of the Ti-Ti interactions. This can be seen in magnetic susceptibility measurements, which find that for all unstrained antiferromagnetic $RTiO_3$ compounds, the rare-earth moments order at a lower temperature than the Ti moments [156]. Therefore, in all calculations, we use PAW potentials which keep the rare earth f electrons in the core.

3.3 Obtaining the magnetic model, magnetic ground states, and mean-field transition temperatures

In the previous section, I briefly explained how we obtain the Heisenberg exchange parameters in a given compound. That is, the DFT-obtained energies of different spin

symm element	symm operation	space group
inversion centers	Ti sites and centers of ab-planar Ti plaquettes	$Pbnm$, $P2_1/m$
mirror planes	$z = \pm 1/4$	$Pbnm$, $P2_1/m$
2_1 screw axes	through the inversion centers, along $\mathbf{c}$	$Pbnm$, $P2_1/m$
b-glide planes	reflection through $x = \pm 1/4$, translation by (0,1/2,0)	$Pbnm$
n-glide planes	reflection through $y = \pm 1/4$, translation by (1/2,0,1/2)	$Pbnm$

Table 3.1: Symmetries of the space groups $Pbnm$ (reproduced from Ref. [5]) and $P2_1/m$.

configurations are fit via linear regression to the following Heisenberg Hamiltonian:

$$H = E_0 + \frac{1}{2}\sum_{ij} J_{ij}\mathbf{S}_i \cdot \mathbf{S}_j. \tag{3.1}$$

In the above equation, E_0 is the paramagnetic energy, and J_{ij} is the exchange parameter coupling spins $\mathbf{S}_i$ and $\mathbf{S}_j$. To use linear regression to extract the exchange parameters, we first identify the different exchanges which exist in a given crystal structure. In this section, we use symmetry arguments to classify the different nearest-neighbor and next-nearest-neighbor exchanges which occur in the $Pbnm$ and $P2_1/m$ crystal structures. This classification is what allows us in practice to extract the different exchanges from our DFT-obtained energies. In addition to classifying the exchanges, in the following sections, I also provide an overview of the analytical methods we use to obtain the magnetic ground states, as well as the mean-field transition temperatures. Further details can be found in Sec. 1.3.2 and Sec. 1.3.3.

3.3.1 $Pbnm$ structure

We begin with the $Pbnm$ structure, found in the bulk $RTiO_3$ rare-earth titanates, and use the space group symmetries to classify the different nearest-neighbor and next-nearest-neighbor Heisenberg exchange parameters within this structure. In Fig. 3.1(b), we label the different Ti atoms in the primitive unit cell. All Ti atoms occupy the

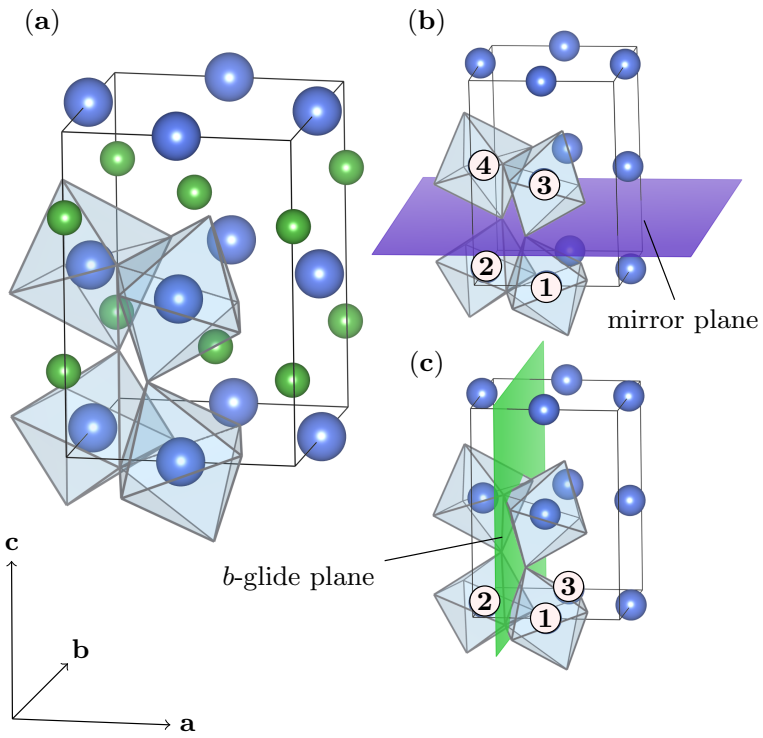

Figure 3.1: (a) Unit cell of $a^-a^-c^+$ $RTiO_3$ in the *Pbnm* space group. Ti atoms are shown in blue, while rare-earth ions are shown in green. The oxygen ions, which form the octahedra, are omitted. (b) Unit cell of $a^-a^-c^+$ $RTiO_3$ in the *Pbnm* space group, and one of the the mirror planes, shown in purple at $z = 1/4$. (c) Unit cell of $a^-a^-c^+$ $RTiO_3$ in the *Pbnm* space group, and one of the *b*-glide planes.

4*b* Wyckoff position, and are therefore symmetry equivalent. In Tab. 3.1, we list the symmetry elements of the *Pbnm* and $P2_1/m$ space groups. Starting with the mirror plane symmetry at $z = 1/4$, highlighted in Fig. 3.1(b), we see that this symmetry maps Ti_1 to Ti_3 and Ti_2 to Ti_4. Therefore, the exchange parameter coupling the spins on Ti_1 and Ti_2, denoted J^{1-2}, must be equal to the exchange parameter coupling spins on Ti_3 and Ti_4, J^{3-4}. Thus, the in-plane exchanges are equivalent from plane to plane due to the mirror plane symmetry.

We can garner additional symmetry information from the glide plane located at $x = 1/4$ (shown in green in Fig. 3.1(c) and detailed in Tab. 3.1). In Fig. 3.1(c), we have labeled three Ti atoms for convenience. The glide symmetry maps Ti_1 to Ti_2, and Ti_2 to Ti_3. Therefore, the exchange parameter couplings the spins on Ti_1 and Ti_2, J^{1-2}, is equivalent to the exchange J^{2-3}, coupling the spins on Ti_2 and Ti_3. Combining this with our above result regarding the mirror plane, we find that all in-plane nearest-neighbor exchanges are symmetry-equivalent. We denote this exchange J_{xy}. Similarly, these glide and mirror planes lead to a unique nearest-neighbor coupling along the z-direction, J_z, and only one next-nearest-neighbor coupling along the z-direction, J_{znnn}. There are two in-plane next-nearest neighbor exchanges J_a and J_b, which describe the coupling between spins on Ti atoms paired along the a and b axes respectively. These exchanges are shown in Fig. 3.2.

Although the *Pbnm* unit cell has four Ti atoms, we see from Fig. 3.2 that, with respect to the Heisenberg exchange interactions, all of the Ti atoms have the same environment. In other words, all of the Ti atoms in the unit cell occupy the same Wyckoff position. Therefore, to derive the magnetic ground state as well as the mean-field transition temperature in the *Pbnm* structure, it is sufficient to work instead with a one-Ti unit cell, using the pseudocubic lattice vectors $\mathbf{a}_c = (\mathbf{a} - \mathbf{b})/2$, $\mathbf{b}_c = (\mathbf{a} + \mathbf{b})/2$, and $\mathbf{c}_c = \mathbf{c}/2$, which connect nearest-neighbor Ti atoms. We emphasize that this one-Ti cell cannot be used as a structural unit cell, since the primitive cell for this *Pbnm* structure contains four Ti atoms. This one-Ti cell is only a unit cell in that it respects the periodicity of our Heisenberg Hamiltonian. Moreover, the use of this one-Ti cell is only possible when we ignore the effect of spin-orbit coupling. The inclusion of spin-orbit coupling introduces anisotropic exchange interactions (such as the Dzyaloshinsky-Moriya interaction) which depend on the local axes of the Ti-O octahedra, which vary

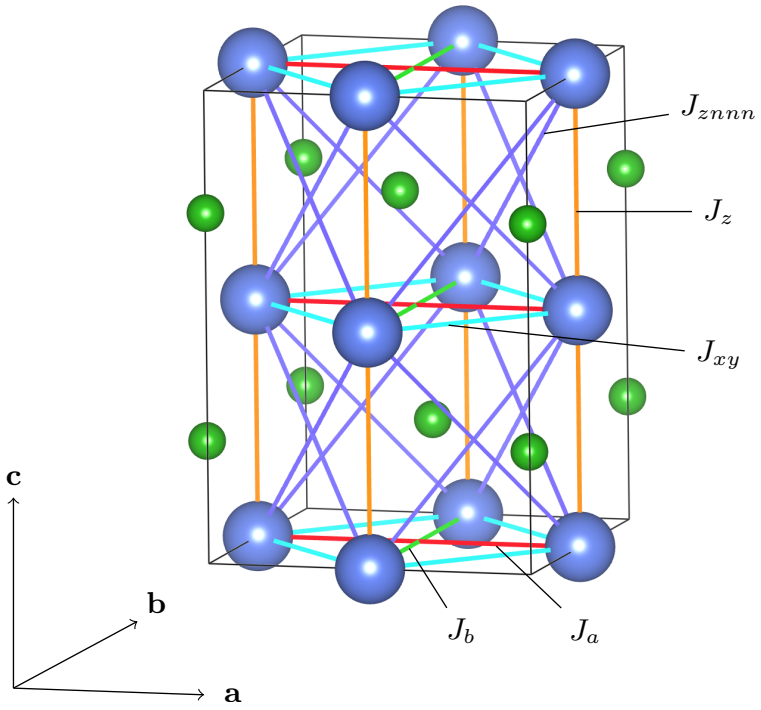

Figure 3.2: Definitions of the magnetic exchange constants.

from site to site. Although we do not include anisotropy into our magnetic model, we use symmetry considerations to gain insight into the effect of anisotropy on our results. This will be discussed further below, when we present our calculated magnetic phase diagrams. To obtain the magnetic ground state, we minimize the classical Heisenberg Hamiltonian

$$H = \frac{1}{2}\sum_{ij} J_{ij}\mathbf{S}_i \cdot \mathbf{S}_j, \tag{3.2}$$

where the labels i and j run over the spins in the system (or equivalently, the one-Ti unit cell defined above.) Here we have dropped the paramagnetic energy E_0, which is not pertinent to the below analysis. Using the Luttinger-Tisza method[3], the classical magnetic ground state in the *Pbnm* structure is given by

$$\mathbf{S}_i = \cos(\mathbf{k}_0 \cdot \mathbf{R}_i)\hat{\mathbf{u}} + \sin(\mathbf{k}_0 \cdot \mathbf{R}_i)\hat{\mathbf{v}}, \tag{3.3}$$

where $\hat{\mathbf{u}}$ and $\hat{\mathbf{v}}$ are any two orthogonal unit vectors. The wavevector $\mathbf{k}_0$ is obtained by searching for the location of the minimum of $J(\mathbf{k}) = \sum_i J_{ij} e^{-i\mathbf{k}\cdot(\mathbf{R}_i - \mathbf{R}_j)}$ in the Brillouin zone of the one-spin unit cell, i.e. $\mathbf{k}_0 = \arg\min_{\mathbf{k}\in \mathrm{BZ}} J(\mathbf{k})$.

This freedom to choose $\hat{\mathbf{u}}$ and $\hat{\mathbf{v}}$ reflects the O(3) symmetry of the Heisenberg model. Going beyond the Heisenberg model and including the effect of spin-orbit coupling leads to anisotropic exchange interactions which break the O(3) symmetry. From the perspective of a Landau free energy analysis, this anisotropic exchange couples order parameters of different magnetic phases, e.g. ferromagnetism and G-type antiferromagnetism [3]. Therefore, one expects in general an superposition of multiple order parameters within a given magnetic structure, an effect not accounted for in the Heisenberg model. However, since the Heisenberg exchanges are typically significantly larger than any anisotropic interactions in the titanates [5, 157], we exclude the effect of spin-orbit coupling from our Hamiltonian. We provide a more in-depth discussion of the effect of spin-orbit coupling below, when we discuss the magnetic phase diagrams we obtain from our Heisenberg model.

Given a magnetic ground state obtained from the analysis above, we also calculate

[3] See Sec. 1.3.2 for details.

the mean-field transition temperature T_{MF}. Relegating the details of the calculation to Appendix 3.6.1, the transition temperature T_{MF} is given by

$$T_{\mathrm{MF}} = -\frac{J(\mathbf{k}_0)}{3}. \tag{3.4}$$

With these results, given a set of DFT-obtained exchanges (J_{xy}, J_z, J_a, ...) corresponding to a crystal structure belonging to the $Pbnm$ space group, we use Eq. 3.4 along with Eq. 3.3 to evaluate the magnetic ground state and the mean-field transition temperature.

3.3.2 $P2_1/m$ structure

We now turn to the case of a $P2_1/m$ structure, which as discussed in the introduction, can be induced through the application of biaxial strain. In particular, if the in-phase rotation axis $\mathbf{c}$, is in the plane of the substrate (so as to mitigate the effect of misfit strain), biaxial strain acts in a plane normal to either the $\mathbf{a}+\mathbf{b}$ or the $\mathbf{a}-\mathbf{b}$ direction. This breaks both the b-glide and the n-glide symmetries, leading to a lowering from the orthorhombic $Pbnm$ space group to the monoclinic $P2_1/m$ space group. However, the remaining symmetry elements of the $Pbnm$ space group, consisting of the inversion centers, screw axes, and mirror planes, also exist in the $P2_1/m$ structure, as shown in Tab. 3.1. Additionally, the translational symmetry of the $Pbnm$ and $P2_1/m$ structures are the same, up to changes in the lattice vectors.

To understand the effect of the lower $P2_1/m$ symmetry on the magnetic Hamiltonian, recall that the combination of the b-glide symmetry and the mirror plane in the $Pbnm$ structure is what allowed us to work with a one-spin unit cell. Without the glide and mirror planes, there is no symmetry operation which maps nearest-neighbor Ti atoms to one another within the a-b plane. This leads to the appearance of two types of Ti atoms, which have different environments.[4] This is depicted in Fig. 3.3(a) which shows the monoclinic structure and highlights the two symmetry-inequivalent Ti environments via two differently-colored octahedra. From this, we expect these two types of Ti atoms, which we will refer to as Ti_1 and Ti_2, to have different magnetic

[4]This can also be understood via the Wyckoff positions: the 4b Wyckoff position splits into the 2b and 2c positions, as the $Pbnm$ space group is lowered to the $P2_1/m$ space group.

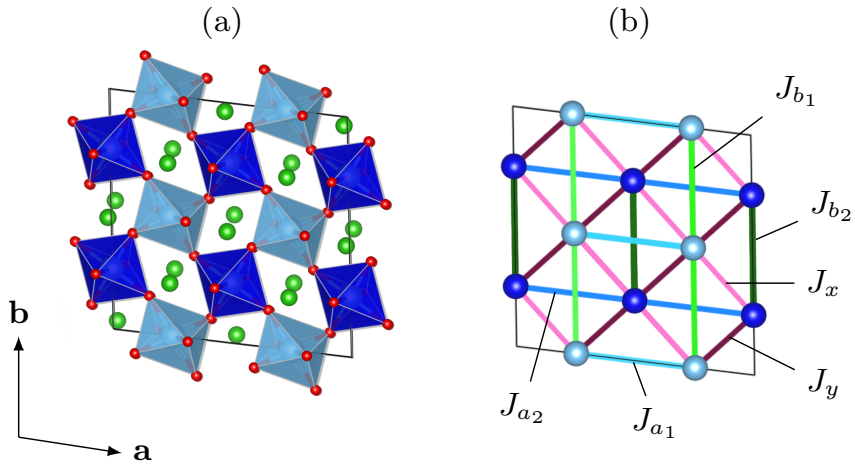

Figure 3.3: A view along the c-axis of the monoclinic $P2_1/m$ structure. In panel (a), we highlight the two inequivalent types of Ti atoms with two differently colored octahedra (light and dark blue). In panel (b), we show the in-plane magnetic exchange couplings.

exchange interactions with their neighbors.[5] For example, in the monoclinic $P2_1/m$ space group, the magnetic exchange coupling J_z splits into the couplings J_{z1} and J_{z2}, in which J_{z1} and J_{z2} connect nearest-neighbor Ti_1 and Ti_2 atoms, respectively, along the c-axis. Moreover, as depicted in Fig. 3.3(b), J_a splits into J_{a1} and J_{a2}, J_b splits into J_{b1} and J_{b2}, while J_{xy} splits into J_x and J_y. Here, J_x and J_y are the nearest-neighbor couplings directed along the pseudocubic $\mathbf{a}_c$ and $\mathbf{b}_c$ axes respectively. Lastly, the exchange parameter J_{znnn} splits into couplings which we denote J_{xz} and J_{yz}.

Though there are now two symmetry-inequivalent types of Ti atoms in the unit cell, we note that the screw axes and mirror planes continue to ensure that each Ti atom experiences the same environment as its nearest neighbors along the c-axis. As such, within our magnetic model, we now work with a two-spin unit cell, with lattice vectors $\mathbf{a}_m = \mathbf{a}$, $\mathbf{b}_m = \mathbf{b}$, and $\mathbf{c}_m = \mathbf{c}/2$.

To find the classical magnetic ground state of our model in the case for which there are two sublattices (i.e. two spins per unit cell), we need to minimize

[5]For simplicity, we do not consider the possibility of charge disproportionation, which could lead to differing magnetic moments on the Ti_1 and Ti_2 sites.

$$H = \frac{1}{2} \sum_{ij\alpha\beta} J_{ij}^{\alpha\beta} \mathbf{S}_i^\alpha \cdot \mathbf{S}_j^\beta, \tag{3.5}$$

where i and j are unit cell labels, and α and β label the sublattices. Obtaining the classical magnetic ground state for unit cells with more than one spin is a nontrivial problem, which has been tackled by a variety of approaches including generalized Luttinger-Tisza methods [63, 64, 65], iterative minimization [158, 159], and Monte-Carlo simulations [160, 71, 161]. In this work, we take a variational approach, using as an ansatz the following spiral state [162]

$$\mathbf{S}_i^\alpha = \cos(\mathbf{k}_0 \cdot \mathbf{R}_i + \phi_\alpha)\hat{\mathbf{u}} + \sin(\mathbf{k}_0 \cdot \mathbf{R}_i + \phi_\alpha)\hat{\mathbf{v}}. \tag{3.6}$$

Here, $\hat{\mathbf{u}}$ and $\hat{\mathbf{v}}$ are arbitrary orthonormal vectors, while the parameters ϕ_α and $\mathbf{k}_0$ are to be determined by minimizing the Hamiltonian with respect to these parameters. This spin configuration represents a pair of spirals, one for each sublattice α, with both spirals having their own phase ϕ_α.[6]

The spin configurations described by Eq. 3.6 are precisely those which can be obtained through the Luttinger-Tisza method [63, 64, 65, 98, 163]. In this sense, our choice of ansatz is just as general as the Luttinger-Tisza method, but with the added benefit that the ansatz satisfies the strong constraint ($\mathbf{S}_i^2 = 1$) automatically. Inserting the ansatz of Eq. 3.6 into the Heisenberg Hamiltonian and minimizing with respect to the phases ϕ_α, we find that the minimum energy of a spin configuration at momentum $\mathbf{k}_0$ is given by

$$\frac{H_{\text{spiral}}(\mathbf{k}_0)}{N} = \frac{J^{11}(\mathbf{k}_0) + J^{22}(\mathbf{k}_0)}{2} - \left|J^{12}(\mathbf{k}_0)\right|, \tag{3.7}$$

[6] From Eq. 3.6, both spin sublattices are enforced to have equal wavevectors $\mathbf{k}_0$. Though it is in principle possible to consider a more general state in which the two sublattices have different wavevectors, we expect such a state to have a large degree of magnetic frustration, and to therefore be energetically unfavorable. In particular, in such a spin configuration, the relative orientation of the two spin sublattices will vary from unit cell to unit cell. As such, although the exchange interactions may be satisfied in one portion of the crystal, the exchange interactions must be frustrated in another portion of the crystal. This follows from the translational symmetry of the exchange interactions between unit cells. Therefore, the energy gain in some regions of the compound would need to dominate the energy loss due to magnetic frustration occurring in the other regions of the compound. We are unaware of any instances of this occurring, and such an analysis is beyond the scope of this chapter.

where the exchange interactions in momentum space are

$$J^{\alpha\beta}(\mathbf{k}) = \sum_i J_{ij}^{\alpha\beta} e^{-i\mathbf{k}\cdot(\mathbf{R}_i - \mathbf{R}_j)}, \tag{3.8}$$

and N is the number of 2-spin unit cells in the system. To obtain the minimum energy spin configuration then, we search for the momentum $\mathbf{k}_0$ in the Brillouin zone such that the energy of the magnetic configuration $H_{\text{spiral}}(\mathbf{k}_0)$ is minimized, i.e. $\mathbf{k}_0 = \arg\min_{\mathbf{k}\in \text{BZ}} H_{\text{spiral}}(\mathbf{k})$.

With this classical magnetic ground state, the mean-field transition temperature is given by

$$T_{\text{MF}} = -\frac{\Psi^\dagger J(\mathbf{k}_0)^2 \Psi}{3\Psi^\dagger J(\mathbf{k}_0)\Psi}, \tag{3.9}$$

where we have defined $\Psi^T = (1, -J^{21}(\mathbf{k}_0)/\left|J^{12}(\mathbf{k}_0)\right|)$, and $J(\mathbf{k})$ is the 2×2 matrix whose elements are given by $J^{\alpha\beta}(\mathbf{k})$.[7] With the above results, given a set of DFT-extracted exchanges (J_x, J_y, J_{z1}, ...) corresponding to a given $P2_1/m$ structure, we can obtain the classical magnetic ground state and associated mean-field transition temperature.

3.4 Magnetic Trends With Uniaxial Strain

In this section, I describe the structural and magnetic trends in the perovskite rare earth titanates under applied uniaxial strain along the three orthorhombic axes[8]. Since uniaxial strain applied along the orthorhombic axes does not break any of the symmetries of the crystal, the space group remains $Pbnm$ for all values of uniaxial strain. Therefore, we can use our analysis described in Secs. 3.2 and 3.3.1 to extract the exchanges from DFT+U, magnetic ground state, and mean-field transition temperature. We present these results in Figs. 3.4-3.6. In particular, in addition to the FM and G orders, two new phases, A_z and C_z appear. These magnetic orders correspond to the wavevectors $(0, 0, \pi)$ and $(\pi, \pi, 0)$ respectively, and the components of the wavevectors refer to the periodicity along the pseudocubic $\mathbf{a}_c$, $\mathbf{b}_c$, and $\mathbf{c}_c$ directions. We emphasize that the subscripts do not refer to the directions of the magnetic moments, which as

[7] For more details regarding the above derivations, we refer the reader to Sec. 1.3.2 and 1.3.3.

[8] We do not consider possible transitions from the $a^-a^-c^+$ structure (e.g. to an $a^-b^+a^-$ structure) with uniaxial strain. Although these transitions are possible in principle, we expect the energy barrier separating such phases to be large.

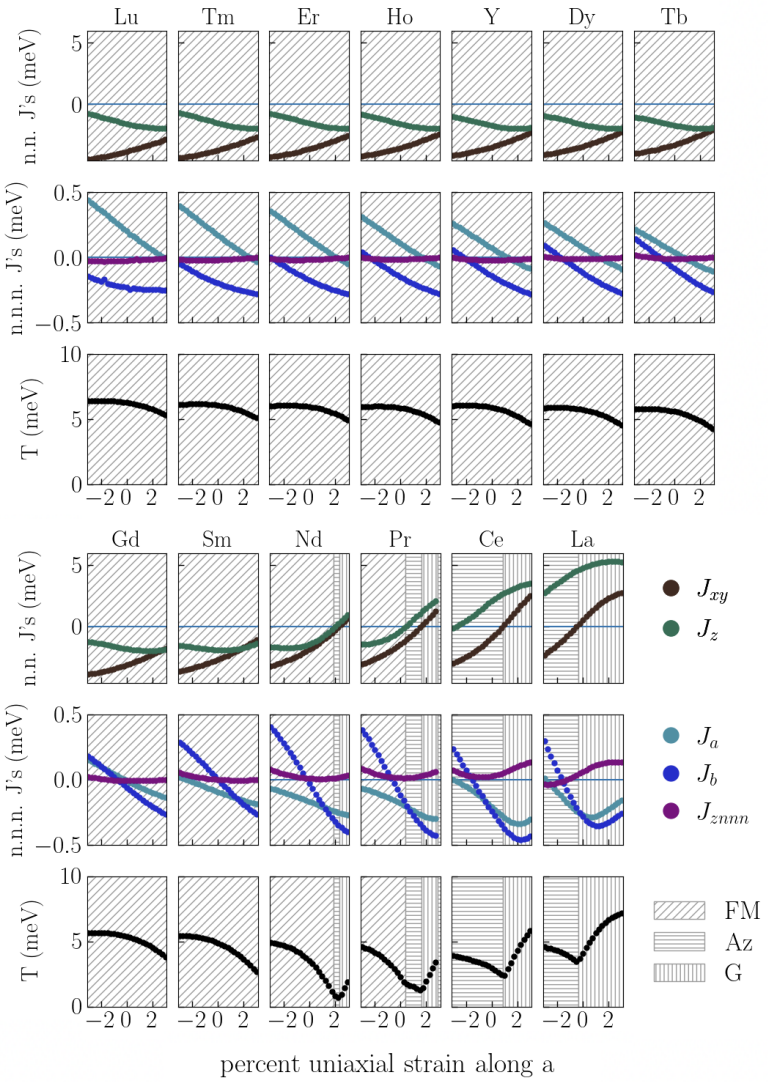

Figure 3.4: Exchange parameters and mean-field magnetic transition temperatures as a function of uniaxial strain along the a-axis. The hatching denotes the different magnetic phases.

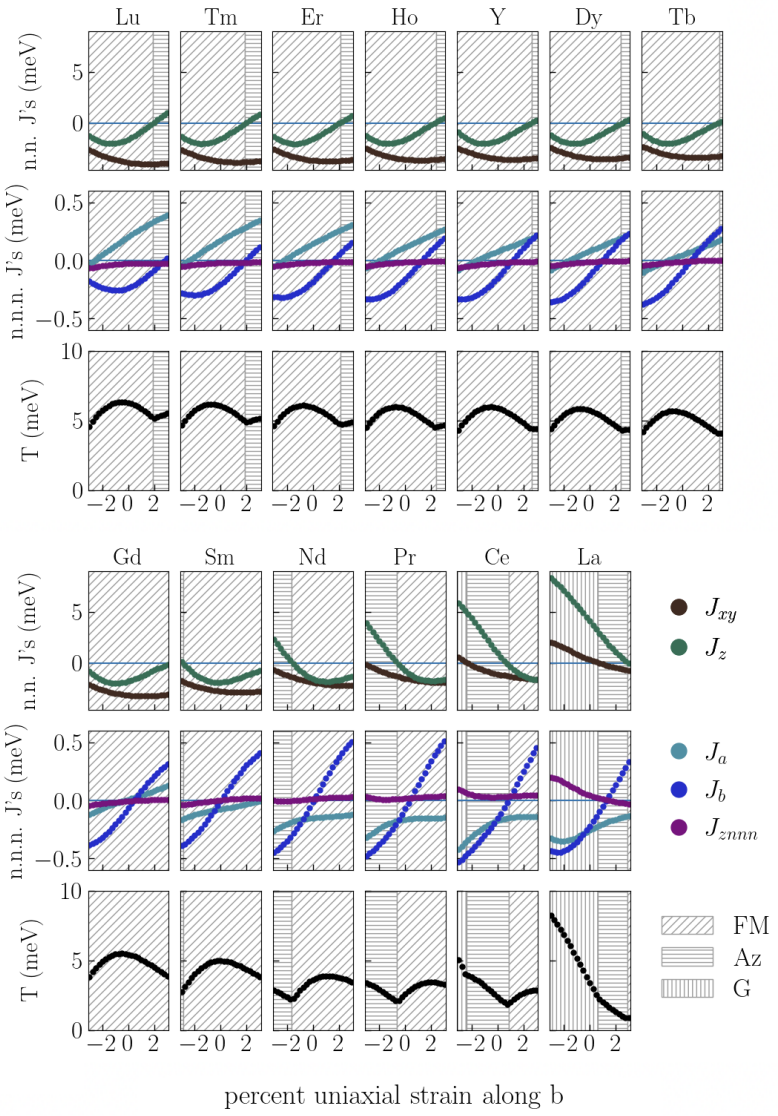

Figure 3.5: Exchange parameters and mean-field magnetic transition temperatures as a function of uniaxial strain along the b-axis. Hatching denotes the different magnetic phases.

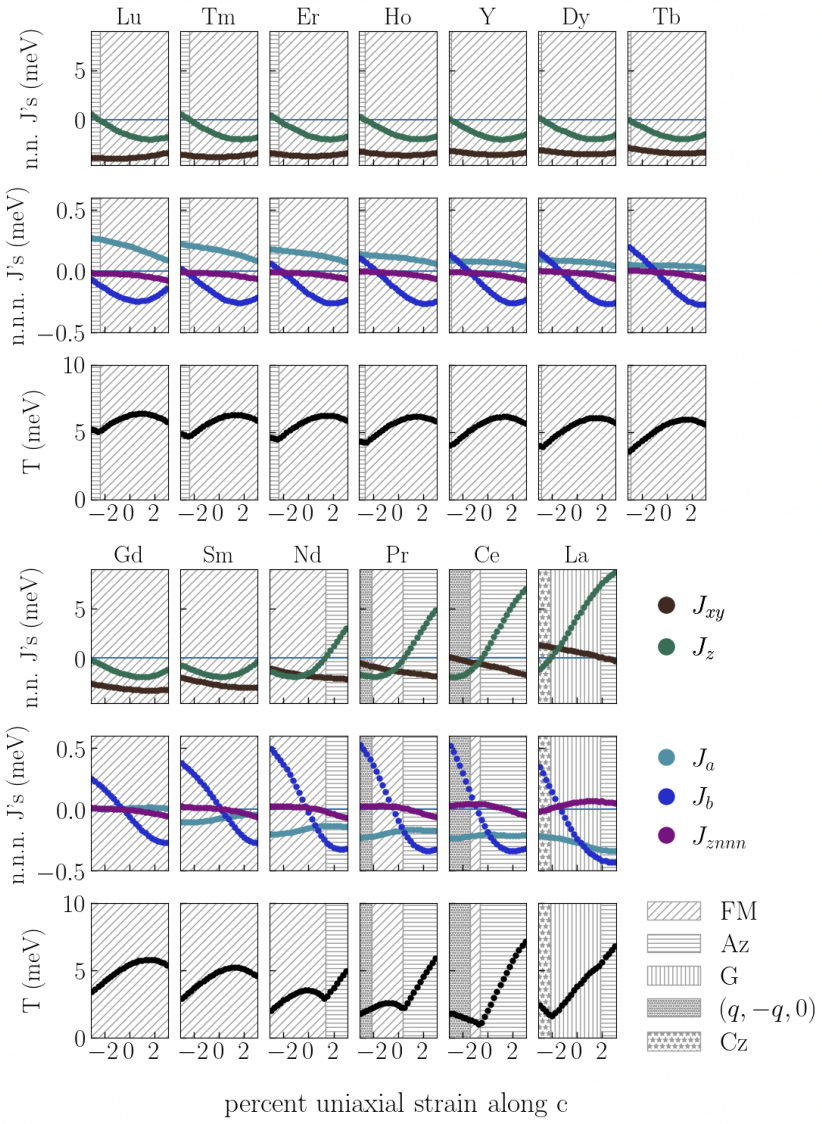

Figure 3.6: Exchange parameters and mean-field magnetic transition temperatures as a function of uniaxial strain along the c-axis. The hatching denotes different magnetic phases.

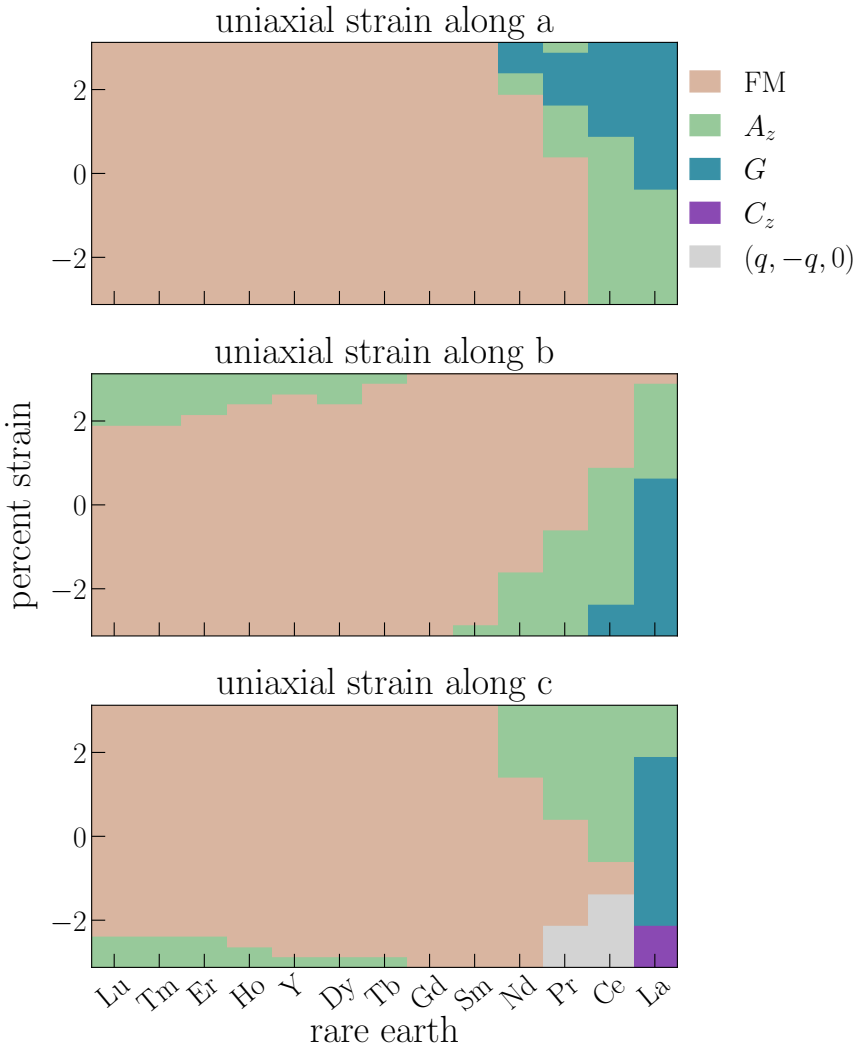

Figure 3.7: The magnetic phase diagrams for applied uniaxial strain along the a, b, and c axes, obtained via the Luttinger-Tisza method on top of DFT.

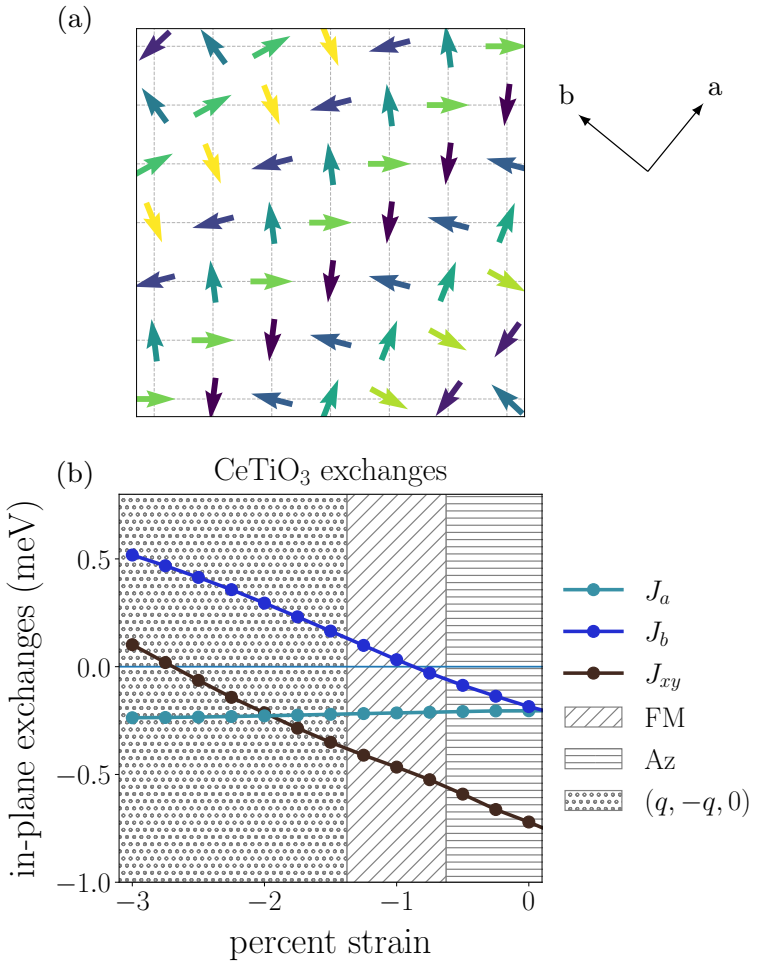

Figure 3.8: The incommensurate ground state observed for sufficiently large compressive strain along the c-axis in $PrTiO_3$ and $CeTiO_3$. For visual convenience, here we have taken $a = b$, so that the Ti sites form a square lattice.

discussed previously, are undetermined up to global rotations of the spins due to the O(3) symmetry of the Heisenberg model.

With uniaxial strain applied along the a-axis (Fig. 3.4), compressive strain causes the nearest-neighbor exchanges J_{xy} and J_z to become dissimilar, while tensile strain leads to more isotropic exchanges. The titanates that are ferromagnetic (FM) in bulk remain FM under all computed values of strain along the a-axis. However, those that are antiferromagnetic in bulk show both G and A_z order. Moreover, we find that the A_z phase separates the FM and G regions. The presence of this intermediate A_z phase agrees with the analysis of Mochizuki and Imada [164, 165], who argued that small octahedral distortions in the FM phase of $YTiO_3$ could induce a sign change in J_z, leading to a transition from the FM phase to the A_z phase. Although Mochizuki and Imada's analysis focused on the microscopic details of $YTiO_3$, one generally expects an intermediate phase between FM and G phases in non-cubic systems. This can be understood as follows: assume that we tune between the FM phase (where $J_{xy}, J_z < 0$) and the G phase (where $J_{xy}, J_z > 0$) by varying some parameter in our system (e.g. rare-earth ion size or uniaxial strain).[9] During this FM$\rightarrow$ G process, J_{xy} and J_z must change sign. However, since J_{xy} and J_z are in general different for non-cubic systems, we expect J_{xy} and J_z to change sign at different points during this transition. This leads to an intermediate region where J_{xy} and J_z have different signs, which could be either A_z ($J_{xy} < 0$ and $J_z > 0$) or C_z ($J_{xy} > 0$ and $J_z < 0$).

In contrast with the results for strain along the a-axis, we find that with strain applied along the b-axis (Fig. 3.5) the nearest-neighbor exchanges become more similar under tensile strain and more dissimilar under compressive strain. Additionally, for the titanates which are FM in bulk, there is a transition with tensile strain to an A_z phase. As in the case of strain applied along the a-axis, we find that an A_z phase separates the FM and G phases.

The corresponding phase diagrams are shown in Fig. 3.7. From the phase diagram for uniaxial strain along the c-axis (Fig. 3.7), we see a region in which there is an incommensurate magnetic ground state with wavevector $(q, -q, 0)$ for uniaxial strain

[9] We neglect the effect of the next-nearest neighbor exchanges during this discussion, which are significantly smaller than the nearest-neighbor exchanges throughout most of the phase diagram. Their inclusion does not change this argument, and only leads to the possibility of more complicated intermediate phases.

applied to $PrTiO_3$ and $CeTiO_3$. Numerically, we find that q takes values between 0.1 and 0.3 (in units of $2\pi/a_c$), implying that the periodicity of this incommensurate state takes values in the range between $3a_c$ and $10a_c$. This incommensurate spiral state is represented in Fig. 3.8, with the spins colored according to their directions. In the incommensurate state, nearest-neighbor spins along the a direction are all aligned, while nearest-neighbor spins along the b direction are predominantly anti-aligned. To understand how this incommensurate state emerges as a function of compressive strain, we first note that as more compressive strain is applied, the next-nearest neighbor couplings J_a and J_b become rather large, becoming twice and five times as large as J_{xy} in magnitude at -3% strain (Fig. 3.8). To minimize the Hamiltonian, we can then first satisfy J_a and J_b. Since $J_a < 0$ and $J_b > 0$, this leads to the aligned spins along the a-axis and anti-aligned spins along the b-axis seen in Fig. 3.8. J_{xy} is then frustrated, leading to the spiral, incommensurate nature observed. Lastly, since $J_z < 0$ in this region, we expect a ferromagnetic alignment of the spins with their nearest neighbors along the c-axis. This agrees with the wavevector of the magnetic ground state, $(q, -q, 0)$.

So far, we have neglected the effect of exchange anisotropy, which could give rise to spin canting, and therefore simultaneous magnetic orders of different types (e.g. FM and G) within a given structure. Indeed, this is what is observed in both bulk $LaTiO_3$ [143] and $YTiO_3$ [126]. Since we expect the anisotropy to be weak compared to the Heisenberg exchanges, the main effect of the exchange anisotropy, if any, would be to smooth out the sharp phase boundaries in Figs. 3.7 obtained from our Heisenberg model. In other words, it may be that when the effect of anisotropy is included, there is only a crossover (as opposed to a first-order transition) between, for example, predominantly FM, predominantly A_z, or predominantly G orders. We however reiterate that even if there are no sharp phase boundaries, our results predict significant changes in the magnetic behavior of $RTiO_3$ with applied uniaxial strain, which may be experimentally observed through trends in the magnetic transition temperatures, for example (see Figs. 3.4-3.6.)

In Ref. [166], Bousquet and Spaldin showed that the magnetic configurations in which the G moment points along the a-axis, the A_z moment points along the b-axis, and the FM moment points along the c-axis (which we denote G^a, A_z^b, and F^c, respectively), all transform under the same irreducible representation, B_{2g}, with respect to the $Pbnm$

space group.[10] As such, we expect bilinear couplings between all three order parameters in the free energy when exchange anisotropy is included. Therefore, all three orders (G^a, A_z^b, F^c) should be nonzero in a given compound. From this, under uniaxial strain along the a and b axes, in which only the FM, A_z, and G phases appear, we cannot conclude from symmetry considerations alone whether sharp phase transitions exist in the presence of exchange anisotropy.

The situation is different in the case of applied uniaxial strain along the c-axis, in which the C_z and incommensurate spiral state appears. In particular, the incommensurate spiral state breaks the translational symmetry of the $Pbnm$ structure, while the surrounding FM, C_z, and G phases do not. As such, if the incommensurate spiral state continues to be stable in the presence of exchange anisotropy, the boundary between this incommensurate phase and the surrounding FM, C_z, and G phases, which are commensurate, must be sharp, and may be first or second order in nature. The stability of the incommensurate spiral state in the presence of exchange anisotropy is not guaranteed however. Although the Dzyaloshinskii-Moriya interaction favors the non-collinearity present in the incommensurate spiral state, the anisotropic symmetric exchange interactions lead to the presence of easy axes, which instead prefers spin collinearity. As such, a detailed examination of the exchange anisotropy present in the system is required to understand the stability of this incommensurate state.

We can also use symmetry considerations to gain insight into the transition between the G and C_z phases in $LaTiO_3$ with applied compressive strain along the c-axis. From neutron diffraction [143], we know that unstrained $LaTiO_3$ has a G-type moment pointing along the a-axis. However, from the analysis of Bousquet and Spaldin, we also know that regardless of the direction of the C-type moment, the C_z phase transforms differently than the G^a phase under operations of the $Pbnm$ space group. In other words, the C_z^a, C_z^b, and C_z^c phases all transform under different irreps than G^a in the $Pbnm$ space group. As such, the C_z and G^a phases are symmetry-inequivalent. Hence, there must be at least one sharp phase transition with compressive strain along the c-axis. This could happen in two ways: First, the system could remain in the G^a phase until the C_z phase appears, at which point the system exhibits a first-order phase transition into

[10] Note that Ref. [166] works in the $Pnma$ setting, and their resulting notation is different from the notation we use here.

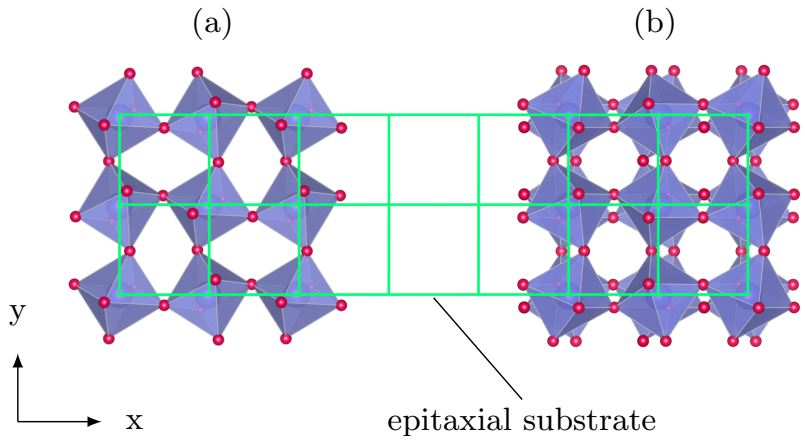

Figure 3.9: A view of the perovskite rare earth structure on a substrate with (a) the c-axis out of the plane of the substrate and (b) the c-axis parallel to the plane of the substrate.

the C_z phase. Second, the system could instead exhibit a spin-flop transition within the predominantly G-type phase with applied compressive strain, with the easy axis switching from pointing along the a-axis to along the b- or c-axes. There would then be a sharp transition between the G^a and G^b or G^c phases, as these are all symmetry-inequivalent phases with respect to the $Pbnm$ space group. Then, since the resulting G^b or G^c phase belongs to the same irrep as the C_z^c or C_z^b phase, respectively, the boundary separating the G and C_z phases could instead be a crossover region, depending on the C-type phase. Distinguishing between these possibilities can only be done through a microscopic analysis of the exchange anisotropy present in the system, and is beyond the scope of this work.

3.5 Magnetic Trends With Biaxial Strain

3.5.1 c-axis normal to the substrate plane

With applied biaxial strain, the $RTiO_3$ compound may be grown with its c-axis (the axis about which octahedral cage rotations are in-phase) either normal to the plane of the substrate or within the plane of the substrate, depending on which of the two orientations leads to a lower-energy structure [154, 155]. These two orientations are

illustrated in Fig. 3.9. As discussed in the introduction and in Sec. 3.3.2, structures with the c-axis normal to the plane of the substrate have $Pbnm$ symmetry, while structures with the c-axis lying within the plane of the substrate have $P2_1/m$ symmetry. As we will discuss in Sec. 3.5.2, the $P2_1/m$ structures in which the c-axis lies within the plane of the substrate dominate most of the phase diagram. However, in this section, we focus only on the case in which the c-axis is normal to the plane of the substrate, i.e. the $Pbnm$ structures. The results we present here may still be experimentally observable, even in the regions of the phase diagram where the $Pbnm$ structures are energetically disfavored relative to the $P2_1/m$ structures. In particular, Rondinelli and Spaldin demonstrated in Ref. [167] that a compound may take on the octahedral tilting pattern present in an underlying substrate, in what has been termed the substrate coherency effect. Hence, it may be possible to stabilize the $Pbnm$ phase through a suitable choice of substrate, e.g. one which hosts in-phase rotations normal to the substrate plane. This point is discussed in detail at the end of Sec. 3.5.1.

When the c-axis is normal to the substrate plane, biaxial strain does not break any crystallographic symmetries and the space group remains $Pbnm$. As such, we use the analysis from Sec. 3.3.1 to obtain the classical magnetic ground states and mean-field transition temperature. We present the results in Figs. 3.10 and 3.11. In Fig. 3.10, we show how the exchange parameters vary as a function of the lattice constant of the cubic substrate, a_c, and present the corresponding magnetic phase diagram in Fig. 3.11.

First-order isosymmetric transition

Interestingly, in contrast with the case of uniaxial strain, in which the exchanges vary smoothly with strain, we observe sharp discontinuities in the exchanges with application of biaxial strain. We find that this behavior is due to a first-order isosymmetric transition. In particular, although there is a sharp change in the internal coordinates, there is no change in the crystallographic space group nor the occupied Wyckoff positions.

We highlight this transition between the two structural states in Fig. 3.12, in which we plot the energy of the two states as a function of biaxial strain in $LuTiO_3$. Here, we clearly see the crossing of the two energy parabolas describing the energy of the two $Pbnm$ phases. This isosymmetric transition is similar to that theoretically predicted in the perovskite $LaGaO_3$ [153], though the transition there occurs in the monoclinic

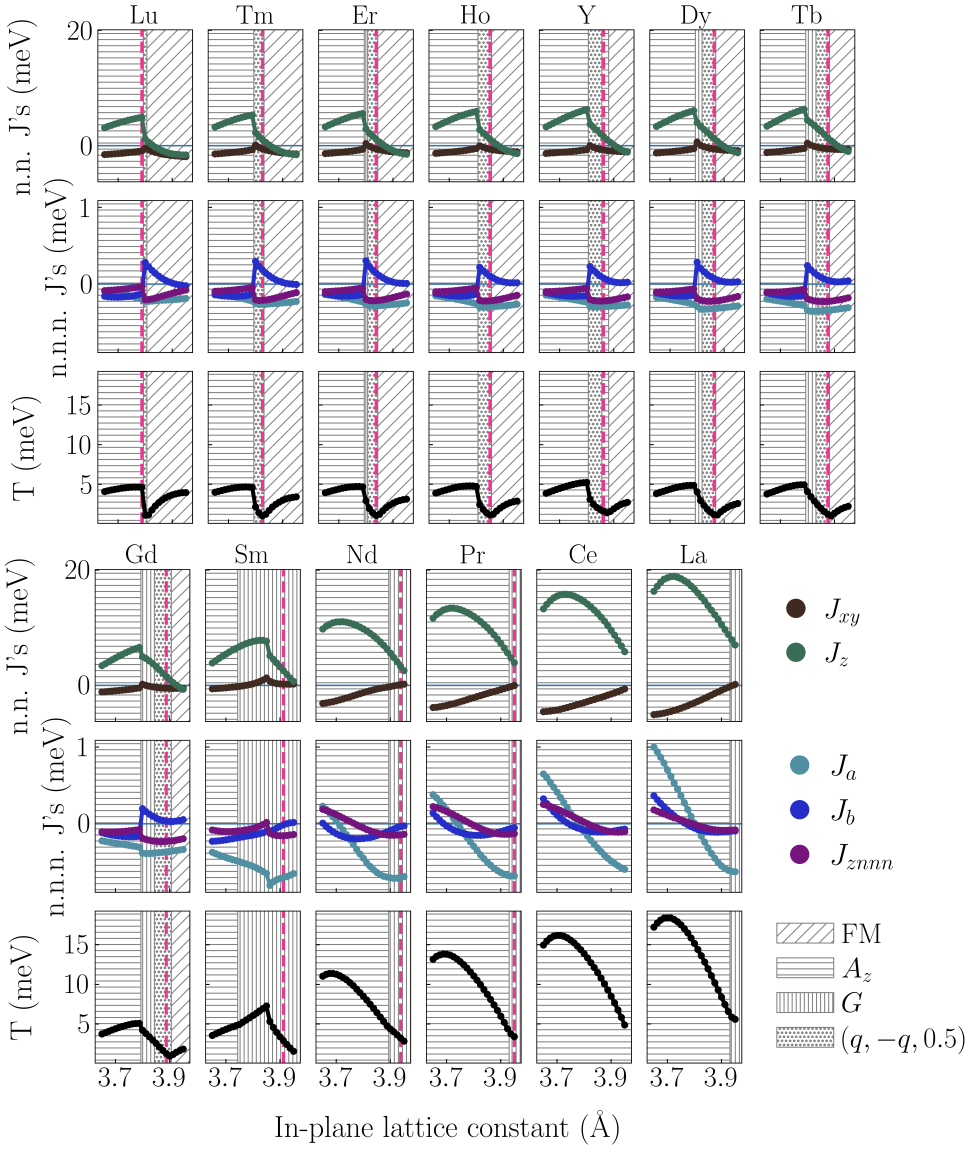

Figure 3.10: The exchange parameters, mean-field transition temperatures, and magnetic phases as a function of the in-plane lattice constant, for the case in which c is normal to the plane of the substrate. We also plot a dashed violet line where we find the stress to be closest to zero. Discontinuities in the exchanges are due to a first-order isosymmetric transition between the orthorhombic structures ($Pbnm \rightarrow Pbnm$).

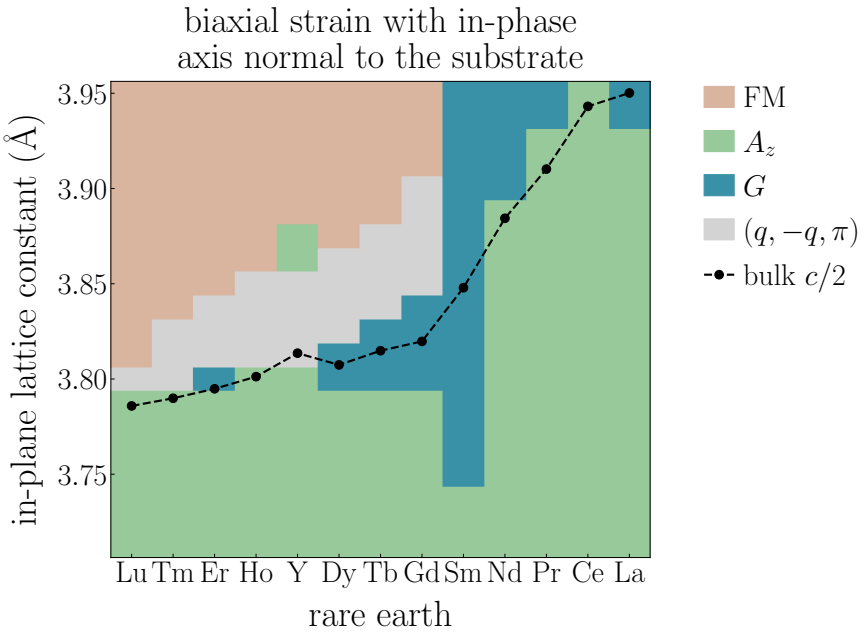

Figure 3.11: The magnetic phase diagram in which biaxial strain is applied while fixing **c** to be out of the plane of the substrate.

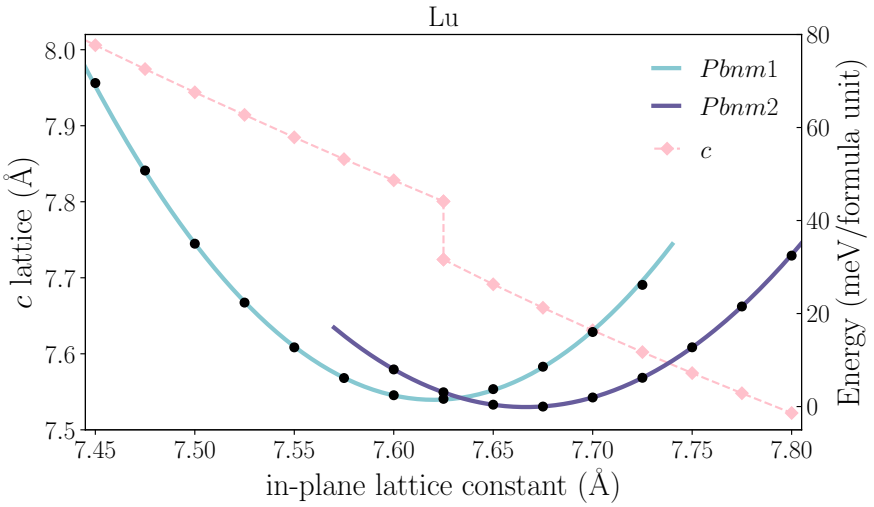

Figure 3.12: The energy parabolas highlighting the transition between the two $Pbnm$, $a^-a^-c^+$ structures.

space group $C2/c$. Moreover, unlike $LaGaO_3$, the B sites in the $RTiO_3$ compounds have magnetic moments. As such, discontinuous changes in the lattice parameters are accompanied by drastic changes in the magnetic behavior. In particular, in Fig. 3.10, we see that the isosymmetric phase transition is accompanied by magnetic phase transitions. However, this isosymmetric transition may not be observed experimentally, since (as we discuss in Sec. 3.5.3) it is common for both *Pbnm* phases are higher in energy than the $P2_1/m$ phase in which the *c*-axis is in the plane of the substrate. Regardless, if we assume that the *c*-axis continues to stay normal to the substrate for all values of strain, evidence of this isosymmetric transition could be observed as a dramatic drop in the magnetic transition temperature as a function of increasing biaxial strain, especially for rare earth elements with smaller ionic radii.

This *c*-axis alignment could possibly be induced experimentally by exploiting the substrate coherency effect [167]. In particular, a substrate's octahedral distortions can substantially modify the relative stability of different tilting patterns in a thin film through a proximity effect. In the case of $SrFeO_3/SrTiO_3$ heterostructures, Rondinelli and Spaldin [167] showed that octahedral distortions from the $SrTiO_3$ substrate creep into the $SrFeO_3$ film, despite the fact that the ground state of bulk $SrFeO_3$ exhibits no octahedral distortions. With respect to our system, since in-phase octahedral rotations occur about the *c*-axis, one might try to enhance the stability of the *Pbnm* phases by growing the $RTiO_3$ thin films on a substrate in which the in-phase octahedral rotations occur normal to the substrate. Indeed, a theoretical analysis by Khalsa and Benedek [168] of strained $GdTiO_3$ found that the *Pbnm* phase is favored over the $P2_1/m$ phase when $GdTiO_3$ is grown on the *Pbnm* scandate $GdScO_3$.

Effect of biaxial strain despite lattice match

In Fig. 3.10, we also plot a dashed violet line where the stress on the compound is closest to zero, where one might expect the system to behave most similarly to the unstrained compound. We refer to these structures as the zero-strain structures[11]. However, from Fig. 3.10, we see that at zero-strain, there are AFM ground states for

[11]The zero-strain compounds for $CeTiO_3$ and $LaTiO_3$ occur for in-plane lattice constants just above 3.9Å, and are not shown in Fig. 3.10.

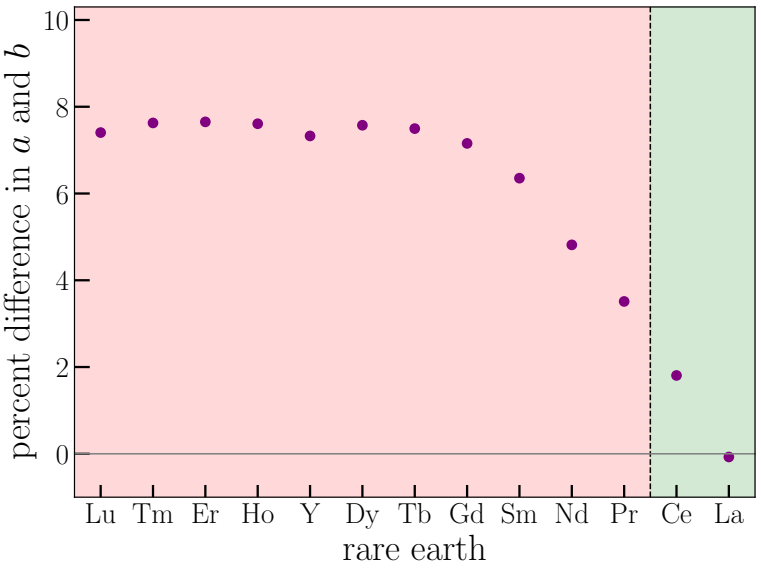

Figure 3.13: The percent difference between a and b in the unstrained, bulk $RTiO_3$ compounds. The background color denotes whether the magnetic ground state of the bulk compound agrees with the zero-strain* compound. If the states do not agree, we denote this with red, while agreement is shown using green. *Here, "zero-strain" refers to the strained compound in which the pressure, obtained from our first-principles calculations, is closest to zero (see dashed line in Fig. 3.10).

all of the compounds which are found to be FM (in our calculations of the unstrained compounds.) To understand this, we note that in all of the $RTiO_3$ compounds, $a \neq b$, since bulk $RTiO_3$ crystallizes in the orthorhombic *Pbnm* space group. Moreover, not only is $a \neq b$, but a and b are significantly different in most of the $RTiO_3$ compounds. This is shown in Fig. 3.13, where we see that the percent difference between a and b for most $RTiO_3$ compounds is rather large, with the bulk FM compounds having a percent difference of around 7%. As such, by growing $RTiO_3$ on a cubic substrate and enforcing $a = b$, we apply significant strain to $RTiO_3$ for all values of a_c, the in-plane lattice constant of the cubic substrate. Indeed, as can be seen in Fig. 3.13, agreement between the zero-strain and bulk magnetic ground states only occurs for $CeTiO_3$ and $LaTiO_3$, where a and b are most similar.

Lastly, we note that all compounds studied here transition through various antiferromagnetic phases with compressive biaxial strain. As with the uniaxial case, there is

a region of the phase diagram in which an incommensurate spiral state is stabilized, as can be seen by the green region in Fig. 3.11. In contrast to the incommensurate spiral state which appeared in the case of uniaxial strain, which had wavevector $(q, -q, 0)$, the incommensurate state appearing here has wavevector $(q, -q, \pi)$, i.e. the spins alternate in direction from a-b plane to a-b plane, along the c-axis. This difference follows from the large positive value of J_z in this region of the phase diagram. In the presence of exchange anisotropy, we cannot conclude whether there is a crossover or first-order transition between the FM, A_z, and G phases in the phase diagram. However, the boundary between these phases and the incommensurate spiral state will continue to denote a well-defined phase boundary, assuming as in Sec. 3.4 that the incommensurate spiral state is also stable in the presence of exchange anisotropy.

3.5.2 c-axis in the plane of the substrate

As discussed in the introduction, when the c-axis is in the plane of the substrate (Fig. 3.9b), the glide-plane symmetry is broken and the crystallographic symmetry is lowered from the orthorhombic $Pbnm$ space group to the monoclinic $P2_1/m$ space group. We reiterate that in the case where the c-axis is in the plane of the substrate, biaxial strain breaks the glide symmetries present in the $Pbnm$ space group. This leads to J_{xy} splitting into J_x and J_y, J_z splitting into J_{z1} and J_{z2}, J_{znnn} splitting into J_{xz} and J_{yz}, J_a splitting into J_{a1} and J_{a2}, and J_b splitting into J_{b1} and J_{b2}. Additionally, in the monoclinic structure, there are two inequivalent Ti sites per unit cell, leading to two Ti spins per unit cell. In this monoclinic case, we use the analysis of Sec. 3.3.2 to calculate the exchanges, magnetic ground state, and mean-field transition temperature.

We present the results for this monoclinic case in Fig. 3.14, which shows the exchanges and their respective transition temperatures as a function of the in-plane lattice constant a_c. Interestingly, for a large range of a_c, J_{z1} and J_{z2} are drastically different, implying that the environments for the Ti_1 and Ti_2 spins are significantly different. This difference is especially stark for the smaller rare earth ions, where J_{z1} and J_{z2} are of opposite sign for most values of a_c. Similar behavior is seen in the trends for J_x and J_y, which are significantly different for smaller R. For the larger rare earth ions such as Pr, Ce and La, J_{z1} and J_{z2} are more comparable (as are J_x and J_y), and behave similarly as a function of a_c. This behavior can be better understood by looking at the

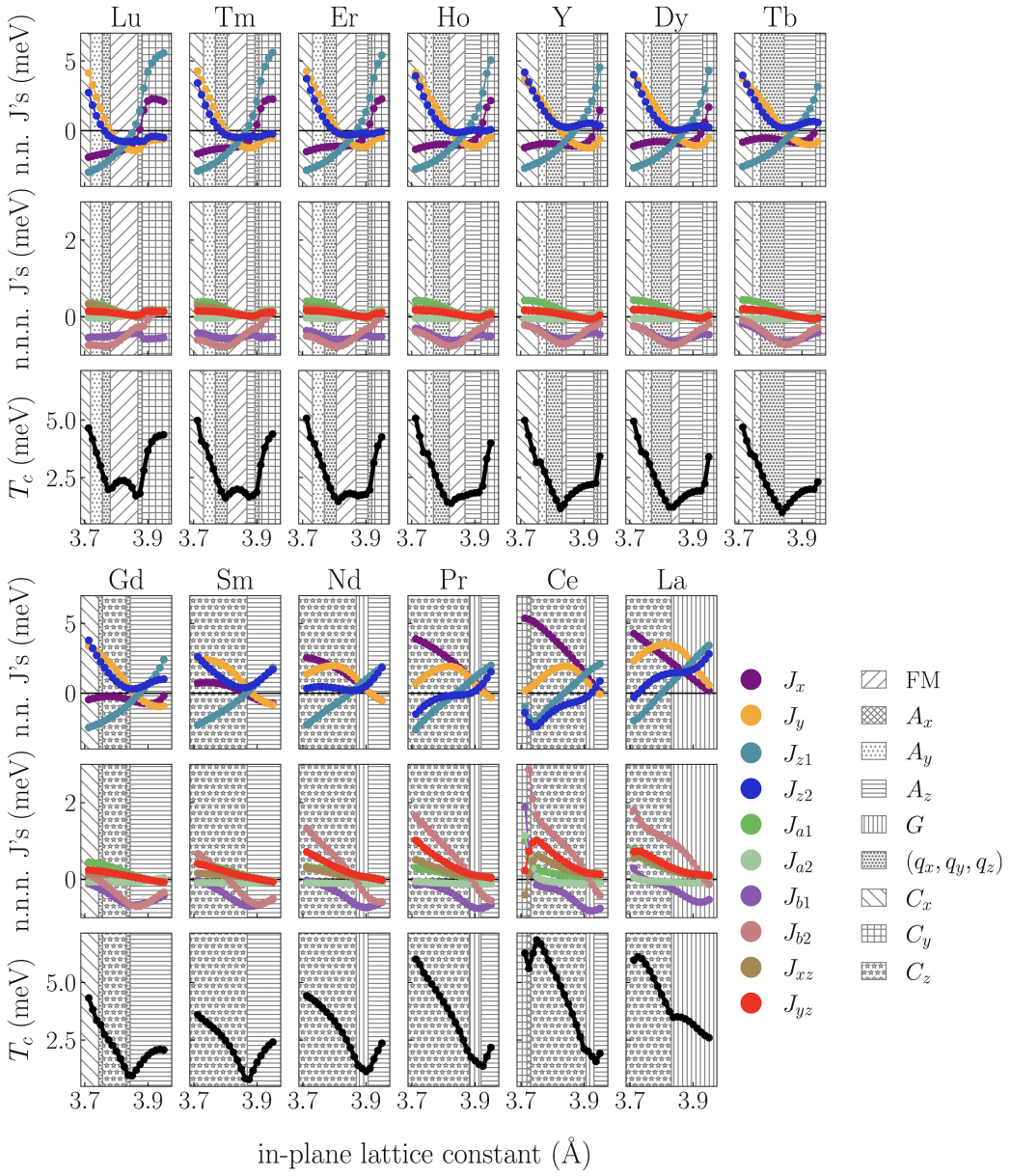

Figure 3.14: The exchange parameters, mean-field transition temperatures, and magnetic phases as a function of in-plane lattice constant, for the case in which the c-axis in in the plane of the substrate.

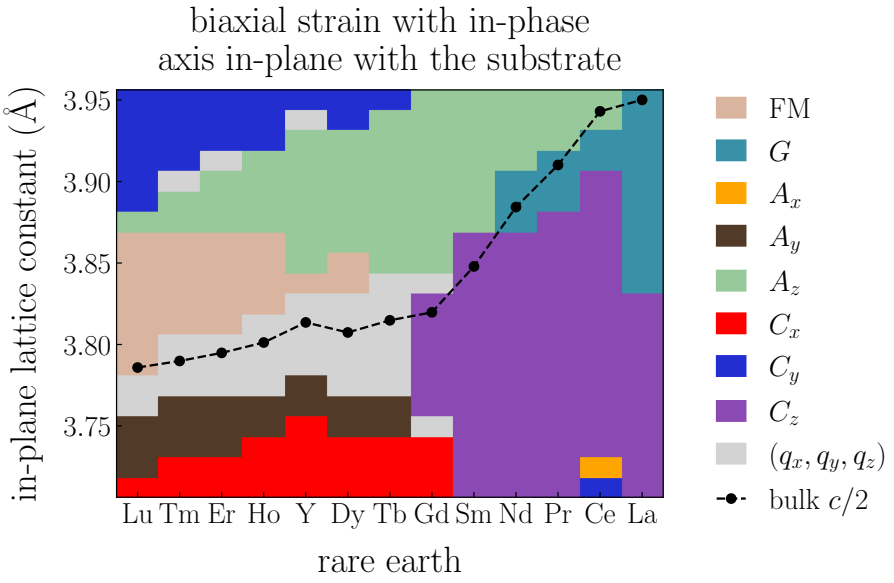

Figure 3.15: The magnetic phase diagram in which biaxial strain is applied, fixing **c** to be in the plane of the substrate.

corresponding magnetic phase diagram in Fig. 3.15, in which we have overlaid the $c/2$ lattice constants of the unstrained bulk structures. The bulk $c/2$ values in Fig. 3.15 provide a rough estimate of where the epitaxial strain on the compounds is minimized. For R =Ce and La, the strain is minimized for the largest values of a_c we consider here, $a_c \sim 3.95$Å. As such, the monoclinicity induced by the epitaxial strain is weak, and we expect the *Pbnm* glide symmetries to approximately hold. As such, we expect $J_{z1} \approx J_{z2}$, $J_x \approx J_y$, $J_{xz} \approx J_{yz}$, $J_{a1} \approx J_{a2}$, and $J_{b1} \approx J_{b2}$. Indeed, this can be verified in the trends in $CeTiO_3$ and $LaTiO_3$ for larger values of a_c.

For the smaller R ions, we also find that both compressive and tensile biaxial strain lead to a large enhancement in the magnitude of nearest-neighbor exchanges. Moreover, we find that these nearest-neighbor exchanges are also positive. This implies that biaxial strain applied to these smaller $RTiO_3$ compounds, which are ferromagnetic in bulk, should induce transitions into antiferromagnetic states. Moreover, the enhancement in the magnitude of the nearest-neighbor exchanges in these antiferromagnetic regions should manifest in larger magnetic transition temperatures. For now, we do not consider the question of whether the *Pbnm* structure (in which the c-axis is normal to the

substrate) is preferred to the $P2_1/m$ structure (in which the c-axis is normal to the substrate). We discuss this point in Sec. 3.5.3.

The magnetic phase diagram for the monoclinic case, in which the c-axis in the epitaxial plane, is shown in Fig. 3.15. Close to the bulk $c/2$ values, there are FM regions for smaller rare-earth ions, and G regions for larger rare-earth ions. This is to be expected, since the effect of biaxial strain should be minimized near values of a_c. Away from these bulk values, we find an abundance of new magnetic phases. In particular, while the A_z phase still occupies a significant region of the phase diagram, we find that the A_x and A_y orders are also stabilized in certain regions of the phase diagram. This is made possible due to the disappearance of the glide plane in the monoclinic $P2_1/m$ structure. That is, since the exchanges along the pseudocubic $\mathbf{a}_c$ and $\mathbf{b}_c$ directions are no longer symmetry equivalent (i.e. $J_x \neq J_y$, $J_{xz} \neq J_{yz}$, etc.), it may happen for example that a magnetic order is stabilized which alternates along the $\mathbf{a}_c$ direction, but not the $\mathbf{b}_c$ direction. This reasoning also implies that C_x and C_y phases may also appear, in addition to the C_z phase. Indeed, for smaller rare-earth ions, the C_x, C_y, and A_y phases are stabilized for a sizable range of a_c values. The appearance of these new phases may be understood by focusing on the trends in the J_x and J_y exchanges as a function of a_c in the smaller rare-earth compounds in Fig. 3.14. J_x and J_y are of opposite sign for the more extreme values of a_c. These regions in which J_x and J_y are of opposite sign are also precisely where we find the non-A_z/C_z phases. The effect of monoclinicity can also be seen in the periodicity of the incommensurate spiral states which appear for the smaller rare-earth ions. We find numerically that these states have $|q_x| \neq |q_y|$, in contrast to the incommensurate spiral states obtained in the $Pbnm$ structure, for which the c-axis is normal to the substrate plane. Similar to the $Pbnm$ structure however, we find that q_z is either 0 or π for all incommensurate states obtained here.

For the larger rare-earth ions, the non-A_z/C_z phases disappear, and the phase diagram is instead dominated by the A_z, C_z, and G phases. This disappearance of the non-A_z/C_z phases is to be expected, since as discussed above, the monoclinicity induced by biaxial strain in these larger rare earth compounds is rather weak.

We now discuss the effects of exchange anisotropy on the resulting monoclinic phase diagram. If we assume that the incommensurate spiral states are stable as in Secs.

3.4 and 3.5.1, the boundary of the incommensurate regions is a true phase boundary, even in the presence of exchange anisotropy. Regarding the other phases which appear, since the space group is no longer $Pbnm$, we can no longer use the analysis of Bousquet and Spaldin [166] to distinguish between the symmetry-inequivalent phases. Here, we simply note that the FM, G, A_z, and C_z phases are invariant under the translations of the monoclinic structure, while the A_x, A_y, C_x, and C_y phases are only invariant under translations along the c-axis. In particular, these phases change sign under translations along the a- and b-axes. From this, we conclude that the FM, G, A_z, and C_z phases are symmetry-inequivalent from the A_x, A_y, C_x, and C_y phases, regardless of the directions of the magnetic moments.

From this observation, we may conclude for example, that under tensile epitaxial strain, $LuTiO_3$ does not undergo a crossover, but a first-order phase transition from the A_z to the C_y phase, even in the presence of exchange anisotropy. Similar reasoning allows us to conclude that there is a well-defined phase boundary separating the C_x and C_z phases at $a_c \sim 3.7$Å.

In addition to the monoclinic $P2_1/m$ phase studied here, our calculations show that sufficiently large compressive biaxial strain stabilizes a triclinic $P\bar{1}$ phase. However, the energy difference between the $P\bar{1}$ and $P2_1/m$ structure is small, being on the order of a few meV/f.u. on average. Moreover, we find that the $P2_1/m$ and $P\bar{1}$ structures are quite similar. That is, the irreps common to both phases have similar mode amplitudes, and the irrep mode amplitudes lowering the symmetry to $P\bar{1}$ are all significantly smaller (by a factor of ~ 10) than the irreps characterizing the monoclinic phase. As such, it is possible that this $P\bar{1}$ structure is an artifact of our calculational method.

In particular, recall that in our first-principles relaxations of these monoclinic structures, we work in the $2 \times 2 \times 2$ pseudocubic unit cell. While the in-plane lattice vectors of our supercell are kept fixed, the out-of-plane supercell lattice vector, which we denote $\mathbf{c}_{sc} = c_x\hat{i} + c_y\hat{j} + c_z\hat{k}$, is relaxed in our first-principles code. Here, $\hat{k}$ represents the direction normal to the substrate. In principle, all three components of $\mathbf{c}_{sc}$ should be relaxed. However, the implementation of the first-principles code which we use fixes c_x and c_y, only relaxing c_z (in addition to the fractional coordinates). As such, to obtain the fully-relaxed structure, we in principle need to relax the system at different values

of c_x and c_y to find which values minimize the energy of the system.[12] Instead, for convenience, we set $c_x = c_y = 0$ for all of our calculations. This is fine in most cases, since in our basis, c_x and c_y are typically smaller than c_z by two orders of magnitude. However, since the energy difference between the $P\bar{1}$ and $P2_1/m$ phases is small, c_x and c_y should be optimized in both structures to obtain the minimum-energy state.

Unfortunately, it is infeasible to perform this procedure for each structure– since we consider 13 rare-earth ions and 20 values for a_c, there are $13 \times 20 = 260$ structures for which we would need to optimize the monoclinic angle (or triclinic angles, if we consider nonzero c_y.) Having undertaken this optimization for a few structures, we find that while the $P\bar{1}$ phase is still stabilized for some values of a_c, the energy difference between the $P\bar{1}$ and $P2_1/m$ states is significantly reduced by this optimization of c_x and c_y. Due to the exceptionally small energy differences between the $P\bar{1}$ and $P2_1/m$ structures, the substantial compressive strains which must be applied to realize the $P\bar{1}$ phase for most rare earths, and the computational infeasibility of optimizing the monoclinic and triclinic angles for each compound, we do not consider the $P\bar{1}$ phase further in the present study.

3.5.3 Complete biaxial strain phase diagrams: *Pbnm* versus $P2_1/m$

Thus far, we have separately considered the case in which the *c*-axis is normal to the substrate (in which the structure crystallizes in the *Pbnm* space group), and the case in which the *c*-axis is in the plane of the substrate (in which the structures crystallizes in the $P2_1/m$ space group.) However, we should in principle obtain the magnetic phase diagram by finding which of the two structures has the lower energy. The resulting structural phase diagram is shown in the top panel of Fig. 3.16, in which we show the lower-energy structural phase of the two structures under consideration ($P2_1/m$ and *Pbnm*). As in the previous phase diagrams, we add the bulk $c/2$ lattice constants to highlight the approximate area where the strain in the system is minimized.

The $P2_1/m$ structure is lower in energy for much of the phase diagram, while the *Pbnm* phase predominantly exists under the application of tensile strain. This agrees

[12] If the system is monoclinic, symmetry constraints force $c_y = 0$, and only c_x needs to be found. In this case, optimizing c_x is equivalent to optimizing the monoclinic angle. Optimizing both c_x and c_y is equivalent to optimizing the triclinic angles.

with the behavior observed in epitaxially strained $CaTiO_3$ [154]. The stabilization of the $Pbnm$ phase under compressive strain for R=Lu, Ce, and La, occurs due to the magnetic contribution to the ground-state energies. In particular, at these points in the phase diagram, we find that the paramagnetic energies of the $Pbnm$ and $P2_1/m$ structures are approximately equal. However, the energy gain arising from the magnetic configuration satisfying the various Heisenberg exchanges leads to the $Pbnm$ phase winning out over the $P2_1/m$ phase.

To complement this structural phase diagram, the bottom panel of Fig. 3.16 shows the lowest-energy magnetic phase for each strain value, taking into account the lower-energy structure at that strain value. As expected from the dominance of the $P2_1/m$ phase for much of the structural phase diagram, the complete magnetic phase diagram shown in Fig. 3.16 is, for the most part, quite similar to that of the monoclinic magnetic phase diagram shown in Fig. 3.15. However, the A_z phase takes up a much smaller region of the phase diagram, while the area in which the FM phase is stabilized grows.

From an experimental standpoint, our analysis predicts that for all $RTiO_3$, the application of compressive or tensile epitaxial strain should lead to numerous magnetic phase transitions. In particular, we expect that application of tensile strain will induce first-order structural phase transitions ($P2_1/m \rightarrow Pbnm$), occurring at epitaxial strain values around $1-3\%$ for most rare-earth ions R, and are therefore likely experimentally accessible.[13] This is especially true for the larger rare-earth compounds, in which the onset of the $Pbnm$ phase occurs close to the bulk. Additionally, as discussed in Sec. 3.5.1, the area of the phase diagram in which the $Pbnm$ phase is stabilized could possibly be extended through a suitable choice of substrate. This could allow one to not only access the $Pbnm$ phase more easily, but to also possibly observe the isosymmetric phase transition discussed in 3.5.1.

3.6 Summary and Conclusions

Our comprehensive DFT study of uniaxially and biaxially strained $RTiO_3$ spans $\sim 1,500$ structures and $\sim 30,000$ first-principles calculations. We find that the application

[13] This strain value is obtained from $\varepsilon = (a_{\text{onset}} - a_{\text{bulk}})/a_{\text{bulk}}$, where we take $a_{\text{bulk}} = c_{\text{bulk}}/2$ and a_{onset} is the in-plane lattice constant where the compound switches from $P2_1/m$ to $Pbnm$ with tensile strain.

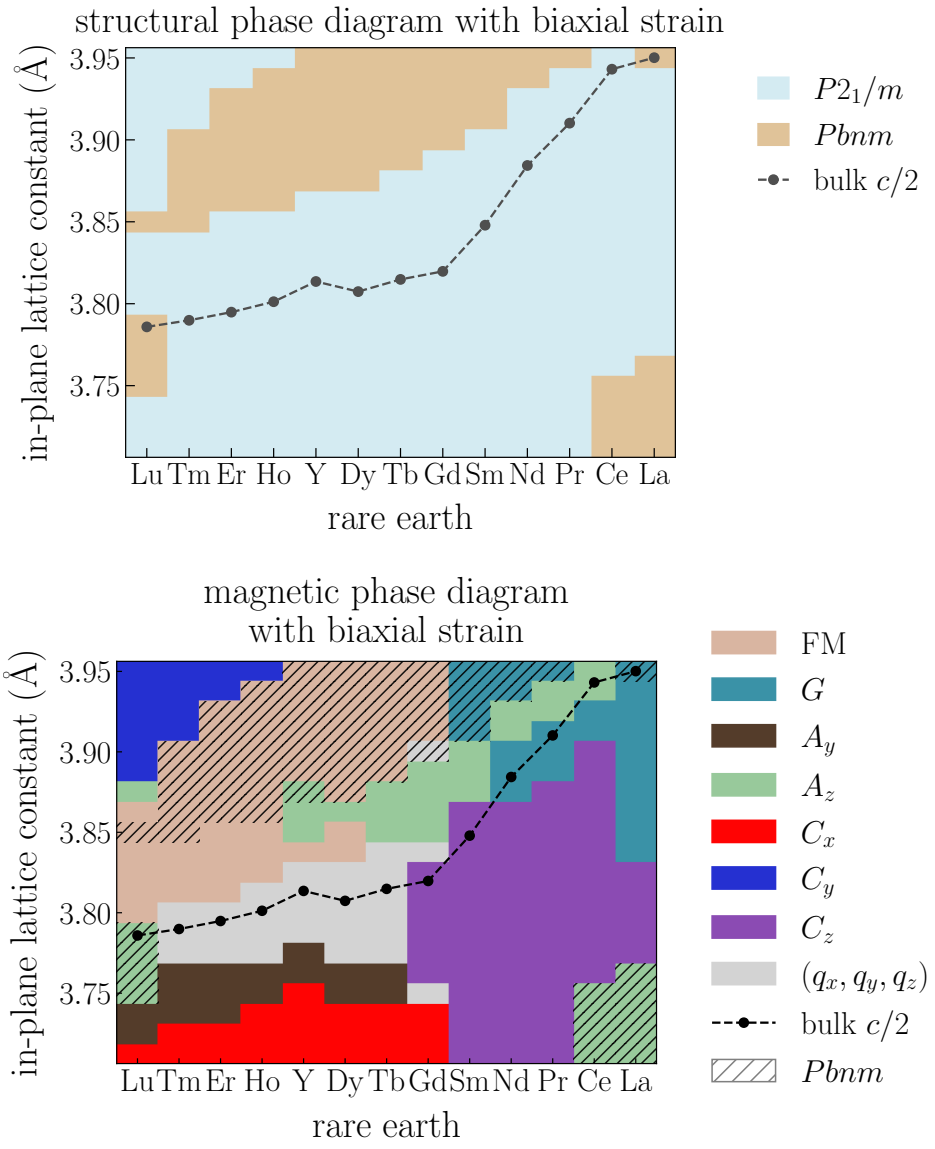

Figure 3.16: Top panel: The structural phase diagram for the rare-earth titanates as a function of R and the substrate lattice constant. The ground state is determined by taking the minimum of the $Pbnm$ and $P2_1/m$ energies. Bottom panel: The magnetic phase diagram for all rare earth elements and in-plane lattice constants. The ground state is determined by taking the minimum of the $Pbnm$ and $P2_1/m$ energies. Cross-hatching denotes the states which have structures belonging to the $Pbnm$ space group, while those without cross-hatching belong to the $P2_1/m$ space group.

of uniaxial and biaxial strain should induce multiple magnetic and structural phase transitions in $RTiO_3$, which have not yet been experimentally observed. Among these strain-induced phases is the as-of-yet unobserved A_z phase discussed by Mochizuki and Imada [164, 165], which we find to be stabilized under both uniaxial and biaxial strain. Additionally, we find that a first-order transition from the G phase to the C_z phase should occur with the application of compressive uniaxial strain along the c-axis of $LaTiO_3$. Depending on the details of the exchange anisotropy present in the compound, this transition may be preceded by a first-order spin-flop transition, where the direction of the G-type moment switches to point along the b- or c-axes.

Under biaxial strain, we also find that in addition to the FM, G, A_z and C_z phases which arise with applied uniaxial strain, biaxial strain leads to the appearance of the A_x, A_y, C_x, and C_y phases. We also predict that both uniaxial and biaxial strain should stabilize incommensurate spiral magnetic orders for some rare earth ions.

With respect to the crystal structure, we find that tensile biaxial strain may induce phase transitions from the monoclinic $P2_1/m$ space group into the orthorhombic $Pbnm$ space group. Within the orthorhombic $Pbnm$ space group, we find that biaxial strain induces an isosymmetric structural phase transition, which should manifest in sharp changes in the magnetic behavior of the system.

Throughout this work, we for the most part have disregarded the effect of spin-orbit coupling. However, using symmetry considerations, we showed that certain phase boundaries must continue to exist even in the presence of exchange anisotropy. A more in-depth investigation of the anisotropic exchange interactions could yield further insight into the nature of the various phase transitions we obtain with our Heisenberg model. Similarly, we have also used a variational method to obtain the classical ground state of the Heisenberg model. Although this method is sufficient to capture most magnetic ground states, there may exist exotic magnetic phases which cannot be captured with our method. As such, a future investigation of the classical magnetic ground state in these compounds would be interesting, especially in the regions of the phase diagram in which magnetic frustration is large. In particular, it is interesting to ask whether the incommensurate spiral states we obtain in the monoclinic $P2_1/m$ structure truly correspond to the classical magnetic ground state, and if so, what the role of quantum fluctuations is in these compounds.

Additionally, recent theoretical studies have argued that the magnetic behavior of $RTiO_3$ could be tuned optically either with ultrafast pulses [168, 169] or Floquet engineering [170]. These works demonstrate that optical driving is a promising avenue to controlling the exchange parameters of $RTiO_3$, and stabilizing new magnetic phases. In particular, the work of Khalsa and Benedek [168] showed that applying optical pulses to biaxially-strained $GdTiO_3$ leads to the stabilization of the A_z phase for moderate values of applied strain and electric fields. While the A_z phase can be stabilized through biaxial strain alone in $GdTiO_3$, Khalsa and Benedek find that the A_z phase can be stabilized at more moderate values of biaxial strain when optically excited. This suggests that optical driving of $RTiO_3$ in combination with applied strain may allow one to experimentally access the more extreme values of strain which we study here.

Appendix

3.6.1 Multicollinearity as an obstacle to feature importance analysis of structural irreps

Due to the exhaustive nature of our DFT calculations, we would like to use our results to better understand the fundamental mechanisms underlying the relationship between the magnetic and structural trends in the rare-earth titanates. Understanding, for example, which distortion mode (corresponding to some irrep) is most important for inducing a magnetic phase transition or for controlling a particular magnetic exchange parameter, could give some insight into an underlying microscopic explanation. In this section, I explain my attempt to analyze our DFT calculations and the fundamental crux in our data set which prohibits us from completing this analysis without a substantial expansion of data.

Accounting for all of the uniaxial and biaxial strain values, we have 1,495 structures and their corresponding exchange parameters, as well as their distortion mode amplitudes. That is, within each of these structures, we have calculated the irrep mode amplitudes of five separate distortion modes (which transform as R_5^-, M_2^+, X_5^-, R_4^-, and M_3^+).

Since we would like to understand how the magnetic degrees of freedom couple to the distortion mode amplitudes, we would like to train a model which predicts the exchange parameters given a set of mode amplitudes which characterize a given structure. In the language of data science, we could use the irrep mode amplitudes as "features", which we use to predict a "target", which in our case is the magnetic exchange parameters. Two techniques which yield interpretable results (rather than the purely predictive results of most "black box" methods) are decision trees and linear/polynomial regression.

With decision trees, one can in principle determine the important features of a data set, i.e. which features have the most predictive power in obtaining a quantity of interest. In order to determine this, a decision tree creates true/false branches and at each branch determines which feature best separates the classes/values of interest. For example, one such branch of a decision tree predicting J_{xy} could state, "If $R_5^- < 2.3$, then $J_{xy} = 2$. Otherwise, $J_{xy} = 1$." In Figs. 3.17 and 3.20, we present decision trees

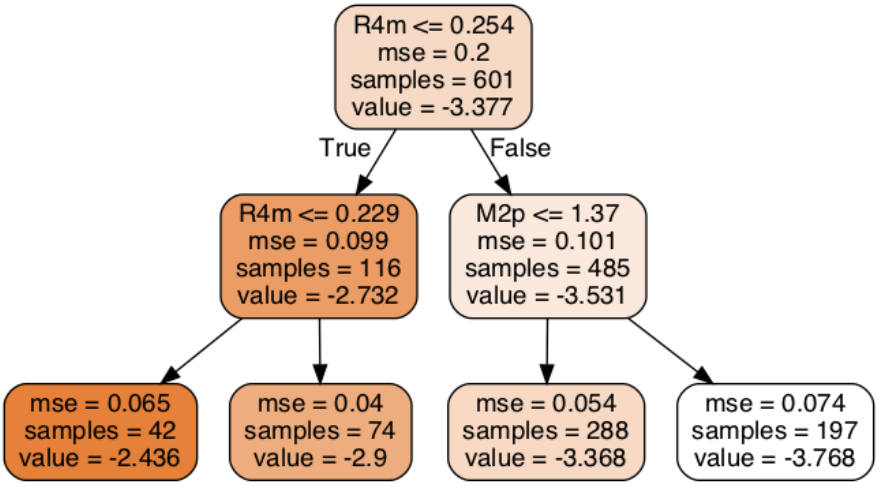

Figure 3.17: The decision tree for J_{xy}, with a depth of two.

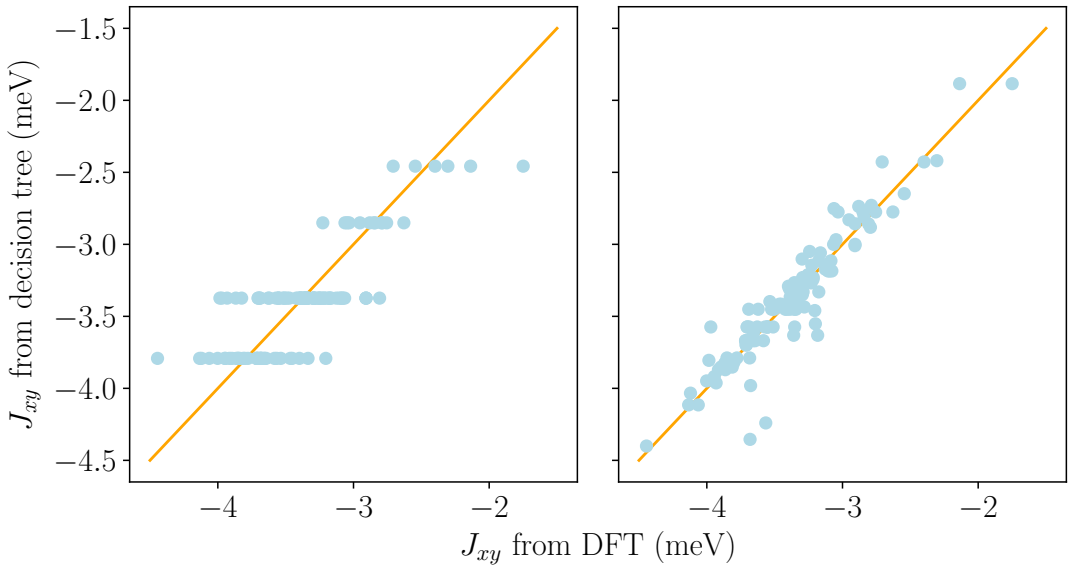

Figure 3.18: Each panel shows J_{xy} predicted from the decision tree as a function of J_{xy} extracted from DFT. We use tree depths of size two and nine for the left and right panels, respectively (see text for discussion of how to choose the optimal tree depth.) Here, only points in the testing set were used (i.e. neither decision tree was trained on any of these data points).

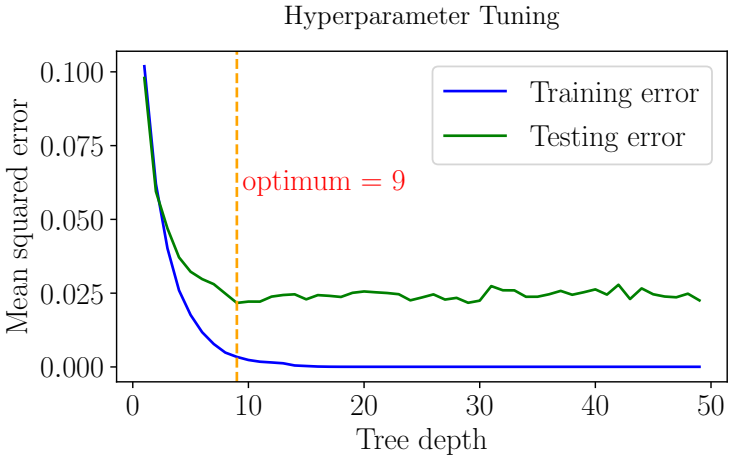

Figure 3.19: We plot the testing and training errors as a function of tree depth to find the optimal tree depth of the decision tree predicting J_{xy}.

which have been trained to predict J_{xy} and J_z from the input irrep mode amplitudes.[14] There are four values listed at each node of the decision tree. The first value is simply that which enters the true/false statement, as mentioned previously. `mse` is the mean-squared error per sample if all samples which reach the node were assigned a value of `value`, and `samples` is number of samples which reach the node. At the top of the tree, `samples` is equal to the number of structures in the training set. The mean-squared error decreases as the number of branches (and thus the number of allowed predicted values) in the decision tree increases.

In practice, the depth of the decision tree should be considered a hyperparameter of the model, which should be optimized by hand[15]. In particular, if the tree depth is too low, the decision tree does not have many values that it can predict, leading to underfitting in the model. In contrast, if the tree depth is too high, the decision tree has too many values it can predict, leading to the possibility of overfitting. Making sure that our model is not too low-complexity (prone to underfitting), nor too high-complexity (prone to overfitting), is known in machine learning as the bias-variance tradeoff [171].

[14] In making these, we specified that the trees only include two levels (i.e. a tree depth of 2) for ease of readability.

[15] In machine learning terminology, a parameter in a model is optimized during training (via gradient descent), while hyperparameters are not optimized during training, but must be optimized by hand.

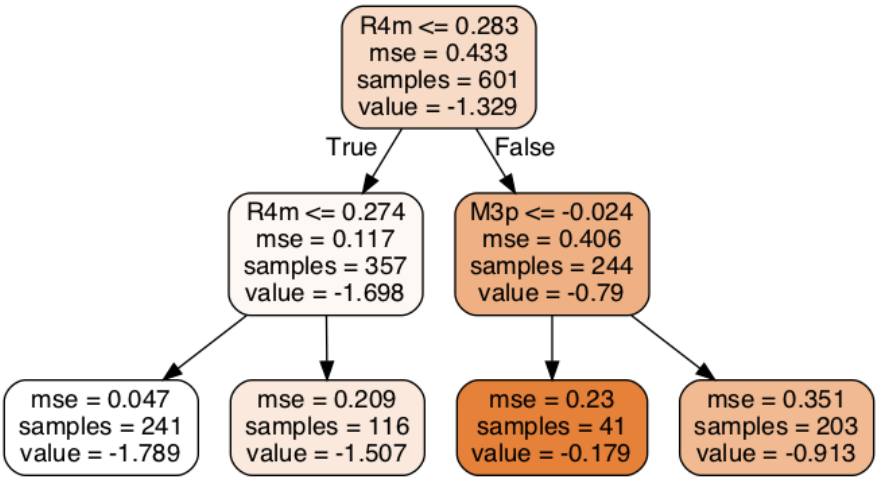

Figure 3.20: The decision tree for J_z. Here, we use a depth of two.

To find the optimal tree depth, we first split the data we have into a training set and a testing set[16]. We then train decision trees of different depths on the training set, afterwards seeing how each tree performs on the testing set. In Fig. 3.19, we show the results of this analysis, plotting the mean-squared error on the training and testing sets of the decision trees as a function of tree depth. For low values of tree depth, we see that the resulting mean-squared errors are large. This is to be expected, since as discussed above, the low-depth decision trees are incapable of predicting many values for the exchanges.

As the tree depth increases, we see that the training error monotonically decays. However, as discussed above, beyond some tree depth, small training errors are simply the result of overfitting. This is seen from the error on the testing set, which we can see does not decay with increasing tree depth (for tree depths larger than 9.) This implies that increasing the tree depth beyond 9 does not lead to a better model, and that the decay in the training error with increasing tree depth beyond this point is simply a product of overfitting on the training set. Therefore, the optimal tree depth for our decision tree is 9. To see how well our optimum-depth decision tree performs, we use our optimum-depth decision tree to predict the values of J_{xy} on the testing set. The results are plotted in the right panel of Fig. 3.18, in which we find good agreement with

[16]To be precise, we use 80% of the data for the training set, and reserve 20% of the data for the testing set.

the values extracted from DFT. For comparison, we also show the results of a decision tree with a tree depth of 2 in the left panel of Fig. 3.18.

If we take the decision trees in Figs. 3.17 and 3.20 at face value, they would tell us that the most important irrep for determining J_{xy} is the antipolar R_4^- mode, followed by the in-phase octahedral rotation mode M_2^+, and that the most important distortion in determining J_x is also the antipolar R_4^- mode, followed instead by the M_3^+ Jahn-Teller mode. Unfortunately, decision trees are notoriously sensitive to the training data, and slight changes in the training set could lead to wildly different decision trees[17]. This implies that one may not be able to trust the feature importance assigned by a trained decision tree. However, there is another, more fundamental reason that we cannot interpret these results, which I explain below after a discussion of polynomial regression.

Since the exchange parameters of the system should be should be invariant under the symmetries of the crystal, just as with the free energy, we can expand each exchange parameter in powers of the irrep mode amplitudes, just as we would with the free energy. The resulting exchange parameters are then polynomials in the mode amplitudes. Hence, this is referred to as polynomial regression[18]. Truncating this expansion at some order, we can then in principle determine the coefficients of this model using least-squares regression. If we normalize our training data so that our features (which here are the mode amplitude monomials) have equal mean and variance, we may be able to use the resulting coefficients of our trained model to interpret which feature is most important in predicting the magnetic behavior of the system. We have performed this polynomial regression analysis for J_{xy} and J_z, and present the coefficients in Figs. 3.21 and 3.23. In Fig. 3.22, we have also plotted the values of J_{xy} from our polynomial regression model vs. the values of J_{xy} obtained from DFT. We see that there is relatively good agreement between the two quantities, i.e. our polynomial regression model has predictive value. Turning to the interpretability our polynomial regression model in Figs. 3.21 and 3.23, the coefficients of our models would seem to imply that two of the most important irreps are R_4^- and X_5^-, evoking [172], which emphasized the importance of the psuedo-Jahn-Teller mode that transforms like $R_4^- X_5^-$.

[17] Models such as random forests have been developed to mitigate the drawbacks of decision trees. We refer the interested reader to Ref. [171].

[18] As an aside, we note that polynomial regression is also referred to as linear regression, since the model is linear in the undetermined coefficients.

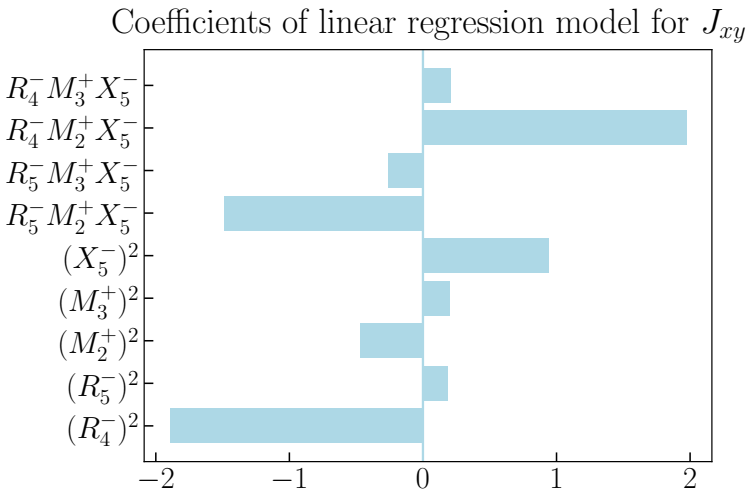

Figure 3.21: The coefficients of J_{xy} expansion terms from our polynomial (or equivalently linear) regression model.

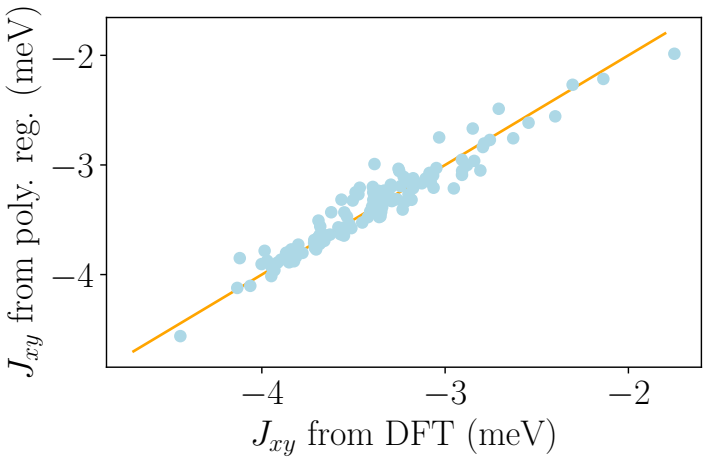

Figure 3.22: J_{xy} predicted from polynomial regression vs. J_{xy} extracted from DFT. As in Fig. 3.18, only data points from the testing set are used here.

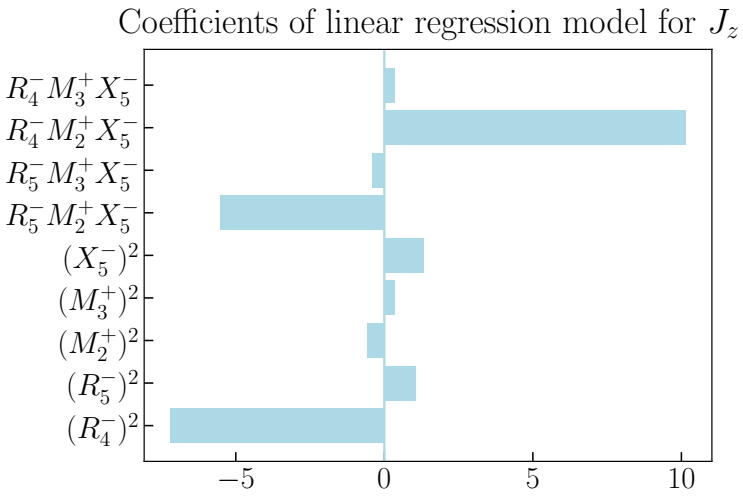

Figure 3.23: The coefficients of J_z expansion terms.

The trouble with both decision trees and the polynomial regression analysis is that the irrep mode amplitudes in our data set are not independent. In particular, all of the data we would use to train our model is determined from calculations in which the crystal structures are relaxed. Since the irrep mode amplitudes couple to one another in the free energy, the resulting values for the different mode amplitudes in a relaxed structure are highly correlated. This means that the value of one irrep mode can be predicted if one knows the values of all the other irrep modes. This leads to a significant issue: if we wish to understand which irrep is most important in predicting the magnetic properties of our system, we cannot use data with high degrees of correlations between the different features (our irrep mode amplitudes). If correlations exist between features in our training data, our model cannot distinguish which of the features is most important in predicting the exchanges, since any of the correlated features could be used to construct a model which performs well at predicting the exchange parameters. Indeed, we find that slight variations in the training data can lead to vastly different values for the resulting coefficients of in our model. In the case of the linear regression model, this means that the coefficients obtained by training the model are essentially useless, when it comes to interpretability, even if the model itself is relatively successful at predicting the targets.

The presence of a high degree of (linear) correlations is referred to as multicollinearity. We can quantify the degree of interdependence of the irrep mode amplitudes using a measure called the variance inflation factor (VIF). To define the variance inflation factor for irrep i, we construct a linear regression model to predict the mode amplitude of irrep i, using all of the other mode amplitudes. We emphasize that this new model is not concerned at all with the exchange parameters. With this, one can train the model on the structural distortion data. The variance inflation factor of the the i'th mode amplitude is then defined as

$$\mathrm{VIF}_i = \frac{1}{1 - R_i^2} \tag{3.10}$$

where R_i^2 is the square of the Pearson correlation coefficient. If R_i^2 is close to 1, then it is very easy to predict the mode amplitude of irrep i given all of the other mode amplitudes. As such, there is a high degree of multicollinearly, leading to a large VIF. As a general rule of thumb, values $\gtrsim 20$ indicate a multicollinearity problem.

We plot in Fig. 3.24 the variance inflation factors for the different irrep modes. We see that, as predicted, the values are substantial. Because of this, we cannot draw any meaningful conclusions from any type of feature analysis. We need a set of data in which the irrep mode amplitudes are independent of each other in order to do this analysis. This would require creating structures in which the mode amplitudes of each irrep are frozen in at random (but physically reasonable) values.

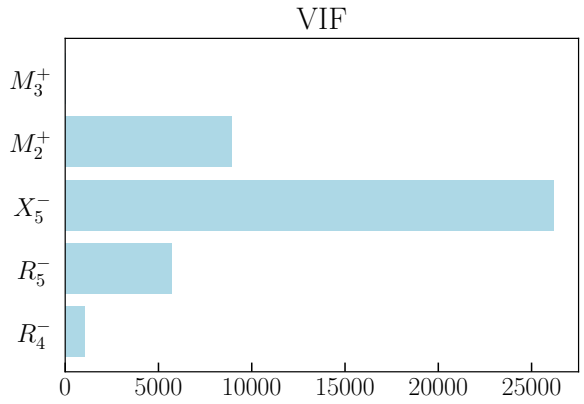

Figure 3.24: The variance inflation factor for each of irrep mode amplitudes. The degree of multicollinearity is substantial, as can be seen from the high values for these VIFs.

Chapter 4

Strain control of electronic and magnetic phase transitions in the perovskites $RTiO_3$ and $Pr_{0.5}Ca_{0.5}CoO_3$ from first-principles

This Chapter describes a series of experiments and theoretical studies on the effects of strain on the electronic and magnetic properties of two systems of perovskite transition metal oxides. Sections 4.1 and 4.2 detail two studies regarding the effects of uniaxial strain on the rare-earth titanates, and Section 4.3 focuses on the effect of biaxial strain on the perovskite $Pr_{0.5}Ca_{0.5}CoO_3$. In Sec. 4.1, I describe a study in which we investigate the effect of uniaxial strain on tuning bulk ferromagnetism in the rare earth titanates. Section 4.2 discusses a study that predicts a first-order transition between two symmetry-equivalent magnetic states in the rare-earth titanates which terminates in a critical endpoint that can be tuned through application of uniaxial strain. Finally, Section 4.3 details a study that shows that biaxial strain can be used to tune a spin and valence transition in PCCO. The work in this Chapter regarding the rare-earth titnates is published in Refs. [2, 3], and the work on $Pr_{0.5}Ca_{0.5}CoO_3$, currently under

peer review, can be found in Ref. [4].

4.1 Control of ferromagnetism in $YTiO_3$ through uniaxial strain

This section is adapted from *Uniaxial strain control of bulk ferromagnetism in rare-earth titanates* [2]. The experimental work of [2] was performed by Ana Najev and Sajna Hameed under the supervision of Martin Greven, while Zhentao Wang and I performed the theoretical calculations under the supervision of Rafael Fernandes and Turan Birol, respectively. In particular, Zhentao Wang performed mean-field theory calculations, while I performed first-principles calculations. While I provide here a brief overview of the experimental results of Ref. [2], this section is focused on the first-principles methods and results therein.

4.1.1 Introduction

Transition-metal oxides exhibit a wealth of distinct structural, magnetic and orbital ordering tendencies, and are thus among the most extensively studied condensed matter systems. A salient feature of these materials is an intricate interplay between structural and electronic properties: ferroelectric, metal-insulator and superconducting transitions can all be strongly influenced by changes in the crystalline lattice. Importantly, the electronic ground states can thus be tuned by manipulating the structure. This has been employed in a wide range of materials, and led to significant breakthroughs, with the emergence of uniaxial strain as a particularly interesting control variable [105, 110, 173, 174, 106, 107, 175, 108, 109, 111, 112]. Prominent examples include the stabilization of ferroelectricity in epitaxially-strained films of strontium titanate [105], as well as uniaxial stress manipulation of superconductivity in strontium ruthenate [106, 107, 175], metal-insulator transitions in vanadium oxides [108, 109], superconductivity and charge-density-wave order in cuprates [110, 111], and antiferromagnetism in pnictides [112]. However, this approach has so far relied either on the proximity to a structural instability, or on the strain-induced lowering of structural symmetry, and it has not yet been applied to bulk ferromagnetic (FM) materials.

The trivalent rare-earth (RE) titanates $RTiO_3$ (R is a rare-earth ion) are prototypical three-dimensional Mott insulators [104] with rich phase diagrams (Fig. 4.1(a)) that are not fully understood. The R ion is surrounded by eight TiO_6 octahedra [176], but due to a considerable atomic-size mismatch, the lattice symmetry is orthorhombic ($Pbnm$), significantly lower than the ideal cubic perovskite. The TiO_6 octahedra are both tilted and rotated, and the distortions are more pronounced for smaller R ions, leading to larger deviations of the Ti-O-Ti bond-angle from 180° [176] (Fig. 4.1(c)). Since the orbital overlap strongly depends on the bond angles, so does the superexchange interaction between unpaired electron spins associated with the Ti 3d t_{2g} orbitals. Consequently, the spin-lattice coupling is strong [177, 145, 178], and the magnetism in RE titanates can be tuned by varying the average R-ion size: the magnetic ground state changes from FM to antiferromagnetic (AFM) with increasing R-ion size [179, 180], or upon atomic substitution, e.g., in $Y_{1-x}La_xTiO_3$ (YLTO) [181, 182] (Fig. 4.1(a)).

The nonmagnetic symmetry of the RE titanate perovskites is low enough to preclude any collinear magnetic order. As a result, spin canting is present in both the FM and G-type AFM phases. In particular, both the predominantly FM $YTiO_3$ and the predominantly G-type AFM $LaTiO_3$ belong to the same magnetic space group, with a G-type AFM moment along the orthorhombic a-axis and a FM moment along the orthorhombic c-axis [126, 5, 178]. No long-range structural changes are known to occur around the Curie and Neel temperatures, but due to the strong and anisotropic spin-lattice coupling, the effects uniaxial stress on T_C are expected to be significant.

Charge doping can also be used to control the magnetic ground state, e.g., in $Y_{1-y}Ca_yTiO_3$ (YCTO), where hole doping destroys the long-range FM order at $y \sim 20\%$, and eventually leads to an insulator-metal transition [183, 184]. Based on the behavior of thermal expansion coefficients across the magnetic transitions, it has been suggested that uniaxial strain might have an effect similar to atomic substitution; strain along the orthorhombic a direction should increase the octahedral distortions, stabilize the FM order, and increase the Curie temperature (T_C), whereas strain along b should decrease the distortion and T_C , similar to the substitution of Y with La (Fig. 4.1(c)) [177].

In Ref. [2], my coauthors show that the Curie temperature of YTO-based materials can be manipulated via *in situ* uniaxial stress in a remarkably wide range. Ref. [2]

presents results on both La- and Ca-substituted YTO, in the substitution range in which a FM ground state is observed (Fig. 4.1(a)), and demonstrates that T_C can be reversibly and continuously suppressed or enhanced by up to a factor of ~ 2[1], depending on the specific crystalline direction in which the uniaxial stress is applied, with nearly complete suppression of ferromagnetism in a Ca-substituted sample close to the FM-paramagnetic phase boundary. Ref. [2] thus demonstrates the potential of uniaxial stress engineering of oxygen octahedral rotations, which are present in most perovskite-based oxides, as a practical means to manipulate magnetism and induce quantum phase transitions. In this chapter, I focus on the ab initio and mean-field calculations, which suggest that the origin of the observed behavior is the strong effect of stress on the octahedral rotation distortions, and the pronounced sensitivity of the magnetic exchange couplings on these distortions. For a more complete overview of the experimental details, as well as a discussion of the Ca-doped YTO compounds, I refer the reader to Ref. [2].

4.1.2 Methods

DFT calculations were performed using the projector augmented wave (PAW) formalism as implemented in the Vienna ab initio Simulation Package (VASP) [91, 92, 93]. The structures were relaxed in the $\sqrt{2}\times\sqrt{2}\times2$ primitive cell. In order to obtain the exchange parameters, we use a $2\sqrt{2}\times2\sqrt{2}\times2$ supercell to accommodate the symmetry-inequivalent in-plane next-nearest-neighbor exchanges. A plane wave cutoff energy of 550 eV and a k-point grid of $4\times4\times4$ for the 20 atom orthorhombic cell or its equivalent for larger cells were used. The PBEsol generalized gradient approximation (GGA) was used for the exchange correlation energy, and the DFT+U correction with $U = 4$ eV was included in order to ameliorate the shortcomings of GGA on the titanium 3d orbitals [32, 36]. Uniaxial strain was simulated by fixing the lattice parameter along an orthorhombic direction and relaxing the internal coordinates of the atoms, as well as the two other lattice parameters. Uniaxial strain was converted to stress by using the calculated stress on the unit cell along the corresponding axis. The structures were relaxed until the energy differences between ionic steps were smaller than 10^{-6} eV. All calculations are performed in the orthorhombic *Pbnm* space group, as uniaxial strain applied along

[1]The most dramatic reduction in T_C was for 20% La-substituted YTO, in which a factor of ~ 2 reduction in T_C was obtained with 0.7 GPa of stress applied along the *b*-axis.

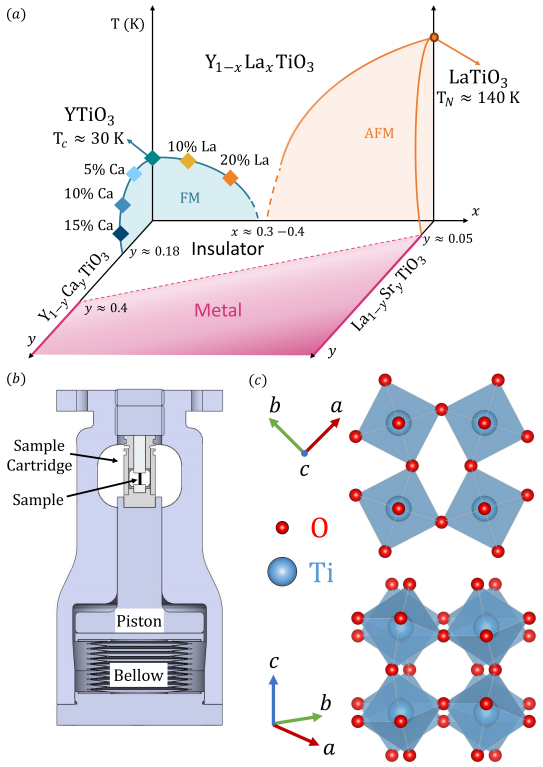

Figure 4.1: (a) Phase diagram of $RTiO_3$ with FM (ferromagnetic), AFM (antiferromagnetic), insulating, and metallic phases. (b) Schematic of the uniaxial strain cell (for more details, see Ref. [2]). (c) $YTiO_3$ structure figures constructed from theory. The red spheres are the oxygen ions, the blue spheres are the titanium ions. The upper figure shows the oxygen base plane with the $a^0a^0c^+$ rotation mode. The bottom figure shows a different orientation with the $a^-a^-c^0$ rotation mode. The effects of uniaxial stress along a ([100]), b ([010]) or c ([001]) on the rotation modes are clearly strong and anisotropic. Figure reproduced from [2].

the orthorhombic axes do not reduce the symmetry of the crystal.

In order to determine the magnetic exchange interactions, the energies of 20 different magnetic configurations were calculated for each stress value. The spin configurations were chosen to capture a wide range of energies and total magnetizations. These energies were in turn used to fit the exchange parameters to a Heisenberg model that has two different nearest neighbor exchange parameters. This Hamiltonian is justified because: 1) spin-orbit coupling, which is expected to be weak in this system, was not taken into account, so there are no Dzyaloshinskii-Moriya type terms; 2) $YTiO_3$ is a Mott insulator, $U/t \gg 1$, implying that higher-order terms are small; and 3) despite the small number of free parameters used in our model, we find good agreement with DFT-calculated energies for a large number of spin configurations, and a value of R^2 close to 1. The behavior of the exchange parameters are shown in Fig. 4.3. We note that the next-nearest-neighbor exchanges (denoted by J_a, J_b, and J_{znnn} in the inset) are significantly smaller than the nearest-neighbor exchanges in magnitude. Moreover, we find that the trends of T_C as a function of stress are not significantly affected if we exclude the next-nearest-neighbor interactions. All irrep mode amplitudes were calculated using the ISODISTORT tool from the Isotropy Software Suite [60].

All experimental results were obtained using a uniaxial pressure-cell design which enables the application of high and spatially homogeneous uniaxial stress [185, 186]. For more details regarding the experimental setup, see Ref. [2] and its corresponding Supplemental Material.

4.1.3 Results

Figure 4.2(c) summarizes the Curie temperatures of all measured YTO samples as a function of uniaxial stress along the orthorhombic axes. We note that the trends observed here agree with that of Ref. [177]. In particular, stress along b and c decreases T_C, whereas compression along a promotes ferromagnetism and increases T_C.

In order to model the observed stress dependence of T_C and to elucidate the connection between the crystal structure and magnetic interactions, we performed first-principles DFT calculations for $YTiO_3$ to predict the crystal structure and the exchange parameters for a Heisenberg model under uniaxial stress along each of the orthorhombic principal axes. Calculations for doped systems were not performed due to the

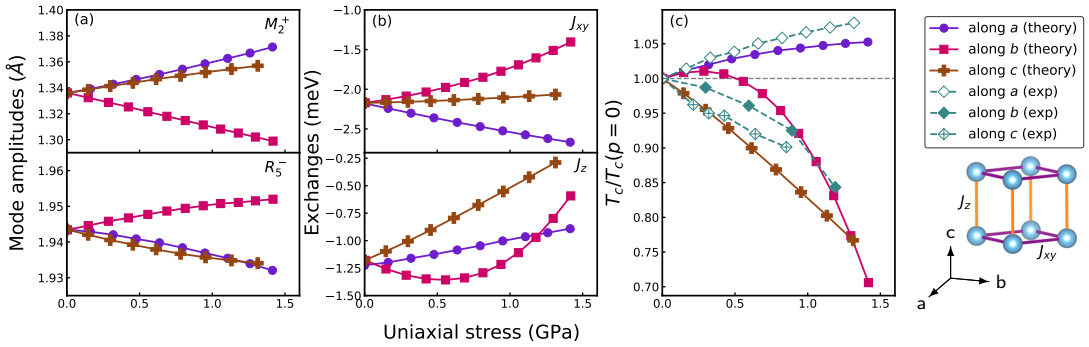

Figure 4.2: DFT results for $YTiO_3$ as a function of compressive uniaxial stress along a, b, and c. (a) Mode amplitudes of the octahedral rotations corresponding to the M_2^+ and R_5^- irreps in $YTiO_3$. (b) Nearest-neighbor exchange parameters J_{xy} and J_z obtained from fits to the Heisenberg model. (c) Mean-field Curie temperatures using the DFT-obtained exchanges, including the sub-leading next-nearest-neighbor exchanges, along with experimental results for $YTiO_3$. For reference, the Curie temperature of unstrained $YTiO_3$ is ∼30K.

exceedingly high numerical cost. However, we believe the qualitative results observed in the undoped system should also apply to doped compounds (see Ref. [2] for more details.) Note that previous studies have shown the suitability of a simple nearest-neighbor Heisenberg model to capture most of the spin-wave dispersion properties [126]. Here, our main modifications are to allow for the exchange interaction to differ along in-plane and out-of-plane directions, i.e. $J_{xy} \neq J_z$ (see inset of Fig.4.2) and to include sub-leading next-nearest-neighbor interactions (see Fig. 4.3). We present the behavior as a function of uniaxial strain applied along the three orthorhombic axes of the nearest-neighbor and next-nearest-neighbor exchanges the DFT-calculated exchanges in Fig. 4.3. We note that for almost all values of strain, the next-nearest-neighbor exchanges are significantly smaller than the nearest-neighbor exchanges. However, we include the next-nearest-neighbor interactions in our calculation of T_C, finding that their inclusion leads to better agreement with the trends observed experimentally. We also note that we obtain the trends in the exchanges as a function of both compressive and tensile uniaxial strain. The trends observed in the case of tensile uniaxial strain may be relevant for future experiments.

We focus on the two types of octahedral rotations in $YTiO_3$, namely the $a^0a^0c^+$ and

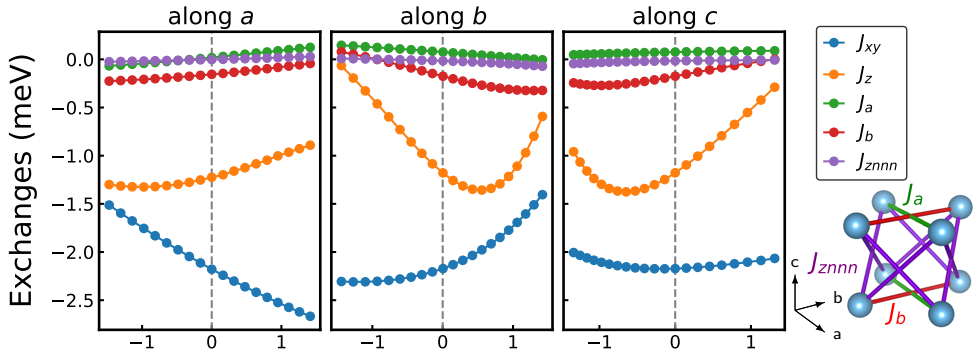

Figure 4.3: Nearest-neighbor and next-nearest-neighbor exchange parameters extracted from DFT as a function of uniaxial stress (in GPa) along the $a = [100]$, $b = [010]$, and $c = [001]$ axes. The next-nearest-neighbor exchanges are defined in the inset.

$a^-a^-c^0$ rotation modes (Fig. 4.1(c)) in Glazer notation, which transform, respectively, as the irreducible representations (irreps) M_2^+ and R_5^- of the space group $Pm\bar{3}m$. We characterize the distortion magnitudes according to their irrep mode amplitudes, that may be understood as follows: Consider some general distortion of a crystal, described as a vector of atomic displacements. To determine the extent to which this distortion is composed of a particular octahedral rotation mode (corresponding to a particular irrep), we calculate the inner products of the total distortion vector with the irrep vectors. This then projects out the weight corresponding to the octahedral rotations, and the magnitude of the inner product is defined as the irrep mode amplitude. As one may expect, these mode amplitudes are proportional to the corresponding octahedral rotation modes, and for small distortions are also proportional to the rotation angles. However, angles can become ill-defined for sufficiently distorted structures, while the irrep mode amplitudes are always well-defined.

We find that the two types of rotations have opposite trends under uniaxial stress along different axes (Fig. 4.2(a)): the M_2^+ rotation angle decreases under compressive stress along b, but increases under compressive stress along a and c. The magnitude of the R_5^- distortions has the opposite trend, as it increases under compressive stress along the b axis. Moreover, the amplitude of the R_5^- distortions is less sensitive to uniaxial stress. Given the low structural symmetry and complex multi-tilt system, it is

not straightforward to intuitively grasp the tilt behavior with applied stress.

The changes in the octahedral rotations alter the Ti-O-Ti angles, which in turn significantly alters the magnetic exchange interactions [187, 188], as shown in Fig. 4.2(b). For stress along a, both nearest-neighbor exchange interactions J_{xy} and J_z vary almost linearly with stress, with J_{xy} increasing in magnitude, whereas the magnitude of J_z decreases. We also find that J_{xy} is more sensitive to stress than J_z. This, in addition to the larger number of J_{xy} vs. J_z bonds, results in an increase of mean field T_C for stress along a, as shown in Fig. 4.2(c).[2] For stress along c, J_{xy} remains mostly unchanged while J_z decreases in magnitude almost linearly, which results in a suppression of T_C with stress (Fig. 4.2(c)). Finally, for uniaxial stress along b, $|J_{xy}|$ decreases while $|J_z|$ first increases with stress. These two competing behaviors lead to a slight increase in T_C for smaller stress values, as indeed also observed in experiment. Yet T_C decreases rapidly under larger values of stress as $|J_z|$ also decreases. As shown in 4.2(b) and 4.2(c), in all three cases the first-principles calculations agree well with the experimentally observed relative change in T_C. This shows that the effect of stress on the magnetic properties can be explained by the crystal's structural changes, and that it is mediated by the octahedral rotations.

As mentioned above, we also performed DFT calculations on $YTiO_3$ under uniaxial tensile strain along each orthorhombic crystallographic axis. The complete results for these calculations are shown in Fig. 4.4. We see that for sufficiently large tensile strain along all three orthorhombic axes leads to a rapid drop in T_C. Moreover, for tensile strain applied along the c-axis, we predict non-monotonic behavior in T_C, as highlighted by the maximum seen in T_c.

4.1.4 Discussion and Conclusion

To conclude, we have shown that the FM transition in RE titanates can be continuously tuned using uniaxial stress. Additionally, we provide a microscopic understanding of the underlying coupling between structural distotions, orbital overlap, and effective spin interactions. The remarkable agreement between measured and calculated changes of T_C with stress shows that the intricate octahedral distortions and their influence on

[2]The mean-field T_C obtained from our Heisenberg model is $T_c = -\frac{2}{3}(2J_{xy} + J_a + J_b + J_z + 4J_{znnn})$. For an overview of this calculation, we refer the reader to Sec. 1.3.3.

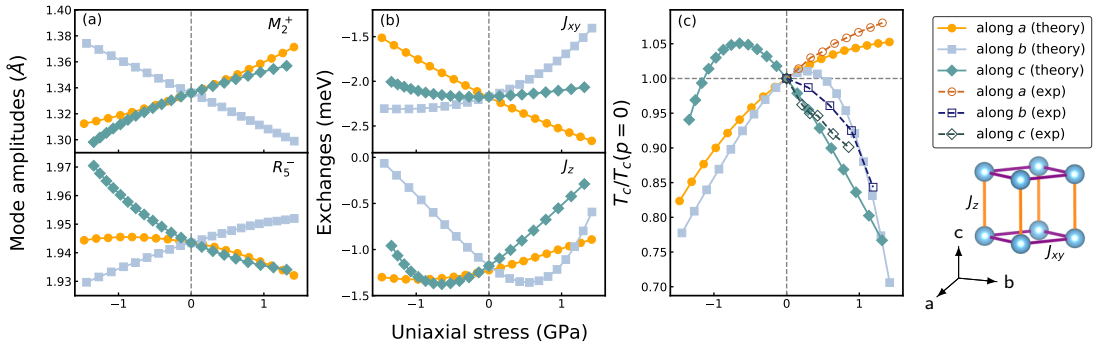

Figure 4.4: We present the (a) mode amplitudes, (b) nearest-neighbor exchange parameters, and (c) mean-field Curie temperatures of $YTiO_3$ as a function of uniaxial stress along the $a = [100]$, $b = [010]$, and $c = [001]$ axes, as in Fig. 4. However, here we include results for both tensile and compressive stress.

the superexchange are well captured by our first-principles calculations. The strong and anisotropic stress response does not rely on a nearby structural instability, which implies that these and related materials have tremendous potential for strain engineering of magnetism, including through the use of epitaxial strain and/or in heterostructures. Indeed, first-principles calculations have predicted strong effects of lattice strain on magnetism in manganite and vanadate oxides [189, 190, 191], although experimental work is still scarce and mostly focused on epitaxial strain in thin films. Additionally, in cobaltates, hydrostatic pressure seems to have a significant effect on the bandwidth and magnetic order [192, 193]. Thus, uniaxial stress could be an important parameter in exploring the complex nature of magnetic transition metal oxides. Finally, our work opens the possibility to study the (quantum) phase transitions between the FM, AFM and paramagnetic ground states using highly homogeneous uniaxial stress as a control variable.

4.2 Strain-induced transition between symmetry-equivalent phases in the rare-earth titanates

This section is adapted from *Strain-tunable metamagnetic critical endpoint in Mott insulating rare-earth titanates* [3]. In Ref. [3], Zhentao Wang and I performed theoretical calculations, under the supervision of Rafael Fernandes and Turan Birol, respectively. In particular, Zhentao Wang performed Ginzburg-Landau calculations, while I performed the group theory analysis and first-principles calculations.

4.2.1 Introduction

Rare-earth titanates are Mott insulators whose magnetic ground state– antiferromagnetic (AFM) or ferromagnetic (FM) – can be tuned by the radius of the rare-earth element. Here, we combine phenomenology and first-principles calculations to shed light on the generic magnetic phase diagram of a chemically-substituted titanate on the rare-earth site that interpolates between an AFM and a FM state. Octahedral rotations present in these perovskites cause the AFM order to acquire a small FM component – and vice-versa – removing any multicritical point from the phase diagram. However, for a wide parameter range, a first-order metamagnetic transition line terminating at a critical end-point survives inside the magnetically ordered phase. Like the liquid-gas transition, a Widom line emerges from the end-point, characterized by enhanced fluctuations. In contrast to metallic FMs, this metamagnetic transition involves two symmetry-equivalent and insulating canted spin states. Moreover, instead of a magnetic field, we show that uniaxial strain can be used to tune this transition to zero temperature, inducing a quantum critical endpoint.

Magnetic quantum phase transitions (QPT) are often associated with exotic phenomena [194], from strange metallic behavior to possible deconfined quantum criticality [195, 196, 197, 198, 199, 200, 201]. Mott insulating perovskites, such as cuprates, iridates, ruthenates, and titanates, are promising candidates to study such QPTs, since many of the pristine compounds display some type of antiferromagnetic (AFM) order [202, 203]. To suppress the AFM transition temperature and attempt to induce a QPT, it is often necessary to dope the compounds, which also favors a metallic state over the Mott phase.

A remarkable exception are the rare-earth titanates, $A\mathrm{TiO}_3$, where A denotes a rare-earth element [104]. By changing the ionic radius of A, the ground state interpolates between an AFM (of the G-type, i.e. a Néel antiferromagnet) Mott insulating phase for larger radii (from Sm to La) and a ferromagnetic (FM) Mott insulating phase for smaller radii (from Yb to Gd) [182, 179, 181, 180, 204, 205, 206], see Fig. 4.5. While the magnetism arises from the Ti^{3+} $3d^1$ state, the size of A strongly affects the rotations of the TiO_6 octahedra, which in turn impact the Ti orbital degrees of freedom [177]. The latter are believed to drive the change from AFM to FM, although the precise mechanism remains under debate [132, 136, 207, 146, 145, 104, 172].

This phenomenology suggests a potential path to realize magnetic QPTs while remaining inside the Mott insulating state via isovalent chemical substitution on the rare-earth site [208, 209], such as in $\mathrm{Sm}_{1-x}\mathrm{Gd}_x\mathrm{TiO}_3$ [204] and $\mathrm{Y}_{1-x}\mathrm{La}_x\mathrm{TiO}_3$ [182, 181, 205, 206]. In principle, there are several possibilities for magnetic QPTs: split transitions from either the AFM or the FM phase to the paramagnetic (PM) phase; split transitions from the AFM or FM phases to a coexistence AFM+FM state; a single first-order AFM to FM transition; or a single second-order AFM to FM transition, which would require fine tuning of parameters.

There is, however, one important ingredient that qualitatively changes this scenario: the ATiO_3 compounds are not cubic, but orthorhombic, due to the pattern of the TiO_6 octahedral rotations shown in Fig. 4.6(a). The corresponding *Pbnm* crystal structure generally promotes an admixture between the AFM and FM order parameters [5, 166], indicating that most, if not all, ATiO_3 pristine compounds display the same mixed AFM+FM phase – a canted spin state, as shown in Fig. 4.5. At first sight, this seems to challenge the notion that a QPT can be induced via substitution on the rare-earth site: since the phases of the end compounds are symmetry-equivalent, the only difference is on the relative amplitudes between the AFM and FM order parameters (and therefore on the canting angle).

In this paper, we combine a phenomenological analysis with first-principles calculations to show that this is not the case, and that a metamagnetic quantum critical end-point (QCEP) could still be realized, particularly in the phase diagrams of $\mathrm{Sm}_{1-x}\mathrm{Gd}_x\mathrm{TiO}_3$ and $\mathrm{Y}_{1-x}\mathrm{La}_x\mathrm{TiO}_3$ [182, 179, 181, 180, 204, 205, 206]. The key point is that the staggered rotation between neighboring TiO_6 octahedra, known as the R_5^- mode

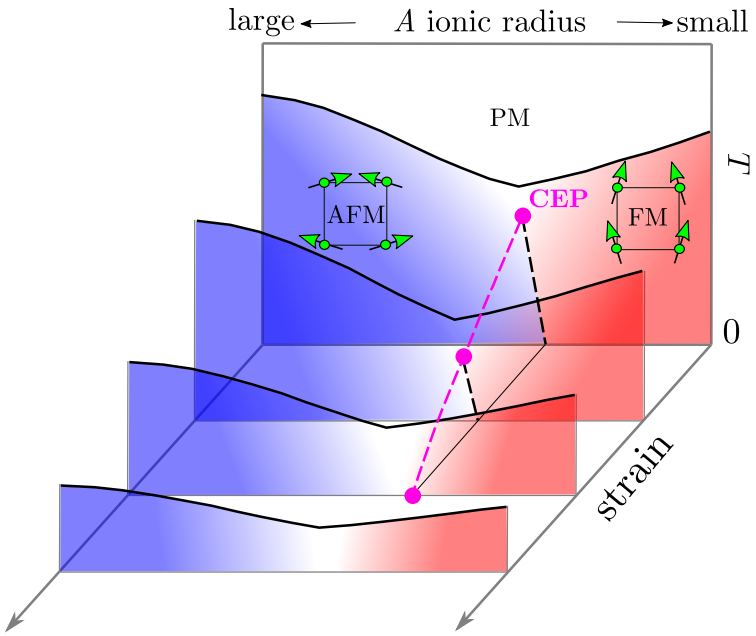

Figure 4.5: Schematic magnetic phase diagram of Mott insulating rare-earth titanates $A\mathrm{TiO}_3$ as a function of applied uniaxial strain. The horizontal axis refers to the average rare-earth radius in both stoichiometric and chemically-substituted compounds such as $\mathrm{Sm}_{1-x}\mathrm{Gd}_x\mathrm{TiO}_3$ and $\mathrm{Y}_{1-x}\mathrm{La}_x\mathrm{TiO}_3$. At low temperatures, the transition between the AFM-dominated (blue-shaded) and the FM-dominated (red-shaded) states is first-order. Due to the TiO_6 octahedral rotations, however, the first-order line (black dashed line) terminates at a critical end-point (CEP, magenta dot) before reaching the PM phase boundary. The CEP can in principle be tuned to $T = 0$ by external strain, resulting in a quantum critical end-point (QCEP). The green arrows show schematically the canted spin configurations in the AFM-dominated and FM-dominated states. Figure reproduced from Ref. [3].

and illustrated in the right panel of Fig. 4.6(a), causes an admixture of the AFM and FM order parameters. Microscopically, this effect arises from the changes in the orbital level splittings promoted by the octahedral rotations, which in turn induce magnetic exchange anisotropies. Because of this admixture, the would-be first-order transition line from the AFM to the FM state splits from the PM phase boundary, as shown schematically in Fig. 4.5. This first-order line, denoted by the dashed line in Fig. 4.5, ends in a critical end-point (CEP, pink dot in Fig. 4.5), above which a Widom line emerges, analogous to the liquid-gas phase transition [210, 211, 212].

The relevant order parameter associated with this transition is not the individual AFM or FM order parameters, but the canting angle θ between the uniform and the staggered magnetizations. As illustrated in Fig. 4.5, θ changes from $\theta \gtrsim 0$ deep inside the AFM-dominated phase to $\theta \lesssim \pi/2$ inside the FM-dominated phase. While θ changes continuously when the phase diagram is traversed above the CEP (but below the magnetic ordering temperature), it undergoes a first-order jump below the CEP, signaling a metamagnetic transition. Such a metamagnetic transition, driven by octahedral rotations of a Mott insulator and characterized by a jump in the canting angle, is an unexplored counterpart of the widely studied magnetic-field-driven metamagnetic transition that occurs in metallic ferromagnets, which is signaled by a jump in the uniform magnetization [213]. Remarkably, while the latter can be tuned to $T = 0$ by a magnetic field, we show that the CEP uncovered here can be tuned to a quantum critical end-point (QCEP) by uniaxial strain. This result is a direct consequence of the sensitivity of the octahedral rotation mode amplitude to strain, which we demonstrate using first-principles calculations [Fig. 4.6(b)]. Because strain has been routinely applied in strongly correlated systems via a variety of experimental setups [214, 107, 215, 185, 186] – including recently in rare-earth titanates [2], our results provide a concrete recipe to promote a QCEP in Mott insulating, magnetically ordered perovskites.

4.2.2 Methods

In the following, we employ a Ginzburg-Landau approach to construct the free energy of the system.[3] As such, we begin by reviewing the structure of the rare-earth titanates as well as its symmetries.

[3]For an introduction to the Ginzburg-Landau approach, see Sec. 1.2.6.

Group-theory analysis

The perovskite rare-earth titanates crystallize in space group #62 due to the combination of two symmetry-inequivalent rotation patterns of the TiO_6 octahedra. As illustrated in Fig. 4.6(a), these rotations transform as the M_2^+ irrep and the R_5^- irrep of the $Pm\bar{3}m$ space group. The pattern corresponding to the M_2^+ irrep has TiO_6 octahedra which rotate about a single cubic axis, while the rotation pattern corresponding to the R_5^- irrep is composed of a combination of octahedral rotations about both of the remaining cubic axes. Using Glazer notation, we denote these two patterns as $a^0a^0c^+$ and $a^-a^-c^0$, respectively. Since these rotations lower the cubic symmetry, we are free to choose any of the three cubic axes as the axis corresponding to the M_2^+ irrep. In the resulting distorted structure, this axis points along the longest of the orthorhombic lattice vectors. If we choose this axis to be $\boldsymbol{c}$, as we have here, then the resulting $a^-a^-c^+$ tilting pattern takes the $Pm\bar{3}m$ cubic symmetry to the $Pbnm$ setting of space group #62.

Had we chosen the long axis to point along $\boldsymbol{b}$ (Glazer tilting pattern $a^-c^+a^-$), we would have the standard $Pnma$ setting of the same space group. The basis transformation from the standard setting $Pnma$ to the non-standard $Pbnm$ is defined by [5]:

$$\{\boldsymbol{a}_n, \boldsymbol{b}_n, \boldsymbol{c}_n\} = \{\boldsymbol{a}_s, \boldsymbol{b}_s, \boldsymbol{c}_s\}P, \tag{4.1}$$

where

$$P = \begin{pmatrix} 0 & 1 & 0 \\ 0 & 0 & 1 \\ 1 & 0 & 0 \end{pmatrix} \tag{4.2}$$

and the subscripts s and n denote the lattice vectors in the standard and nonstandard settings respectively.

Using standard group-theory techniques and the Isotropy Software Suite [216, 62], we determine how the two types of octahedral rotations, M_2^+ and R_5^-, couple the FM order parameter to the three types of AFM order parameters (G-type, C-type, and A-type) in the free energy, see also Ref. [5]. One can show that the FM order parameter transforms as $m\Gamma_4^+$ with respect to symmetry operations of the cubic $Pm\bar{3}m$ space group, while the G-type AFM order parameter transforms as mR_5^-. Here, the prefix m allows us

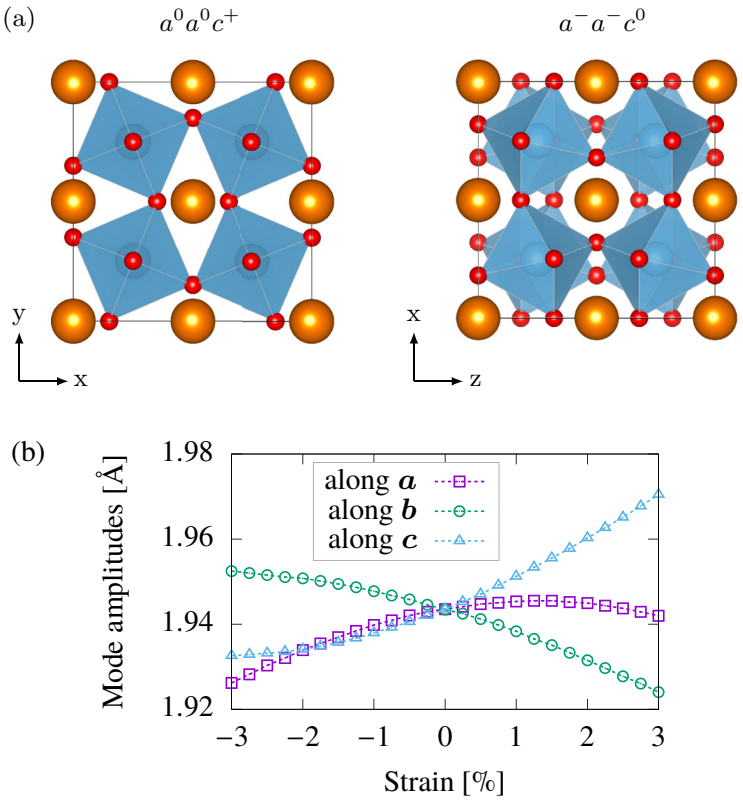

Figure 4.6: (a) Schematics of the two types of octahedral rotation patterns in rare-earth titanates: in the Glazer notation, they are the $a^0a^0c^+$ pattern (left, which transforms like M_2^+), and the $a^-a^-c^0$ pattern (right, which transforms like R_5^-). Here x, y, z refer to the cubic axes. (b) Change in the amplitude of the R_5^- mode as a function of uniaxial strain along three different orthorhombic axes of $YTiO_3$. Figure reproduced from Ref. [3].

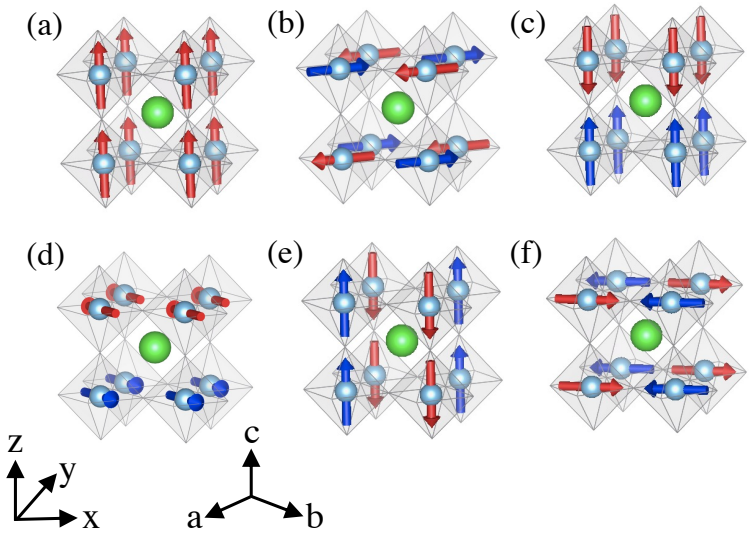

Figure 4.7: The magnetic orders considered in this letter, corresponding to the (a) $m\Gamma_4^+$ (FM order), (b) mR_5^- (G-type AFM order), (c) mX_1^- (A-type AFM order), (d) mX_5^- (A-type AFM order), (e) mM_2^+ (C-type AFM order), and (f) mM_5^+ (C-type AFM order) irreps of the cubic $Pm\bar{3}m$ space group. The blue spheres correspond to Ti atoms and the green, to the rare-earth atoms.

denote magnetic irreps, as opposed to irreps corresponding to atomic displacements, which transform differently under mirror reflections and inversion. These irreps are three-dimensional, since the magnetic moments can point along any of the three axes, and the stars of Γ and R contain only one wave vector. The order parameters described by these irreps are shown in Figs. 4.7(a) and 4.7(b).

The A-type AFM order parameters have the wave vector $X = (\pi/a, 0, 0)$, which has 3 vectors in its star. For each of these wave vectors, the magnetic moments can point along 3 orthogonal directions, and as a result, there are 9 possible A-type AFM orders. These orders correspond to the three-dimensional irrep ${}^*mX_1^-$, in which the magnetic moments align along the wave vector direction, and the six-dimensional irrep ${}^*mX_5^-$, in which the magnetic moments align perpendicular to the wave vector. We use the * symbol to differentiate the representations of the space group, which contain all vectors in the star of a wavevector, from the representations of the little group. For a single wave vector in the star, the magnetic little group representations mX_1^- and mX_5^- are one and two dimensional, respectively. These modes are depicted in Figs. 4.7(c) and 4.7(d). Similarly, the C-type AFM orders, which have one of the three wave vectors in the star of $M = (\pi/a, \pi/a, 0)$, are described by the magnetic space group irreps ${}^*mM_2^+$ (three dimensional), and ${}^*mM_5^+$ (six dimensional), which have magnetic little group irreps mM_2^+ and mM_5^+ that are one and two dimensional, respectively [Figs. 4.7(e) and 4.7(f)].

Obtaining the relevant order parameter directions

Thus far, we have obtained the irreps which correspond to our magnetic order parameters. We would like to understand how these irreps couple to one another and to the R_5^- and M_2^+ octahedral distortions in the free energy. However, we specialize to the symmetry of $RTiO_3$, which as discussed above, has space group $Pbnm$ in both the non-magnetic and magnetically ordered phases [126]. This restricts the possible directions of the various magnetic moments which we would like to consider in the free energy. In particular, stipulating that the resulting system has space group $Pbnm$ places constraints on the possible order parameter directions (OPDs) of our irreps. Since the OPD

of the structural irreps are already known[4], we only need to obtain the OPDs of the magnetic irreps. For concreteness, we take the $m\Gamma_4^+$ irrep corresponding to the ferromagnetic order, the mR_5^- irrep corresponding to G-type AFM order, and the mX_5^- irrep corresponding to A-type AFM order. This is relevant for the behavior experimentally observed in the $RTiO_3$ compounds [126].

Specializing to this example, we now obtain the OPDs of the $m\Gamma_4^+$, mR_5^-, and mX_5^- irreps. To do so, we insert our magnetic and structural irreps (R_5^- and M_2^+) into the ISOSUBGROUP software, which loops through the possible OPDs for the inputted irreps and compiles a list of space groups for the corresponding structures. We then determine the relevant OPDs of our magnetic irreps by searching for the structure with the correct OPDs for the R_5^- and M_2^+ irreps as well as the desired $Pnma$ space group. The resulting OPDs are listed in Tab. 4.1 in the $G_aA_bF_c$ column. The subscripts correspond to the directions of the magnetic moments, which point along the orthorhombic directions. Here, a, b, and c correspond to the orthorhombic directions in the $Pbnm$ setting.[5]

In Tab. 4.1, we have also listed the OPDs for the $F_aC_bG_c$ magnetic ground state, which could be stabilized in the case of some other magnetic $Pnma$ perovskite.[6]

4.2.3 Obtaining the terms in the Free Energy

Using the OPDs obtained above, we now use the INVARIANTS software [59] to obtain the symmetry-allowed terms in the free energy, which will be various products of the amplitudes for our given irreps. The results are shown in Table 4.2.

For a term to exist in the free energy, the term must be invariant under all operations of the symmetry group (here the space group $Pm\bar{3}m$). One simple consequence of this is that the wavevectors in a given term must sum to 0 modulo reciprocal lattice vectors, so that the term is invariant under translations. One can verify that all terms in Table

[4]To uniquely determine the OPDs of the magnetic irreps, we recall that the tilting pattern in the rare-earth titanates is $a^-a^-c^+$. This corresponds to an out-of-phase (R_5^-) rotation about the x and y axes, and an in-phase rotation M_2^+ rotation about the z axis. This implies that the OPD for the R_5^- distortion is $(1,1,0)$ and the OPD for the M_2^+ distortion is $(0,0,1)$.

[5]This is the same notation used in Ref. [5], except the subscripts x, y, and z have been replaced with a, b, and c. This is because we use x, y, and z to refer to the cubic axes, and a, b, and c to refer to the orthorhombic axes.

[6]Ref. [166] uses the $Pnma$ setting to denote the different magnetic ground states and one should be careful comparing their results to those listed here.

Distortions	$G_aA_bF_c$	$F_aC_bG_c$
$\mathbf{R_5^-} = R_5^-(1,1,0)$	$\mathbf{mR_5^-} = G_a(1,1,0)$	$\mathbf{m\Gamma_4^+} = F_a(1,1,0)$
$\mathbf{M_2^+} = M_2^+(0,0,1)$	$\mathbf{mX_5^-} = A_b(0,0;0,0;1,-1)$	$\mathbf{mM_5^+} = C_b(0,0;0,0;1,-1)$
	$\mathbf{m\Gamma_4^+} = F_c(0,0,1)$	$\mathbf{mR_5^-} = G_c(0,0,1)$

Table 4.1: Order Parameter directions for the irreps, using the notation of the ISOTROPY software. In the left-hand column appear the order parameter directions for the octahedral rotations. Bold variables denote the full order parameter, including both magnitude and direction. The semicolons in the middle row separate different wavevectors in the star. The notation for the irrep amplitudes is used below in the table of free energy terms.

4.2 satisfy this condition.

3rd order	4th order
$R_5^-G_aF_c$	$R_5^-M_2^+A_bF_c$
$M_2^+G_aA_b$	

3rd order	4th order
$R_5^-F_aG_c$	$R_5^-M_2^+C_bG_c$
$M_2^+F_aC_b$	

3rd order	4th order
$R_5^-C_aA_c$	$R_5^-M_2^+F_bA_c$
$M_2^+C_aF_b$	

3rd order	4th order
$R_5^-A_aC_c$	$R_5^-M_2^+C_cG_b$
$M_2^+A_aG_b$	

Table 4.2: Symmetry-allowed third-order and fourth-order terms in the free-energy expansion that couple the magnetic order parameters with the octahedral rotation modes in the rare-earth titanates, using the *Pbnm* setting. Note that different sub-tables correspond to the different magnetic ground states listed in Table 4.3. Here, R_5^- and M_2^+ should be understood as the mode amplitudes of their corresponding irreps.

Here, the free energy terms have been grouped according to the four different magnetic ground states which do not break the translational symmetry of the *Pbnm* space group and transform as four different Γ-point irreps of *Pbnm* [166]. Table 4.3 lists these four ground states in both *Pbnm* and *Pnma* notations. These terms agree with the previous work done by Bousquet and Spaldin [166].[7] However, our analysis now shows how the coupling between these order parameters depend on the R_5^- and M_2^+ octahedral rotations present in the system.

[7]We however re-emphasize that Ref. [166] works in the *Pnma* setting rather than the *Pbnm* setting used here.

In the following analysis, we focus on the $G_aA_bF_c$ ground state, with a G_a-dominated phase crossing over to a F_c-dominated phase. This corresponds to the situation observed in the $RTiO_3$ compounds. However, similar conclusions hold for other combinations of FM and AFM order parameters, as long as the coupled order parameters are associated with the same magnetic ground state. Additionally, in all cases, note that the two magnetic irreps are coupled through the out-of-phase ($a^-a^-c^0$) and in-phase ($a^0a^0c^+$) octahedral rotations, corresponding to the R_5^- and M_2^+ irreps respectively. As such, this bilinear coupling between the AFM and FM moments is highly sensitive to the degree of lattice distortions present in the structure. In the following section, we present first-principles calculations which show that the octahedral distortions can be tuned via application of uniaxial strain. As such, it may be possible to experimentally control the magnitude of the bilinear coupling between the AFM and FM moments, and thereby the location of the CEP.

$Pnma$	$Pbnm$
$A_aF_bG_c$	$G_aA_bF_c$
$C_aG_bF_c$	$F_aC_bG_c$
$F_aA_bC_c$	$C_aF_bA_c$
$G_aC_bA_c$	$A_aG_bC_c$

Table 4.3: The four different types of translational-symmetry preserving magnetic ground states in the different basis settings of the space group #62.

First-principles calculations

To illustrate how one might experimentally tune the amplitude of the octahedral rotations, we use first-principles calculations to obtain the rotation amplitude of the R_5^- irrep as a function of uniaxial strain applied along the three orthorhombic axes. To do this, we fix the strained lattice parameter along an orthorhombic axis to different values while allowing the other two lattice parameters and the internal coordinates of the atoms to relax to minimize the forces on the atoms and the stresses on the unit cell. DFT calculations were performed using the projector augmented wave approach as implemented in the Vienna Ab Initio Simulation Package (VASP) [91, 92, 93]. These calculations on $YTiO_3$ used the PBEsol exchange-correlation functional [32], a plane

wave cutoff of 550 eV, and a $4 \times 4 \times 4$ Monkhorst-Pack grid. In addition, to properly reproduce the local magnetic moments on the Ti ions, we used the rotationally invariant LSDA+U scheme introduced by Dudarev et al. with U=4 eV [36].

In Fig. 4.6(b) of the main text, we plot the total displacement amplitude of the R_5^- octahedral rotation mode. While this quantity is proportional to the octahedral rotation angles to first order, it is more well defined. In particular, the definition of the octahedral rotation angles can become non-unique when there are multiple different structural distortions that lead to unequal bond lengths, etc., as is the case in $YTiO_3$. The mode amplitude is calculated by projecting the displacements of all atoms to the symmetry adapted basis modes of the R_5^- irrep, and calculating the total magnitude of the projected displacements. We use the ISODISTORT tool [217] for this calculation.

Ginzburg-Landau analysis

With the above analysis, we now have all the symmetry-allowed terms in the free energy. However, for simplicity, we start by considering the artificial case where there is no spin-orbit coupling and the octahedral rotations can be neglected, implying a cubic crystal structure for $ATiO_3$ (space group $Pm\bar{3}m$). In this case, the FM and AFM order parameters transform as vectors under the O(3) spin-rotational group, and are denoted respectively by $\boldsymbol{m}$ and $\boldsymbol{n}$. The only restriction we impose on the AFM wave vector $\boldsymbol{Q}$ is that $2\boldsymbol{Q} = 0$, which encompasses the configurations known as G-type, $\boldsymbol{Q} = (\pi, \pi, \pi)$, C-type, $\boldsymbol{Q} = (\pi, \pi, 0)$, and A-type, $\boldsymbol{Q} = (0, 0, \pi)$. In terms of this artifical cubic lattice, they correspond to the momenta R, M, and X, respectively. The most general Ginzburg-Landau (GL) free energy expansion is given by:

$$f = \frac{a_F}{2} m^2 + \frac{1}{4} m^4 + \frac{a_A}{2} n^2 + \frac{1}{4} n^4 + \frac{\gamma_1}{2} m^2 n^2 + \frac{\gamma_2}{2} (\boldsymbol{m} \cdot \boldsymbol{n})^2 . \tag{4.3}$$

Here, $a_F = a_{F,0}(T - T_F)$ and $a_A = a_{A,0}(T - T_A)$, where T_F and T_A are the bare FM and AFM ordering temperatures, respectively, and γ_i are Landau parameters. Note that we set the positive quartic coefficients of m^4 and n^4 to 1, which can always be done upon rescaling the other parameters. To traverse between the AFM and FM phases, we consider an abstract parameter ϵ, which is a function of the relative concentration of a substituted rare-earth element (as in the cases of $Sm_{1-x}Gd_xTiO_3$ and $Y_{1-x}La_xTiO_3$)

and encompasses not only the structural, but also the chemical effects of rare-earth substitution [130]. As a result, both T_F and T_A are implicit functions of ϵ. The available experimental phase diagrams of isovalent-substituted rare-earth titanates indicate that T_F and T_A cross with opposite slopes at ϵ^*, i.e. $T_F(\epsilon^*) = T_A(\epsilon^*)$. Near this multi-critical point, it is convenient to parameterize the quadratic coefficients as:

$$a_F = a\left(t - \frac{x}{2}\right), \quad a_A = \left(t + \frac{x}{2}\right), \tag{4.4}$$

where we defined $t \equiv \tilde{T} - \frac{\tilde{T}_F + \tilde{T}_A}{2}$, $x \equiv \tilde{T}_F - \tilde{T}_A$, $a \equiv a_{F,0}/a_{A,0}$, and $\tilde{T} \equiv a_{A,0}T$. Note that x, not to be confused with doping, is implicitly related to the distance to the multi-critical point as $x \approx \left(\frac{\partial \tilde{T}_F}{\partial \epsilon} - \frac{\partial \tilde{T}_A}{\partial \epsilon}\right)(\epsilon - \epsilon^*)$.

A straightforward minimization of Eq. (4.3) shows that the nature of the multi-critical point depends on the parameter $\gamma \equiv \gamma_1 + \min(\gamma_2, 0)$, being either a bicritical point (BCP) for $\gamma > 1$ or a tetracritical point (TCP) for $\gamma < 1$ [218, 219]. In the former case, shown in Fig. 4.8(a), the AFM and FM phases are separated by a single first-order transition (dashed line). In the latter, displayed in Fig. 4.8(b), there is an intermediate AFM+FM coexistence phase, separated from the pure AFM and FM phases by two second-order transitions (solid lines).

We proceed by first turning on the spin-orbit coupling while keeping the octahedra un-rotated. Now, $\boldsymbol{m}$ and $\boldsymbol{n}$ must transform according to the magnetic irreducible representations (irreps) associated with the cubic $Pm\bar{3}m$ space group. The FM and G-type AFM order parameters can still be parametrized by three-component vectors, as they transform according to the three-dimensional irreps $m\Gamma_4^+$ and mR_5^- , respectively. On the other hand, in the case of C-type and A-type orders, the AFM order parameter splits in a one-dimensional little-group irrep (mM_2^+ and mX_1^-, respectively) plus a two-dimensional little-group irrep (mM_5^+ and mX_5^-, respectively) depending on whether the magnetization is parallel or perpendicular to the wave vectors M and X, respectively.

We are now in a position to include the effects of the octahedral rotations that lower the space group from cubic to the orthorhombic $Pbnm$ (or equivalently $Pnma$ in the standard setting, see the Supplementary Material of Ref. [3]). As derived above, the R_5^- and M_2^+ octahedral distortions couple the FM and AFM modes bilinearly. In

particular, one component of the FM order parameter $\boldsymbol{m} = (m_a, m_b, m_c)$ couples to orthogonal components of two AFM order parameters $\boldsymbol{n}^{(\mu)} = \left(n_a^{(\mu)}, n_b^{(\mu)}, n_c^{(\mu)}\right)$ (see also [5, 166]). Here, $\{a, b, c\}$ denote the $Pbnm$ orthorhombic axes and $\mu = G, A, C$ refer to the type of AFM order. For instance, m_c couples bilinearly to both $n_a^{(G)}$ and to $n_b^{(A)}$ via combinations of R_5^- and M_2^+.

These couplings change the form of the free-energy expansion in Eq. (4.3). Hereafter we focus on the case where the leading instabilities for $x > 0$ and $x < 0$ are FM with magnetization along the c-axis and G-type AFM with magnetization along the a-axis, since this is the common ground state of most pristine $A\mathrm{TiO}_3$ compounds. Denoting $m \equiv m_c$ and $n \equiv n_a^{(G)}$, the free energy becomes:

$$f = \frac{a_F}{2}m^2 + \frac{1}{4}m^4 + \frac{a_G}{2}n^2 + \frac{1}{4}n^4 + \frac{\gamma}{2}m^2n^2 - Rmn, \tag{4.5}$$

where $\gamma = \gamma_1$ and R is a parameter related to the strength of the R_5^--mode octahedral rotations and the spin-lattice coupling [188].

4.2.4 Results

We can now discuss what happens to the phase diagrams of Figs. 4.8(a)-(b) for $R \neq 0$ (for concreteness, we consider $R > 0$). The first observation is that $m \neq 0$ and $n \neq 0$ everywhere inside the magnetically ordered phase, resulting in a single PM to magnetic transition and in the disappearance of the multi-critical points. In the case where the unperturbed phase diagram displayed a TCP and two second-order transition lines ($\gamma < 1$), all that remains is a smooth crossover and no phase transitions [Fig. 4.8(d)]. On the other hand, in the case $\gamma > 1$, the first-order transition line detaches from the PM-to-magnetic transition line [Fig. 4.8(c)]. While this kills the BCP, it gives rise to a critical end-point (CEP), located where the first-order line terminates. The phase diagram of Fig. 4.8(c) in the region inside the magnetically ordered state is reminiscent of the liquid-gas phase diagram of water. While the relevant order parameter in the water case is the difference in densities of the two fluid phases, in our magnetic analogue it is the canting of the magnetization, defined as $\theta \equiv \tan^{-1}(m/n)$ (see Fig. 4.8).

To gain a deeper insight, we first plot in Figs. 4.9(a)-(b) cuts of the phase diagram of Fig. 4.8(c) that show how the order parameters m and n change as a function of t

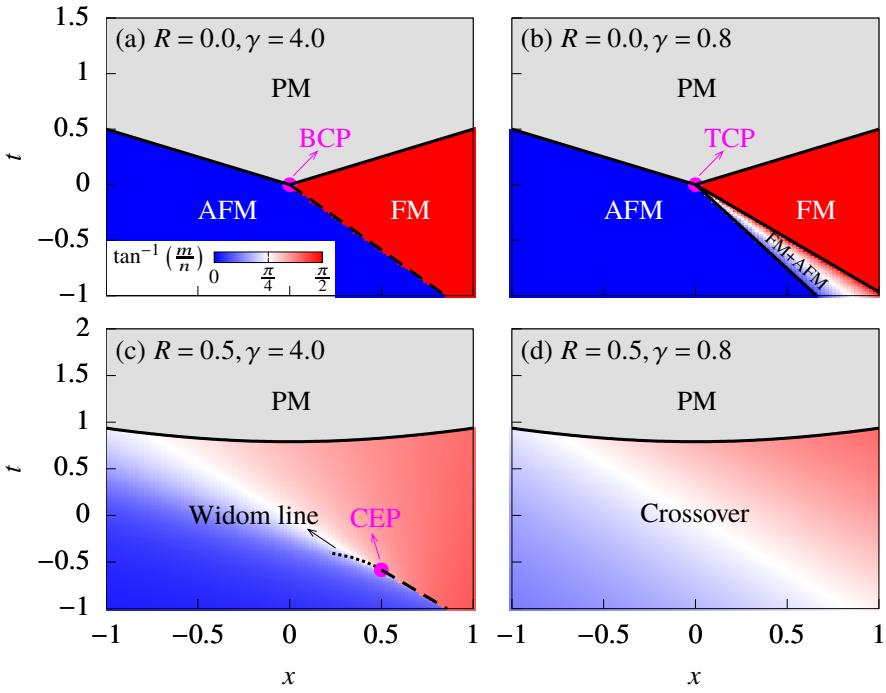

Figure 4.8: Phase diagrams obtained by minimizing the free-energy Eq. (4.5) with $a = 0.4$. The solid (dashed) lines correspond to second (first) order transitions. The dotted line in (c) is the Widom line, defined by the local maxima in the specific heat [see Fig. 4.9(d)]. Figure reproduced from Ref. [3].

and x in different regions. Motivated by these results, we introduce a new set of order parameters, $\alpha \equiv (m+n)/2$ and $\beta \equiv m-n$. Note from Figs. 4.9(a)-(b) that only β, but not α, jumps across the first-order line. The free-energy expansion becomes

$$f = \left(\frac{a_F + a_G}{2} - R\right)\alpha^2 + \frac{1+\gamma}{2}\alpha^4 + \frac{1}{4}\left(\frac{a_F + a_G}{2} + R\right)\beta^2 + \frac{1+\gamma}{32}\beta^4 + \frac{a_F - a_G}{2}\alpha\beta + \frac{3-\gamma}{4}\alpha^2\beta^2. \tag{4.6}$$

Therefore, the transition temperature for α (β) increases (decreases) due to R. Near the CEP, we can eliminate α and obtain a free-energy expansion only in terms of β, $f = \sum_{\nu=0}^{4} b_\nu \beta^\nu$ (see the Supplementary Material of Ref. [3]). The first-order line, where β jumps, is determined by the condition that the odd-power coefficients, b_1 and b_3, become zero. Since both are proportional to $a_F - a_G$, this condition gives $a_F = a_G$, leading to

$$x = \frac{2(a-1)}{a+1}t. \tag{4.7}$$

The position of the CEP is given by combining the above expression with the condition $b_2 = 0$, which yields:

$$x_c = -\frac{2(a-1)R}{a(\gamma-1)}, \quad t_c = -\frac{(a+1)R}{a(\gamma-1)}. \tag{4.8}$$

Along the first-order line, the order parameter β vanishes according to the usual mean-field result $\beta|_{b_1=b_3=0} = \sqrt{-b_2/(2b_4)} \propto (t_c - t)^{1/2}$. Beyond a mean-field approximation, however, the CEP is expected to belong to the Ising universality class. Indeed, by applying the transformation $x = \frac{2}{a+1}x' + (a-1)t'$ and $t = \frac{a+1}{2}t'$, the first-order line becomes the vertical line $x' = 0$ terminating at the CEP at $t'_c = -2R/a(\gamma-1)$. Thus, x' plays a similar role as of the magnetic field in the Ising model, and t', of the reduced temperature. In models described by the Ising universality class, a Widom line is expected to emerge from the CEP and to extend to higher temperatures [210, 211, 212]. To investigate it, we compute the specific heat $C/T \propto -\partial^2 f/\partial t^2$ as a function of t (or x) for fixed x (or t). As shown in Figs. 4.9(c)-(d), C/T displays a pronounced maximum above the CEP, indicative of the enhanced fluctuations that characterize the Widom

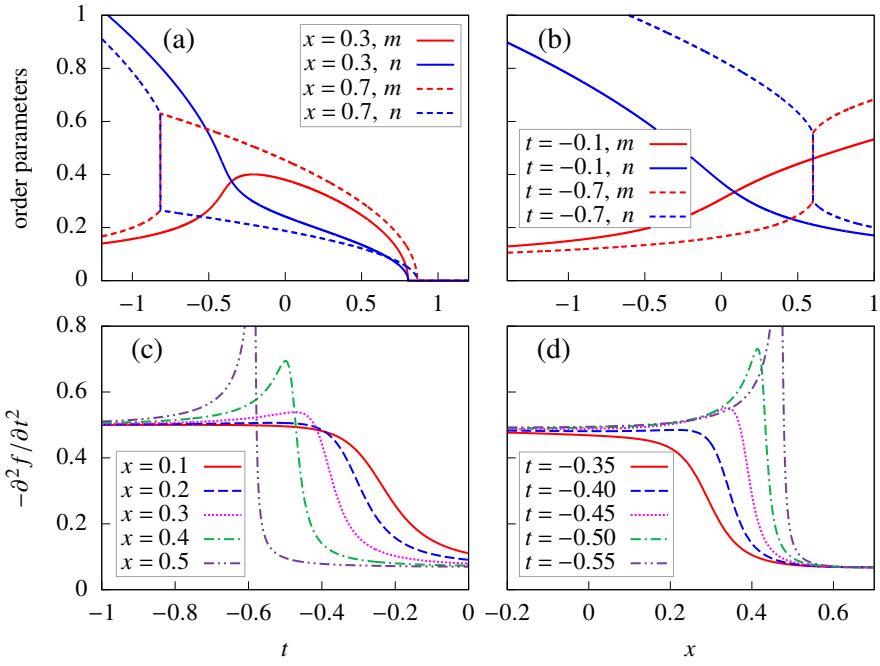

Figure 4.9: The FM and AFM order parameters, m and n, in the phase diagram of Fig. 4.8(c), plotted as a function of t for fixed x [panel (a)] and as a function of x for fixed t [panel (b)]. Panels (c) and (d) show the specific heat $C/T \propto -\partial^2 f/\partial t^2$ as a function of t for fixed x and as a function of x for fixed t, respectively. The maxima correspond to the Widom line [dotted line in Fig. 4.8(c)]. Figure reproduced from Ref. [3].

line.[8] As one moves farther from the CEP, this C/T maximum becomes weaker, and the Widom line fades away, as shown by the dotted line in the phase diagram of Fig. 4.8(c).

Our results in Eq. (4.8) show that the temperature of the CEP decreases linearly with the parameter R. Importantly, the R_5^- rotation mode is very sensitive to the lattice parameters, which opens up the possibility of tuning the position of the CEP experimentally by applying uniaxial stress. In Fig. 4.6(b), we show how the R_5^- mode amplitude changes as a function of uniaxial strain along each one of the three main orthorhombic axes, determined via first-principles calculations for the specific case of $YTiO_3$ (see the Supplementary Material of Ref. [3]). While it is difficult to establish the relative change in R corresponding to the relative change in the mode amplitude without input from microscopics, previous first-principles calculations show that even modest changes of the order of a few % in the amplitudes of the R_5^- and M_2^+ modes can cause changes of a factor of 2 or more in the exchange parameters [2]. This indicates a strong spin-lattice coupling in rare-earth titanates and the potential to drastically change the temperature of the CEP via uniaxial strain to promote a QCEP. This is also consistent with the strong dependence of the FM transition temperature on uniaxial pressure observed experimentally in $YTiO_3$ [177].

4.2.5 Discussion and Conclusion

We now discuss some experimental consequences of our results. The existence of a first-order line inside the magnetically-ordered state in the chemically-substituted rare-earth titanates, such as $Sm_{1-x}Gd_xTiO_3$ and $Y_{1-x}La_xTiO_3$, could be detected by measurements of the temperature-dependence of the canting angle, which would jump across the transition line and display hysteresis. To the best of our knowledge, these experiments have not yet been performed.[9] Thermodynamic measurements, such as specific heat and magnetic susceptibility, should also display typical signatures of a first-order transition. In the crossover region above the first-order line, the specific heat is expected to display a pronounced maximum near the CEP as the Widom line is crossed, indicative

[8] The Widom line defined by the maxima in Fig. 4.9(c) deviates slightly from the one defined by the maxima in Fig. 4.9(d), since they are not generally local maxima in the two-dimensional $\{x, t\}$ space.

[9] In compounds like $Sm_{1-x}Gd_xTiO_3$, the rare-earth atoms possess magnetic moments and order magnetically [204, 220]. Our conclusions remain qualitatively the same as long as the CEP takes place above the ordering temperature of the rare-earth atoms, or when the ordering of the rare-earth atoms is a secondary effect induced by coupling between rare-earth and Ti atoms.

of enhanced fluctuations. While a fine control of the concentration of the substituted rare-earth may be challenging, one can alternatively use uniaxial strain as a tuning parameter to smoothly move a given composition across the first-order and/or Widom lines.

More broadly, for appropriate concentrations, uniaxial strain could even be used to tune the CEP to zero temperature, thus promoting a QCEP. The general properties of a QCEP have been discussed in the context of other materials, most notably quasi-2D organic salts [221] and metallic ferromagnets [213]. In the former, a pressure-induced first-order line separates the PM Mott insulating and metallic phases, and the transition temperature associated with the CEP is very low [222, 223, 224]. Behaviors typically associated with quantum criticality have been observed in transport properties in the vicinity of the CEP [221]. In metallic ferromagnets, an external magnetic field can be used to suppress the ferro-metamagnetic transition down to $T = 0$ [213]. In the particular case of the bilayer ruthenate $Sr_3Ru_2O_7$, the putative magnetic-field-driven QCEP is preempeted by nematic order [225] and is associated with unusual transport and thermodynamic properties [195, 226]. Recently, a CEP associated with a first-order QPT was also observed in a frustrated quantum magnet [201]. The rare-earth titanates thus provide a novel framework to investigate magnetic QCEPs. In contrast to the more usual case of metallic ferromagnets, the metamagnetic transition involves two symmetry-equivalent insulating canted spin states, where orthogonal FM and AFM order parameters coexist. As a result, the dynamical critical exponent of the QCEP is expected to be $z = 1$, placing the system at the upper critical dimension, since $d + z = 4$. Another important difference is that the metamagnetic transition can be tuned by strain even in the absence of magnetic fields. Finally, rare-earth titanates can also be doped with charge carriers, which promotes a Mott insulating to metal transition [180]. An interesting direction for future studies is to investigate the fate of the QCEP uncovered here as the system is tuned across the band-filling driven Mott transition, since a metallic QCEP would have fundamentally different dynamics than an insulating one.

4.3 Strain-tuned valence transition in the perovskite oxide $Pr_{0.5}Ca_{0.5}CoO_3$

This section is adapted from *Room-Temperature Valence Transition in a Strain-Tuned Perovskite Oxide* [4]. In particular, this section focuses on the DFT contributions to Ref. [4]. The experimental work of Ref. [4] was carried out primarily by Vipul Chaturvedi under the supervision of Chris Leighton. First-principles calculations were performed by me under the supervision of Turan Birol.

4.3.1 Introduction

The prospect of controlling the behavior of materials through the application of external stimuli has been a persistent interest of the materials science and physics community [18, 227, 228, 229]. From the perspective of applications, being able to control the magnetic, transport, or optical properties via application of epitaxial strain, for example, could lead to novel device functionalities. Similarly, being able to control the ground-state properties of a material is interesting from the perspective of fundamental physics, allowing one to study, for example, the effect of structure on the ground-state behavior of a material.

Here, I discuss the methods and results of a first-principles analysis of the strain-tuned metal-insulator/spin/valence transition in $Pr_{0.5}Ca_{0.5}CoO_3$ (PCCO). In Ref. [4], my coauthors and I demonstrate that the electronic and magnetic ground state of $(Pr_{1-y}Y_y)_{1-x}Ca_xCoO_{3-\delta}$ (PYCCO) can be tuned via the application of epitaxial strain. Under large tensile strain, PYCCO is a metallic ferromagnet with a Curie temperature of $T_C \approx 85$ K. With compressive biaxial strain, thin films of PYCCO instead become non-magnetic and strongly insulating. In fact, under compressive strain values near -2.1%, thin films of PYCCO exhibit room-temperature first-order metal-insulator transitions [4]. This behavior (metallic and FM under tensile strain, and nonmagnetic and insulating under compressive strain) is analogous to the behavior found by Tsubouchi et al. in bulk PCCO, as a function of temperature rather than strain [230]. With respect to the structural phase transition, the unit cell volume of PCCO contracts by $\sim 2\%$ upon cooling through the transition temperature at 90 K. This transition is isosymmetric, with PCCO belonging to the *Pnma* space group on either side of the transition. Aside from

this structural transition, there are (just as we find with epixatial strain in [4]) simultaneous first-order spin-state and metal-insulator transitions [230, 231, 232, 233, 234, 235].

While Ref. [4] provides a study of the strain-induced transition in both PYCCO and PCCO, my first-principles calculations focus on the PCCO system. As we argue below, the exotic behavior of PYCCO is best understood through a study of PCCO, which also exhibits simultaneous metal-insulator/spin/valence transitions. The introduction of Y simply serves to raise the temperature of the transition [4]. For the purposes of studying the underlying theory then, we focus on PCCO, in which we may disregard the effects of Y rare-earth substitution, as well as the effects of Ca doping away from $x = 0.5$. Within PCCO, previous studies have shown that there is a thermal spin-state transition accompanied by a simultaneous metal-insulator transition and structural transition [230, 231, 232, 233, 234, 235]. Upon lowering through the valence transition temperature (T_{vt}) at which these phase transitions occur, the unit cell undergoes a sharp decrease in volume. Using first-principles calculations, I show that the thermal spin-state/metal-insulator/structural transition is directly analogous to the strain-induced transition observed in PYCCO in Ref. [4]. In particular, I perform first-principles calculations which show that the larger-volume (high V_{uc} phase) FM metallic phase is stabilized under tensile strain, while the lower-volume (low V_{uc}) nonmagnetic insulating phase is stabilized under compressive strain. This behavior agrees with the behavior seen experimentally in Ref. [4].

4.3.2 Methods

Biaxial-strain-dependent calculations were performed by initializing PCCO in the high- and low-V_{uc} states and constraining the in-plane lattice parameters to those of the relevant substrate, while relaxing the atomic positions and out-of-plane lattice parameters in DFT+U. For this we used the high- and low-V_{uc} parameters from the 10- and 295-K *Pnma* structures determined by Fujita et al. [6]. Choosing initial structures far from T_{vt}, i.e., deep in the high- and low-V_{uc} states was found to help stabilize the states. Following Knizek et al. [232], rock-salt-like arrangements of Pr and Ca were used to model PCCO[10]. To stabilize the desired valences (Pr^{4+}/Co^{3+}) in the insulating low-V_{uc} state,

[10]We note that the valence transition is driven predominantly by the crystal field felt by the Co ion, which to first approximation is independent of the A-site ordering employed in our calculations

we constrained the Co density matrix to that of low-spin Co^{3+} during relaxation, using the occupation control method implemented in Ref. [237]. The Co^{3+} density matrix for this purpose was extracted from a calculation for undoped $PrCoO_3$, which is *Pnma* with low-spin Co^{3+} in its ground state. After the calculation for the initial constrained relaxation converged, the relaxation was repeated without imposing the density matrix constraint. Pr occupations were not constrained during this whole process. Similarly, to stabilize the desired valences ($Pr^{3+}/Co^{3.5+}$(intermediate spin)) in the metallic high-$V_{\rm uc}$ state, we fixed the Pr^{3+} density matrix to that of $PrCoO_3$ during an initial relaxation. The Co occupation matrix was not constrained during this relaxation, as it was found sufficient to simply initialize the Co magnetic moment to 2 μ_B, which then relaxed to the desired 1.5 μ_B. A second relaxation was then performed without the density matrix constraint. Note that spin-orbit coupling was not included, meaning that spin-only Pr moments of 2 and 1 μ_B were obtained in the two states.

FM alignment of the Co and Pr moments was initialized in both states. While a full investigation of the stability of this FM configuration versus variables such as strain, $U_{\rm Pr}$, and $U_{\rm Co}$ (the U values on Pr and Co) was beyond the scope of [4], we performed tests for the specific $U_{\rm Pr}$ and $U_{\rm Co}$ in our reported calculations, which confirm an energetic preference for FM alignment. However, the energy difference between the FM and AFM configurations ($\sim 10^{-3}$ eV/formula unit) is two orders of magnitude smaller than the difference between the metallic and insulating states, implying that the magnetic configuration is of little significance for our purposes. All calculations were performed using the PBE exchange correlation functional revised for solids [32] as implemented in VASP [93], in combination with the Dudarev (effective) Hubbard $U_{\rm eff}$ correction [36] for both Pr f and Co d states. We used the VASP Pr PAW potential with f electrons in the valence states [238]. Results for $U_{\rm Pr} = 4$ eV and $U_{\rm Co} = 3$ eV are shown in Fig. 4.10(b), although, as shown in Fig. 4.11(a-c), the same qualitative trend as in Fig. 4.10(b) holds over a range of $U_{\rm Pr}$ and $U_{\rm Co}$. A Monkhorst-Pack grid of $4\times4\times4$ k-points was used to sample reciprocal space for all values of biaxial strain. We used

(there are 2 Pr and 2 Ca ions surrounding each Co ion for all A-site ordering configurations.) As such, the rock-salt ordering used here should not affect the physics of the transition to first order. In fact, rock-salt order leads to more similar anion environments than other A-site ordering configurations [236]. Hence, our calculations more closely model high-symmetry random A-site occupation than other ordering choices. A more in-depth first-principles investigation of the choice of the A-site order would require a significantly larger number of calculations, and is beyond the scope of this work.

a plane-wave energy cutoff of 550 eV and relaxed the internal coordinates, as well as the lattice constant normal to the biaxially-strained plane, until forces were converged below 10^{-3} eV/Å.

4.3.3 Results

We show that tensile strain stabilization of an FM metallic phase and compressive strain stabilization of a nonmagnetic insulating phase can be reproduced using strain-dependent DFT calculations for PCCO. As noted in the Introduction, DFT is capable of reproducing the valence/spin-state transition in bulk PCCO. This was achieved by imposing the experimental high-T V_{uc} to model the high-T phase, and the experimental collapsed V_{uc} to model the low-T phase [232]. We extended this method to heteroepitaxial strain tuning by taking the bulk structures in the metallic (high V_{uc}) and insulating (low V_{uc}) states [232], constraining the in-plane lattice parameters to those of the experimental substrates, and then relaxing the atomic positions and out-of-plane lattice parameters in DFT+U (see Methods for further details). Using the occupation control method of Ref. [237], we ensured that the system remains in the defined V_{uc}/valence/spin-state throughout the relaxation.

The central results from our DFT calculations are shown in Fig. 4.10(b), which plots the ε_{xx}[11] dependence of the difference in total energy per formula unit of PCCO between the low- and high-V_{uc} states ($E_{\mathrm{low}\ V_{\mathrm{uc}}} - E_{\mathrm{high}\ V_{\mathrm{uc}}}$, left axis, solid points), and the energy gap of the ground-state structure (E_g, right axis, open points). The results strongly support the experimental observations that the high-V_{uc} state is significantly lower in energy than the low-V_{uc} state under tensile biaxial strain (i.e., $E_{\mathrm{low}\ V_{\mathrm{uc}}} - E_{\mathrm{high}\ V_{\mathrm{uc}}}$ is positive for positive ε_{xx}). Furthermore, $E_{\mathrm{low}\ V_{\mathrm{uc}}} - E_{\mathrm{high}\ V_{\mathrm{uc}}}$ gradually decreases towards compressive strain values (negative ε_{xx}), eventually inverting, with the low-V_{uc} state becoming energetically favored under higher values of compressive strain. At the same time, the energy gap E_g of the ground-state structure transitions from zero at positive ε_{xx} (tensile strain), to greater than 100 meV per formula unit at negative ε_{xx} (compressive strain). This corresponds to stabilization of the metallic FM state under tension and the insulating non-FM state under compression, exactly as in Fig. 4.10(a)

[11] The in-plane strain induced by the substrate is calculated as $\varepsilon_{xx} = (a - a_c)/a_c$, where $a_c = 3.780$ Å is the pseudocubic lattice parameter and a is the lattice parameter imposed by the substrate [239].

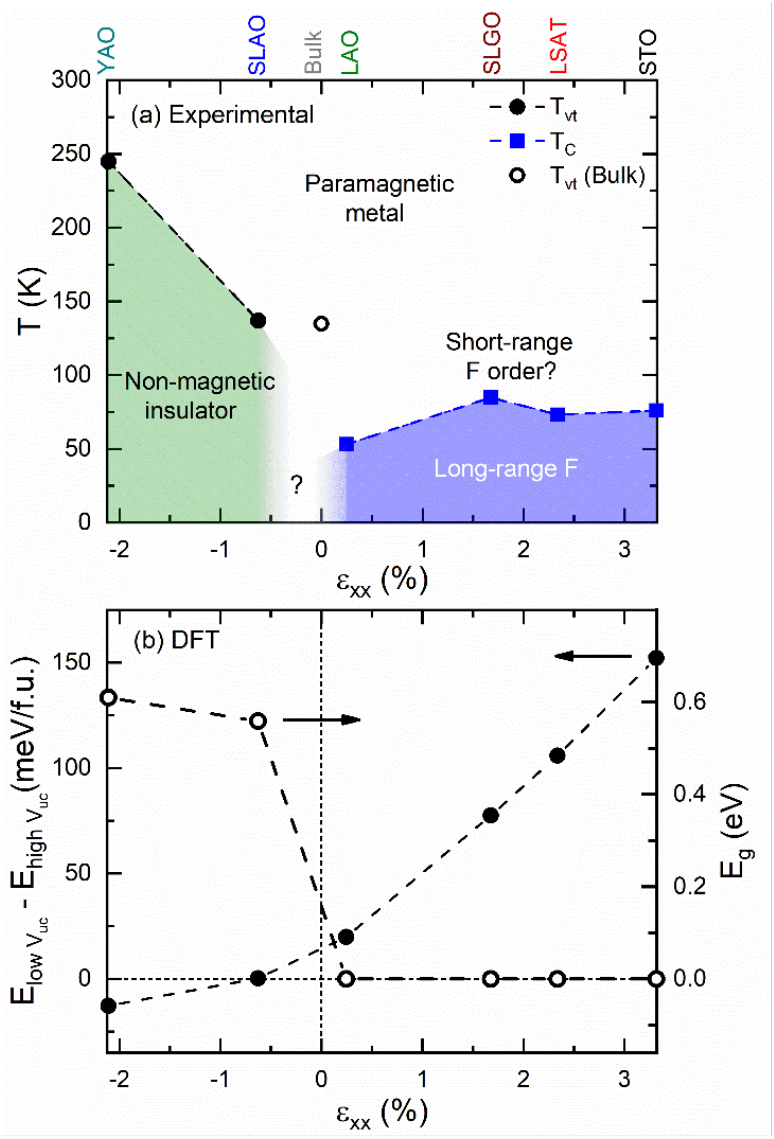

Figure 4.10: Strain "phase diagram" of $(Pr_{0.85}Y_{0.15})_{0.7}Ca_{0.3}CoO_{3-\delta}$ and DFT results. (a) Experimental temperature vs. T "in-plane strain" ε_{xx} phase diagram for $(Pr_{0.85}Y_{0.15})_{0.7}Ca_{0.3}CoO_{3-\delta}$. Thin film (solid points, ∼30-unit-cell-thick) and bulk (open point) data are shown, with the relevant substrate indicated at the top. The substrates on which $(Pr_{0.85}Y_{0.15})_{0.7}Ca_{0.3}CoO_{3-\delta}$ was grown are $YAlO_3(101)$ (YAO), $SrLaAlO_4(001)$ (SLAO), $LaAlO_3(001)$ (LAO), $SrLaGaO_4(001)$ (SLGO), and $La_{0.18}Sr_{0.82}Al_{0.59}Ta_{0.41}O_3(001)$ (LSAT). The valence transition temperature T_{vt} (circles) and Curie temperature T_C (squares) are plotted. Green, white, and blue phase fields indicate "nonmagnetic insulator", "paramagnetic metal", and "long-range ferromagnet (FM)", respectively. (b) Energy difference between the low- and high-unit-cell-volume states of $Pr_{0.5}Ca_{0.5}CoO_3$ vs. ε_{xx} (left axis, solid points) as obtained from DFT calculations. On the right axis is the corresponding energy gap E_g (open points) of the ground-state structure, obtained from DFT DOS calculations. Figure reproduced from [4].

for $(Pr_{0.85}Y_{0.15})_{0.7}Ca_{0.3}CoO_{3-\delta}$.

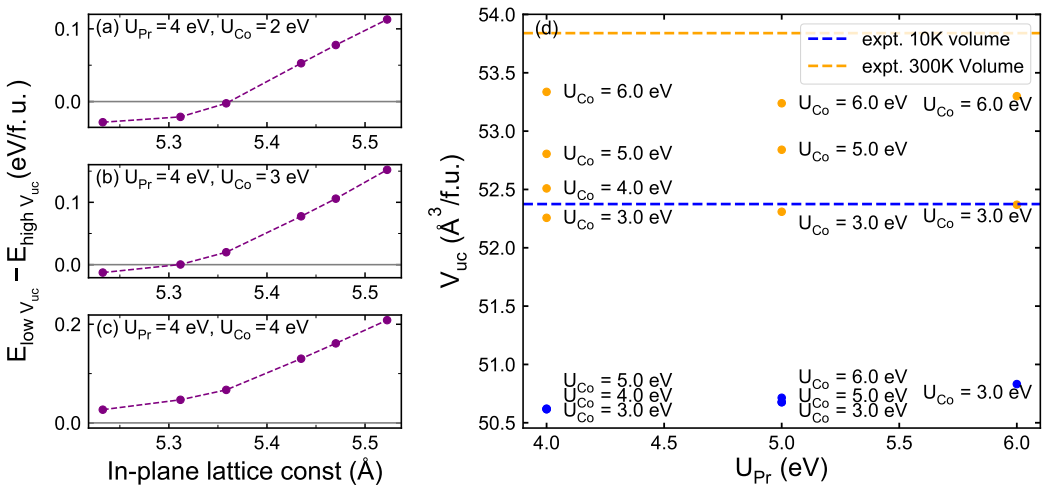

Figure 4.11: (a-c) DFT+U-calculated energy differences between low-volume insulating and high-volume metallic states in $Pr_{0.5}Ca_{0.5}CoO_3$ (PCCO) as a function of the in-plane lattice constant (and thus biaxial strain), for different sets of U on Pr and Co. Since all reasonable U_{Pr} and U_{Co} values were found to underestimate the experimental volumes of both the high- and low-volume states, we report results using U values such that the DFT-predicted difference in bulk volumes is similar to that seen in experiment ($U_{Pr} = 4$ eV and $U_{Co} = 3$ eV)[12]. Panel (d) shows the results for DFT-calculated volumes of bulk PCCO, compared to experiment (horizontal dashed lines). The absolute volumes of both the low- and high-volume states are underestimated by DFT, as noted above. U_{Pr} values of 5 eV and higher, in combination with U_{Co} values higher than 3 eV, overestimate the volume difference between the low- and high-volume states in bulk PCCO.

While different factors will impact the exact energies in Fig. 4.10(b), including the U values imposed on Co and Pr (see Methods and Fig. 4.11), and the exact Ca and Y composition, the overall trend is robust across various parameter choices (Fig. 4.11), strongly supporting the experimental observations in Fig. 4.10(a). In particular, although the precise location of the transition predicted by DFT (i.e., the sign change in $(E_{\text{low Vuc}} - E_{\text{high Vuc}})$ is sensitive to the choice of U values (see Fig. 4.11(a-c)), and should thus not be taken as exact, we find that for a wide range of U_{Pr} and U_{Co} the high-volume state becomes more stable/favorable under tensile strain (large in-plane lattice constant).

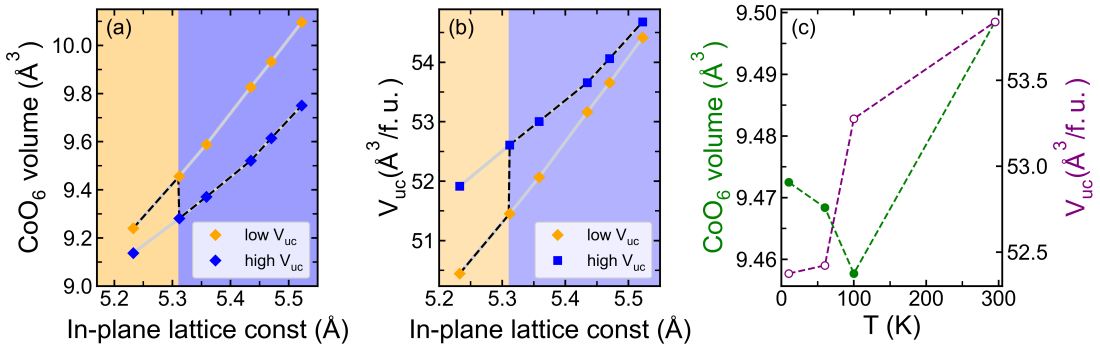

Figure 4.12: DFT-calculated (a) CoO_6 octahedral volume and (b) unit cell volume in both the low and high-volume phases as a function of in-plane lattice constant (and thus biaxial strain), for $U_{\mathrm{Co}} = 3$ eV and $U_{\mathrm{Pr}} = 4$ eV. The background color denotes which phase is energetically favorable. The gray lines highlight the trends within a given phase, while the dashed lines track the behavior of the lower-energy phase across the transition. To obtain the location of the phase boundary, we find the in-plane lattice constant for which the energy difference between the two phases is zero. This is accomplished using linear interpolation of the energy differences between neighboring data points (see the dashed line in Fig. 4.11(b).) In panel (c), we reproduce data from Ref. [6], showing the experimental behavior of the octahedral and unit cell volumes as a function of temperature in $Pr_{0.5}Ca_{0.5}CoO_3$. We find good qualitative agreement between the DFT calculations and the experimental data across the phase transition (compare (a,b) with (c)).

In addition to the energies, we also find qualitative agreement between the structural changes observed across the thermal valence transition in $Pr_{0.5}Ca_{0.5}CoO_3$ and the structural changes predicted by DFT vs. strain (see Fig. 4.12). In particular, DFT calculations predict a discontinuous drop in the unit-cell volume (and increase in the octahedral volume) across the transition with increasing compressive strain, analogous to the trends seen experimentally with decreasing temperature. This provides further evidence that the strain-driven phase transition reported in Ref. [4] is similar in nature to the thermal phase transition in these systems. In Fig. 4.13b, we show the full strain evolution of the density-of-states in the high- and low-V_{uc} states. We see from the density-of-states that the high-V_{uc} state is always metallic, while the low-V_{uc} state is always insulating. By extracting the band gap from the density-of-states, we can plot the gap as a function of strain. This is shown in Fig. 4.13a. We note that there is a discontinuity in the band gap as we transition between the high- and low-V_{uc} with

strain, in agreement with the behavior seen in Fig. 4.10(b).

4.3.4 Discussion and Conclusion

Using a first-principles approach, we provide a theoretical understanding of the strain-tuned transitions observed in PCCO and PYCCO in Ref. [4], which reported the effects of a wide-range of compressive and tensile biaxial strains on epitaxial thin films of $(Pr_{1-y}Y_y)_{1-x}Ca_xCoO_{3-\delta}$ perovskite cobaltites. In particular, Ref. [4] showed that through application of heteroepitaxial strain, a transition can be induced between a FM metallic state and a nonmagnetic insulating state, thereby demonstrating extensive control over the electronic and magnetic ground states.

Our first-principles calculations complement this experimental analysis, finding that the strain-tuned metal-insulator/spin-state transitions in PCCO are analogous to those driven by temperature. That is, the simultaneous spin-state, valence, structural, and metal-insulator transitions controlled with temperature (see Refs. [230, 231, 232, 233, 234, 235]) are also realized with applied biaxial strain. Moreover, the agreement between our first-principles analysis and experiment, in addition to the experimental analysis of Ref. [4], suggest that the underlying physics driving the transitions seen in PCCO and PYCCO are one and the same.

In addition to the fundamental physics elucidated by this work, this unique valence-driven first-order coupled structural/spin-state/metal-insulator transition in this material system has been strain-stabilized under large compression to at least 291 K [4]. This brings a valence transition in a perovskite oxide from the cryogenic temperatures in bulk, to room temperature, realizing not only a metal-insulator transition rivaling classic systems such as vanadium oxides [202, 240], but also additional functionality stemming from valence and spin-state control, with abundant device potential. With recent experimental advances in the application of uniaxial stress [2], it is also interesting to consider the effect of uniaxial pressure on epitaxially grown compounds. In particular, it may be possible to continuously tune a compound near the transition (via

[12] Because the volumes are underestimated, the in-plane lattice constant corresponding to zero biaxial strain is smaller in our calculations than in experiment. As a result, while the DFT-predicted transition occurs at in-plane lattice constants close to the experimental zero-strain lattice parameter, this lattice parameter is larger than that predicted by DFT when the unit cell is completely optimized; the predicted transition thus occurs in the tensile region. However, the transition moves into the compressive region with slightly larger U's (see, for example, the trend above with increasing U_{Co}.)

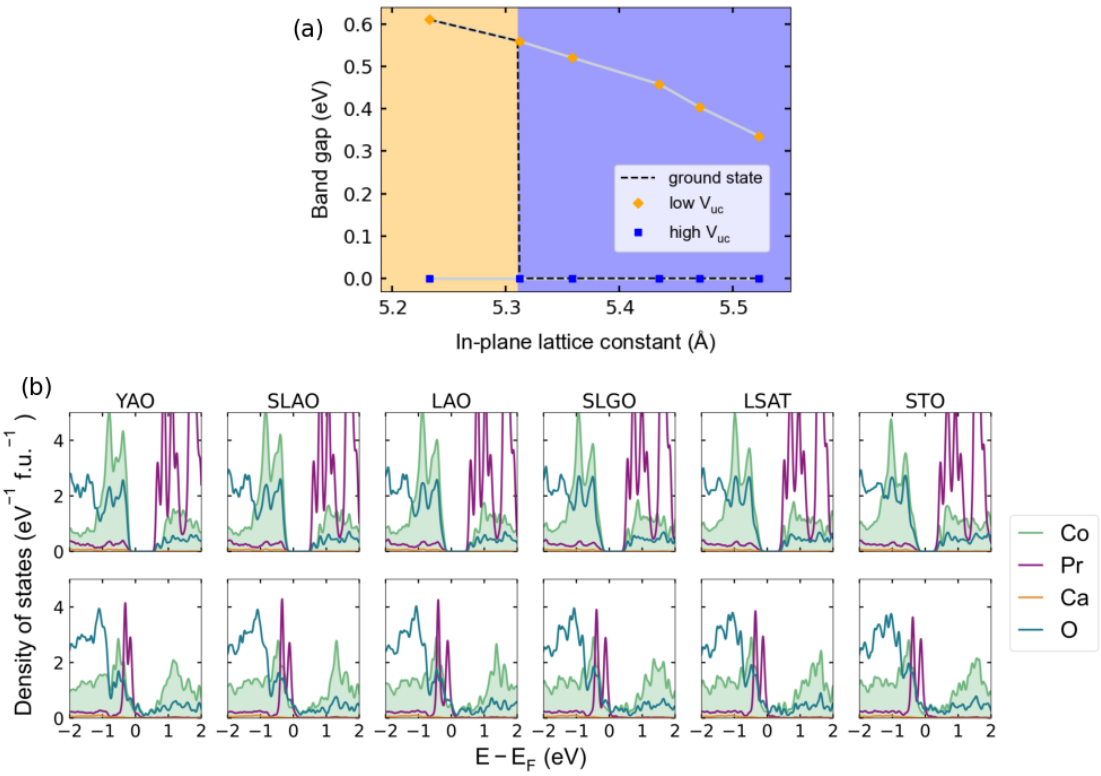

Figure 4.13: (a) DFT-calculated band gaps as a function of in-plane lattice constant for the low and high-volume states of $Pr_{0.5}Ca_{0.5}CoO_3$ (PCCO), for U_{Co}=3 eV and U_{Pr}=4 eV. The background color denotes whether the ground state is the high- or low-volume unit cell state, and the phase transition boundary is obtained where there is zero energy difference between the two phases, as described in the caption to Fig. 4.12. The gray lines highlight the trends within each phase, while the dashed line tracks the behavior of the band gap of the ground state across the transition. The dashed line was obtained in a similar manner to the dashed lines in Figs. 4.12(a,b). (b) Corresponding density-of-states (DOS) vs. energy plots (E_F is the Fermi energy) for each in-plane lattice constant, i.e., each substrate. The top row shows the results for the low-volume unit cell states, while the bottom row is for the high-volume unit cell states. We see that the low-volume unit cell states are insulating, while the high-volume unit cell states are metallic. These calculations therefore show that there is a high-volume metallic state under tensile biaxial strain and a low-volume insulating state under compressive biaxial strain, in agreement with experiment.

application of epitaxial strain) through the phase transition point via application of *in situ* uniaxial stress. Such a system may be studied through first-principles calculations analogous to the ones we provide here.

Chapter 5

Conclusion

In this thesis, I have employed a suite of analytical and computational tools to develop an understanding of the intricate interplay between structural, orbital, spin, and electronic degrees of freedom in transition metal oxides. In Chapter 2, my first-principles and exact diagonalization calculations highlighted the exotic magnetic excitations present in the botallackite $Cu_2(OH)_3Br$. In particular, this study reveals the quasi-1D nature of the magnetic excitations in the compound, and provides numerical evidence for the possible coexistence of magnons and spinons. While the exact diagonalization results strongly suggest that magnon and spinon excitations coexist in $Cu_2(OH)_3Br$, we did not study in detail the effect of the spinon-magnon couplings. It would be interesting to understand how the magnon-spinon couplings affect quantities such as the magnon and spinon lifetimes, or the spinon continuum.

In Chapter 3, I provided a comprehensive theoretical analysis of the magnetic behavior in the rare-earth titanates, using a combination of first-principles calculations and analytical methods. In particular, my calculations suggests that the application of either uniaxial or epitaxial strain should give rise to a host of magnetic and structural phases beyond those found in the bulk rare-earth titanates. As such, we believe an experimental investigation of the effect of uniaxial and biaxial strain on $RTiO_3$ should be fruitful.

In Chapter 4, I then reviewed the results of my collaborations with other experimental and theory groups. In Sec. 4.1, I reported the results of a joint experimental and theoretical study of the rare-earth titanates $RTiO_3$ (focusing on $YTiO_3$) [2], in which

my coauthors and I demonstrate that the application of uniaxial strain leads to dramatic changes in the Curie temperatures of $YTiO_3$, demonstrating the extraordinary sensitivity of the magnetic behavior to the crystal structure in the rare-earth titanates. In Sec. 4.2, I then detailed a different investigation of the rare-earth titanates, in which my coauthors and I studied in detail the nature of the FM to G-type AFM transition in $RTiO_3$. Using group-theoretical methods, I showed explicitly that the octahedral distortions couple the FM and AFM order parameters, and in particular how the FM and AFM order parameters couple in the free energy. Using these results, my collaborators showed, using a free-energy analysis, that the predominantly FM and predominantly AFM phases in $RTiO_3$, while symmetry-equivalent, do not need to be connected by a crossover. Instead, depending on the magnitude of the various interactions, these two extremes may be separated by a first-order phase transition line, which ends at a critical end point inside the magnetic phase. We then suggested that it may be possible to experimentally control the position of the critical end point to 0 K via the application of uniaxial strain. In particular, I then performed first-principles calculations to explicitly demonstrate that the FM-AFM coupling, which is related to the position of the critical end point, can be tuned via the application of uniaxial strain. Due to these results, as well as those of Chapter 3, I believe that future theoretical and experimental efforts to study the nature of the magnetic transitions of $RTiO_3$, and in particular how this magnetic behavior is affected by strain, will be very fruitful.

In Sec. 4.3, I reviewed the results of Ref. [4], in which my coauthors and I provided a detailed analysis of the strain-induced spin-state/valence-state/metal-insulator phase transition in the $(Pr_{1-y}Y_y)_{1-x}Ca_xCoO_{3-\delta}$ (PYCCO) and $Pr_{0.5}Ca_{0.5}CoO_3$ (PCCO) compounds. In particular, my first-principles calculations show explicitly that the strain-induced phase transitions in PYCCO are directly analogous to the thermal phase transitions observed in PCCO, complementing the experimental analysis provided by my coauthors.

Overall, transition metal oxides represent a wide class of materials, exhibiting phases such as superconductivity [241], ferroelectricity [242], and magnetism [104]. Within the field of magnetism, we have seen in Chapter 2 that some transition metal oxides can even host exotic fractionalized excitations. In this thesis, I have demonstrated that first-principles methods, complemented with analytical approaches (such as linear

spin wave theory or mean-field theory) and computational approaches (such as exact diagonalization), can yield significant insights into the magnetic properties of these compounds.

References

[1] Dominique M. Gautreau, Amartyajyoti Saha, and Turan Birol. First-principles characterization of the magnetic properties of $Cu_2(OH)_3Br$. *Phys. Rev. Materials*, 5:024407, Feb 2021.

[2] A. Najev, S. Hameed, D. Gautreau, Z. Wang, J. Joe, M. Požek, T. Birol, R. M. Fernandes, M. Greven, and D. Pelc. Uniaxial strain control of bulk ferromagnetism in rare-earth titanates. *Phys. Rev. Lett.*, 128:167201, Apr 2022.

[3] Zhentao Wang, Dominique Gautreau, Turan Birol, and Rafael M. Fernandes. Strain-tunable metamagnetic critical endpoint in Mott insulating rare-earth titanates. *Phys. Rev. B*, 105:144404, Apr 2022.

[4] Vipul Chaturvedi, Supriya Ghosh, Dominique Gautreau, Patrick Quarterman, Purnima P Balakrishnan, Brian J Kirby, Hua Zhou, Huikai Cheng, Amanda Huon, Timothy Charlton, et al. Near-room-temperature valence transition in a strain-tuned perovskite oxide. *arXiv preprint arXiv:2112.10917*, 2021.

[5] Robert Schmitz, Ora Entin-Wohlman, Amnon Aharony, A. Brooks Harris, and Erwin Müller-Hartmann. Magnetic structure of the Jahn-Teller system $LaTiO_3$. *Phys. Rev. B*, 71:144412, Apr 2005.

[6] Toshiaki Fujita, Takeshi Miyashita, Yukio Yasui, Yoshiaki Kobayashi, Masatoshi Sato, Eiji Nishibori, Makoto Sakata, Yutaka Shimojo, Naoki Igawa, Yoshinobu Ishii, et al. Transport and magnetic studies on the spin state transition of $Pr_{1-x}Ca_xCoO_3$ up to high pressure. *Journal of the Physical Society of Japan*, 73(7):1987–1997, 2004.

[7] Erwin Schrodinger. Quantisierung als eigenwertproblem (series of papers). *Ann. Phys.(Leipzig)*, 79(361-376):489–527, 1926.

[8] Paul Adrien Maurice Dirac. Quantum mechanics of many-electron systems. *Proceedings of the Royal Society of London. Series A, Containing Papers of a Mathematical and Physical Character*, 123(792):714–733, 1929.

[9] Walter Heitler and Fritz London. Wechselwirkung neutraler atome und homöopolare bindung nach der quantenmechanik. *Zeitschrift für Physik*, 44(6):455–472, 1927.

[10] Douglas Rayne Hartree. The wave mechanics of an atom with a non-Coulomb central field. Part I. theory and methods. In *Mathematical Proceedings of the Cambridge Philosophical Society*, volume 24, pages 89–110. Cambridge university press, 1928.

[11] Douglas Rayne Hartree. The wave mechanics of an atom with a non-Coulomb central field. Part II. some results and discussion. In *Mathematical Proceedings of the Cambridge Philosophical Society*, volume 24, pages 111–132. Cambridge University Press, 1928.

[12] Douglas Rayne Hartree. The wave mechanics of an atom with a non-Coulomb central field. Part III. term values and intensities in series in optical spectra. In *Mathematical Proceedings of the Cambridge Philosophical Society*, volume 24, pages 426–437. Cambridge University Press, 1928.

[13] Douglas Rayne Hartree. The distribution of charge and current in an atom consisting of many electrons obeying dirac's equations. In *Mathematical Proceedings of the Cambridge Philosophical Society*, volume 25, pages 225–236. Cambridge University Press, 1929.

[14] Felix Bloch. Bemerkung zur elektronentheorie des ferromagnetismus und der elektrischen leitfähigkeit. *Zeitschrift für Physik*, 57(7):545–555, 1929.

[15] J. C. Slater. Cohesion in monovalent metals. *Phys. Rev.*, 35:509–529, Mar 1930.

[16] Leon Balents. Spin liquids in frustrated magnets. *Nature*, 464(7286):199–208, 2010.

[17] J. Bardeen, L. N. Cooper, and J. R. Schrieffer. Theory of superconductivity. *Phys. Rev.*, 108:1175–1204, Dec 1957.

[18] Darrell G Schlom, Long-Qing Chen, Chang-Beom Eom, Karin M Rabe, Stephen K Streiffer, and Jean-Marc Triscone. Strain tuning of ferroelectric thin films. *Annual Review of Materials Research*, 37(1):589–626, 2007.

[19] P. L. Kapitza. Heat transfer and superfluidity of helium ii. *Phys. Rev.*, 60:354–355, Aug 1941.

[20] A Hausoel, M Karolak, E Şaşıoğlu, A Lichtenstein, K Held, A Katanin, A Toschi, and G Sangiovanni. Local magnetic moments in iron and nickel at ambient and earth's core conditions. *Nature communications*, 8(1):1–9, 2017.

[21] K. v. Klitzing, G. Dorda, and M. Pepper. New method for high-accuracy determination of the fine-structure constant based on quantized hall resistance. *Phys. Rev. Lett.*, 45:494–497, Aug 1980.

[22] Philip W Anderson. More is different: broken symmetry and the nature of the hierarchical structure of science. *Science*, 177(4047):393–396, 1972.

[23] P. Hohenberg and W. Kohn. Inhomogeneous electron gas. *Phys. Rev.*, 136:B864–B871, Nov 1964.

[24] W. Kohn and L. J. Sham. Self-consistent equations including exchange and correlation effects. *Phys. Rev.*, 140:A1133–A1138, Nov 1965.

[25] W. Kohn. Nobel lecture: Electronic structure of matter—wave functions and density functionals. *Rev. Mod. Phys.*, 71:1253–1266, Oct 1999.

[26] J. H. van Vleck. Nonorthogonality and ferromagnetism. *Phys. Rev.*, 49:232–240, Feb 1936.

[27] J. P. Perdew and Alex Zunger. Self-interaction correction to density-functional approximations for many-electron systems. *Phys. Rev. B*, 23:5048–5079, May 1981.

[28] A. D. Becke. Density-functional exchange-energy approximation with correct asymptotic behavior. *Phys. Rev. A*, 38:3098–3100, Sep 1988.

[29] R. O. Jones and O. Gunnarsson. The density functional formalism, its applications and prospects. *Rev. Mod. Phys.*, 61:689–746, Jul 1989.

[30] John P. Perdew and Yue Wang. Pair-distribution function and its coupling-constant average for the spin-polarized electron gas. *Phys. Rev. B*, 46:12947–12954, Nov 1992.

[31] John P. Perdew, Kieron Burke, and Matthias Ernzerhof. Generalized gradient approximation made simple. *Phys. Rev. Lett.*, 77:3865–3868, Oct 1996.

[32] John P. Perdew, Adrienn Ruzsinszky, Gábor I. Csonka, Oleg A. Vydrov, Gustavo E. Scuseria, Lucian A. Constantin, Xiaolan Zhou, and Kieron Burke. Restoring the density-gradient expansion for exchange in solids and surfaces. *Phys. Rev. Lett.*, 100:136406, Apr 2008.

[33] T. Oguchi, K. Terakura, and A. R. Williams. Band theory of the magnetic interaction in MnO, MnS, and NiO. *Phys. Rev. B*, 28:6443–6452, Dec 1983.

[34] T Oguchi, K Terakura, and AR Williams. Transition-metal monoxides: Itinerant versus localized picture of superexchange. *Journal of Applied Physics*, 55(6):2318–2320, 1984.

[35] K. Terakura, T. Oguchi, A. R. Williams, and J. Kübler. Band theory of insulating transition-metal monoxides: Band-structure calculations. *Phys. Rev. B*, 30:4734–4747, Oct 1984.

[36] S. L. Dudarev, G. A. Botton, S. Y. Savrasov, C. J. Humphreys, and A. P. Sutton. Electron-energy-loss spectra and the structural stability of nickel oxide: An LSDA+U study. *Phys. Rev. B*, 57:1505–1509, Jan 1998.

[37] John Hubbard. Electron correlations in narrow energy bands. *Proceedings of the Royal Society of London. Series A. Mathematical and Physical Sciences*, 276(1365):238–257, 1963.

[38] Daniel P. Arovas, Erez Berg, Steven A. Kivelson, and Srinivas Raghu. The Hubbard model. *Annual Review of Condensed Matter Physics*, 13(1):239–274, 2022.

[39] V. I. Anisimov, I. V. Solovyev, M. A. Korotin, M. T. Czyżyk, and G. A. Sawatzky. Density-functional theory and NiO photoemission spectra. *Phys. Rev. B*, 48:16929–16934, Dec 1993.

[40] A. I. Liechtenstein, V. I. Anisimov, and J. Zaanen. Density-functional theory and strong interactions: Orbital ordering in Mott-Hubbard insulators. *Phys. Rev. B*, 52:R5467–R5470, Aug 1995.

[41] Siheon Ryee and Myung Joon Han. The effect of double counting, spin density, and hund interaction in the different DFT+U functionals. *Scientific reports*, 8(1):1–11, 2018.

[42] I. V. Solovyev, P. H. Dederichs, and V. I. Anisimov. Corrected atomic limit in the local-density approximation and the electronic structure of d impurities in Rb. *Phys. Rev. B*, 50:16861–16871, Dec 1994.

[43] Matteo Cococcioni and Stefano de Gironcoli. Linear response approach to the calculation of the effective interaction parameters in the LDA + U method. *Phys. Rev. B*, 71:035105, Jan 2005.

[44] U von Barth and L Hedin. A local exchange-correlation potential for the spin polarized case. i. *Journal of Physics C: Solid State Physics*, 5(13):1629–1642, Jul 1972.

[45] A. K. Rajagopal and J. Callaway. Inhomogeneous electron gas. *Phys. Rev. B*, 7:1912–1919, Mar 1973.

[46] Gerald Burns. Introduction to group theory with applications. *Materials Science Series*, 1977.

[47] David M. Bishop. *Group Theory and Chemistry*. Dover, 1993.

[48] Michael Tinkham. *Group theory and quantum mechanics*. Courier Corporation, 2003.

[49] Mildred S Dresselhaus, Gene Dresselhaus, and Ado Jorio. *Group theory: application to the physics of condensed matter*. Springer Science & Business Media, 2007.

[50] Laszlo Lovasz. *Combinatorial problems and exercises*, volume 361. American Mathematical Soc., 1993.

[51] Michael Glazer, Gerald Burns, and Alexander N Glazer. *Space groups for solid state scientists*. Elsevier, 2012.

[52] Barry Bradlyn, L. Elcoro, M. G. Vergniory, Jennifer Cano, Zhijun Wang, C. Felser, M. I. Aroyo, and B. Andrei Bernevig. Band connectivity for topological quantum chemistry: Band structures as a graph theory problem. *Phys. Rev. B*, 97:035138, Jan 2018.

[53] Gennadii Levikovich Bir, Grigorii Ezekielevich Pikus, et al. *Symmetry and strain-induced effects in semiconductors*, volume 484. Wiley New York, 1974.

[54] E Kroumova, MI Aroyo, JM Perez-Mato, A Kirov, C Capillas, S Ivantchev, and HJPTAMJ Wondratschek. Bilbao crystallographic server: useful databases and tools for phase-transition studies. *Phase Transitions: A Multinational Journal*, 76(1-2):155–170, 2003.

[55] Mois Ilia Aroyo, Juan Manuel Perez-Mato, Cesar Capillas, Eli Kroumova, Svetoslav Ivantchev, Gotzon Madariaga, Asen Kirov, and Hans Wondratschek. Bilbao crystallographic server: I. databases and crystallographic computing programs. *Zeitschrift für Kristallographie-Crystalline Materials*, 221(1):15–27, 2006.

[56] Mois I Aroyo, Asen Kirov, Cesar Capillas, JM Perez-Mato, and Hans Wondratschek. Bilbao crystallographic server. II. representations of crystallographic point groups and space groups. *Acta Crystallographica Section A: Foundations of Crystallography*, 62(2):115–128, 2006.

[57] Anthony Zee. *Group theory in a nutshell for physicists*, volume 17. Princeton University Press, 2016.

[58] G Ya Lyubarskii. *The application of group theory in physics*. Elsevier, 2013.

[59] Dorian M Hatch and Harold T Stokes. Invariants: program for obtaining a list of invariant polynomials of the order-parameter components associated with irreducible representations of a space group. *Journal of applied crystallography*, 36(3):951–952, 2003.

[60] Harold T Stokes, Dorian M Hatch, Branton J Campbell, and David E Tanner. Isodisplace: a web-based tool for exploring structural distortions. *Journal of Applied Crystallography*, 39(4):607–614, 2006.

[61] Harold T Stokes, Dorian M Hatch, and Branton J Campbell. Isotropy software suite. 2007.

[62] Harold T. Stokes, Seth van Orden, and Branton J. Campbell. *ISOSUBGROUP*: an internet tool for generating isotropy subgroups of crystallographic space groups. *Journal of Applied Crystallography*, 49(5):1849–1853, Oct 2016.

[63] J. M. Luttinger and L. Tisza. Theory of dipole interaction in crystals. *Phys. Rev.*, 70:954–964, Dec 1946.

[64] D. H. Lyons and T. A. Kaplan. Method for determining ground-state spin configurations. *Phys. Rev.*, 120:1580–1585, Dec 1960.

[65] D. H. Lyons, T. A. Kaplan, K. Dwight, and N. Menyuk. Classical theory of the ground spin-state in cubic spinels. *Phys. Rev.*, 126:540–555, Apr 1962.

[66] S. Blundell. *Magnetism in Condensed Matter*. Oxford Master Series in Condensed Matter Physics. OUP Oxford, 2001.

[67] T. Holstein and H. Primakoff. Field dependence of the intrinsic domain magnetization of a ferromagnet. *Phys. Rev.*, 58:1098–1113, Dec 1940.

[68] Patrik Fazekas. *Lecture Notes on Electron Correlation and Magnetism*, volume 5. World Scientific, 1999.

[69] A V Chubukov and D I Golosov. Quantum theory of an antiferromagnet on a triangular lattice in a magnetic field. *Journal of Physics: Condensed Matter*, 3(1):69–82, Jan 1991.

[70] S. Toth and B. Lake. Linear spin wave theory for single-q incommensurate magnetic structures. *Journal of Physics: Condensed Matter*, 27:166002, 2015.

[71] Anders W. Sandvik. Computational studies of quantum spin systems. In *AIP Conference Proceedings*, volume 1297, pages 135–338. AIP, 2010.

[72] Cornelius Lanczos. *An iteration method for the solution of the eigenvalue problem of linear differential and integral operators*. United States Gov. Press Office Los Angeles, CA, 1950.

[73] Cornelius Lanczos. Solution of systems of linear equations by minimized iterations. *Journal of research of the National Bureau of Standards*, 49(1):33, 1952.

[74] Philip W Anderson. An approximate quantum theory of the antiferromagnetic ground state. *Physical Review*, 86(5):694, 1952.

[75] B Bernu, C Lhuillier, and L Pierre. Signature of Néel order in exact spectra of quantum antiferromagnets on finite lattices. *Phys. Rev. Lett.*, 69(17):2590, 1992.

[76] Tamás A. Tóth, Andreas M. Läuchli, Frédéric Mila, and Karlo Penc. Three-sublattice ordering of the SU(3) Heisenberg model of three-flavor fermions on the square and cubic lattices. *Phys. Rev. Lett.*, 105:265301, Dec 2010.

[77] Alexander Wietek, Michael Schuler, and Andreas M. Läuchli. Studying continuous symmetry breaking using energy level spectroscopy. 2017.

[78] R. Coldea, D. A. Tennant, A. M. Tsvelik, and Z. Tylczynski. Experimental realization of a 2d fractional quantum spin liquid. *Phys. Rev. Lett.*, 86:1335–1338, Feb 2001.

[79] Masanori Kohno, Oleg A Starykh, and Leon Balents. Spinons and triplons in spatially anisotropic frustrated antiferromagnets. *Nature Physics*, 3:790–795, 2007.

[80] Martin Mourigal, Mechthild Enderle, Axel Klöpperpieper, Jean-Sébastien Caux, Anne Stunault, and Henrik M Rønnow. Fractional spinon excitations in the quantum Heisenberg antiferromagnetic chain. *Nature Physics*, 9:435–441, 2013.

[81] Chanchal K. Majumdar and Dipan K. Ghosh. On next-nearest-neighbor interaction in linear chain. i. *Journal of Mathematical Physics*, 10(8):1388–1398, 1969.

[82] Chanchal K. Majumdar and Dipan K. Ghosh. On next-nearest-neighbor interaction in linear chain. ii. *Journal of Mathematical Physics*, 10(8):1399–1402, 1969.

[83] Alexei Kitaev. Anyons in an exactly solved model and beyond. *Annals of Physics*, 321:2–111, 2006.

[84] M. R. Norman. Colloquium: Herbertsmithite and the search for the quantum spin liquid. *Reviews of Modern Physics*, 88:041002, Dec 2016.

[85] J. S. Helton, K. Matan, M. P. Shores, E. A. Nytko, B. M. Bartlett, Y. Yoshida, Y. Takano, A. Suslov, Y. Qiu, J.-H. Chung, D. G. Nocera, and Y. S. Lee. Spin dynamics of the spin-1/2 kagome lattice antiferromagnet $ZnCu_3(OH)_6Cl_2$. *Phys. Rev. Lett.*, 98:107204, Mar 2007.

[86] D.S. Inosov. Quantum magnetism in minerals. *Advances in Physics*, 67:149–252, 2018.

[87] X. G. Zheng and C. N. Xu. Antiferromagnetic transition in botallackite $Cu_2Cl(OH)_3$. *Solid State Communications*, 131:509–511, 2004.

[88] X. G. Zheng, Takashi Mori, Kusuo Nishiyama, Wataru Higemoto, Hiroshi Yamada, Keiko Nishikubo, and C. N. Xu. Antiferromagnetic transitions in polymorphous minerals of the natural cuprates atacamite and botallackite $Cu_2Cl(OH)_3$. *Phys. Rev. B*, 71:174404, May 2005.

[89] X.G. Zheng, T. Yamashita, M. Hagihala, M. Fujihala, and T. Kawae. Magnetic transitions in botallackite-structure $Cu_2(OH)_3Br$ and $Cu_2(OH)_3I$. *Physica B: Condensed Matter*, 404(0921–4526):680–682, 2009.

[90] H. Zhang, Z. Zhao, D. Gautreau, M. Raczkowski, A. Saha, V. O. Garlea, H. Cao, T. Hong, H. O. Jeschke, Subhendra D. Mahanti, T. Birol, F. F. Assaad, and X. Ke. Coexistence and interaction of spinons and magnons in an antiferromagnet with alternating antiferromagnetic and ferromagnetic quantum spin chains. *Phys. Rev. Lett.*, 125:037204, Jul 2020.

[91] G. Kresse and J. Hafner. Ab initio molecular dynamics for liquid metals. *Phys. Rev. B*, 47:558–561, Jan 1993.

[92] Georg Kresse and Jürgen Furthmüller. Efficiency of ab-initio total energy calculations for metals and semiconductors using a plane-wave basis set. *Computational materials science*, 6(1):15–50, 1996.

[93] G. Kresse and J. Furthmüller. Efficient iterative schemes for ab initio total-energy calculations using a plane-wave basis set. *Phys. Rev. B*, 54:11169–11186, Oct 1996.

[94] Pauli Virtanen, Ralf Gommers, Travis E. Oliphant, Matt Haberland, Tyler Reddy, David Cournapeau, Evgeni Burovski, Pearu Peterson, Warren Weckesser, Jonathan Bright, Stéfan J. van der Walt, Matthew Brett, Joshua Wilson, K. Jarrod Millman, Nikolay Mayorov, Andrew R. J. Nelson, Eric Jones, Robert Kern, Eric Larson, CJ Carey, İlhan Polat, Yu Feng, Eric W. Moore, Jake Vand erPlas, Denis Laxalde, Josef Perktold, Robert Cimrman, Ian Henriksen, E. A. Quintero, Charles R Harris, Anne M. Archibald, Antônio H. Ribeiro, Fabian Pedregosa, Paul van Mulbregt, and SciPy 1. 0 Contributors. SciPy 1.0: Fundamental Algorithms for Scientific Computing in Python. *Nature Methods*, 17:261–272, 2020.

[95] S. van der Walt, S. C. Colbert, and G. Varoquaux. The numpy array: A structure for efficient numerical computation. *Computing in Science Engineering*, 13(2):22–30, 2011.

[96] J.B. Goodenough. *Magnetism and the Chemical Bond*. Inorganic chemistry section. Interscience Publishers, 1963.

[97] Arpita Paul, Chia-Min Chung, Turan Birol, and Hitesh J. Changlani. Spin-lattice coupling and the emergence of the trimerized phase in the S=1 kagome antiferromagnet $Na_2Ti_3Cl_8$. *Phys. Rev. Lett.*, 124(16):167203, Apr 2020.

[98] Daniel Bernard Litvin. The Luttinger-Tisza method. *Physica*, 77(2):205–219, 1974.

[99] Günter Bergerhoff and O. Schmitz-Dumont. Die kristallstruktur des kaliumhexachlorocadmats(II). *Zeitschrift fuer anorganische und allgemeine Chemie*, 284(1-3):10–19, Mar 1956.

[100] TN Nguyen and H-C Zur Loye. A family of one-dimensional oxides: Sr_3MIrO_6 (M=Ni, Cu, Zn): Structure and magnetic properties. *Journal of Solid State Chemistry*, 117(2):300–308, 1995.

[101] Turan Birol, Kristjan Haule, and David Vanderbilt. Nature of the magnetic interactions in Sr_3niiro_6. *Phys. Rev. B*, 98(13):134432, Oct 2018.

[102] Hans Bethe. Zur theorie der metalle. *Zeitschrift für Physik*, 71(3-4):205–226, 1931.

[103] Michael Karbach, Kun Hu, and Gerhard Müller. Introduction to the bethe ansatz ii. *Computers in Physics*, 12(6):565–573, 1998.

[104] Masahito Mochizuki and Masatoshi Imada. Orbital physics in the perovskite Ti oxides. *New Journal of Physics*, 6:154–154, Nov 2004.

[105] J. H. Haeni, P. Irvin, W. Chang, R. Uecker, P. Reiche, Y. L. Li, S. Choudhury, W. Tian, M. E. Hawley, B. Craigo, A. K. Tagantsev, X. Q. Pan, S. K. Streiffer, L. Q. Chen, S. W. Kirchoefer, J. Levy, and D. G. Schlom. Room-temperature ferroelectricity in strained $SrTiO_3$. *Nature*, 430(7001):758–761, Aug 2004.

[106] Clifford W. Hicks, Daniel O. Brodsky, Edward A. Yelland, Alexandra S. Gibbs, Jan A. N. Bruin, Mark E. Barber, Stephen D. Edkins, Keigo Nishimura, Shingo Yonezawa, Yoshiteru Maeno, and Andrew P. Mackenzie. Strong increase of T_c of Sr_2RuO_4 under both tensile and compressive strain. *Science*, 344(6181):283–285, 2014.

[107] Alexander Steppke, Lishan Zhao, Mark E. Barber, Thomas Scaffidi, Fabian Jerzembeck, Helge Rosner, Alexandra S. Gibbs, Yoshiteru Maeno, Steven H. Simon, Andrew P. Mackenzie, and Clifford W. Hicks. Strong peak in T_c of Sr_2RuO_4 under uniaxial pressure. *Science*, 355(6321):eaaf9398, 2017.

[108] Zewei Shao, Xun Cao, Hongjie Luo, and Ping Jin. Recent progress in the phase-transition mechanism and modulation of vanadium dioxide materials. *NPG Asia Materials*, 10(7):581–605, Jul 2018.

[109] Nagaphani B Aetukuri, Alexander X Gray, Marc Drouard, Matteo Cossale, Li Gao, Alexander H Reid, Roopali Kukreja, Hendrik Ohldag, Catherine A Jenkins, Elke Arenholz, et al. Control of the metal–insulator transition in vanadium dioxide by modifying orbital occupancy. *Nature Physics*, 9(10):661–666, 2013.

[110] Nao Takeshita, Takao Sasagawa, Takenari Sugioka, Yoshinori Tokura, and Hidenori Takagi. Gigantic anisotropic uniaxial pressure effect on superconductivity within the CuO_2 plane of $La_{1.64}Eu_{0.2}Sr_{0.16}CuO_4$: Strain control of stripe criticality. *Journal of the Physical Society of Japan*, 73(5):1123–1126, 2004.

[111] H-H Kim, SM Souliou, Mark E Barber, E Lefrançois, Matteo Minola, M Tortora, Rolf Heid, Nabhanila Nandi, Rodolfo Alberto Borzi, Gaston Garbarino, et al. Uniaxial pressure control of competing orders in a high-temperature superconductor. *Science*, 362(6418):1040–1044, 2018.

[112] Chetan Dhital, Z. Yamani, Wei Tian, J. Zeretsky, A. S. Sefat, Ziqiang Wang, R. J. Birgeneau, and Stephen D. Wilson. Effect of uniaxial strain on the structural and magnetic phase transitions in $BaFe_2As_2$. *Phys. Rev. Lett.*, 108:087001, Feb 2012.

[113] E. C. Blomberg, A. Kreyssig, M. A. Tanatar, R. M. Fernandes, M. G. Kim, A. Thaler, J. Schmalian, S. L. Bud'ko, P. C. Canfield, A. I. Goldman, and R. Prozorov. Effect of tensile stress on the in-plane resistivity anisotropy in $bafe_2as_2$. *Phys. Rev. B*, 85:144509, Apr 2012.

[114] Jack Y. Zhang, Clayton A. Jackson, Santosh Raghavan, Jinwoo Hwang, and Susanne Stemmer. Magnetism and local structure in low-dimensional Mott insulating $GdTiO_3$. *Phys. Rev. B*, 88:121104, Sep 2013.

[115] Xin Huang, Yankun Tang, and Shuai Dong. Strain-engineered a-type antiferromagnetic order in $YTiO_3$: A first-principles calculation. *Journal of Applied Physics*, 113(17):17E108, 2013.

[116] Yakui Weng, Xin Huang, Yankun Tang, and Shuai Dong. Magnetic orders of $LaTiO_3$ under epitaxial strain: A first-principles study. *Journal of Applied Physics*, 115(17):17E108, 2014.

[117] Li-Juan Yang, Ya-Kui Weng, Hui-Min Zhang, and Shuai Dong. Strain driven sequential magnetic transitions in strained $GdTiO_3$ on compressive substrates: a first-principles study. *Journal of Physics: Condensed Matter*, 26(47):476001, 2014.

[118] Xin Huang, Qingyu Xu, and Shuai Dong. Orientation-dependent magnetism and orbital structure of strained $YTiO_3$ films on $LaAlO_3$ substrates. *Journal of Applied Physics*, 117(17):17C703, 2015.

[119] Yakui Weng, Fei Long, and Xing'ao Li. Magnetic order and electronic structure of [110]-oriented $LaTiO_3$ films: A theoretical study. *Europhysics Letters*, 136(2):27005, 2022.

[120] SC Chae, YJ Chang, SSA Seo, TW Noh, D-W Kim, and CU Jung. Epitaxial growth and the magnetic properties of orthorhombic $YTiO_3$ thin films. *Applied physics letters*, 89(18):182512, 2006.

[121] Pouya Moetakef, Daniel G Ouellette, Jack Y Zhang, Tyler A Cain, S James Allen, and Susanne Stemmer. Growth and properties of $GdTiO_3$ films prepared by hybrid molecular beam epitaxy. *Journal of crystal growth*, 355(1):166–170, 2012.

[122] MN Grisolia, FY Bruno, D Sando, HJ Zhao, E Jacquet, XM Chen, L Bellaiche, A Barthélémy, and M Bibes. Structural, magnetic, and electronic properties of $GdTiO_3$ Mott insulator thin films grown by pulsed laser deposition. *Applied Physics Letters*, 105(17):172402, 2014.

[123] Yanwei Cao, P Shafer, Xiaoran Liu, D Meyers, M Kareev, S Middey, JW Freeland, E Arenholz, and J Chakhalian. Magnetism and electronic structure of $YTiO_3$ thin films. *Applied Physics Letters*, 107(11):112401, 2015.

[124] Raphaël Aeschlimann, Daniele Preziosi, Philipp Scheiderer, Michael Sing, Sergio Valencia, Jacobo Santamaria, Chen Luo, Hanjo Ryll, Florin Radu, Ralph Claessen, et al. A living-dead magnetic layer at the surface of ferrimagnetic $DyTiO_3$ thin films. *Advanced Materials*, 30(29):1707489, 2018.

[125] R. Aeschlimann, M. N. Grisolia, G. Sanchez-Santolino, J. Varignon, F. Choueikani, R. Mattana, V. Garcia, S. Fusil, T. Fröhlich, M. Braden, B. Delley, M. Varela,

P. Ohresser, J. Santamaria, A. Barthélémy, C. Piamonteze, and M. Bibes. X-ray absorption and x-ray magnetic circular dichroism in bulk and thin films of ferrimagnetic $GdTiO_3$. *Phys. Rev. Materials*, 5:014407, Jan 2021.

[126] C. Ulrich, G. Khaliullin, S. Okamoto, M. Reehuis, A. Ivanov, H. He, Y. Taguchi, Y. Tokura, and B. Keimer. Magnetic order and dynamics in an orbitally degenerate ferromagnetic insulator. *Phys. Rev. Lett.*, 89:167202, Sep 2002.

[127] Anthony M Glazer. The classification of tilted octahedra in perovskites. *Acta Crystallographica Section B: Structural Crystallography and Crystal Chemistry*, 28(11):3384–3392, 1972.

[128] TR McGuire, MW Shafer, RJ Joenk, HA Alperin, and SJ Pickart. Magnetic structure of $EuTiO_3$. *Journal of Applied Physics*, 37(3):981–982, 1966.

[129] Shahid P Shafi, Bradley C Hernden, Lachlan MD Cranswick, Thomas C Hansen, and Mario Bieringer. Topotactic oxidation pathway of $ScTiO_3$ and high-temperature structure evolution of $ScTiO_{3.5}$ and $Sc_4Ti_3O_{12}$-type phases. *Inorganic Chemistry*, 51(3):1269–1277, 2012.

[130] Masahito Mochizuki and Masatoshi Imada. Orbital-spin structure and lattice coupling in $R\mathrm{TiO}_3$ where $R =$ La, Pr, Nd, and Sm. *Phys. Rev. Lett.*, 91:167203, Oct 2003.

[131] T. Mizokawa and A. Fujimori. Unrestricted Hartree-Fock study of transition-metal oxides: Spin and orbital ordering in perovskite-type lattice. *Phys. Rev. B*, 51:12880–12883, May 1995.

[132] T. Mizokawa and A. Fujimori. Electronic structure and orbital ordering in perovskite-type $3d$ transition-metal oxides studied by Hartree-Fock band-structure calculations. *Phys. Rev. B*, 54:5368–5380, Aug 1996.

[133] H Sawada, N Hamada, and K Terakura. Theoretical study of orbital ordering in $YTiO_3$. *Physica B: Condensed Matter*, 237:46–47, 1997.

[134] H. Sawada and K. Terakura. Orbital and magnetic orderings in localized t_{2g} systems, $YTiO_3$ and YVO_3: Comparison with a more itinerant e_g system $LaMnO_3$. *Phys. Rev. B*, 58:6831–6836, Sep 1998.

[135] Masayuki Itoh, Hirotaka Tanaka, and Kiyoichiro Motoya. NMR study of microscopic magnetic properties of Mott-Hubbard insulators $RTiO_3$ (R=Y and La). *Physica B: Condensed Matter*, 237:19–20, 1997.

[136] Masayuki Itoh, Michitoshi Tsuchiya, Hirotaka Tanaka, and Kiyoichiro Motoya. Orbital ordering and local magnetic properties of Mott-Hubbard insulators $YTiO_3$ and $LaTiO_3$: NMR study. *Journal of the Physical Society of Japan*, 68(8):2783–2789, 1999.

[137] Masayuki Itoh and Michitoshi Tsuchiya. Orbital ordering in $YTiO_3$ observed by NMR. *Journal of magnetism and magnetic materials*, 226:874–875, 2001.

[138] H. Ichikawa, J. Akimitsu, M. Nishi, and K. Kakurai. Direct observation of orbital ordering in $YTiO_3$. *Physica B: Condensed Matter*, 281-282:482–484, 2000.

[139] Jun Akimitsu, Hirohiko Ichikawa, Naotoshi Eguchi, Tomoko Miyano, Masakazu Nishi, and Kazuhisa Kakurai. Direct observation of orbital ordering in $YTiO_3$ by means of the polarized neutron diffraction technique. *Journal of the physical society of Japan*, 70(12):3475–3478, 2001.

[140] H. Nakao, Y. Wakabayashi, T. Kiyama, Y. Murakami, M. v. Zimmermann, J. P. Hill, Doon Gibbs, S. Ishihara, Y. Taguchi, and Y. Tokura. Quantitative determination of the atomic scattering tensor in orbitally ordered $YTiO_3$ by using a resonant x-ray scattering technique. *Phys. Rev. B*, 66:184419, Nov 2002.

[141] I. A. Kibalin, Z. Yan, A. B. Voufack, S. Gueddida, B. Gillon, A. Gukasov, F. Porcher, A. M. Bataille, F. Morini, N. Claiser, M. Souhassou, C. Lecomte, J.-M. Gillet, M. Ito, K. Suzuki, H. Sakurai, Y. Sakurai, C. M. Hoffmann, and X. P. Wang. Spin density in $ytio_3$: I. joint refinement of polarized neutron diffraction and magnetic x-ray diffraction data leading to insights into orbital ordering. *Phys. Rev. B*, 96:054426, Aug 2017.

[142] Z. Yan, I. A. Kibalin, N. Claiser, S. Gueddida, B. Gillon, A. Gukasov, A. B. Voufack, F. Morini, Y. Sakurai, M. Brancewicz, M. Itou, M. Itoh, N. Tsuji, M. Ito, M. Souhassou, C. Lecomte, P. Cortona, and J.-M. Gillet. Spin density in $YTiO_3$: II. momentum-space representation of electron spin density supported by position-space results. *Phys. Rev. B*, 96:054427, Aug 2017.

[143] M. Cwik, T. Lorenz, J. Baier, R. Müller, G. André, F. Bourée, F. Lichtenberg, A. Freimuth, R. Schmitz, E. Müller-Hartmann, and M. Braden. Crystal and magnetic structure of $LaTiO_3$: Evidence for nondegenerate t_{2g} orbitals. *Phys. Rev. B*, 68:060401, Aug 2003.

[144] Takashi Kiyama and Masayuki Itoh. Presence of $3d$ quadrupole moment in $LaTiO_3$ studied by ^{47,49}Ti NMR. *Phys. Rev. Lett.*, 91:167202, Oct 2003.

[145] J. Hemberger, H.-A. Krug von Nidda, V. Fritsch, J. Deisenhofer, S. Lobina, T. Rudolf, P. Lunkenheimer, F. Lichtenberg, A. Loidl, D. Bruns, and B. Büchner. Evidence for Jahn-Teller distortions at the antiferromagnetic transition in $LaTiO_3$. *Phys. Rev. Lett.*, 91:066403, Aug 2003.

[146] G. Khaliullin and S. Maekawa. Orbital liquid in three-dimensional Mott insulator: $LaTiO_3$. *Phys. Rev. Lett.*, 85:3950–3953, Oct 2000.

[147] G. Khaliullin. Order from disorder: Quantum spin gap in magnon spectra of $LaTiO_3$. *Phys. Rev. B*, 64:212405, Nov 2001.

[148] Giniyat Khaliullin and Satoshi Okamoto. Theory of orbital state and spin interactions in ferromagnetic titanates. *Phys. Rev. B*, 68:205109, Nov 2003.

[149] Giniyat Khaliullin. Orbital order and fluctuations in Mott insulators. *Progress of Theoretical Physics Supplement*, 160:155–202, 2005.

[150] C. Ulrich, A. Gössling, M. Grüninger, M. Guennou, H. Roth, M. Cwik, T. Lorenz, G. Khaliullin, and B. Keimer. Raman scattering in the Mott insulators $LaTiO_3$ and $YTiO_3$: Evidence for orbital excitations. *Phys. Rev. Lett.*, 97:157401, Oct 2006.

[151] C. Ulrich, G. Khaliullin, M. Guennou, H. Roth, T. Lorenz, and B. Keimer. Spin-orbital excitation continuum and anomalous electron-phonon interaction in the Mott insulator $LaTiO_3$. *Phys. Rev. Lett.*, 115:156403, Oct 2015.

[152] ZY Zhao, O Khosravani, M Lee, L Balicas, XF Sun, JG Cheng, J Brooks, HD Zhou, and ES Choi. Spin-orbital liquid and quantum critical point in $Y_{1-x}La_xTiO_3$. *Phys. Rev. B*, 91(16):161106, 2015.

[153] James M. Rondinelli and Sinisa Coh. Large isosymmetric reorientation of oxygen octahedra rotation axes in epitaxially strained perovskites. *Phys. Rev. Lett.*, 106:235502, Jun 2011.

[154] C.-J. Eklund, C. J. Fennie, and K. M. Rabe. Strain-induced ferroelectricity in orthorhombic $CaTiO_3$ from first principles. *Phys. Rev. B*, 79:220101, Jun 2009.

[155] A. Vailionis, H. Boschker, W. Siemons, E. P. Houwman, D. H. A. Blank, G. Rijnders, and G. Koster. Misfit strain accommodation in epitaxial ABO_3 perovskites: Lattice rotations and lattice modulations. *Phys. Rev. B*, 83:064101, Feb 2011.

[156] HD Zhou and JB Goodenough. Localized or itinerant TiO_3 electrons in $RTiO_3$ perovskites. *Journal of Physics: Condensed Matter*, 17(46):7395, 2005.

[157] Robert Schmitz, Ora Entin-Wohlman, Amnon Aharony, and Erwin Müller-Hartmann. Orbital order, anisotropic spin couplings, and the spin-wave spectrum of the ferromagnetic Mott insulator $YTiO_3$. *Annalen der Physik*, 16(5-6):425–428, 2007.

[158] Matthew F Lapa and Christopher L Henley. Ground states of the classical antiferromagnet on the pyrochlore lattice. *arXiv preprint arXiv:1210.6810*, 2012.

[159] Sophia R. Sklan and Christopher L. Henley. Nonplanar ground states of frustrated antiferromagnets on an octahedral lattice. *Phys. Rev. B*, 88:024407, Jul 2013.

[160] C. Pinettes, B. Canals, and C. Lacroix. Classical Heisenberg antiferromagnet away from the pyrochlore lattice limit: Entropic versus energetic selection. *Phys. Rev. B*, 66:024422, Jul 2002.

[161] Bhilahari Jeevanesan and Peter P. Orth. Classical ground states of Heisenberg and XY antiferromagnets on the windmill lattice. *Phys. Rev. B*, 90:144435, Oct 2014.

[162] Nic Shannon, Burkhard Schmidt, Karlo Penc, and Peter Thalmeier. Finite temperature properties and frustrated ferromagnetism in a square lattice Heisenberg model. *The European Physical Journal B-Condensed Matter and Complex Systems*, 38(4):599–616, 2004.

[163] TA Kaplan and N Menyuk. Spin ordering in three-dimensional crystals with strong competing exchange interactions. *Philosophical Magazine*, 87(25):3711–3785, 2007.

[164] Masahito Mochizuki and Masatoshi Imada. Magnetic phase transition of the perovskite-type Ti oxides. *Journal of the Physical Society of Japan*, 69(7):1982–1985, 2000.

[165] Masahito Mochizuki and Masatoshi Imada. Magnetic and orbital states and their phase transition of the perovskite-type Ti oxides: strong coupling approach. *Journal of the Physical Society of Japan*, 70(6):1777–1789, 2001.

[166] Eric Bousquet and Nicola Spaldin. Induced magnetoelectric response in $Pnma$ perovskites. *Phys. Rev. Lett.*, 107:197603, Nov 2011.

[167] James M. Rondinelli and Nicola A. Spaldin. Substrate coherency driven octahedral rotations in perovskite oxide films. *Phys. Rev. B*, 82:113402, Sep 2010.

[168] Guru Khalsa and Nicole A Benedek. Ultrafast optically induced ferromagnetic/anti-ferromagnetic phase transition in $GdTiO_3$ from first principles. *npj Quantum Materials*, 3(1):1–8, 2018.

[169] Mingqiang Gu and James M. Rondinelli. Nonlinear phononic control and emergent magnetism in mott insulating titanates. *Phys. Rev. B*, 98:024102, Jul 2018.

[170] Jianpeng Liu, Kasra Hejazi, and Leon Balents. Floquet engineering of multiorbital mott insulators: Applications to orthorhombic titanates. *Phys. Rev. Lett.*, 121:107201, Sep 2018.

[171] Aurélien Géron. *Hands-on machine learning with Scikit-Learn, Keras, and TensorFlow: Concepts, tools, and techniques to build intelligent systems.* " O'Reilly Media, Inc.", 2019.

[172] Julien Varignon, Mathieu N. Grisolia, Daniele Preziosi, Philippe Ghosez, and Manuel Bibes. Origin of the orbital and spin ordering in rare-earth titanates. *Phys. Rev. B*, 96:235106, Dec 2017.

[173] F. Hardy, N. J. Hillier, C. Meingast, D. Colson, Y. Li, N. Barišić, G. Yu, X. Zhao, M. Greven, and J. S. Schilling. Enhancement of the critical temperature of hgba$_2$cuo$_{4+\delta}$ by applying uniaxial and hydrostatic pressure: Implications for a universal trend in cuprate superconductors. *Phys. Rev. Lett.*, 105:167002, Oct 2010.

[174] Jiun-Haw Chu, James G. Analytis, Kristiaan De Greve, Peter L. McMahon, Zahirul Islam, Yoshihisa Yamamoto, and Ian R. Fisher. In-plane resistivity anisotropy in an underdoped iron arsenide superconductor. *Science*, 329(5993):824–826, 2010.

[175] Vadim Grinenko, Shreenanda Ghosh, Rajib Sarkar, Jean-Christophe Orain, Artem Nikitin, Matthias Elender, Debarchan Das, Zurab Guguchia, Felix Brückner, Mark E. Barber, Joonbum Park, Naoki Kikugawa, Dmitry A. Sokolov, Jake S. Bobowski, Takuto Miyoshi, Yoshiteru Maeno, Andrew P. Mackenzie, Hubertus Luetkens, Clifford W. Hicks, and Hans-Henning Klauss. Split superconducting and time-reversal symmetry-breaking transitions in Sr_2RuO_4 under stress. *Nature Physics*, 17(6):748–754, Jun 2021.

[176] David A MacLean, Hok-Nam Ng, and JE Greedan. Crystal structures and crystal chemistry of the $RETiO_3$ perovskites: RE= La, Nd, Sm, Gd, Y. *Journal of Solid state chemistry*, 30(1):35–44, 1979.

[177] W. Knafo, C. Meingast, A. V. Boris, P. Popovich, N. N. Kovaleva, P. Yordanov, A. Maljuk, R. K. Kremer, H. v. Löhneysen, and B. Keimer. Ferromagnetism and lattice distortions in the perovskite $YTiO_3$. *Phys. Rev. B*, 79:054431, Feb 2009.

[178] A. C. Komarek, H. Roth, M. Cwik, W.-D. Stein, J. Baier, M. Kriener, F. Bourée, T. Lorenz, and M. Braden. Magnetoelastic coupling in $R\mathrm{TiO}_3$ ($R = \mathrm{La, Nd, Sm, Gd, Y}$) investigated with diffraction techniques and thermal expansion measurements. *Phys. Rev. B*, 75:224402, Jun 2007.

[179] J.E. Greedan. The rare earth-titanium (III) perovskite oxides - an isostructural series with a remarkable variation in physical properties. *Journal of the Less Common Metals*, 111(1):335 – 345, 1985.

[180] T. Katsufuji, Y. Taguchi, and Y. Tokura. Transport and magnetic properties of a Mott-Hubbard system whose bandwidth and band filling are both controllable: $\mathrm{R}_{1-x}\mathrm{Ca}_x\mathrm{TiO}_{3+y/2}$. *Phys. Rev. B*, 56:10145–10153, Oct 1997.

[181] Y. Okimoto, T. Katsufuji, Y. Okada, T. Arima, and Y. Tokura. Optical spectra in $(\mathrm{La,Y})\mathrm{TiO}_3$: Variation of Mott-Hubbard gap features with change of electron correlation and band filling. *Phys. Rev. B*, 51:9581–9588, Apr 1995.

[182] J.P. Goral, J.E. Greedan, and D.A. MacLean. Magnetic behavior in the series $\mathrm{La}_x\mathrm{Y}_{1-x}\mathrm{TiO}_3$. *Journal of Solid State Chemistry*, 43(3):244 – 250, 1982.

[183] Y Tokura. Metal-insulator phenomena in perovskites of transition metal oxide. *Physica B: Condensed matter*, 237:1–5, 1997.

[184] S. Hameed, J. Joe, D. M. Gautreau, J. W. Freeland, T. Birol, and M. Greven. Two-component electronic phase separation in the doped mott insulator $\mathrm{y}_{1-x}\mathrm{ca}_x\mathrm{tio}_3$. *Phys. Rev. B*, 104:045112, Jul 2021.

[185] D. Pelc, Z. Anderson, B. Yu, C. Leighton, and M. Greven. Universal superconducting precursor in three classes of unconventional superconductors. *Nat. Commun.*, 10(1):2729, Jun 2019.

[186] Sajna Hameed, Damjan Pelc, Zachary W Anderson, Avraham Klein, RJ Spieker, L Yue, Bhaskar Das, Justin Ramberger, Marin Lukas, Yaohua Liu, et al. Enhanced superconductivity and ferroelectric quantum criticality in plastically deformed strontium titanate. *Nature Materials*, 21(1):54–61, 2022.

[187] J.B. Goodenough. *Magnetism and the Chemical Bond*. Interscience monographs on chemistry. R. E. Krieger Publishing Company, 1976.

[188] Turan Birol, Nicole A. Benedek, Hena Das, Aleksander L. Wysocki, Andrew T. Mulder, Brian M. Abbett, Eva H. Smith, Saurabh Ghosh, and Craig J. Fennie. The magnetoelectric effect in transition metal oxides: Insights and the rational design of new materials from first principles. *Current Opinion in Solid State and Materials Science*, 16(5):227–242, Oct 2012.

[189] Pablo Rivero, Vincent Meunier, and William Shelton. Uniaxial pressure-induced half-metallic ferromagnetic phase transition in $LaMnO_3$. *Phys. Rev. B*, 93(9):094409, 2016.

[190] Ruihao Qiu, Eric Bousquet, and Andres Cano. Pressure-induced insulator–metal transition in $EuMnO_3$. *Journal of Physics: Condensed Matter*, 29(30):305801, 2017.

[191] Peter Horsch, Andrzej M Oleś, Louis Felix Feiner, and Giniyat Khaliullin. Evolution of spin-orbital-lattice coupling in the RVO_3 perovskites. *Phys. Rev. Lett.*, 100(16):167205, 2008.

[192] I Fita, R Szymczak, R Puzniak, IO Troyanchuk, J Fink-Finowicki, Ya M Mukovskii, VN Varyukhin, and H Szymczak. Pressure-tuned spin state and ferromagnetism in $La_{1-x}M_xCoO_3$ (M= Ca, Sr). *Phys. Rev. B*, 71(21):214404, 2005.

[193] K Mydeen, P Mandal, D Prabhakaran, and CQ Jin. Pressure-and temperature-induced spin-state transition in single-crystalline $La_{1-x}Sr_xCoO_3$ (x=0.10 and 0.33). *Phys. Rev. B*, 80(1):014421, 2009.

[194] Subir Sachdev. *Quantum Phase Transitions*. Cambridge University Press, Cambridge, England, second edition, 2011.

[195] S. A. Grigera, R. S. Perry, A. J. Schofield, M. Chiao, S. R. Julian, G. G. Lonzarich, S. I. Ikeda, Y. Maeno, A. J. Millis, and A. P. Mackenzie. Magnetic field-tuned quantum criticality in the metallic ruthenate $Sr_3Ru_2O_7$. *Science*, 294(5541):329–332, 2001.

[196] Ar. Abanov, Andrey V. Chubukov, and J. Schmalian. Quantum-critical theory of the spin-fermion model and its application to cuprates: Normal state analysis. *Advances in Physics*, 52(3):119–218, 2003.

[197] T. Senthil, Ashvin Vishwanath, Leon Balents, Subir Sachdev, and Matthew P. A. Fisher. Deconfined quantum critical points. *Science*, 303(5663):1490–1494, 2004.

[198] Hilbert v. Löhneysen, Achim Rosch, Matthias Vojta, and Peter Wölfle. Fermi-liquid instabilities at magnetic quantum phase transitions. *Rev. Mod. Phys.*, 79:1015–1075, Aug 2007.

[199] Ch. Rüegg, B. Normand, M. Matsumoto, A. Furrer, D. F. McMorrow, K. W. Krämer, H. U. Güdel, S. N. Gvasaliya, H. Mutka, and M. Boehm. Quantum magnets under pressure: Controlling elementary excitations in $TlCuCl_3$. *Phys. Rev. Lett.*, 100:205701, May 2008.

[200] R. Coldea, D. A. Tennant, E. M. Wheeler, E. Wawrzynska, D. Prabhakaran, M. Telling, K. Habicht, P. Smeibidl, and K. Kiefer. Quantum criticality in an Ising chain: Experimental evidence for emergent E_8 symmetry. *Science*, 327(5962):177–180, 2010.

[201] J. Larrea Jiménez, S. P. G. Crone, E. Fogh, M. E. Zayed, R. Lortz, E. Pomjakushina, K. Conder, A. M. Läuchli, L. Weber, S. Wessel, A. Honecker, B. Normand, Ch. Rüegg, P. Corboz, H. M. Rønnow, and F. Mila. A quantum magnetic analogue to the critical point of water. *Nature*, 592(7854):370–375, Apr 2021.

[202] Masatoshi Imada, Atsushi Fujimori, and Yoshinori Tokura. Metal-insulator transitions. *Rev. Mod. Phys.*, 70:1039–1263, Oct 1998.

[203] Patrick A. Lee, Naoto Nagaosa, and Xiao-Gang Wen. Doping a Mott insulator: Physics of high-temperature superconductivity. *Rev. Mod. Phys.*, 78:17–85, Jan 2006.

[204] G. Amow, J.-S. Zhou, and J.B. Goodenough. Peculiar magnetism of the $Sm_{1-x}Gd_xTiO_3$ system. *Journal of Solid State Chemistry*, 154(2):619–625, 2000.

[205] H. D. Zhou and J. B. Goodenough. Evidence for two electronic phases in $Y_{1-x}La_xTiO_3$ from thermoelectric and magnetic susceptibility measurements. *Phys. Rev. B*, 71:184431, May 2005.

[206] S. Hameed, S. El-Khatib, K. P. Olson, B. Yu, T. J. Williams, T. Hong, Q. Sheng, K. Yamakawa, J. Zang, Y. J. Uemura, G. Q. Zhao, C. Q. Jin, L. Fu, Y. Gu, F. Ning, Y. Cai, K. M. Kojima, J. W. Freeland, M. Matsuda, C. Leighton, and M. Greven. Nature of the ferromagnetic-antiferromagnetic transition in $Y_{1-x}La_xTiO_3$. *Phys. Rev. B*, 104:024410, Jul 2021.

[207] B. Keimer, D. Casa, A. Ivanov, J. W. Lynn, M. v. Zimmermann, J. P. Hill, D. Gibbs, Y. Taguchi, and Y. Tokura. Spin dynamics and orbital state in $LaTiO_3$. *Phys. Rev. Lett.*, 85:3946–3949, Oct 2000.

[208] Z. Y. Zhao, O. Khosravani, M. Lee, L. Balicas, X. F. Sun, J. G. Cheng, J. Brooks, H. D. Zhou, and E. S. Choi. Spin-orbital liquid and quantum critical point in $Y_{1-x}La_xTiO_3$. *Phys. Rev. B*, 91:161106, Apr 2015.

[209] Bing Li, Despina Louca, Jennifer Niedziela, Zongyao Li, Libin Zhang, Jianshi Zhou, and John B. Goodenough. Lattice and magnetic dynamics in perovskite $Y_{1-x}La_xTiO_3$. *Phys. Rev. B*, 94:224301, Dec 2016.

[210] G O Jones and P A Walker. Specific heats of fluid argon near the critical point. *Proceedings of the Physical Society. Section B*, 69(12):1348–1350, Dec 1956.

[211] Limei Xu, Pradeep Kumar, S. V. Buldyrev, S.-H. Chen, P. H. Poole, F. Sciortino, and H. E. Stanley. Relation between the Widom line and the dynamic crossover in systems with a liquid–liquid phase transition. *Proc. Natl. Acad. Sci. U.S.A.*, 102(46):16558–16562, 2005.

[212] G. G. Simeoni, T. Bryk, F. A. Gorelli, M. Krisch, G. Ruocco, M. Santoro, and T. Scopigno. The Widom line as the crossover between liquid-like and gas-like behaviour in supercritical fluids. *Nat. Phys.*, 6(7):503–507, Jul 2010.

[213] M. Brando, D. Belitz, F. M. Grosche, and T. R. Kirkpatrick. Metallic quantum ferromagnets. *Rev. Mod. Phys.*, 88:025006, May 2016.

[214] Jiun-Haw Chu, Hsueh-Hui Kuo, James G. Analytis, and Ian R. Fisher. Divergent nematic susceptibility in an iron arsenide superconductor. *Science*, 337(6095):710–712, 2012.

[215] Y. Sato, S. Kasahara, H. Murayama, Y. Kasahara, E.-G. Moon, T. Nishizaki, T. Loew, J. Porras, B. Keimer, T. Shibauchi, and Y. Matsuda. Thermodynamic evidence for a nematic phase transition at the onset of the pseudogap in $YBa_2Cu_3O_y$. *Nat. Phys.*, 13(11):1074–1078, Nov 2017.

[216] H. T. Stokes, D. M. Hatch, and B. J. Campbell. ISOSUBGROUP, ISOTROPY Software Suite, iso.byu.edu.

[217] Branton J. Campbell, Harold T. Stokes, David E. Tanner, and Dorian M. Hatch. ISODISPLACE : a web-based tool for exploring structural distortions. *Journal of Applied Crystallography*, 39(4):607–614, Aug 2006.

[218] Kao-Shien Liu and Michael E. Fisher. Quantum lattice gas and the existence of a supersolid. *Journal of Low Temperature Physics*, 10(5):655–683, Mar 1973.

[219] Amnon Aharony. Old and new results on multicritical points. *Journal of Statistical Physics*, 110(3):659–669, Mar 2003.

[220] H. D. Zhou and J. B. Goodenough. Evidence for two electronic phases in $Y_{1-x}La_xTiO_3$ from thermoelectric and magnetic susceptibility measurements. *Phys. Rev. B*, 71:184431, May 2005.

[221] Tetsuya Furukawa, Kazuya Miyagawa, Hiromi Taniguchi, Reizo Kato, and Kazushi Kanoda. Quantum criticality of Mott transition in organic materials. *Nat. Phys.*, 11(3):221–224, Mar 2015.

[222] H. Terletska, J. Vučičević, D. Tanasković, and V. Dobrosavljević. Quantum critical transport near the Mott transition. *Phys. Rev. Lett.*, 107:026401, Jul 2011.

[223] G. Sordi, K. Haule, and A.-M. S. Tremblay. Finite doping signatures of the Mott transition in the two-dimensional Hubbard model. *Phys. Rev. Lett.*, 104:226402, Jun 2010.

[224] Heike Eisenlohr, Seung-Sup B. Lee, and Matthias Vojta. Mott quantum criticality in the one-band Hubbard model: Dynamical mean-field theory, power-law spectra, and scaling. *Phys. Rev. B*, 100:155152, Oct 2019.

[225] R. A. Borzi, S. A. Grigera, J. Farrell, R. S. Perry, S. J. S. Lister, S. L. Lee, D. A. Tennant, Y. Maeno, and A. P. Mackenzie. Formation of a nematic fluid at high fields in $Sr_3Ru_2O_7$. *Science*, 315(5809):214–217, 2007.

[226] A. J. Millis, A. J. Schofield, G. G. Lonzarich, and S. A. Grigera. Metamagnetic quantum criticality in metals. *Phys. Rev. Lett.*, 88:217204, May 2002.

[227] Darrell G Schlom, Long-Qing Chen, Craig J Fennie, Venkatraman Gopalan, David A Muller, Xiaoqing Pan, Ramamoorthy Ramesh, and Reinhard Uecker. Elastic strain engineering of ferroic oxides. *Mrs Bulletin*, 39(2):118–130, 2014.

[228] Clifford W Hicks, Daniel O Brodsky, Edward A Yelland, Alexandra S Gibbs, Jan AN Bruin, Mark E Barber, Stephen D Edkins, Keigo Nishimura, Shingo Yonezawa, Yoshiteru Maeno, et al. Strong increase of T_c of Sr_2RuO_4 under both tensile and compressive strain. *Science*, 344(6181):283–285, 2014.

[229] Sara Riccò, Minjae Kim, Anna Tamai, Siobhan Mckeown Walker, Flavio Yair Bruno, Irène Cucchi, Edoardo Cappelli, Céline Besnard, Timur K Kim, Pavel Dudin, et al. In situ strain tuning of the metal-insulator-transition of Ca_2RuO_4 in angle-resolved photoemission experiments. *Nature communications*, 9(1):1–7, 2018.

[230] Shingo Tsubouchi, Toru Kyomen, Mitsuru Itoh, Parthasarthy Ganguly, Masaharu Oguni, Yutaka Shimojo, Yukio Morii, and Yoshinobu Ishii. Simultaneous metal-insulator and spin-state transitions in $Pr_{0.5}Ca_{0.5}CoO_3$. *Phys. Rev. B*, 66(5):052418, 2002.

[231] Shingo Tsubouchi, Tôru Kyômen, Mitsuru Itoh, and Masaharu Oguni. Electric, magnetic, and calorimetric properties and phase diagram of $Pr_{1-x}Ca_xCoO_3$ ($0 < x < 0.55$). *Phys. Rev. B*, 69:144406, Apr 2004.

[232] K Knížek, J Hejtmánek, P Novák, and Z Jirák. Charge transfer, valence, and the metal-insulator transition in $Pr_{0.5}Ca_{0.5}CoO_3$. *Phys. Rev. B*, 81(15):155113, 2010.

[233] José Luis García-Muñoz, Carlos Frontera, Aura J Barón-González, Sergio Valencia, Javier Blasco, Ralf Feyerherm, Esther Dudzik, Radu Abrudan, and Florin Radu. Observation of a valence transition in (Pr,Ca)CoO_3 cobaltites: charge migration at the metal-insulator transition. *arXiv preprint arXiv:1103.3646*, 2011.

[234] J Herrero-Martín, JL García-Muñoz, S Valencia, C Frontera, J Blasco, AJ Barón-González, G Subías, R Abrudan, F Radu, E Dudzik, et al. Valence change of praseodymium in $Pr_{0.5}Ca_{0.5}CoO_3$ investigated by x-ray absorption spectroscopy. *Phys. Rev. B*, 84(11):115131, 2011.

[235] Javier Herrero-Martín, Josep Lluís García-Muñoz, K Kvashnina, Erik Gallo, G Subías, JA Alonso, and Aura J Barón-González. Spin-state transition in $Pr_{0.5}Ca_{0.5}CoO_3$ analyzed by x-ray absorption and emission spectroscopies. *Phys. Rev. B*, 86(12):125106, 2012.

[236] Graham King and Patrick M Woodward. Cation ordering in perovskites. *Journal of Materials Chemistry*, 20(28):5785–5796, 2010.

[237] Jeremy P Allen and Graeme W Watson. Occupation matrix control of *d*- and *f*-electron localisations using DFT+U. *Physical Chemistry Chemical Physics*, 16(39):21016–21031, 2014.

[238] Georg Kresse and Daniel Joubert. From ultrasoft pseudopotentials to the projector augmented-wave method. *Phys. Rev. B*, 59(3):1758, 1999.

[239] Daniel Phelan, Kanwal Preet Bhatti, Matthew Taylor, Shun Wang, and Christopher Leighton. Magnetically inhomogeneous ground state below the first-order valence transition in $(Pr_{1-y}Y_y)_{0.7}Ca_{0.3}CoO_{3-\delta}$. *Phys. Rev. B*, 89(18):184427, 2014.

[240] Kai Liu, Sangwook Lee, Shan Yang, Olivier Delaire, and Junqiao Wu. Recent progresses on physics and applications of vanadium dioxide. *Materials Today*, 21(8):875–896, 2018.

[241] Cyril Proust and Louis Taillefer. The remarkable underlying ground states of cuprate superconductors. *Annual Review of Condensed Matter Physics*, 10:409–429, 2019.

[242] Philippe Ghosez and Javier Junquera. Modeling of ferroelectric oxide perovskites: From first to second principles. *Annual Review of Condensed Matter Physics*, 13:325–364, 2022.